

Resistance is Futile: Physical science, systems
biology and single-cell analysis to
understanding the plastic and heterogeneous
nature of melanoma and their role in non-
genetic drug resistance

Thesis by
Yapeng Su

In Partial Fulfillment of the Requirements for
the degree of
Doctor of Philosophy

The logo for the California Institute of Technology (Caltech), featuring the word "Caltech" in a bold, orange, sans-serif font.

CALIFORNIA INSTITUTE OF TECHNOLOGY
Pasadena, California

2020
(Defended November 22, 2019)

© 2020

Yapeng Su
ORCID: 0000-0002-6305-8467

ACKNOWLEDGEMENTS

As I come close to the end of the Ph.D. chapter in my life, I look back on this unforgettable journey and feel thankful for the help and support of so many amazing people without whom I would not have been able to complete this thesis. I would like to especially mention some individuals.

First and foremost, I would like to express my deepest gratitude to my primary advisor, Prof. James Heath, for having me in the lab and guiding and supporting me to explore the most cutting-edge science throughout my graduate study. He has given me an incredible amount of intellectual freedom to pursue my own research ideas and interest while always supporting me with unlimited resources and inspiring intellectual guidance throughout my scientific adventures. He, as an example of a great scientist and visionary leader, has indelibly enriched me and shaped my identity as a researcher. I feel lucky and proud to work with Jim and I could not imagine having a better advisor and mentor for my entire Ph.D. study.

I also want to extend my heartfelt thanks to my thesis co-advisor, Prof. David Baltimore, and my academic co-advisor, Prof. Mark Davis. In the most difficult times of my Ph.D., both of them took me under their wings and provided me with lab space, important guidance, and support throughout my graduate study.

My biology training from David and the Baltimore lab has been crucial for my Ph.D. research and for my training towards a mature scientist. David's support, enthusiasm, and guidance for the physical science and engineering approaches that I utilize to understand biology have been critical to shaping my scientific career. David's unlimited support and care for my career development have also been something I will always cherish.

Mark also had very strong influence on my academic training, especially in the field of chemical engineering, which is the major for both my undergraduate and my Ph.D. degrees. I am grateful for his unwavering guidance and support for my career advancement. He has set a remarkable example of how chemical engineering approaches can shift the paradigm of biomedical fields and help people fight against cancer. He is the ideal role model of a chemical engineer whom I want to learn from in my future career.

I also want to thank Prof. Zhen-Gang Wang and Prof. Dave Tirrell for taking the time to serve on my committee, providing me with research guidance, and being a part of my academic growth. Zhen-Gang is like one of my family: he cares about me as a person and

provided me with guidance and encouragement throughout my entire graduate life. In addition, Zhen-Gang's teaching really impressed me and set an example for how a great teacher should be. Dave has always been so nice to me in person and is willing to offer the most insightful points to guide my research. Many of his questions in my committee meetings are very critical and challenge me to grow as a better scientist and critical thinker.

I have been extremely fortunate to have the great opportunity to work with many great scientists throughout my entire Ph.D. Dr. Wei Wei, Dr. Min Xue, and Dr. Guideng Li were my postdoc mentors when I first started working in the Heath and Baltimore labs. They taught me the basic skillset that set the foundations for many of my research projects. They all now have their own research groups in different universities, but I still have the opportunity to continue collaborating with them. I want to thank Prof. Antoni Ribas for introducing me to the non-genetic drug resistance problem in melanoma, which turned out to be the main theme of my Ph.D. thesis. He also taught me all of the relevant melanoma biology and guided me throughout all of my research projects. Prof. Raphael Levine is my computational analysis mentor; the surprisal analysis he invented and taught me has been the most beautiful computational tool used throughout most of my Ph.D. projects for scientific discovery within huge dimensions of data.

I also want to thank my other senior collaborators from ISB, Stanford, and MIT, including Prof. Leroy Hood, Prof. Nathan Price, Prof. Nitin Baliga, Prof. Ilya Shmulevich, Prof. Sui Huang, Prof. Gary Nolan, Prof. Sylvia Plevritis, Prof. Aviv Regev, and Prof. Eric Lander for their support in many of the exciting collaborative projects.

My heartfelt appreciation also goes to my lab mates in the Heath, Baltimore and the Davis groups, including Dr. Wei Wei, Dr. Min Xue, Dr. Jing Zhou, Dr. Songming Peng, Dr. Jun Wang, Dr. Jing Yu, Dr. Nataly Balasha, Dr. David Bunk, Dr. Jake Kim, Dr. Amy McCarthy, Dr. Jingxin Liang, Dr. Alex Xu, Dr. Alphonsus Ng, Dr. Yue Lu, Dr. Matt Idso, William Chour, Dan Yuan, Dr. Guideng Li, Dr. Alok Joglekar, Dr. Shuai Jiang, Dr. Mati Mann, Dr. Luke Frankiw, Michael Leonard, Dr. Emily Wyatt and Dr. Jong Hun Kevin Kang, Dr. Viktor Cybulskis, Dr. Matthew Kale, and all other current and past members of the labs. I have the habit of working late nights in the lab, and was so fortunate to have the company of such a diverse group of people throughout different periods of my Ph.D.: when I started in the Heath lab at Caltech, Amy was always the person to keep me company during late nights in the lab, and she allowed me to use her "gaming computer" to analyze huge RNA-seq datasets for my research project; later on, when I moved to the Baltimore lab, I was lucky to have Luke be together with me when I worked late in the lab. Kevin is the one in the Davis lab who will

always make Chinese teas for me late at night; and now when I move to ISB, I have William, who stays late together with me working in the lab. Their company and support throughout my graduate journey across different labs and institutions is something that always warms my heart when I look back.

I also want to give special thanks to many other Caltech faculties. Prof. Frances Arnold was my first mentor in Caltech when I did my first graduate-school rotation. She is the one who arranged my pickup from LAX when I first arrived in this new country far from home. She and her lab helped me adapt to life in the U.S. Although I did not end up joining her lab, I feel lucky to still have her guidance and advice for my future career development. Prof. Lu Wei (and her student Jiajun Du) has been such a great and supportive collaborator; I really enjoyed the beautiful science we discovered during our collaboration and I wish to continue working with her in my future academic career. Prof. Ellen Rothenberg and her student Xun Wang (and Xun's wife Can Li) has been a great resource for me in the epigenomics fields, which is a critical part of my Ph.D. research. When I TA'd for Prof. Ismagilov, I learned how to be a well-planned and organized teacher. As the option representative of the chemical engineering department, Prof. Giapis has been a great resource for me throughout my graduate study and life.

I would also like to acknowledge my undergraduate advisors Prof. Yingjin Yuan, Prof. Rongxin Su, and Prof. Zhimin He, who first got me into scientific research and gave me the tools I needed to pursue my Ph.D.

One of the most fulfilling and unforgettable experience in my graduate school is to mentor young, hardworking, and talented undergraduate students. I was so fortunate to mentor and work with Jihoon Lee, Rachel Ng, Marcus Bintz, Gabe Dreiman, Anne Chen, Victoria Liu, Stephanie Wong, Jessica Wang, Kaitlyn Takata, Sarah Pack, and Daniel Chen. They all have made great contributions to my papers and I am so glad to see many of them now becoming Ph.D. or M.D. Ph.D. candidates in many top universities.

My life in graduate school would not have been nearly as enjoyable without the many friends I met at Caltech, including but not limited to Dr. Xiaozhou Ruan, Dr. Qifan Yang, Dr. Shuai Wang, Xiawei Huang, Yandong Zhang, Xiaozhe Ding, Ronghui Zhu, Xun Wang, Can Li, Jiajun Du, Dr. Peng He, Dr. Haoqing Wang, Dr. Zixuan Shao, Chengcheng Fan, Yicheng Luo, Sheng Wang, Yitong Ma, Hanwei Liu, Weilai Yu, Shan Huang, Jiaming Li, Kai Chen, Kun Miao, Chenxi Qian, Xinyan Liu, Xinhong Chen, Ruohan Wang, Yalu Chen, Dr. Yufeng Huang, Dr. Yuanyue Liu, Dr. Sijia Dong, Dr. Jin Qian, Dr. Amy McCarthy, William Chour,

Dr. Alphonsus Ng, Dr. Yue Lu, Dr. Matt Idso, Dr. Luke Frankiw, Dr. Alok Joglekar, Dr. Mati Mann, Dr. Emily Wyatt, Dr. Jong Hun Kevin Kang, Dmitriy Zhukov, Roberta Poceviute, Ahmad Omar, Nick Porubsky, and many others.

I would also like to thank every staff member of my labs, my department, and graduate office and international student program of Caltech, including but not limited to Elyse Garlock, Katrine Museth, Dazy Johnson, Rick Edmark, Theresa Davis, Katie Clark, Julie Kelly, Martha Hepworth, Allison Kinard, Kathy Bubash, Natalie Gilmore, Angelica Medina-Cuevas, Laura Flower Kim, and Daniel Yoder.

Last, and by no means least, I owe a debt of gratitude to my family, especially my parents who have shaped the person I have become. I can never repay them for their unlimited love and care.

ABSTRACT

Melanoma is the most deadly form of skin cancer due to its great metastatic potential. Targeted therapy that inhibits the BRAF-V600E driver mutation has shown impressive initial responses in melanoma patients. However, drug resistance, as the universal phenomenon for any cancer therapy, always limits treatment efficacy and compromises outcomes. As the early-step of resistance development, non-genetic mechanisms enable cancer cells to transition into a drug-resistant state in as early as a few days after drug treatment without alteration of the genome. This early mechanism is, to a large extent, due to the heterogeneous and highly plastic nature of tumor cells. Therefore, it is imperative to understand the plastic and heterogeneous nature of the melanoma cells in order to identify combination therapies that can overcome resistance.

In this thesis, we investigate these two fundamental natures of non-genetic drug resistance using BRAF inhibition of BRAF-mutant melanomas as the model system. These melanoma cells undergo multi-step, reversible drug-induced cell-state transitions from the original sensitive phenotype to a drug-resistant one.

We first conducted bulk analysis to characterize the detailed kinetics of the entire transition from drug-sensitive state towards drug-resistant state, revealing expression changes of thousands of genes and extensive chromatin remodeling. A 3-step computational biology approach greatly simplified the complexity and revealed that the whole cell-state transition was controlled by a gene module activated within just the first three days of drug treatment, with the RelA transcription factor driving chromatin remodeling to establish an epigenetic program encoding long-term phenotype changes towards resistance. From there, a detailed mechanism connecting tumor epigenetic plasticity with non-genetic drug resistance was resolved through in-depth molecular biology experiments. The mechanism was validated in clinical patient samples.

We further investigated heterogeneity by moving from bulk cellular studies to single-cell analysis. The single-cell view further revealed that two driving forces from both cell-state interconversions and phenotype-specific drug selection control the cell-state transition

dynamics. The single-cell studies also pinpointed the signaling network hub, RelA, as the driver molecule of the initiation of the adaptive transition. These two competing driving forces were further quantitatively modeled via a thermodynamic-inspired surprisal analysis and a modified Fokker-Planck-type kinetic model.

Finally, using integrated single-cell proteomic and metabolic technology I developed to characterize the early-stage signaling and metabolic changes upon initial drug responses, we further identified two distinct paths connecting drug-sensitive and drug-tolerant states. Melanoma cells exclusively traverse one of the two paths depending on the level of MITF in the drug-naïve cells. The two trajectories are associated with distinct signaling and metabolic susceptibilities and are independently druggable.

In total, this thesis combines and synergizes various physical science and systems biology approaches together with several unique single-cell technologies and analysis to obtain a deep and comprehensive understanding of non-genetic drug resistance in cancer. The findings from this thesis provide several novel insights into the rational design of effective combination therapy for overcoming the development of resistance in response to cancer treatments.

PUBLISHED CONTENT AND CONTRIBUTIONS

- [1] **Su, Yapeng**, Guideng Li, Melissa E. Ko, Hanjun Cheng, Ronghui Zhu, Min Xue, Jessica Wang et al. "Trajectories from Snapshots: Integrated proteomic and metabolic single-cell assays reveal multiple independent adaptive responses to drug tolerance in a BRAF-mutant melanoma cell line." *Nature Communications* (Under revision). doi: 10.1101/767988
Y.S. participated in conception of the project, performed most of the experiments, lead the analysis and interpretation of the data, and participated in writing the paper.
- [2] **Su, Yapeng**, Xiang Lu, Guideng Li, Chunmei Liu, Yan Kong, Jihoon W. Lee, Rachel Ng et al. "Kinetic Inference Resolves Epigenetic Mechanism of Drug Resistance in Melanoma." *Cancer cell* (Under revision). doi: 10.1101/724740
Y.S. participated in conception of the project, performed most of the experiments, established the computational models, analyzed the data, and participated in writing the paper.
- [3] **Su, Yapeng**, Marcus Bintz, Yezi Yang, Lidia Robert, Alphonsus HC Ng, Victoria Liu, Antoni Ribas, James R. Heath, and Wei Wei. "Phenotypic heterogeneity and evolution of melanoma cells associated with targeted therapy resistance." *PLoS computational biology* 15, no. 6 (2019): e1007034. doi: 10.1371/journal.pcbi.1007034.
Y.S. participated in conceptualization, formal analysis, experimental investigation, methodology development, and writing the paper.
- [4] **Su, Yapeng**, Wei Wei, Lidia Robert, Min Xue, Jennifer Tsoi, Angel Garcia-Diaz, Blanca Homet Moreno et al. "Single-cell analysis resolves the cell state transition and signaling dynamics associated with melanoma drug-induced resistance." *Proceedings of the National Academy of Sciences* 114, no. 52 (2017): 13679-13684. doi:10.1073/pnas.1712064115
Y.S. participated in conception of the project, performed most of the experiment, developed the computational model, and participated in analysis of the data and writing of the paper.
- [5] **Su, Yapeng**, Qihui Shi, and Wei Wei. "Single cell proteomics in biomedicine: High-dimensional data acquisition, visualization, and analysis." *Proteomics* 17, no. 3-4 (2017): 1600267. doi: 10.1002/pmic.201600267.
Y.S. participated in the conception of the study and writing of the manuscript.
- [6] Xue, Min, Wei Wei, **Yapeng Su**, Dazy Johnson, and James R. Heath. "Supramolecular probes for assessing glutamine uptake enable semi-quantitative metabolic models in single cells." *Journal of the American Chemical Society* 138, no. 9 (2016): 3085-3093. doi: 10.1021/jacs.5b12187
Y.S. participated in the conception of the study, experiments, and data analysis.
- [7] Xue, Min, Wei Wei, **Yapeng Su**, Jungwoo Kim, Young Shik Shin, Wilson X. Mai, David A. Nathanson, and James R. Heath. "Chemical methods for the simultaneous quantitation of metabolites and proteins from single cells." *Journal of the American Chemical Society* 137, no. 12 (2015): 4066-4069. doi: 10.1021/jacs.5b00944.
Y.S. participated in the conception of the study, experiments, and data analysis.

- [8] Wei, Wei, Young Shik Shin, Min Xue, Tomoo Matsutani, Kenta Masui, Huijun Yang, Shiro Ikegami, Yuchao Gu, Ken Herrmann, Dazy Johnson, Xiangming Ding, Kiwook Hwang, Jungwoo Kim, Jian Zhou, **Yapeng Su**, Xinmin Li, Bruno Bonetti, Rajesh Chopra, C. David James, Webster K. Cavenee, Timothy F. Cloughesy, Paul S. Mischel, James R. Heath, Beatrice Gini. "Single-cell phosphoproteomics resolves adaptive signaling dynamics and informs targeted combination therapy in glioblastoma." *Cancer cell* 29, no. 4 (2016): 563-573. doi: 10.1016/j.ccell.2016.03.012.
Y.S. participated in the conception of the study, experiments, and data analysis.
- [9] Zhou, Jing, Michael T. Bethune, Natalia Malkova, Alexander M. Sutherland, Begonya Comin-Anduix, **Yapeng Su**, David Baltimore, Antoni Ribas, and James R. Heath. "A kinetic investigation of interacting, stimulated T cells identifies conditions for rapid functional enhancement, minimal phenotype differentiation, and improved adoptive cell transfer tumor eradication." *PloS one* 13, no. 1 (2018): e0191634. doi: 10.1371/journal.pone.0191634.
Y.S. participated in the conception of the study, experiments, and data analysis.
- [10] Li, Guideng, Michael T. Bethune, Stephanie Wong, Alok V. Joglekar, Michael T. Leonard, Jessica K. Wang, Jocelyn T. Kim, Donghui Cheng, Songming Peng, Jesse M. Zaretsky, **Yapeng Su**, Yicheng Luo, James R. Heath, Antoni Ribas, Owen N. Witte and David Baltimore. "T cell antigen discovery via trogocytosis." *Nature methods* 16, no. 2 (2019): 183. doi: 10.1038/s41592-018-0305-7.
Y.S. participated in experiments and data analysis.
- [11] Li, Guideng, Alex Yick-Lun So, Reeshelle Sookram, Stephanie Wong, Jessica K. Wang, Yong Ouyang, Peng He, **Yapeng Su**, Rafael Casellas, and David Baltimore. "Epigenetic silencing of miR-125b is required for normal B-cell development." *Blood* 131, no. 17 (2018): 1920-1930. doi: 10.1182/blood-2018-01-824540.
Y.S. participated in experiments and data analysis.
- [12] Peng, Songming, Jesse M. Zaretsky, Alphonsus HC Ng, William Chour, Michael T. Bethune, Jongchan Choi, Alice Hsu, Elizabeth Holman, Xiaozhe Ding, Katherine Guo, Jungwoo Kim, Alexander M. Xu, John E. Heath, Won Jun Noh, Jing Zhou, **Yapeng Su**, Yue Lu, Jami McLaughlin, Donghui Cheng, Owen N. Witte, David Baltimore, Antoni Ribas, James R. Heath. "Sensitive Detection and Analysis of Neoantigen-Specific T Cell Populations from Tumors and Blood." *Cell reports* 28, no. 10 (2019): 2728-2738. doi: 10.1016/j.celrep.2019.07.106.
Y.S. participated in experiments and data analysis.
- [13] Xu, Alexander M., Qianhe Liu, Kaitlyn L. Takata, Sarah Jeoung, **Yapeng Su**, Igor Antoshechkin, Sisi Chen, Matthew Thomson, and James R. Heath. "Integrated measurement of intracellular proteins and transcripts in single cells." *Lab on a Chip* 18, no. 21 (2018): 3251-3262. doi: 10.1039/c8lc00639c.
Y.S. participated in the conception of the study, experiments, and data analysis.

TABLE OF CONTENTS

Acknowledgements.....	iii
Abstract	vii
Published Content and Contributions.....	ix
Table of Contents.....	xii
Chapter 1: Introduction.....	1
Melanoma, BRAFi Targeted Therapy, and Drug Resistance	1
Non-Genetic Drug Resistance and Cellular Plasticity.....	4
Physical Science and Systems Biology Approaches to Understanding Cancer	6
Tumor Heterogeneity and Single-Cell Analysis.....	7
Thesis Overview	11
References	14
Chapter 2: Kinetic Inference Resolves Epigenetic Mechanism of Drug Resistance in Melanoma.....	20
Introduction.....	21
Results.....	22
Discussion.....	34
Experimental Model and Subject Details	38
Quantification and Statistical Analysis	44
Data and Software Availability.....	50
Figures.....	51
Supplementary Information	63
References.....	80
Chapter 3: Single Cell Analysis Resolves the Cell State Transition and Signaling Dynamics associated with Melanoma Drug-Induced Resistance....	87
Introduction.....	88
Results.....	89
Discussion.....	94
Materials and Methods	96
Figures.....	97
References.....	102
SI Appendix	104
Chapter 4: Phenotypic Heterogeneity and Evolution of Melanoma Cells associated with Targeted Therapy Resistance	148
Introduction.....	149
Results.....	150
Discussion.....	157
Materials and Methods	160
Figures.....	166
Supplementary Information	172

References.....	186
Chapter 5: Trajectories from Snapshots: Integrated Proteomic and Metabolic Single-Cell Assays Reveal Multiple Independent Adaptive Responses to Drug Tolerance in a Braf-Mutant Melanoma Cell Line.....	191
Introduction.....	192
Results.....	193
Discussion.....	199
Methods	202
Figures.....	207
Supplementary Information	214
References.....	223

INTRODUCTION

Melanoma, BRAFi Targeted Therapy and Drug Resistance

Cancer is a leading cause of death worldwide, accounting for an estimated 9.6 million deaths in 2018. With all of the cancer deaths, 90% are caused by metastases [1]. Melanoma, as one of the most metastatic of all cancers, is the most deadly form of skin cancer. It is the fifth most common type of new cancer diagnosis in American men and the seventh most common type in American women [2,3]. During 40 years of employing chemotherapy, radiation, and combinations of the two, limited progress has been made in the treatment of metastatic melanoma [4].

A deeper and more detailed understanding of the molecular drivers of cancer development facilitated a trend from the old "one-size-fits-all" chemo/radiotherapy towards a more personalized and less cytotoxic "molecular targeted therapy" [5–8]. Molecular targeted therapy is a class of medication that interferes with specific molecules that are critical for tumor progression to block the growth and spread of cancer [5,7]. Targeted therapy focuses on a specific abnormal molecular property present in cancer but not in normal cells. This potentially makes targeted therapy more effective and less toxic to normal cells given that traditional chemotherapy targets all rapidly dividing cells (Fig1.1) [4,5,7].

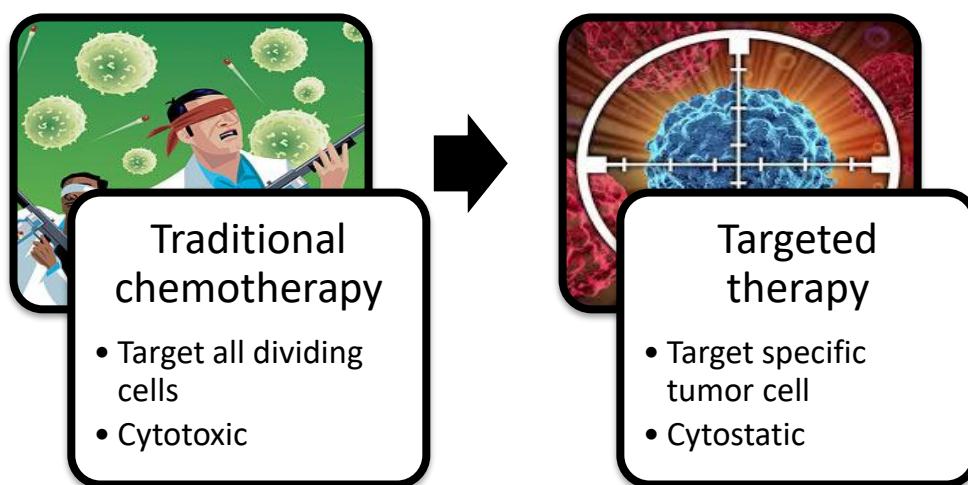


Figure 1.1. Comparison of traditional chemotherapy and targeted therapy. The targeted therapy is superior to traditional chemotherapy in both increased specificity and less cytotoxicity.

Targeted therapy tailored to specific mutations that dominantly activate mitogenic signaling of the tumor has been shown to be effective in several recent examples: ALK, EGFR, KIT, HER2, and ABL kinases inhibitor have unprecedented clinical activity in those tumors that are caused by a certain genetic mutation [9–11]. However, in most cases, the patient relapsing and the cancer progress after the significant but temporary clinical response. Melanoma with BRAF *V600E* driver mutation is one of the most remarkable illustrations of this phenomenon [12–14].

The RAS/RAF/MEK/ERK signaling pathway plays a key role in melanoma development making it an important therapeutic target [15]. In normal cells, the tightly regulated pathway relays extracellular proliferative signals from cell surface receptor into the nucleus via a cascade of protein phosphorylation. In melanomas, oncogenic mutations dysregulate the pathway which leads to increased signaling activity promoting cell proliferation, invasion, metastasis, migration, survival, and angiogenesis (Fig. 1.2) [16–18]. Among all mutated genes in the MAPK signaling cascade in melanoma, BRAF is the highest, with more than 60% of advanced tumors expressing constitutively active mutant protein. Almost all of the BRAF mutants are the single substitution *V600E*, whose discovery spurred investigations into the development of targeted therapies for melanoma [13–15,19].

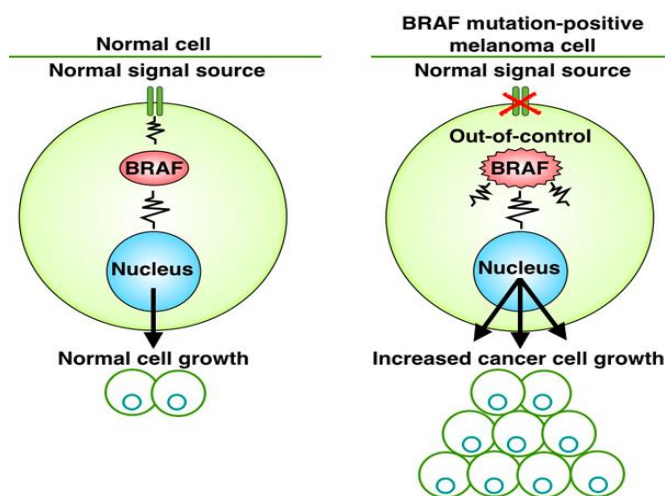


Figure 1.2. BRAF-*V600E* oncogenic driver mutation and its effects. In normal cells, if growth signal exists, will BRAF become active and promote cell growth. In BRAF-*V600E* melanoma, the mutated BRAF is always activated even if there is no growth signal. This effect will cause the cell to hyperactively proliferate and lead to cancer formation. (Figure is taken from [20])

Inhibition of the oncogenic BRAF-*V600E* protein with the small, orally available molecule inhibitor PLX4032 (vemurafenib, also known as VEM) showed impressive initial responses in patients with BRAF mutant melanoma [13,14]. Patients treated with vemurafenib had a significant response: the great majority of treated patients experienced a reduction in tumor volume and nearly half had a confirmed partial or complete response [12–14]. These led to the FDA (Food and Drug Administration)-approval of vemurafenib in 2011 and a dramatic improvement in the standard of care for the patients with BRAF-*V600E* oncogenic mutation [14].

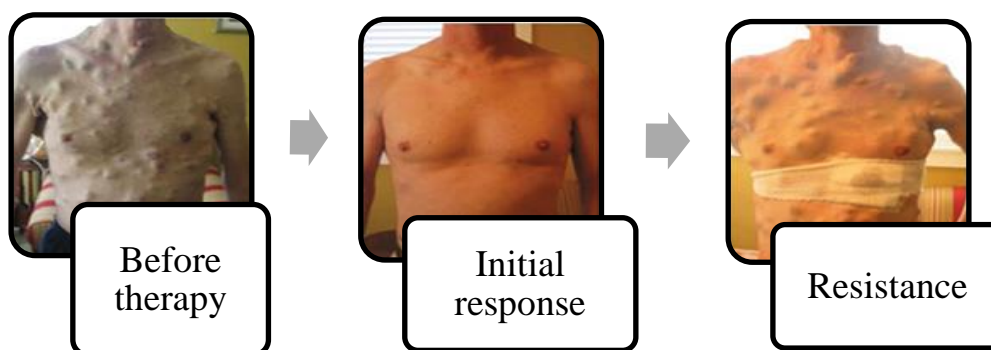


Figure 1.3. Targeted therapy resistance in melanoma. It is a very common phenomenon that BRAF mutated melanoma patients treated with BRAFi targeted therapy will have a good initial response, but will almost always suffer from tumor reoccurrence. Figure adapted from [21].

However, in most of these patients, despite their initial tumor shrinkage, tumor relapse is inevitable after a median duration of around 5 to 7 months indicating resistance development (Fig. 1.3) [9,21]. A diverse range of molecular mechanisms have been reported in drug resistance; these include increased rates of drug efflux, mutation of drug targets, adaptive activation of survival signaling pathway, epigenetic changes, etc. [22–27] Moreover, the high plasticity and heterogeneity of melanoma make the investigation of resistance mechanism more complicated [28–30]. Therefore, it is imperative first to understand the plastic and heterogeneous nature of the tumor and the connections to drug resistance, and second to identify potential combination therapies that will overcome resistance.

Non-Genetic Drug Resistance And Cellular Plasticity

Traditionally, drug resistance was believed to derive from the selection of clones with secondary mutations or other genomic alterations that are generated by chance during the time course of treatment [31]. Although this genetic mechanism of resistance is still the dogma for explaining resistance development, recently, the non-genetic type of mechanism has also been recently recognized as another important alternative route for acquiring resistance without even alternating the genome [32–35]. In fact, these two types of mechanisms are not mutually exclusive, since the non-genetic resistance is believed to occur early on and provide a reservoir of drug-tolerant cells from which the genetic-resistant cells can be selected (Fig. 1.4) [36,37] (Fig.1.4).

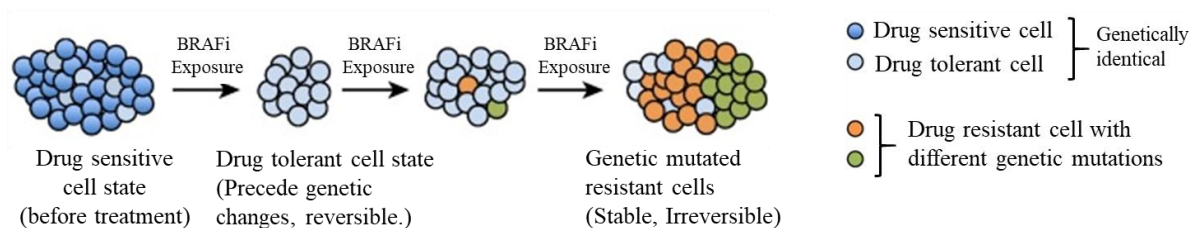


Figure 1.4. The relationship between genetic and non-genetic mechanisms of resistance. Upon drug treatment, the cancer cells will first enter a drug-tolerant state, which shares the exact same genome as the untreated cells but can tolerate the drug and survive. Cells at this drug-tolerant cell state can reversibly return to the drug-sensitive state upon drug removal. With prolonged drug treatment, this reservoir of drug-tolerant cells will have some chance to gain secondary mutations or other genetic alterations to become genetic-resistant cells. These genetic resistant cells once generated from the reservoir of tolerant cells can then be further enriched due to drug selection pressure as they are stable and are irreversibly different from the original tumor cells due to changes in the genome. Figures adapted from [38].

The non-genetic resistance is, to a large extent, caused by the plasticity of cancer cells, formally defined as the cells' ability to change phenotype without alternating the genome. In fact, such an ability to change phenotype is not unique to cancer cells, but rather a universal process utilized in all healthy cells. A simple example is to consider the human body: as a multi-cellular organism, all humans have many different cell types (e.g. blood cell, skin cell, muscle cell, etc.), displaying different gene expression programs and performing very different functions; but considering the origin of life, those different cell types are all originally derived from the same single cell (a fertilized egg cell) and therefore share the exact same genome. It is the cellular plasticity that grants the diverse cellular phenotypes in our bodies. Many healthy cells, once committed to their respective phenotypes, will lose their ability to change phenotype (e.g. a skin cell cannot spontaneously change to a blood cell and vice versa). In contrast, cancer cells maintain their cellular plasticity and can easily switch phenotypes upon exposure to environmental changes. In particular, during the time course

of treatment the cancer cell can utilize this plasticity to survive by changing its phenotype from the original drug-sensitive one to a new drug-tolerant one.

Several labs including the Heath group recently discovered that melanoma cells can utilize their innate plasticity to develop resistance to BRAF inhibitor drugs [30,39–41]. Upon BRAFi treatment, melanoma cells can acquire a new stem-cell-like phenotype simply by accessing the cell states of their developmental precursors. Melanoma is skin cancer that is originally derived from a healthy skin cell type called melanocyte, which are the cells that produce the skin-color pigment melanin. Healthy melanocytes are originally differentiated from healthy neural-crest stem cells [42]. In melanoma, the drug-resistance development process resembles the reverse process of such developmental biology. Before drug treatment, melanoma cells are typically in the melanocytic cell state with many melanocytic genes highly upregulated. However, upon BRAF inhibitor treatment, cells gradually lose their melanocytic features and gain neural-crest stem cell features to dedifferentiate into a neural-crest-like cell state, which is a drug-tolerant and slow cycling cell state [39–41]. After prolonged BRAFi treatment, the cell can undergo further transition from the neural-crest-like state to a fully dedifferentiated mesenchymal phenotype (Fig. 1.5), which is also a well-known fully resistant phenotype in BRAFi treatment melanoma cells [43,44]. All three phenotypes involved in this multi-step cell state transition share the same genome but the last two phenotypes are not sensitive to the drug anymore. Investigating the molecular mechanism of such cell-state transitions is an unmet need in order to understand and prevent resistance development. This is the central topic of the thesis and will be discussed in more detail in the subsequent chapters.

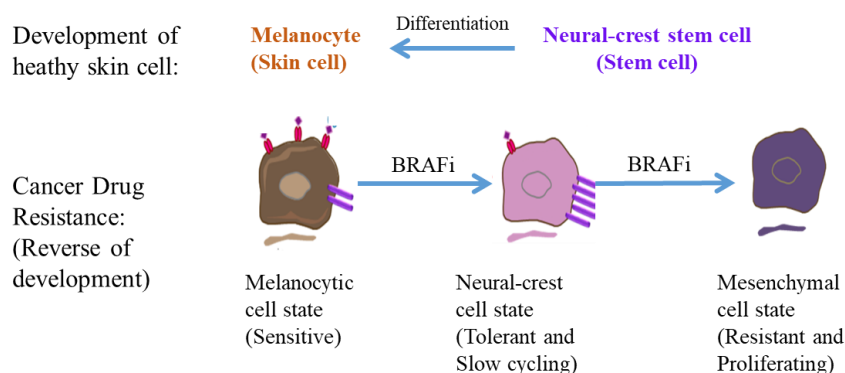


Figure 1.5 Melanocyte to neural-crest transition in BRAFi induced drug resistance of melanoma cell. Upon BRAFi treatment, melanoma cells will de-differentiate from a melanocytic phenotype to the neural-crest like phenotype and eventually move towards the mesenchymal phenotype to gain drug resistance.

Physical Science and Systems Biology Approaches to Understanding Cancer

Non-genetic drug resistance and the associated cell state transitions are usually systems-level changes accompanied by expression changes of thousands of genes, with a dramatic restructuring of the epigenome, as well as rewiring of many signaling pathways and reprogramming of the metabolism. Luckily, recent technological advances have enabled investigation of the major changes and the reprogramming of the epigenome [45,46], transcriptome [47], proteome [48], and metabolome [49] of either bulk cell populations or even single cells [50,51]. This capability enables researchers to have a more complete, unbiased view of complex biological events.

From the perspectives of physical scientists and engineers, this thesis views biological processes as highly coordinated systems with many interacting units (genes, proteins, metabolites) functioning under the constraint of a regulatory network. The unbiased systems-level view from many of the recent or emergent technologies is just starting to provide physical scientists and engineers with the proper foundation to better understand the biological complexity through statistical mechanics, thermodynamics and reaction kinetics.

Such physical science and systems biology approaches, when utilized to investigate drug resistance in cancer, can have many unique advantages. First, it is highly unbiased since a systems-level view enables people to see many regulators simultaneously [52]. On the contrary, traditional approaches are a bit biased since they usually focus on no more than a few molecules of interest. Second, systems-level approaches can be predictive and preventative [53]. Instead of waiting until drug resistance occurs and proceeding to treat the resistant cells, these approaches anticipate how the cancer cell will become resistant by looking for the molecular drivers that initiate resistance early on. By drugging such molecular drivers, one could potentially prevent resistance before it actually establishes. With such advantages, an interdisciplinary physical science and systems biology approach is perfectly suited for understanding both the nature of resistance and the underlying mechanism. In fact, thermodynamics-inspired information-theoretical analysis (surprisal analysis) [54], as well as reaction kinetics (ordinary differential equations and partial differential equations), are the key systems-biology approaches utilized in this thesis in resolving the puzzles of drug resistance, which will be discussed in many of the following chapters.

Tumor Heterogeneity and Single-Cell Analysis

Biological processes under single-cell levels are rarely deterministic [55]. Such stochastic information it is very hard to gain from the traditional bulk assay, which is often based on lysis of complex cell populations into mixtures to enable an analysis of their component parts. The differences among cells, which have been recently repeatedly shown to be important, are often lost in traditional bulk biochemical approaches due to averaging cell

signals across the entire cell mixture sample. When it comes to a tumor with an immense amount of genetic and epigenetic heterogeneity the phenotypic differences among subpopulations (including renewal capacity and drug resistance, etc.) are far from fully characterized [56–58]. An incomplete understanding of the tumor was previously largely due to the lack of effective tools for characterizing the difference among individual cells [56]. Luckily, many powerful single-cell technologies have just been developed in the past few years, including many from the Heath lab [59–62]. Now is the perfect time to utilize these novel single-cell tools to study heterogeneous tumor systems. A deeper understanding of resistance from single-cell tools can guide the rationale design of a more effective combination therapy to overcome the clinical negative effects of classic therapeutic approaches (including non-response to therapy or drug resistance after the initial response).

In recent years, major advances in single-cell technology have mostly focused on the genomic and transcriptomic levels, which are both studying nucleic acids that can be amplified through PCR reactions for sequencing. Reported technologies include whole-genome sequencing (WGS), whole mRNA transcriptome sequencing; and targeted sequencing of DNA regions (that is, exome sequencing) or mRNA transcripts [51,59,63,64]. Protein abundance and protein-phosphorylation states are also of great importance to study tumor heterogeneity, but are difficult to characterize because proteins cannot be amplified, in a manner similar to PCR, to provide enough material for analysis. Currently, single-cell functional proteomics technologies are not as mature, with just a few technologies presently available, ranging from flow cytometry to microfluidics-based platforms (many of which are listed and briefly characterized in Table 1.) Within all of these single-cell proteomic techniques, this thesis primarily utilizes the single-cell barcode chip (SCBC) technology that has been developed and well used in the Heath group.

Table 1.1 Single-cell proteomics technologies (adapted from [63])

<i>Technique</i>	Numbers and types of protein assayed	Through put	Detection limit	Statistical accuracy and signal quantification	Notes and feature
<i>Fluorescence flow cytometry</i>	Up to 15 proteins but mostly membrane protein	10 ⁴ cell per second	500 copies per cell	90% phenotyping accuracy; relative protein abundance	Standard for sorting and enumeration of cellular phenotypes. Secretion blocked and cell fixed for cytoplasmic protein
<i>Cytof</i>	Up to around 40	10 ³ cell per second	more than 1000 copies per cell	good counting statistics; relative protein abundance	cell handled in bulk prior to analysis. Secretion blocked and cell fixed for cytoplasmic protein
<i>Micro-engraving</i>	3 secreted plus 3 membrane proteins	10 ⁵ cell per chip	Not available	Very good cell number statistics; relative protein abundance	Cells isolated in microwells; surface immunoassay: protein colorimetrically detected; secretome kinetics from single cells; proteomic and functional assays from the same cell
<i>Single-cell barcode chips</i>	Up to 46 secreted membrane or cytoplasmic proteins	10 ³ to 10 ⁵ cell per chip	100 copies	Good cell counting statistics, absolute quantification	Cells isolated in microchambers miniature antibody arrays yield spatial separation of specific protein assay; proteomic and functional assay from the same single cell; adaptable for small cell group study

SCBCs can connect genomic information to biological function via quantitative assays of a panel of functional proteins (typically 14 to 46 proteins) across hundreds to thousands of single cells [61,62,65,66]. The SCBC concept is simple: a single or defined number of cells are isolated within a small volume microchamber that contains a miniature antibody array for the capture and detection of a panel of proteins via sandwich ELISA-like assays. Although the amount of proteins from a single cell is very low and cannot be amplified directly through PCR reaction, the microfluidic device shrinks the reaction volume of the chamber to several nanoliter; therefore, the concentration is maintained at a high enough level for detection and quantification.

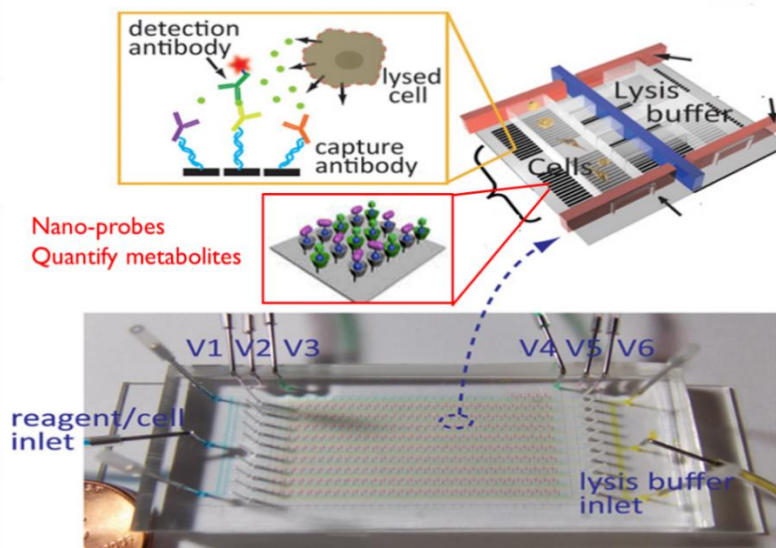


Figure 1.6. The workflow of a single-cell barcode chip. The single-cell suspension has flowed into the microfluidic device and cells will be captured into nano-liter-sized chambers. Once the cells are captured, perturbing, lysing and analyzing single cells within the chamber is also feasible through programming the nano-liter fluid. As shown in the zoom-in view of an individual chamber, cells were trapped at the left-hand side of the chamber and the lysis buffer is at the other side of the chamber, separated by the blue valve in between. When releasing the blue valve, the lysis buffer will be able to diffuse to the other side and lyse the cell. The intracellular proteins will then be released into the chamber for quantification. At the bottom of each chamber, there are barcoded arrays of antibodies installed orderly. These antibodies will capture proteins of our interest in order. So, simply by adding stripes in the chamber we can increase the multiplicity all the way to more than 40 different analytes. After the proteins are capture onto the antibody, we will be loading another set of detection antibodies with dye on it to convert the captured protein abundance into fluorescent intensity readout. Based on such multi-functional, programmable, nano-chamber, many important regulators from each individual cell are quantified simultaneously, and hundreds to thousands of single-cells can be analyzed simultaneously on one chip. Figure adapted from [67,68]

SCBCs have been developed into a robust tool with benchtop to bedside applications already demonstrated, and are currently being commercialized through a company called “IsoPlexis”. Applications of SCBC include predicting drug resistance in GBM tumors [67], predicting tissue structures [69], and patient monitoring for cancer immunotherapy trials [61,70]. SCBCs have also been validated against flow cytometry and various bulk immunoassays on cell lines and primary cells. Compared to flow cytometry or mass cytometry (cytof), SCBC offers the following advantages: (i) as few as 1000 cells can be studied [71], (ii) protein levels and measurement errors are both absolutely quantitated, in copy numbers of molecules [72], (iii) the local environment of the cell can be controlled (iv) discrete cell populations can be assayed to measure cell-cell interactions [73] and (v) SCBCs are cost-effective. Absolute quantitation of protein levels enables direct comparisons across cell types, proteins, time

points, and patient samples, etc. While such quantitation is standard in the physical sciences, it is novel (and challenging) in biology. Absolute quantitation of protein level quantitation also opens up the possibility of using theories derived from physico-chemical principles and/or statistic methods to investigate cellular steady states, perturbations, etc. In fact, the combination of SCBC based single-cell proteomic measurement with physico-chemical principle enables identification of the central regulators of drug resistance as early as a few days after drug treatment. It is further illustrated in Chapter 3 and Chapter 5 of the thesis.

Meanwhile, compared to single-cell proteomic technologies, there are even fewer single-cell metabolic assays currently available. SCBC technology addresses this shortcoming, with its ability to co-measure metabolites from the same single cell together with many proteins or phosphor-proteins. Considering the importance of metabolic rewiring in drug resistance and the heterogeneous nature of the tumor, it is also worthwhile to investigate the metabolic phenotypes of single tumor cells, ideally in conjunction with their signaling activities. Since SCBC can co-measure the metabolites together with proteomics from the same single cell [65,68,74], we applied the SCBC-based integrated single-cell proteomic and metabolic assay to drug resistance development of melanoma. This technology provides us with a very deep insight into the signaling rewiring and metabolic reprogramming during the heterogeneous drug-response trajectories of tumor cells. We now have the capability to augment the paradigm of adaptive resistance development in an isogenic cell population and can use this information to offer insight into the design of more effective combination therapies.

Thesis Overview

This thesis investigated the fundamental plastic and heterogeneous nature of cancer cells and their connection with non-genetic drug-resistance development, using BRAF inhibition of BRAF-mutant melanomas as the model system. These melanoma cells undergo multi-step, reversible drug-induced cell-state transitions, ultimately yielding a drug-resistant mesenchymal-like phenotype.

In Chapter 2, bulk analysis was conducted to characterize the detailed kinetics of the entire cell-state transition, revealing expression changes of thousands of genes and extensive chromatin remodeling. A 3-step computational systems biology approach greatly simplified the complexity, and revealed that the whole adaptive process was controlled by a gene module activated within just three days of treatment, with RelA driving chromatin remodeling to establish an epigenetic program encoding long-term phenotype changes. From there a detailed mechanism connecting tumor epigenetic plasticity with non-genetic adaptive resistance to therapy was resolved. These findings were confirmed across several patient-

derived cell lines and in melanoma patients under MAPK inhibitor treatment. Co-targeting BRAF and histone-modifying enzymes arrest adaptive transitions towards drug tolerance in epigenetically plastic melanoma cells and may be exploited therapeutically. (Chapter 2 has been adapted from a manuscript currently under review in *Cancer cell*, doi: 10.1101/724740).

From Chapter 3, the resolution of the investigation went a step further by moving from bulk study to single-cell analysis. The single-cell view further uncovered the fundamental biophysical nature of the cell-state transition as joint efforts from both cell state interconversion and phenotype-specific drug selection. It also pinpointed to signaling network hubs, RelA, as the driver molecule of the initiation of the adaptive transition. Targeting those hubs halted the transition and arrested resistance development. (Chapter3 has been taken in part from *PNAS*, doi: 10.1073/pnas.1712064115).

In Chapter 4, the various driving forces of phenotypic changes and evolution of melanoma cells during the resistance development process were further quantitatively modeled and validated via a thermodynamic inspired surprisal analysis and a modified Fokker-Planck-type kinetic model. Joint experimental and computational approaches were employed, using either bulk or single-cell measurements as input, to interrogate the epigenetic landscape of the phenotypic evolution. the observed stable phenotypic equilibria of multiple drug-resistant subpopulations were found to be established via competition between state-dependent net proliferation rates and landscape potential. The results reveal how the tumor cells maintain a phenotypic heterogeneity that facilitates appropriate responses to external cues. (Chapter4 has been taken in part from *PLOS Computational Biology*, doi: 10.1371/journal.pcbi.1007034)

Finally, in Chapter 5 of the thesis, using integrated single-cell proteomic and metabolic analysis of the early stage signaling and metabolic changes upon initial drug responses, two distinct paths connecting drug-naïve and drug-tolerant states were identified. Cells are shown to exclusively traverse one of the two paths depending on the level of a master transcription factor MITF before drug treatment. The two trajectories are associated with distinct signaling and metabolic susceptibilities. The results update the paradigm of adaptive resistance development in an isogenic cell population and offer insight into the design of more effective combination therapies. (Chapter5 has been taken in part from a manuscript that is currently under review in *Nature Communications*, doi: 10.1101/767988).

Notably, in addition to the above contents mentioned in the thesis, two other exciting projects are future directions of the thesis. One of the projects analyzed the transcriptome of drug-induced resistant cell populations with single-cell resolution. We discovered, in addition to

the well-known drug-resistant mesenchymal phenotype, there is a novel drug-resistant subpopulation co-existing, which has not been reported before. Detailed molecular-mechanism associated with the drug-resistant subpopulations are discovered which guided the co-blocking of both resistant subpopulations as effective combination therapy. The other project utilized Raman-based single-cell sub-cellular metabolomics as an effective tool for investigating the metabolic features of the highly-aggressive mesenchymal phenotype by imaging the metabolomics phenotype of its subcellular organelle, which resolved the metabolic susceptibilities unique to this previously undruggable phenotype.

In total, this thesis combines various physical science and systems biology approaches with many single-cell technologies and analyses to obtain a deep and thorough understanding of the fundamental nature and underlying mechanisms of non-genetic drug resistance in cancer. It provides several novel insights into the rational design of better and more effective combination therapies for overcoming drug resistance.

References

1. Seyfried TN, Huysentruyt LC. On the origin of cancer metastasis. *Crit Rev Oncog*. 2013;18: 43–73. doi:10.1615/CritRevOncog.v18.i1-2.40
2. Chakraborty R, Wieland CN, Comfere NI. Molecular targeted therapies in metastatic melanoma. *Pharmacogenomics and Personalized Medicine*. 2013. doi:10.2147/PGPM.S44800
3. Cutaneous Melanoma: Etiology and Therapy. *Cutaneous Melanoma: Etiology and Therapy*. 2017. doi:10.15586/codon.cutaneoumelanoma.2017
4. Eggermont AMM, Kirkwood JM. Re-evaluating the role of dacarbazine in metastatic melanoma: What have we learned in 30 years? *Eur J Cancer*. 2004. doi:10.1016/j.ejca.2004.04.030
5. Sawyers C. Targeted cancer therapy. *Nature*. 2004. doi:10.1038/nature03095
6. Midorikawa Y, Tsuji S, Takayama T, Aburatani H. Genomic approach towards personalized anticancer drug therapy. *Pharmacogenomics*. 2012. doi:10.2217/pgs.11.157
7. Huang M, Shen A, Ding J, Geng M. Molecularly targeted cancer therapy: Some lessons from the past decade. *Trends in Pharmacological Sciences*. 2014. doi:10.1016/j.tips.2013.11.004
8. Awada A, Vandone AM, Aftimos P. Personalized management of patients with solid cancers: Moving from patient characteristics to tumor biology. *Current Opinion in Oncology*. 2012. doi:10.1097/CCO.0b013e3283521349
9. Poulidakos PI, Rosen N. Mutant BRAF melanomas-dependence and resistance. *Cancer Cell*. 2011. doi:10.1016/j.ccr.2011.01.008
10. Druker BJ, Ohno-Jones S, Talpaz M, Kantarjian H, Resta DJ, Peng B, et al. Efficacy and safety of a specific inhibitor of the BCR-ABL tyrosine kinase in chronic myeloid leukemia. *N Engl J Med*. 2001;344: 1031–1037. doi:10.1056/NEJM200104053441401
11. Hyman DM, Diamond EL, Baselga J, Puzanov I, Chan E, Subbiah V, et al. Vemurafenib in multiple nonmelanoma cancers with BRAF V600 mutations. *N Engl J Med*. 2015;373: 726–736. doi:10.1056/NEJMoA1502309
12. Flaherty KT, Puzanov I, Kim KB, Ribas A, McArthur GA, Sosman JA, et al. Inhibition of Mutated, Activated BRAF in Metastatic Melanoma. *N Engl J Med*. 2010;363: 809–819. doi:10.1056/nejmoa1002011
13. Sosman JA, Kim KB, Schuchter L, Gonzalez R, Pavlick AC, Weber JS, et al. Survival in BRAF V600-mutant advanced melanoma treated with vemurafenib. *N Engl J Med*. 2012. doi:10.1056/NEJMoA1112302
14. Chapman PB, Hauschild A, Robert C, Haanen JB, Ascierto P, Larkin J, et al. Improved Survival with Vemurafenib in Melanoma with BRAF V600E Mutation. *N Engl J Med*. 2011;364: 2507–2516. doi:10.1056/nejmoa1103782
15. Davies H, Bignell GR, Cox C, Stephens P, Edkins S, Clegg S, et al. Mutations of the BRAF gene in human cancer. *Nature*. 2002;417: 949–954. doi:10.1038/nature00766
16. Inamdar GS, Madhunapantula SR V., Robertson GP. Targeting the MAPK pathway in melanoma: Why some approaches succeed and other fail. *Biochemical*

- Pharmacology. 2010. doi:10.1016/j.bcp.2010.04.029
17. Wang AX, Qi XY. Targeting RAS/RAF/MEK/ERK signaling in metastatic melanoma. *IUBMB Life*. 2013. doi:10.1002/iub.1193
 18. Samatar AA, Poulidakos PI. Targeting RAS-ERK signalling in cancer: Promises and challenges. *Nature Reviews Drug Discovery*. 2014. doi:10.1038/nrd4281
 19. Flaherty KT, Puzanov I, Kim KB, Ribas A, McArthur GA, Sosman JA, et al. Inhibition of mutated, activated BRAF in metastatic melanoma. *N Engl J Med*. 2010. doi:10.1056/NEJMoa1002011
 20. Hoak DC. BRAF Mutation in Metastatic Melanoma | Incyte Diagnostics' Blog. 2012 [cited 5 Nov 2019]. Available: <https://incytepathology.wordpress.com/2012/04/10/braf/>
 21. Wagle N, Emery C, Berger MF, Davis MJ, Sawyer A, Pochanard P, et al. Dissecting therapeutic resistance to RAF inhibition in melanoma by tumor genomic profiling. *J Clin Oncol*. 2011;29: 3085–3096. doi:10.1200/JCO.2010.33.2312
 22. Gottesman MM, Fojo T, Bates SE. Multidrug resistance in cancer: Role of ATP-dependent transporters. *Nature Reviews Cancer*. 2002. doi:10.1038/nrc706
 23. Fojo T, Bates S. Strategies for reversing drug resistance. *Oncogene*. 2003. doi:10.1038/sj.onc.1206951
 24. Shi H, Hugo W, Kong X, Hong A, Koya RC, Moriceau G, et al. Acquired resistance and clonal evolution in melanoma during BRAF inhibitor therapy. *Cancer Discov*. 2014;4. doi:10.1158/2159-8290.CD-13-0642
 25. Lu H, Liu S, Zhang G, Wu B, Zhu Y, Frederick DT, et al. PAK signalling drives acquired drug resistance to MAPK inhibitors in BRAF-mutant melanomas. *Nature*. 2017;550: 133–136. doi:10.1038/nature24040
 26. Johannessen CM, Boehm JS, Kim SY, Thomas SR, Wardwell L, Johnson LA, et al. COT drives resistance to RAF inhibition through MAP kinase pathway reactivation. *Nature*. 2010;468: 968–972. doi:10.1038/nature09627
 27. Ramsdale R, Jorissen RN, Li FZ, Al-Obaidi S, Ward T, Sheppard KE, et al. The transcription cofactor c-JUN mediates phenotype switching and BRAF inhibitor resistance in melanoma. *Sci Signal*. 2015;8: ra82. doi:10.1126/scisignal.aab1111
 28. Sharma S V., Lee DY, Li B, Quinlan MP, Takahashi F, Maheswaran S, et al. A chromatin-mediated reversible drug tolerant state in cancer cell subpopulations. *Cell*. 2010;141: 69–80. doi:10.1016/j.cell.2010.02.027.A
 29. Dagogo-Jack I, Shaw AT. Tumour heterogeneity and resistance to cancer therapies. *Nature Reviews Clinical Oncology*. 2018. pp. 81–94. doi:10.1038/nrclinonc.2017.166
 30. Shaffer SM, Dunagin MC, Torborg SR, Torre EA, Emert B, Krepler C, et al. Rare cell variability and drug-induced reprogramming as a mode of cancer drug resistance. *Nature*. 2017;546: 431–435. doi:10.1038/nature22794
 31. Greaves M, Maley CC. Clonal evolution in cancer. *Nature*. 2012. doi:10.1038/nature10762
 32. Pisco AO, Huang S. Non-genetic cancer cell plasticity and therapy-induced stemness in tumour relapse: “What does not kill me strengthens me.” *British Journal of Cancer*. 2015. doi:10.1038/bjc.2015.146
 33. Brock A, Chang H, Huang S. Non-genetic heterogeneity a mutation-independent driving force for the somatic evolution of tumours. *Nature Reviews Genetics*. 2009.

- pp. 336–342. doi:10.1038/nrg2556
34. Ramirez M, Rajaram S, Steininger RJ, Osipchuk D, Roth MA, Morinishi LS, et al. Diverse drug-resistance mechanisms can emerge from drug-tolerant cancer persister cells. *Nat Commun.* 2016;7. doi:10.1038/ncomms10690
 35. Pisco AO, Brock A, Zhou J, Moor A, Mojtahedi M, Jackson D, et al. Non-Darwinian dynamics in therapy-induced cancer drug resistance. *Nat Commun.* 2013;4. doi:10.1038/ncomms3467
 36. Salgia R, Kulkarni P. The Genetic/Non-genetic Duality of Drug ‘Resistance’ in Cancer. *Trends in Cancer.* 2018. pp. 110–118. doi:10.1016/j.trecan.2018.01.001
 37. Hata AN, Niederst MJ, Archibald HL, Gomez-Caraballo M, Siddiqui FM, Mulvey HE, et al. Tumor cells can follow distinct evolutionary paths to become resistant to epidermal growth factor receptor inhibition. *Nat Med.* 2016;22: 262–269. doi:10.1038/nm.4040
 38. Lin JJ, Shaw AT. Resisting Resistance: Targeted Therapies in Lung Cancer. *Trends in Cancer.* 2016. doi:10.1016/j.trecan.2016.05.010
 39. Su Y, Bintz M, Yang Y, Robert L, Ng AHC, Liu V, et al. Phenotypic heterogeneity and evolution of melanoma cells associated with targeted therapy resistance. *PLOS Comput Biol.* 2019. doi:10.1371/journal.pcbi.1007034
 40. Su Y, Wei W, Robert L, Xue M, Tsoi J, Garcia-Diaz A, et al. Single-cell analysis resolves the cell state transition and signaling dynamics associated with melanoma drug-induced resistance. *Proc Natl Acad Sci U S A.* 2017;114. doi:10.1073/pnas.1712064115
 41. Fallahi-Sichani M, Becker V, Izar B, Baker GJ, Lin J, Boswell SA, et al. Adaptive resistance of melanoma cells to RAF inhibition via reversible induction of a slowly dividing de-differentiated state. *Mol Syst Biol.* 2017;13: 905. doi:10.15252/msb.20166796
 42. Sauka-Spengler T, Bronner-Fraser M. A gene regulatory network orchestrates neural crest formation. *Nature Reviews Molecular Cell Biology.* 2008. doi:10.1038/nrm2428
 43. Hugo W, Zaretsky JM, Sun L, Song C, Moreno BH, Hu-Lieskovan S, et al. Genomic and Transcriptomic Features of Response to Anti-PD-1 Therapy in Metastatic Melanoma. *Cell.* 2016;165: 35–44. doi:10.1016/j.cell.2016.02.065
 44. Kemper K, De Goeje PL, Peeper DS, Van Amerongen R. Phenotype switching: Tumor cell plasticity as a resistance mechanism and target for therapy. *Cancer Research.* 2014. pp. 5937–5941. doi:10.1158/0008-5472.CAN-14-1174
 45. Buenrostro JD, Giresi PG, Zaba LC, Chang HY, Greenleaf WJ. Transposition of native chromatin for fast and sensitive epigenomic profiling of open chromatin, DNA-binding proteins and nucleosome position. *Nat Methods.* 2013. doi:10.1038/nmeth.2688
 46. Barski A, Cuddapah S, Cui K, Roh TY, Schones DE, Wang Z, et al. High-Resolution Profiling of Histone Methylations in the Human Genome. *Cell.* 2007. doi:10.1016/j.cell.2007.05.009
 47. Mortazavi A, Williams BA, McCue K, Schaeffer L, Wold B. Mapping and quantifying mammalian transcriptomes by RNA-Seq. *Nat Methods.* 2008;5: 621–628. doi:10.1038/nmeth.1226
 48. Westont AD, Hood L. Systems Biology, Proteomics, and the Future of Health Care:

- Toward Predictive, Preventative, and Personalized Medicine. *Journal of Proteome Research*. 2004. doi:10.1021/pr0499693
49. Nicholson JK, Wilson ID. Understanding “global” systems biology: Metabonomics and the continuum of metabolism. *Nature Reviews Drug Discovery*. 2003. doi:10.1038/nrd1157
 50. Heath JR, Ribas A, Mischel PS. Single-cell analysis tools for drug discovery and development. *Nature Reviews Drug Discovery*. 2016. pp. 204–216. doi:10.1038/nrd.2015.16
 51. Gawad C, Koh W, Quake SR. Single-cell genome sequencing: Current state of the science. *Nature Reviews Genetics*. 2016. doi:10.1038/nrg.2015.16
 52. Chuang H-Y, Hofree M, Ideker T. A Decade of Systems Biology. *Annu Rev Cell Dev Biol*. 2010. doi:10.1146/annurev-cellbio-100109-104122
 53. Hood L, Heath JR, Phelps ME, Lin B. Systems biology and new technologies enable predictive and preventative medicine. *Science*. 2004. doi:10.1126/science.1104635
 54. Remacle F, Kravchenko-Balasha N, Levitzki A, Levine RD. Information-theoretic analysis of phenotype changes in early stages of carcinogenesis. *Proc Natl Acad Sci*. 2010;107: 10324–10329. doi:10.1073/pnas.1005283107
 55. Spencer SL, Sorger PK. Measuring and modeling apoptosis in single cells. *Cell*. 2011. doi:10.1016/j.cell.2011.03.002
 56. Bendall SC, Nolan GP. From single cells to deep phenotypes in cancer. *Nature Biotechnology*. 2012. doi:10.1038/nbt.2283
 57. Tirosh I, Izar B, Prakadan SM, Wadsworth MH, Treacy D, Trombetta JJ, et al. Dissecting the multicellular ecosystem of metastatic melanoma by single-cell RNA-seq. *Science* (80-). 2016;352: 189–196. doi:10.1126/science.aad0501
 58. Azizi E, Carr AJ, Plitas G, Cornish AE, Konopacki C, Prabhakaran S, et al. Single-Cell Map of Diverse Immune Phenotypes in the Breast Tumor Microenvironment. *Cell*. 2018;174: 1293-1308.e36. doi:10.1016/j.cell.2018.05.060
 59. Wu AR, Neff NF, Kalisky T, Dalerba P, Treutlein B, Rothenberg ME, et al. Quantitative assessment of single-cell RNA-sequencing methods. *Nat Methods*. 2014. doi:10.1038/nmeth.2694
 60. Bendall SC, Simonds EF, Qiu P, Amir EAD, Krutzik PO, Finck R, et al. Single-cell mass cytometry of differential immune and drug responses across a human hematopoietic continuum. *Science* (80-). 2011;332: 687–696. doi:10.1126/science.1198704
 61. Ma C, Fan R, Ahmad H, Shi Q, Comin-Anduix B, Chodon T, et al. A clinical microchip for evaluation of single immune cells reveals high functional heterogeneity in phenotypically similar T cells. *Nat Med*. 2011;17: 738–743. doi:10.1038/nm.2375
 62. Shi Q, Qin L, Wei W, Geng F, Fan R, Shik Shin Y, et al. Single-cell proteomic chip for profiling intracellular signaling pathways in single tumor cells. *Proc Natl Acad Sci*. 2012;109: 419–424. doi:10.1073/pnas.1110865109
 63. Wei W, Shin YS, Ma C, Wang J, Elitas M, Fan R, et al. Microchip platforms for multiplex single-cell functional proteomics with applications to immunology and cancer research. *Genome Medicine*. 2013. doi:10.1186/gm479
 64. Huang L, Ma F, Chapman A, Lu S, Xie XS. Single-Cell Whole-Genome Amplification and Sequencing: Methodology and Applications. *Annu Rev Genomics*

- Hum Genet. 2015. doi:10.1146/annurev-genom-090413-025352
65. Xue M, Wei W, Su Y, Kim J, Shin YSYS, Mai WXWX, et al. Chemical methods for the simultaneous quantitation of metabolites and proteins from single cells. *J Am Chem Soc.* 2015;137. doi:10.1021/jacs.5b00944
 66. Lu Y, Xue Q, Eisele MR, Sulistijo ES, Brower K, Han L, et al. Highly multiplexed profiling of single-cell effector functions reveals deep functional heterogeneity in response to pathogenic ligands. *Proc Natl Acad Sci.* 2015;112: E607–E615. doi:10.1073/pnas.1416756112
 67. Wei W, Shin YS, Xue M, Matsutani T, Masui K, Yang H, et al. Single-Cell Phosphoproteomics Resolves Adaptive Signaling Dynamics and Informs Targeted Combination Therapy in Glioblastoma. *Cancer Cell.* 2016;29: 563–573. doi:10.1016/j.ccell.2016.03.012
 68. Xue M, Wei W, Su Y, Johnson D, Heath JR. Supramolecular Probes for Assessing Glutamine Uptake Enable Semi-Quantitative Metabolic Models in Single Cells. *J Am Chem Soc.* 2016;138. doi:10.1021/jacs.5b12187
 69. Kravchenko-Balasha N, Wang J, Remacle F, Levine RD, Heath JR. Glioblastoma cellular architectures are predicted through the characterization of two-cell interactions. *Proc Natl Acad Sci.* 2014;111: 6521–6526. doi:10.1073/pnas.1404462111
 70. Ma C, Cheung AF, Chodon T, Koya RC, Wu Z, Ng C, et al. Multifunctional T-cell analyses to study response and progression in adoptive cell transfer immunotherapy. *Cancer Discov.* 2013. doi:10.1158/2159-8290.CD-12-0383
 71. Zhao JL, Ma C, O'Connell RM, Mehta A, Diloreto R, Heath JR, et al. Conversion of danger signals into cytokine signals by hematopoietic stem and progenitor cells for regulation of stress-induced hematopoiesis. *Cell Stem Cell.* 2014;14: 445–459. doi:10.1016/j.stem.2014.01.007
 72. Shin YS, Remacle F, Fan R, Hwang K, Wei W, Ahmad H, et al. Protein signaling networks from single cell fluctuations and information theory profiling. *Biophys J.* 2011. doi:10.1016/j.bpj.2011.04.025
 73. Kravchenko-Balasha N, Shin YS, Sutherland A, Levine RD, Heath JR. Intercellular signaling through secreted proteins induces free-energy gradient-directed cell movement. *Proc Natl Acad Sci.* 2016;113: 5520–5525. doi:10.1073/pnas.1602171113
 74. Li Z, Cheng H, Shao S, Lu X, Mo L, Tsang J, et al. Surface Immobilization of Redox-Labile Fluorescent Probes: Enabling Single-Cell Co-Profiling of Aerobic Glycolysis and Oncogenic Protein Signaling Activities. *Angew Chemie - Int Ed.* 2018;57: 11554–11558. doi:10.1002/anie.201803034

KINETIC INFERENCE RESOLVES EPIGENETIC MECHANISM OF DRUG RESISTANCE IN MELANOMA

We resolved a mechanism connecting tumor epigenetic plasticity with non-genetic adaptive resistance to therapy, with MAPK inhibition of BRAF-mutant melanomas providing the model. These cancer cells undergo multiple, reversible drug-induced cell-state transitions, ultimately yielding a drug-resistant mesenchymal-like phenotype. A kinetic series of transcriptome and epigenome data, collected over two months of drug treatment and release, revealed changing levels of thousands of genes and extensive chromatin remodeling. However, a 3-step computational algorithm greatly simplified the interpretation of these changes, and revealed that the whole adaptive process was controlled by a gene module activated within just three days of treatment, with RelA driving chromatin remodeling to establish an epigenetic program encoding long-term phenotype changes. These findings were confirmed across several patient-derived cell lines and in melanoma patients under MAPK inhibitor treatment. Co-targeting BRAF and histone-modifying enzymes arrests adaptive transitions towards drug tolerance in epigenetically plastic melanoma cells and may be exploited therapeutically.

This chapter includes content from our previously published article:

- [1] Su, Yapeng, Xiang Lu, Guideng Li, Chunmei Liu, Yan Kong, Jihoon W. Lee, Rachel Ng et al. "Kinetic Inference Resolves Epigenetic Mechanism of Drug Resistance in Melanoma." *Cancer cell* (Under revision). doi: 10.1101/724740

Introduction

The acquisition of therapy resistance in cancer patients remains a major clinical challenge [1–4]. While various genetic mutations have been reported to cause resistance [5,6], recent literature also points to the importance of epigenetic modulations to drug-tolerance that can precede the emergence of drug-resistant genotypes in a variety of tumor types [7–14]. For such epigenetic processes, tumor cells adapt to the drug treatment by orchestrating master transcription factors and chromatin remodelers within a regulatory network. The resultant changes of chromatin profile via histone modifications eventually establish specific gene expression programs of the drug-tolerant state [15–24]. Unlike genetic mechanisms, epigenetic cell-state transitions can be reversed upon drug removal [10,25,26]. Indeed, such reversibility has been observed in *in vitro* and *in vivo* tumor models [10,25–28] and increasingly reported in clinical settings [29–32]. Nevertheless, the mechanistic details of these epigenetic modulations remain incompletely understood, thus limiting the options for therapeutic interventions designed to arrest the non-genetic resistance.

Accumulating evidence suggests that phenotypic plasticity is an essential characteristic associated with non-genetic resistance [15,33–35]. Phenotypic plasticity, defined as the ability of cells to reside in distinct phenotypes and switch between them without genomic alterations, is an intrinsic property of cells to survive stressful conditions. Cancer cells can also exploit plasticity to survive drug treatment by transitioning from a drug-sensitive phenotype to drug-tolerant phenotypes [15,36]. Paradigmatic examples include certain *BRAF*-mutant melanomas under MAPK pathway inhibitor (MAPKi) treatment. The drug-naïve melanoma cells initially reside as drug-sensitive melanocytic phenotypes (MITF^{high} and elevated pigmentation genes). Upon continuous MAPK inhibition, they can evolve into a transient, slow-cycling, neural-crest-like phenotype (MITF^{low}/NGFR^{high}) [25,37] and eventually towards a mesenchymal phenotype (MITF^{low}, SOX10^{low}, and elevated mesenchymal markers) [25,35,38,39]. The mesenchymal phenotype is notorious for its resistance to MAPKi as well as many other treatment regimens including immunotherapy [9,40,41].

Several studies have explored the molecular markers associated with the drug-tolerant or drug-resistant phenotypes including: down-regulation of SOX10 [21,26] and upregulation of JNK/c-JUN [37,40,42] in the mesenchymal phenotype, as well as upregulation of KDM5 [28,43] in a slow-cycling (likely neural crest) drug-tolerant phenotype. However, there remains a clear unmet need to identify the early-stage adaptive processes that are triggered immediately following the drug exposure to lead the transition towards drug-tolerant phenotypes. Such an understanding may unveil the molecular nature of phenotypic plasticity

and compelling drug targets that can arrest the entire adaptive resistance process prior to the establishment of resistant phenotypes.

We sought to resolve the early-acting regulatory process of adaptive resistance through kinetic characterizations of the transcriptome and functional epigenome of patient-derived *BRAF*-mutant melanoma cell lines featuring varying degrees of phenotypic plasticity. Systems-level analysis of the transition dynamics, followed by experimental validations, discerned the critical transcription factors and chromatin remodelers within a regulatory network that initiated and drove the adaptive cell state transition. The mechanism informed the design of combination therapies to disrupt the chromatin remodeling and to arrest the adaptive transition at a very early stage. The phenotypic plasticity was found to correlate with the efficacy of the drug combinations across multiple melanoma cell lines, implicating that the plasticity may be epigenetically encoded in the baseline chromatin profiles. The signatures of the adaptive mechanism were also found in sequential patient biopsies. Together, our study resolved an early-acting epigenetic mechanism of non-genetic resistance, which may be exploited to prevent targeted therapy resistance in melanoma.

Results

Reversibility of the adaptive transition in patient-derived *BRAF*-mutant melanoma cell lines

We used an epigenetically plastic *BRAF*^{V600E}-mutant melanoma cell line M397 as a model system to interrogate the kinetics of the adaptive cell state transition in response to continuous BRAF inhibition. We treated the cells with a BRAF inhibitor (BRAFi) for a month, then separated them into two sets: one with an additional month of continuous drug treatment, and the other untreated for one month (Figure 1A). Cells were collected for a time-series transcriptome and functional characterization (Figures 1 and S1; Table S1). The resultant gene expression data after 29 days (D29) of drug exposure showed significant enrichments of mesenchymal signatures, cellular invasiveness, migration, and loss of MITF targets (Figures 1C and S1D; Table S2). The adapted cells were slow-cycling, as evidenced by reduced proportion of cells in the S and G2/M phases (Figure 1E). An additional month of drug exposure maintained the cells in a steady state with a relatively stable transcriptome profile (Figures 1B and S1C). Drug removal (DR) triggered a reversion to a state with a transcriptome profile that resembled the untreated (D0) state (Figures 1B, S1C and S1D), as illustrated by the fact that the molecular signature enrichments of D29 vs. D0 and DR30 vs. D29 were essentially mirror images of each other (Figure 1C). Furthermore, the reverted cells recovered their proliferative and cell cycle characteristics, and were re-sensitized to BRAF inhibition (Figures 1D-1F). These results suggest a fully reversible adaptive transition

at the transcriptomic, phenotypic, and functional levels. We further confirmed the existence of such reversibility, at the functional level, in other *BRAF*-mutant melanoma cell lines with varying sensitivities to BRAFi (Figures 1D, 1F, S1A, and S1D). Therefore, the BRAFi-induced adaptive resistance is reversible at both transcriptomic and functional levels with generality across a panel of patient-derived *BRAF*-mutant melanoma cell lines.

Information theoretic analysis of the transcriptome kinetics resolved two gene modules associated with the reversible transition

To extract the underlying regulatory modules that change coordinately in the reversible transition, we applied information theory-based surprisal analysis to the time-course transcriptome data (Eq. 1). Surprisal analysis was initially formulated to understand the dynamics of nonequilibrium systems [44]. It has been extended, in multiple publications [45–52], to characterize biological processes in living cells. It approximates quantum state distributions of molecular species within a cell’s molecular ensemble in order to assess the maximum entropy of those biomolecules. Particularly, for a system characterized by a kinetic series of transcriptome, Equation 1 from surprisal analysis can de-convolute the changes of thousands of genes into one unchanged gene expression baseline and a series of gene expression modules. Each module contains a group of genes that are coordinately changing together across time points (an example gene list for module-1 is visualized in dashed-line, circled regions in Figure 2A). We applied this analysis, and then used the resulting gene modules to computationally estimate and visualize cell-state transition trajectories (STAR Methods).

$$\underbrace{\ln X_i(t)}_{\substack{\text{measured expression} \\ \text{level of transcript } i \\ \text{at time } t}} = \underbrace{\ln X_i^0(t)}_{\substack{\text{baseline} \\ \text{expression level of} \\ \text{transcript } i}} - \underbrace{\sum_j \lambda_j(t) G_{ij}}_{\substack{\text{deviation terms from} \\ \text{the baseline} \\ \text{of transcript } i \text{ (gene modules)}}}$$

amplitude of
module j at
time t

contribution
of transcript i
to module j

(Eq.1)

Specifically, in Equation 1, $\ln X_i(t)$, the natural logarithm of the measured level of transcript i at time t , is defined as the expression baseline of transcript i ($\ln X_i^0$), minus the sum of gene module alterations weighted by the relative contribution to each module by transcript i ($\sum_j \lambda_j(t) G_{ij}$). Each gene module is represented by a time-dependent module amplitude (or score $\lambda_j(t)$) that denotes the importance of the gene module j to the global

transcriptome at time t . Module-specific contribution scores from each transcript G_{ij} denote weight of gene i on module j . Thus, the biological functions of each module j can be inferred from genes with higher positive or negative module-specific contribution scores G_{ij} . The gene expression baseline is the reference point for the entire transition.

The application of Eq. 1 to the time-series of transcriptome data de-convoluted them into two time-dependent gene modules plus the gene expression baseline. To visualize the kinetic changes of the entire transcriptome and each gene module, we plotted the time-series transcriptome profiles and de-convoluted gene modules as self-organizing mosaic maps (SOMs) (Figures 2A and S2A). The gene expression baseline calculated from the surprisal analysis (top row of SOMs in Figures 2A and S2A) shows no time dependence. This demonstrates the validity of surprisal analysis in analyzing this system [51]. The second and third rows are plots of the two resolved, time-varying gene modules. The SOMs for D0 and DR30 appear nearly identical, reflecting the reversibility of the adaptive response at the transcriptome level as well as at the resolved gene module level. When the baseline state and the two regulatory gene modules are summed (the row labeled ‘sum’ in Figures 2A and S2A), the resultant SOMs from surprisal analysis closely matched the experimental transcriptome data (bottom row of Figures 2A and S2A). Thus, the expression change of thousands of genes during the reversible transition can be delineated by a time-invariant expression baseline, plus the changes of two time-varying gene modules.

The reduction of the transcriptome kinetic series into two gene modules enables visualization of drug-adaptation trajectories taken by the cells. This is achieved by projecting the time-series transcriptome onto the 2-D cell-state space defined by the gene modules, with each axis representing the module score of each gene module. The plot is a cyclic loop (Figure 2B) comprised of a forward trajectory (blue), and a drug-removal, reverse trajectory (green), which indicates that the cells undertake a different return path to the original drug-sensitive state. This cyclic shape suggests that the two gene modules operate sequentially. The first module, M_{early} , was fully activated within the first 3 days of drug treatment (y-axis of Figure 2B), while the second module, M_{late} , (x-axis of Figure 2B) gradually activated between days 3 and 29 (D3 and D29). Continued treatment beyond D29 caused minimal change in either module (blue dash line circled region of Figure 2B), in agreement with the stable transcriptome profile observed from D29 to D59 (Figures 1B and S2A). Interestingly, upon drug removal, there was an immediate reduction in the first module, followed by a gradual reversion of the second module to its original pre-treatment module score. The different operational dynamics of these modules resulted in the cyclic transition trajectories that the cells took.

To further investigate the biological meaning of the two gene modules, we conducted gene set enrichment analysis (GSEA) on genes ranked by their module-specific contribution scores (G_{ij}). M_{late} was positively associated with melanocytic signatures (e.g. MITF targets) and negatively correlated with mesenchymal signatures, cell invasiveness, and NF κ B, TGF β , and JNK signaling pathways (Figure 2B; Table S3). Consequently, the gradual change of the M_{late} score from positive to negative values between D3 and D29 indicates that the drug-treated cells de-differentiated towards neural-crest and mesenchymal phenotypes, with loss of melanocytic signatures, and an increase of NF κ B, TGF β , and JNK signaling. Similarly, M_{early} was positively associated with HDAC1 activity and negatively associated with cell cycle regulation (Figure 2B), suggesting that the initial drug exposure led to an immediate histone deacetylation and cell cycle arrest. Therefore, the two gene modules resolved from surprisal analysis delineated the stepwise, reversible dynamic changes of cellular functions during the cyclic transitions associated with adaptive resistance development.

Dynamic system modeling discerned the regulatory relationship between the early- and late-gene modules

A possible implication of the sequential operation of M_{early} and M_{late} is that the biological processes associated with the two modules are coupled where the completion of the M_{early} gene program triggers the expression of M_{late} genes. This implies a co-dependency of these two modules. We tested this hypothesis by fitting the dynamic dependence of the two modules to a coarse-grained model resembling a simple two-gene feedback circuit (Eq. 2). This approximation yields an estimate for how the two gene modules are coupled (Figure 2C; see STAR Methods).

$$\begin{aligned} \frac{d[\text{gene}_{M_{\text{early}}}]}{dt} &= B_e + M_{e-e} [\text{gene}_{M_{\text{early}}}] + M_{l-e} [\text{gene}_{M_{\text{late}}}] \\ \frac{d[\text{gene}_{M_{\text{late}}}]}{dt} &= B_l + M_{e-l} [\text{gene}_{M_{\text{early}}}] + M_{l-l} [\text{gene}_{M_{\text{late}}}] \end{aligned} \quad (\text{Eq.2})$$

Here, the brackets denote the averaged expression level of module-associated genes at a given time point. B_e and B_l represent the basal production of M_{early} - and M_{late} -associated genes, respectively. Coefficients M_{e-e} and M_{l-l} reflect self-regulation of M_{early} and the M_{late} expression, respectively, while coefficients M_{l-e} and M_{e-l} reflect the M_{late} regulation over the expression of M_{early} genes and vice versa.

The ODE fitting of gene expression associated with M_{late} and M_{early} for both forward and reverse trajectories revealed that M_{early} exerted significant control over both itself and M_{late} .

This is evidenced by the significantly larger pre-factors M_{e-e} and M_{e-l} (Figures 2D and S3; Table S4). By contrast, M_{late} yielded only minimal influence over itself or M_{early} . The strong influence of M_{early} applied to both the drug-treated forward and drug-release reverse trajectories (Figures 2D, 2E, S2B and S3). In other words, M_{early} dominated the entirety of the forward D0-D29 transition path towards drug resistance as well as the drug removal trajectory back to the drug-sensitive state. Further, the dependence of M_{late} on M_{early} suggested an orchestrated process whereby certain important transcription factors associated with M_{early} played a key role in regulating downstream genes associated with M_{late} , ultimately driving the adaptive transition towards the drug resistant phenotype. Thus, dynamic system modeling revealed the strong influence of the early-acting gene module on the late-acting gene module, and implied that M_{early} may contain the key regulators that initiated the adaptive cell state transition.

Inference of critical early-acting upstream transcriptional regulators based upon the inter-dependence of the two gene modules

Guided by the importance of M_{early} module in driving the adaptive resistance (Figure 2D), we hypothesized that certain key transcription factors (TFs) or co-factors within M_{early} regulate the downstream genes within M_{late} and thus drive the adaptive transition. To test this hypothesis, we used two complementary approaches to infer the early-acting TFs in M397. For the first approach (Figures 3A and S4A), we hypothesized that functionally relevant TFs associated with M_{early} should have their target effector genes enriched in the gene set associated with the subsequent action of M_{late} . Therefore, we first filtered out all the possible TFs and co-factors within M_{early} and then acquired their downstream targets from the TF targets database, followed by assessing their enrichment in the genes associated with M_{late} (STAR Methods). This identified that subset of M_{early} -related TFs whose downstream targets are overrepresented within the genes associated with M_{late} module. Five statistically enriched TFs and co-factors were identified, with Pearson correlation coefficients $\rho > 0.9$ (Figures 3B, panel i). These include MEIS3, which is required for neural-crest invasion [53], NKX3-2, which mediates the epithelial-mesenchymal transition in neural crest development [54], and LEF1 whose down-regulation is related to non-genomic MAPKi resistance in melanomas [9]. These enriched TFs may regulate the cancer cell phenotype changes associated with the forward and reverse transitions (Figure 3C). Most interestingly, the histone modifying enzyme KDM5B (H3K4 demethylase), whose expression displayed a sharp increase by D3, was also found to have many target genes overrepresented in M_{late} (Figure 3D). Importantly, this histone modifier has been previously associated with reversible drug-tolerant states in several tumor types, including melanomas [28,43,55].

For the second inference approach, we performed enrichment analysis of cis-regulatory elements in the promoter regions of all genes strongly associated with M_{late} (Figure S4B). We ranked these elements according to their statistical significance (Figure 3B, panel ii). The top one ranked element was the binding motif of the NF κ B family member RelA, which was recently identified as an important regulator associated with this adaptive transition [25]. The expression kinetics of RelA was not associated with either M_{late} or M_{early} . Instead, the expression level of RelA gradually increased from the start of BRAF inhibition to D29, implying its consistent activity over the entire adaptive transition towards the mesenchymal state (Figure 3D). Interestingly, NFKBIE, which is highly anti-correlated with M_{early} ($\rho = -0.88$) and represses NF κ B activation by preventing RelA nuclear translocation, displayed a sharp drop by D3 (Figure 3D). This suggests that activation of RelA and associated downstream genes in M_{late} might be mediated by the immediate down-regulation of NFKBIE, thus releasing RelA into the nucleus. A second transcription regulator similarly identified was AP-2 α , which has been reported to be involved in melanoma progression and metastasis [56]. Taken together, these analyses greatly simplified the interpretation of the kinetic transcriptome data by inferring a few controlling, early-acting TFs and co-factors (Figures 3B and S4B), including RelA and KDM5B, from the large numbers of transcripts altered during the course of BRAF inhibition and drug release (Figures S5A and S5B).

Reversibility of chromatin accessibility and histone modification profiles shed light on downstream transcription factors associated with the adaptive transition

Information theory analysis and dynamic ODE modeling of transcriptome kinetics pinpointed a few key early-acting TFs that likely trigger the initiation of the cell state transition towards resistance. To obtain a complete mechanistic picture, we seek to further identify the late-acting driver regulators that are the downstream targets of those early-acting TFs via cellular epigenome characterization at different stages of the reversible transition (Figure 5A).

Since the previous inference and enrichment analyses pointed to the fast activation of histone modifiers KDM5B and HDAC1 in M_{early} that represses activation histone marks (Figures 2B and 3B), we first accessed the regulatory regions associated with open chromatin. We accomplished this via transposase-accessible chromatin with high-throughput sequencing (ATAC-seq) and chromatin immunoprecipitation sequencing (ChIP-seq) against two activation histone marks, H3K4me3 and H3K27ac, which are targets of KDM5B and HDAC1. Similar to the transcriptome profiles, the overall chromatin accessibility displayed reversible changes during drug treatment and removal. That accessibility gradually decreased following BRAFi exposure, but after a month of drug removal reverted to a profile similar to that of untreated cells (Figures 4A, 4B and S5C). Overall modification levels of the two

histone marks displayed the same reversibility (Figure S5D and S5E). However, the drop in these marks after 3-day BRAFi exposure was large relative to the corresponding small reduction of the ATAC-seq signal (Figures 4A and S5D), suggesting that these histone modifications may precede and perhaps drive the changes in chromatin accessibility. Further, the promoter region of many well-reported regulators for the adaptive resistance in melanoma also displayed reversible changes that aligned well with their reversible expression patterns (Figure S5E). We also tabulated the numbers of differential peaks of H3K4me3 and H3K27ac that changed between day 0 and subsequent time points (Figure 4C). The differences between states at long-term drug removal (DR30) and at day 0 were minimal. This was especially true for H3K27ac, where only two peaks reflected acetylation differences between day 0 and long-term drug removal. These data demonstrated the genome-scale chromatin landscape underwent reversible changes upon drug treatment and removal, thus supporting a potential epigenetic mechanism of the reversible adaptive transition.

To search for causal TFs driving the dynamic changes of the chromatin landscape, we used K-means clustering to analyze the genome-wide chromatin restructuring at four time points spread across the reversible transition (Figure 4B). We identified four clusters of chromatin accessibility peaks with unique kinetics, plus a fifth, time-invariant cluster. For these four clusters, we mined the underlying DNA sequences and searched for over-represented TF binding motifs. The highly enriched motifs in the reversible transition (right side of Figure 4B) contain binding motifs of certain TFs reported previously to be involved in the adaptive resistance of melanomas, including MITF [57], SOX10 [26], Jun-AP1 [37,40,42], and RelA [25]. Some of these TFs, such as RelA and AP-2, were overlapping with those inferred from the transcriptome data (Figure S4B). To further resolve whether these modifications were modulated by RelA whose motif is ranked top one in the common cis-regulatory element inference (Figures 3B and S4B), we quantified the H3K4me3 and H3K27ac ChIP-seq signals across all the RelA binding sites and found marked reduction after 3 days of drug exposure, with recovery upon drug removal (Figure 4D). It suggests that RelA binds primarily to distal sequences containing both activation histone marks H3K4me3 and H3K27ac, and might regulate them through interactions with the KDM5B and HDAC1 during the adaptive transition.

In addition to confirming RelA as a critical early-acting regulator that may cause the epigenome changes, we further mined downstream regulators that may be the direct targets of RelA and showed consistent epigenome alteration patterns at the RelA binding region across the reversible transition. We achieved this by quantifying the changes in chromatin accessibility and two activation histone marks of all TFs/co-factors associated with M_{late} that contain RelA binding motifs (STAR Methods). *SOX10* was identified to display the most

significant changes across all three epigenome alterations at the RelA binding region (Table S5). Consider the importance of *SOX10* in regulating mesenchymal phenotype in melanoma [21,26,58], we hypothesized that *SOX10* is likely one key downstream regulator for the cell state transition towards resistance. Taken together, these data illustrated the reversibility of adaptive resistance at the level of the global chromatin landscape. The kinetics of the reversible epigenome profiles further pointed to a collection of early-acting and downstream-effector TFs, particularly RelA and SOX10, in regulating such adaptive epigenetic resistance.

Mechanistic regulatory network of adaptive resistance

Based on the transcriptional regulators inferred from gene module interactions and epigenome profiling, we tied these inferences together with prior knowledge and formed a mechanistic regulatory network (Figure 5A). We hypothesized that for drug-naïve cells, *NFKBIE* and *SOX10* are both epigenetically activated and that downstream TGF β signaling is repressed [26]. BRAF inhibition triggers a sharp drop in *NFKBIE* expression and a sharp increase in the expression of the histone demethylase KDM5B (Figure 3D). The reduction of *NFKBIE* would promote the nuclear translocation of RelA [59]. In the nucleus, RelA would then recruit KDM5B and HDAC1 to repress *SOX10* and *NFKBIE* expression by erasing the activation histone marks in their promoter regions, consistent with the rapid decrease of activation histone marks at RelA binding sites (Figures 4D). The downregulation of *SOX10* expression has been reported to promote BRAFi adaptive resistance through promoting the up-regulation of TGF β signaling and mesenchymal transition (Figure 3C) [21,26]. Our mechanistic hypothesis provides a rationale for how this happens, and further indicates how the downregulation of *NFKBIE* promotes RelA nuclear translocation, thus establishing a positive feedback loop (Figure 5A). Drug removal reverses this process, starting with the gradual recovery of *SOX10* expression (Figure 3D), the loss of mesenchymal signatures (Figure 3C), and the eventual re-opening of the chromatin (Figure 4A). We extensively tested this mechanism in the following ways.

We first examined the change in overall chromatin accessibility and levels of the histone marks H3K4me3 and H3K27ac at the promoter regions of *SOX10* and *NFKBIE* over the course of the adaptive transition. We found reduction of the overall chromatin accessibility and of the levels of both histone marks upon BRAF inhibition, and a recovery of these signals upon drug removal (Figure 5B). These observations confirmed the involvement of chromatin alterations in the gene expression changes of *SOX10* and *NFKBIE*. We next explored the role of RelA in recruiting histone remodelers. We tested whether RelA, KDM5B and HDAC1 simultaneously bind to the promoter regions of *SOX10* and *NFKBIE*. We performed ChIP-PCR experiments on untreated cells using primers targeting the promoter regions of *SOX10*

and *NFKBIE*. The results confirmed the co-localization of RelA, KDM5B, HDAC1, and the two histone marks (Figure 5C). Quantitative assessment of binding profiles via ChIP-qPCR further revealed that BRAFi treatment elevated binding of RelA, KDM5B, and HDAC1 to the *SOX10* and *NFKBIE* promoter sites and consequently diminished H3K4me3 and H3K27ac histone marks (Figure 5D). These binding enrichment profiles reverted to the levels of the untreated cells after drug removal (Figure 5D). Co-immunoprecipitation (Co-IP) assays confirmed the binding of RelA to KDM5B and HDAC1 (Figure 5E), suggesting that RelA can form a complex with either KDM5B or HDAC1. These findings support the role of RelA in recruiting histone remodelers in regulating the expression of *SOX10* and *NFKBIE*.

To further validate that *SOX10* and *NFKBIE* are directly repressed by the recruitment of KDM5B and HDAC1 through RelA, we sought to perturb RelA with a drug that inhibits its nuclear translocation. According to our hypothesis, such inhibition should decrease the recruitment of the histone-modifying enzymes KDM5B and HDAC1, which, in turn, will increase the H3K4me3 and H3K27ac levels at the promoter regions of *SOX10* and *NFKBIE*. We first treated the M397 cells with BRAFi for 21 days to induce adaptive resistance with reduced *SOX10* expression (Figure 5F). Under continued BRAFi treatment, we added a drug (JSH-23) to inhibit RelA nuclear translocation [60], and monitored short-term interval changes in *SOX10* expression. *SOX10* expression rapidly increased following JSH-23 treatment and returned to the level originally observed at D0 after 24 hours of drug exposure (Figure 5F). Furthermore, we observed barely detectable binding of RelA, KDM5B, and HDAC1 and consequently increased binding of H3K4me3 and H3K27ac at the *SOX10* and *NFKBIE* promoter regions after 24 hours of JSH-23 treatment (Figure 5G). The immediate increase of *SOX10* expression and decrease of HDAC1 and KDM5B enrichment within 24 hours of JSH-23 exposure further validated our hypothesis that the repression of *SOX10* and *NFKBIE* is directly through RelA-mediated epigenetic silencing.

We performed additional independent perturbations to validate the proposed molecular mechanism using genetically engineered M397 cells. We first triggered RelA nuclear translocation through CRISPR knockout (KO) of *NFKBIE* to release the cytoplasmic retention of RelA [61]. According to our proposed mechanism, this translocation should in turn enhance recruitment of the histone modifying enzymes HDAC1 and KDM5B, and thus diminish levels of activation histone marks H3K4me3 and H3K27ac at the promoter regions of *SOX10*. This prediction was confirmed by ChIP-qPCR result (Figure 5H). The actual expression of *SOX10* was consequently reduced in *NFKBIE*-KO cells relative to control cells (Figure 5I). Similarly, knockout of KDM5B partially upregulated H3K4me3 levels at the *SOX10* and *NFKBIE* promoters (Figure 5J), thus increasing *SOX10* and *NFKBIE* expression (Figure 5K). In addition, we also observed elevated H3K27ac at the *SOX10* and *NFKBIE*

promoters, possibly through the decreased recruitment of HDAC1 by RelA due to the elevated NFKBIE expression. As a functional validation, we tested *SOX10*-KO and *NFKBIE*-KO M397 cells, expecting that both engineered cells would develop drug tolerance to BRAFi more rapidly than the wild type counterpart. These engineered cell lines indeed behaved as expected according to our proposed mechanism (Figure 5L). Collectively, these experiments provide strong evidences for the proposed mechanism. They validate the critical role of RelA as a rapid-acting regulator of resistance development by recruiting KDM5B and HDAC1 to epigenetically suppressed *SOX10* and *NFKBIE* expression and consequently induce BRAFi drug tolerance (Figure 5A).

Baseline epigenome states correlate with the phenotypic plasticity and drug response across melanoma cell lines

We now turn towards understanding whether the mechanism of adaptive response of M397 cells to BRAF inhibition can be generalized to other *BRAF*-mutant melanoma cell lines that exhibit varying degrees of phenotypic plasticity and baseline level of resistance to BRAFi. We first tested the generality of M_{early} and M_{late} modules in other melanoma cell by evaluating the co-occurrence of gene sets associated with two modules across the CCLE melanoma cell lines. We observed higher co-occurrence score relative to random gene permutation (Figure S6A, see STAR Method), suggesting the various gene sets associated with two modules are not specific to the cell line we studied, but similarly modulated and co-expressed across other cohorts of melanoma cells.

Furthermore, we investigated the BRAFi-induced transcriptome changes in additional six patient-derived *BRAF*-mutant cell lines, each with a unique drug-naïve phenotypic composition that varies from largely mesenchymal (M381) to in-between neural crest and melanocytic (M263), to mostly melanocytic (M229) [25]. In order to permit comparisons between different cells, we projected the whole transcriptome kinetic data of each cell line onto the two-dimensional space defined by M_{early} and M_{late} , similar to the two-dimensional plot in Figure 2B (Figure 6A). Cell lines at the left side displayed much higher baseline IC50 value than those at the right side, suggesting that cells at the BRAFi-induced dedifferentiated state are intrinsically resistant to BRAF inhibition. Similar trends were also observed across various *BRAF*-mutant melanoma cell lines from the GDSC database (Figure S6B), indicating cells with higher M_{early} and lower M_{late} scores are generally resistant to BRAFi. Similar to M397, upon BRAF inhibition, each cell line exhibited an initial change in the positive direction along M_{early} , followed by a motion along the negative direction of M_{late} (Figure 6A), which implied some mechanistic similarities between the cells. However, different cell lines also exhibited widely different amplitudes of motion along this 2D landscape, reflecting large variations in transcriptome plasticity (Figure 6A). Our hypothesis was that these different

amplitudes of transcriptome motion, particularly the motion along the controlling module M_{early} , were related to the pre-treatment (baseline) epigenome state of the cells.

M_{early} was enriched with early-acting epigenetic modulations that dictate the subsequent adaptive transition in M397 (Figure 2B-2E). Thus, for comparison across cell lines, motion along M_{early} was chosen as a surrogate of transcriptome plasticity. We correlated the BRAFi-induced motion along M_{early} with the baseline epigenetic characteristics of the cells. These correlations included the average chromatin accessibility (Figure 6B), the average levels of the two histone marks across all the enriched domains (Figures 6C, 6D, and S6C), and the levels of two histone marks on the TSS region of *SOX10* (Figures 6E, 6F, and S6D). The strong correlations, particularly with *SOX10*-specific H3K4me3/H3K27ac signals, suggest that cellular plasticity is associated with the baseline chromatin state of the drug-naïve cells and implicate the generality of the chromatin remodeling mechanism in the adaptive resistance of melanoma cells. These findings also imply that cellular plasticity that permits adaptation to BRAFi may be encoded in cells before treatment through general and specific structural details of the chromatin.

The relationships between cellular plasticity, chromatin accessibility (Figure 6G), and adaptive resistance to BRAFi suggest that drug targeting the chromatin remodeling machinery in combination with BRAFi would arrest the adaptive transition and inhibit the development drug resistance in the most plastic cell lines (e.g. M397 or M262) but should have little effect on the least plastic lines (e.g. M381). We used a recently-developed KDM5 inhibitor CPI-455 [62] and a second generation HDAC1 inhibitor Quisinostat [63] to treat the cells in combination with BRAFi vemurafenib. We employed the minimal doses of CPI-455 and Quisinostat that were sufficient to inhibit KDM5B and HDAC1 without significant cytotoxicity (Figures S6E and S6F). Clonogenic assays revealed that, in comparison with BRAFi monotherapy, both of the dual drug combinations (BRAFi + KDM5Bi or BRAFi + HDACi) could lead to a sustained growth inhibition across several epigenetically plastic melanoma cell lines, including M397 (Figure 6H). These results demonstrate the potential utility of co-targeting the driver oncogene *BRAF* along with chromatin-remodeling machinery to treat certain melanomas which demonstrate significant epigenetic changes upon BRAF inhibition. Importantly, the M381 and M233 cell lines, which exhibited the lowest levels of plasticity (Figure 6A) and chromatin accessibility (Figure 6G), did not respond to the therapy combinations (Figures 6H). Thus, the responsiveness towards combination therapy with epigenetic drugs can be predicted through the degree of cellular plasticity, which may be encoded by the baseline epigenome of cells prior to treatment. Collectively, the strong associations across different cell lines between transcriptome changes and the baseline chromatin permissiveness suggest both a generality and predictable

limitations of the molecular mechanism (Figure 5A), and also inform the use of epigenetic drugs across melanoma cells of different phenotypes.

The presence of the epigenetic resistance mechanism in MAPKi-treated melanoma patients

To determine whether the adaptive resistance mechanism identified in melanoma cell lines is present in melanoma patient samples, we collected paired tumor biopsies from patients bearing *BRAF*^{V600}-mutant tumors prior to MAPKi treatment and at the onset of therapy resistance. Paraffin-embedded cross sections were stained for MITF, SOX10, NFKBIE, and KDM5B. Prior to the therapy, these four protein markers showed relatively uniform spatial distributions (Figure 7A). After MAPKi exposure, some regions of the tumor tissues retained similar MITF, SOX10, and NFKBIE expression and loss of KDM5B, while other regions showed elevated KDM5B but loss of MITF and SOX10 (Figures 7A and 7B). The mutually exclusive spatial distribution of KDM5B and SOX10/MITF was consistent with the chromatin remodeling-mediated adaptive resistance mechanism observed (Figure 5A), and suggested the presence of the adaptive resistance mediated by the epigenetic reprogramming in melanoma patients undergoing MAPKi treatments.

To investigate the generality of our findings, we interrogated the expression levels of phenotypic markers and critical TFs using published transcriptome data of *BRAF*-mutant melanoma patients [9,64]. Gene expression levels from seven paired samples before and after MAPKi treatment were compared and enriched against curated gene sets (Figures 7C, and S7A; Table S6; STAR Methods). The reduced expression of *MITF*, *NFKBIE*, *SOX10*, and other melanocytic genes as well as the elevated expression of *KDM5B*, *JUN*, and other mesenchymal-related genes after treatment suggested the existence of the chromatin remodeling-mediated adaptive resistance in these patients. Furthermore, we also analyzed the published transcriptome data [64] of the paired melanoma patient samples by projecting them onto the two-dimensional plot defined by M_{early} and M_{late} and calculating the changes of M_{early} and M_{late} score upon MAPKi treatment. Like M397, M_{early} score increased and M_{late} score decreased after treatment, indicating the gene signatures associated with M_{early} and M_{late} displayed consistent changes with our cell line model (Figure S7B). In addition, we also evaluated the co-occurrence of gene sets associated with M_{early} and M_{late} modules across the TCGA melanoma patient samples (STAR Method). We observed higher co-occurrence score relative to random gene permutation (Figure S7C). This suggests that the various functional gene sets associated with two modules are not cell line specific, but similarly modulated and co-expressed across other cohorts of melanoma patient samples. We further performed Kaplan-Meier survival analysis using the melanoma dataset in TCGA (STAR Methods). Consistent with our mechanism, patients with either low baseline expression level of *KDM5B*

or higher level of *NFKBIE* are less likely to develop adaptive resistance to MAPK inhibition and consequently have longer overall survival (Figure 7D). Taken together, these results confirmed the existence of adaptive resistance in melanoma patients, and validated the clinical relevance of the epigenetic mechanism.

Discussion

Epigenetic plasticity is precisely titrated during normal development to stabilize cell fate commitment and facilitate appropriate cellular responses to external cues [15,17,65]. Cancer cells with dysfunctional epigenome homeostasis can exploit this built-in chromatin plasticity to survive drug challenges and other stressful conditions [24,66–68]. Accumulating evidence indicates that epigenetic dysregulation can vary across different tumor cells and can also give rise to all the classic hallmarks of cancer [15]. For example, for epigenetically plastic cancer cells, a highly permissive epigenetic landscape allows them to rapidly adapt to drug challenges by reversibly transitioning into a drug-tolerant state that fuels malignant progression. Such adaptive transitions have been recently observed in clinical biospecimens of glioblastoma [23], breast cancer [69], and many other tumor types [18,28,70]. Despite the strong influence of epigenetic plasticity on therapy resistance, the mechanistic underpinnings of the drug-induced epigenetic reprogramming that initiates the adaptive transition are less clear. A systems-level characterization aimed at capturing the dynamic drug adaptation is a pressing need for solving this mechanistic puzzle.

Our goal was to establish a firm mechanistic link between epigenetic plasticity and the development of adaptive drug resistance in *BRAF*-mutant melanomas. Using BRAFi-treated patient-derived melanoma cell lines as models, our study revealed several properties of cellular plasticity. First, the drug-induced cell state changes were completely reversible upon drug removal at the transcriptome, epigenome, and functional levels. Second, the cell state changes proceeded via the sequential operations of two distinct gene expression programs, with the early-acting gene module setting in motion epigenetic and transcriptional programs that encode for longer-term changes associated with the late-acting gene module, ultimately yielding the drug-resistant mesenchymal-like phenotype. Finally, the activation of the early-acting module upon BRAF inhibition is extremely rapid. For M397 cells, activation involves nuclear translocation of the key transcription factor RelA, aided by rapid down-regulation of *NFKBIE* and coupled with the rapid recruitment of histone modifiers. These cells are thus poised with a ‘hair-trigger’ response to drug challenge.

A mechanistic link between epigenetic plasticity and the development of adaptive drug resistance was successfully established through a systems-level, multi-omics approach that focused on the kinetics of the adaptive response. We first acquired time-resolved

transcriptome and epigenome data to track the kinetics of the reversible cell state transition over a two-month period. Critical regulators that underlie the adaptive transition were distilled from thousands of candidate TFs/co-factors through the sequential application of two distinct systems biology approaches followed by bioinformatics inferences. First, a top-down information theoretic analysis [44,46,51,52,71] simplified the transcriptome changes into the changes of two gene modules, one of which (M_{early}) was fully activated within the first 3 days of BRAF inhibition. Next, dynamic ODE modeling [72] precisely identified co-dependencies between two modules and uncovered the dominating influence of M_{early} over both itself and the second module, M_{late} . Guided by these gene module relationships, bioinformatic inference further identified key TFs and epigenetic regulators from which we extracted and experimentally validated a mechanistic regulatory network for the adaptive resistance. Such mechanistic understanding would be difficult to uncover without the synergistic integration of this three-part systems-level computational analysis. This analytic methodology could potentially be adapted for the understanding of cell state changes in other biological contexts.

We find that the adaptive response was not truly reversible, in that the trajectory that the cancer cells took upon drug exposure was not retraced following drug removal. Although drug release reversed the transcriptional changes, it did not reverse the order of the two modules, so that M_{early} was deactivated first upon drug removal. Therefore, the cells took a cyclic route as they traversed from drug-naïve to drug-resistant and back (Figure 2B). Similar to the adaptive response to drugging, this finding implicates the involvement of M_{early} -associated epigenetic reprogramming in regulating the first step of the reverse transition as well. It emphasizes the importance of those epigenetic regulations that manifest as an early-acting transcriptional program for the rapid adaptation to therapeutic challenges in melanomas. Indeed, the sequential operation of M_{early} and M_{late} modules associated with cell state regression was generally observed across several other melanoma cell lines, although with different magnitudes of motion (Figure 6A). By interpreting that magnitude of motion as a metric of transcriptome plasticity, we found that the plasticity was strongly correlated with baseline chromatin accessibility and with the levels of activation histone marks of untreated melanoma cell lines (Figure 6B-6F). These findings imply that transcriptome plasticity may be epigenetically encoded prior to drug exposure. The sequential operations of M_{early} and M_{late} also resemble observations of sequential transcriptional waves that guide cell differentiation in other biological systems [73–76]. The molecular causes of the differences in baseline epigenome profiles across cell lines are unclear. Deciphering the causes of the intertumoral epigenetic heterogeneity provides an important area for future investigation.

A distinct chromatin state was observed in the drug-induced resistant cells compared with untreated or long-term drug removal cells. We identified histone remodelers KDM5B and HDAC1 as important players for establishing the resistant epigenetic state. However, other epigenetic remodelers may also contribute to the cell state changes. In fact, the SIRT6 and BET protein families have been reported as regulators of MAPKi resistance in other melanoma systems [20,37]. Histone remodelers are generally recruited by TFs to regulate specific downstream genes. While other TFs could potentially recruit histone remodelers to regulate downstream resistance-associated genes, we identified RelA as a key player in regulating *SOX10*, whose repression is well-documented to trigger the resistant mesenchymal phenotype in melanomas [21,26]. In fact, the immediate recovery of *SOX10* expression levels after inhibition of RelA nuclear translocation in drug-tolerant cells confirmed the critical role of RelA as a key upstream TF in regulating *SOX10* expression and associated resistance development (Figure 5F). In addition, the rapid recruitment of histone remodelers by RelA to the promoter regions of *SOX10* within as early as 3 days after BRAF inhibition confirmed the critical role of RelA for initiating the adaptive resistance early on. The question of how BRAF inhibition induces the subsequent RelA-dependent molecular circuit was not resolved. The elevated level of reactive oxygen species (ROS) in melanoma cells upon BRAF inhibition [11] might be relevant, since ROS is known to activate the proinflammatory NF κ B signaling pathway [77]. Phosphoproteomics that can resolve early signaling events immediately after BRAF inhibition may prove useful for such endeavor [78,79].

One of the most exciting aspects of epigenetic therapy is the ability to potentiate responses to existing therapies, which effectively multiplies the drug arsenal against cancer progression [80]. The intimate role of epigenetic dysregulation in therapy resistance development suggested that the epigenetic regulators KDM5B and HDAC1 would be attractive targets for combining with BRAFi for arresting the development of adaptive resistance at least in epigenetically plastic melanoma cells. This hypothesis was validated in clonogenic assays (Figure 6H). It is worth noting that BRAF and HDAC inhibitors were reported to be used in sequential order to eliminate the melanoma cells that acquired resistance to BRAF inhibition by exploiting the lethal ROS levels [11]. However, our results pointed to an alternative therapeutic strategy that using them in combination at the very beginning could retain tumor cells in the drug-sensitive stage and thus lead to sustained growth inhibition. While *in vitro* models may not fully recapitulate the cellular behavior *in vivo*, evidence of our epigenetic mechanism was also observed in melanoma tissue samples from patients under MAPK inhibitor treatments. This implies a potential role for these combination therapies in treating *BRAF*-mutant melanomas, with the provocative goal of disrupting the development of adaptive resistance against MAPKi (Figure 7A). In an interesting parallel, the adaptive regression in melanoma towards the drug-tolerant state has

also been reported to contribute to resistance development in various immunotherapy regimens [9,25,33,81]. Indeed, by analyzing transcriptome data of melanoma patients from a recent trial of PD-1 checkpoint blockade [41], we observed lower M_{late} module score in non-responders than responders (Figure S7D), implying the more dedifferentiated melanoma phenotype was less likely to respond to PD-1 checkpoint blockade. With the increasing options of immunotherapy in treating metastatic melanomas in the clinic, combinations of epigenetic drugs with drugs targeting immune modulations may warrant further exploration. Moreover, how to sensitize the melanoma cells with minimal epigenetic plasticity (e.g. M381) to combinatory targeted inhibitions also requires further studies.

Experimental Model and Subject Details

Cell culturing

M-series patient-derived cell lines used in this study were generated under UCLA institutional review board approval # 11-003254. Cells were cultured in a water-saturated incubator at 37 °C with 5% CO₂ in RPMI 1640 with L-glutamine (Life Technologies), supplemented with 10% fetal bovine serum (Omega), and 0.2% antibiotics (MycoZap™ Plus-CL from Lonza). The cell lines were tested for mycoplasma and were periodically authenticated to its early passage using GenePrint 10 System (Promega). BRAF inhibitor (vemurafenib), KDM5B inhibitor (CPI-455), HDAC inhibitor (Quisinostat) and RelA translocation inhibitor (JSH-23), all from Selleck Chemicals LLC, were dissolved in DMSO at designated concentrations before applying to cell culture media. Cells were plated in 10 cm tissue culture plate at 60% confluency and treated with certain drugs for the specified numbers of days. M397 cells were treated with 3 μM of vemurafenib for 59 days or for 29 days followed by drug removal removed and cell culture with normal medium for another 35 days. Gender of the patients from whom the cell lines were derived: M397, female; M229, male; M262, female; M249, female; M263, female; M233, male; M381, male.

Patient samples

Melanoma samples before treatment were obtained from surplus biopsies stored in the melanoma biobank at the Peking University Cancer Hospital and Institute (Beijing, China). The patient #1 received vemurafenib and patient #2 received dabrafenib and trametinib combinations. Both patients exhibited partial response (PR) to these MAPK inhibitors. The secondary biopsies were performed when patients showed progressive disease (PD). The patients consented to the use of their biopsy materials for scientific studies and all research was conducted in accordance to the guidelines and protocols approved by the institutional ethics review committee and abiding by all local laws for research on human derived tissue. Gender of the reported patient samples: patient#1, female; patient#2, female.

Method Details

RNA-seq

Total RNA was extracted from cell pellets using RNeasy Mini Kit (Qiagen). RNA sequencing libraries were prepared with Kapa RNA mRNA HyperPrep kit (Kapa Biosystems) according to the manufacturer's protocol. Briefly, 100 ng of total RNA from each sample was used for polyA RNA enrichment using magnetic oligo-dT beads. The

enriched mRNA underwent fragmentation using heat and magnesium, and the first-strand cDNA was made using random priming. The combined 2nd cDNA synthesis with dUTP and A-tailing reaction generated the resulting ds cDNA with dAMP to the 3' ends. The barcoded adaptors (Illumina) finally were ligated to the ds cDNA fragments. A 10-cycle of PCR was performed to produce the final sequencing library. The libraries were validated with the Agilent Bioanalyzer DNA High Sensitivity Kit and quantified with Qubit.

ATAC-seq

A previously published protocol [82] was used for cell lysis, tagmentation, and DNA purification. The Tn5 treated DNA was amplified with a 5-cycle PCR in 50 μ l reaction volumes. The tubes were removed from thermocycler and used 5 μ l of a partially amplified library to perform qPCR to determine how many additional PCR cycles were needed. For the samples in this study, an additional 4-5 cycles of PCR was performed on the remaining 45 μ l of each partially amplified product. 1.8X AmpurXP beads purification was used for the final PCR cleanup. The libraries were validated with the Agilent Bioanalyzer DNA High Sensitivity Kit, and quantified with qPCR.

ChIP-seq, ChIP-PCR, and ChIP-qPCR

H3K4me3, H3K27ac, NFkB p65, KDM5B, and HDAC1 ChIP were performed by using Magna ChIP A/G Chromatin Immunoprecipitation Kit. Briefly, cells were cultured to ~80% confluency in a petri dish containing 10 mL of growth media and then fixed in 1% formaldehyde by adding 275 μ l of 37% formaldehyde for 10 minutes to cross-link protein–DNA complexes at room temperature. The unreacted formaldehyde was quenched by adding glycine to a final concentration 0.125 M. Gently swirl dish to mix. The nuclear pellet was isolated with Cell Lysis Buffer. The pellet was resuspended with 500 μ l SDS Lysis Buffer containing 1X Protease Inhibitor Cocktail II before sonication for 4 min (10 s on, 30 s off, 10% strength in a Bioruptor to yield DNA fragments of 0.2-1.0 kb in length. The lysates were cleared by centrifugation (12,000g for 10 min at 4 °C) and diluted tenfold in ChIP dilution buffer to decrease the concentration of SDS. After keeping 10% of the sample as input, 500 μ l supernatant was incubated overnight at 4 °C with antibody and 20 μ L of fully resuspended protein A/G magnetic beads. The washing, elution, reverse cross-linking, and purification steps were performed according to the manufacturer's description. Eluted DNA was quantified by Qubit dsDNA HS Assay Kit, and used for further PCR, qPCR or ChIP-seq library preparation.

ChIP-seq libraries were prepared with Kapa DNA HyperPrep Kit (Kapa, Cat KK 8700) according to the manufacturer's protocol. Briefly, 5-10 ng of immunoprecipitated DNA was

underwent end-repaired, A tailing and adaptor ligation. A 10 cycles of PCR was performed to produce the final sequencing library. The libraries were validated with the Agilent Bioanalyzer DNA High Sensitivity Kit and quantified with Qubit.

ChIP-PCR was performed by using KAPA Taq ReadyMix PCR Kit on CFX96 Real Time PCR Detection System without adding plate read. ChIP qPCR was performed by using SsoAdvanced Universal SYBR Green Supermix on CFX96 Real-Time PCR Detection System. In each PCR/qPCR reaction, 2 µl eluted DNA was added.

Sequencing of RNA-seq, ChIP-seq, and ATAC-seq library

RNA and ChIP-seq library templates were prepared for sequencing using Illumina HiSeq SR Cluster V4 Kit. Sequencing runs were performed on Illumina HiSeq 2500 in the single read mode of 51 cycle of read1 and 7 cycles of index read with SBS V4 Kits. ATAC-seq library templates were prepared for sequencing with Illumina HiSeq PE Cluster V4 Kit, sequencing runs were performed in the paired-end mode of 101 cycle on Illumina HiSeq 2500 with HiSeq SBS V4 Kits. Real-time analysis (RTA) 2.2.38 software was used to process the image analysis and base calling.

CellTiter-Glo

5000k cells were seeded onto each well of a 96well plate and were treated with indicated drug concentrations for 72hours. ATP-based CellTiter-Glo (Promega) luminescent cell viability assay was utilized to quantify the cell number for constructing dose-response curves. IC50 values were calculated as standard from at least three biological replicates.

Cell cycle and apoptosis assays

For cell cycle analysis, 500k cells were plated and were then treated with EdU. After treatment, cells were washed with PBS and fixed. Next, cells were processed for EdU detection using the Click-iT EdU Alexa Fluor 488 Flow Cytometry Assay Kit (Thermo Fisher) according to the manufacturer's protocol. DNA content was visualized using SYTOX AADvanced (Thermo Fisher). Gates were determined using an unstained control. All experiments were performed with at least two biological replicates.

Cell apoptosis assays were performed by treating indicated cell lines cultured under respective conditions. Cells were stained with Annexin V-FITC and propidium iodide for 15 minutes at room temperature before flow cytometry analysis. Gates were determined using an unstained control. All experiments were performed with at least two biological replicates.

Fluorescence imaging of cell lines

Fluorescent micrographs of cells were acquired with a Nikon C2plus confocal microscope (Ti) using Plan Apo λ 20 \times objective (Nikon Inc., Melville, NY) controlled by NIS elements AR software (4.51.00) with the following settings: 30 μ m pin hole, 12-bit acquisition, 25-30 PMT gain, and laser power of 0.7% (405 nm), 1.0% (488 nm), or 0.4% (640 nm). The cells adhered on gelatin-coated glass surfaces in 96-well glass bottom plates (Greiner Sensoplate Plus, Cat# 655892). To prepare the surface, 100 μ L of 0.1% gelatin solution was incubated in each well at room temperature for 10 minutes. After incubation, the solution was removed, and the wells were air-dried for at least 15 minutes. Typically, 10,000 cells were seeded per well in 100 μ L culture media and grown to ~70% confluency. To fix the cells, equal volumes of 4% PFA solution was gently added to each well. After fixing for 20 minutes at room temperature, the cells were washed twice in wash buffer (0.1% BSA in PBS), and blocked and permeabilized in blocking buffer (10% normal donkey serum, 0.3% Triton X-100 in PBS) for 45 minutes at room temperature. After removing blocking buffer, cells were incubated in mouse anti-MITF primary antibodies (Thermo Fisher Scientific, Cat# MA5-14154) diluted to 5 μ g/mL in antibody diluent (1% BSA, 1% normal donkey serum, 0.3% Triton X-100 in PBS) for 4 hours at room temperature. After washing twice in wash buffer, cells were incubated in donkey anti-Mouse IgG, Alexa Fluor 647 secondary antibody (Thermo Fisher Scientific, Cat# A31571, RRID:AB_162542) diluted to 4 μ g/mL in antibody diluent for 1 hour at room temperature. After washing twice in washer buffer, cells were counterstained for 20 min at room temperature with Alexa Fluo 488 Phalloidin (Thermo Fisher Scientific Cat# A12379), as per manufacturer's instructions. After washing twice in wash buffer, cells were further counterstained for 5 min with 4',6-Diamidino-2-Phenylindole (DAPI) (Thermo Fisher Scientific Cat# D1306) diluted to 1 μ g/mL in PBS. Finally, after washing twice in PBS, the wells were filled with 78% glycerol.

Western blotting

Histone proteins were extracted using the Histone Extraction Kit (ab113476). The Invitrogen precast gel system NuPAGE was used for SDS-PAGE. The 4–12% Bis-Tris gels were loaded with samples. After blotting, the membranes were blocked in 5% BSA with TBS + 0.1% Tween-20 (TBST) mix for at least 1 hour at room temperature. Membranes were then incubated overnight with the primary antibody in 5% BSA with TBST at 4°C. The next day, membranes were washed three times for 5 min in TBST, incubated with a suitable HRP-coupled secondary antibody for 1 hour at room temperature, and washed three times and proteins were visualized with SuperSignal™ West Pico PLUS Chemiluminescent Substrate (Cat.No.34577) using the ChemiDoc™ XRS+ System.

RT-qPCR

For quantitative reverse transcription-polymerase chain reaction (qRT-PCR), total RNA was extracted by TRIzol™ Plus RNA Purification Kit (Cat.No.12183555) and reversed to cDNAs. Real-time PCR was performed with gene-specific primers on the two-color real-time PCR detection system (BIO-RAD) using the SsoAdvanced™ Universal SYBR® Green Supermix (Cat.No.1725272) to represent the relative expression levels.

Co-IP and protein detection

For cell lysis, cells were cultured to ~80% confluency in a petri dish containing 10 mL of growth media and were washed with ice-cold PBS three times. Then the cells were collected with a scraper in 1 mL ice-cold PBS supplemented with 1X proteinase inhibitor cocktail (Cell Signalling) and centrifuged. The cell pellets were resuspended in cell lysis buffer containing 50 mM Tris-HCl pH 7.5, 250 mM NaCl, 1 mM EDTA, 0.5% Triton X-100, 10% glycerol, and 1X proteinase inhibitor cocktail (Cell Signalling). The resuspended cell pellets were incubated in a cold room (4°C) for 30 min and sonicated in ice-water bath three times for 5-second pulses each. Then the cell lysates were cleared by 10,000 × g centrifuge at 4°C for 10 min. The protein was quantified by Qubit Protein Assay Kit (Invitrogen).

For cross-linking antibody to magnetic beads, 20 µl magnetic protein A/G beads (Millipore) were washed with cell lysis buffer twice and resuspended in 100 µl cell lysis buffer without glycerol. 5 µg Anti-NFκB p65 (RelA) antibody was coupled to Magnetic protein A/G beads by incubation at 4°C overnight on a rotator. The RelA antibody-coupled Protein A/G beads were washed three times in 200 µL Conjugation Buffer (20 mM Sodium Phosphate, 0.15M NaCl, pH 7.5). Then the RelA antibody-coupled beads were suspended in 250 µL 5 mM BS3 with conjugation buffer and incubated at room temperature for 30 min with rotation. The cross-linking reaction was quenched by adding 12.5 µl 1M Tris-HCl (pH 7.5) and incubated at room temperature for 15 min with rotation. The RelA antibody conjugated protein A/G beads were washed with Cell Lysis buffer three times.

For co-immunoprecipitation (Co-IP) experiment, 200 µl pre-cleared cell lysates were added to RelA antibody conjugated protein A/G beads and incubated overnight at 4°C with rotation. The beads were then washed 5 times with 500 µl cell lysis buffer without glycerol. The pellet beads were collected by a magnetic stand and resuspended in 65 µl SDS buffer (50mM Tris-HCl pH6.8, 2% SDS, 10% glycerol, 1% β-mercaptoethanol).

For immunoblotting, the elutes were boiled for 10 min at 95 °C. The 20 µl boiled elutes were electrophoresed on 10% Mini-PROTEAN TGX Precast Gels with running buffer containing

SDS. Then the gels were transferred on the PVDF membranes in Bio-Rad Wet Blotting Systems. The membranes were blocked with 5% non-fat dried milk (Bio-Rad) dissolved in PBS for 1 h at room temperature and incubated at 4 °C overnight with the following primary antibodies: JARID1B/KDM5B (Bethyl Lab #A301-813A), NFκB p65 (Millipore # 17-10060), HDAC1 (Millipore # 17-608). After incubating with secondary Goat anti-Mouse/Rabbit antibodies coupled with HRP (Thermo), membranes were visualized by ChemiDoc XRS+ Imaging Systems.

CRISPR engineering of cell lines

LentiCRISPR v2 plasmids targeting the coding sequence of *KDM5B* or *NFKBIE*, and control LentiCRISPR v2 plasmid were purchased from GenScript. Lentiviruses were produced in HEK-293T cells by transient transfection of LentiCRISPR v2 plasmid and their packaging vectors psPAX2 and pMD2.G as previously described [83]. The virus was collected, filtered through a 0.45µm syringe filter after 48 hours and the M397 cells were spin-infected with viral supernatant supplemented with 10 µg/mL polybrene at 2,500 rpm and 30°C for 90 min. The transduced cells were selected using puromycin, starting at 3 days post-transduction. Genome editing in the respective locus was examined using a surveyor assay, which was performed according to the manufacturer's instructions (Integrated DNA Technologies) [84].

Clonogenic assay

Melanoma cells were plated onto six-well plates with fresh media at an optimal confluence. The media (with drug or DMSO) were replenished every two days. Upon the time of staining, 4% paraformaldehyde was applied onto colonies to fix the cells and 0.05% crystal violet solution was used for staining the colonies.

Patient multiplexed IHC and quantification

Multiplexed IHC staining was performed on FFPE tissue samples from melanoma primary tumors and metastatic lesions. Multiplexed IHC staining and antibody validation were performed by PerkinElmer. Briefly, the slides were firstly deparaffinized in xylene, followed by treatment with microwave for epitope recovery. Hematoxylin and eosin (H&E) staining was performed for histopathological evaluation and multiplexed IHC staining was then conducted on the slides via an Opal 7-Color IHC Kit (NEL811001KT, PerkinElmer) and a panel of antibodies including anti-KDM5B (Sigma-Aldrich), anti-MITF (Sigma-Aldrich), anti-SOX10 (Sigma-Aldrich) and anti-NFKBIE (Sigma-Aldrich). The protocol was based on the manual of PerkinElmer Opal staining Kit and previous studies [85]. Finally, DAPI (PerkinElmer) was stained to visualize cell nuclei. Images were acquired using a Vectra

Polaris Multispectral Imaging System (PerkinElmer) for whole-slide scanning. inForm Image Analysis software (inForm 2.4, PerkinElmer) was used to process and analyze all images. Image J was employed to quantitate the fluorescence intensities of cells in the designated areas.

Quantification and Statistical Analysis

RNA-seq analysis

Reads were aligned against the human genome (hg19) using TopHat2 [86]. Read counts were quantified using htseq-count [87], with known gene annotations from UCSC [88] with anti-sense (AS) genes removed. Fold-change values were calculated from Fragments Per Kilobase per Million reads (FPKM) [89] normalized expression values, which were also used for visualization (following a \log_2 transformation). Aligned reads were counted using GenomicRanges [90]. Separate comparison p-values were calculated from raw counts using limma-voom [91], and false discovery rate (FDR) values were calculated using the method of Benjamini and Hochberg [92]. Prior to p-value calculation, genes were filtered to only include transcripts with an FPKM expression level of 0.1 (after a rounded \log_2 -transformation) in at least 50% of samples [89]. Genes were defined as differentially expressed if they had a $|\text{fold-change}| > 1.5$ and $\text{FDR} < 0.05$. Candidate genes were selected based upon the inverse overlap between the early and late time series. The “Early Drug” time series included 5 samples from Day 3 to Day 29 (with active drug treatment). The “Late No-Drug” had 6 time-points after drug removal at Day 29 (4-35 days post-drug removal). There were also 3 samples with active drug treatment after Day 29, but no genes were differentially expressed for that comparison consistent with the expectation of similar gene expression patterns after developing resistance; however, those 3 late drug samples (along with an untreated control sample) were used for visualization in a heatmap of candidate genes (defined as genes with a significant increase in expression with drug treatment and a significant decrease in expression after drug removal, or a significant decrease in expression with drug treatment and a significant increase in expression after drug removal).

A heatmap of $\log_2(\text{FPKM} + 0.1)$ standardized expression (mean of 0, standard deviation of 1, per-gene) was visualized using the ‘ggplots’ package in R. More specifically, standardized expression was limited to be within the range of -2 and 2 (so, all values less than -2 were set to -2, and all values greater than 2 were set to 2), and clustering was only performed by genes (with samples ordered by time, within each category). Hierarchical clustering was performed using Euclidian Distance as the distance metric.

Consensus clustering of M397 transcriptome

To inspect the similarity of the transcriptome of M397 in different time points, we applied consensus clustering using the R package of ConsensusClusterPlus [93] to define clusters. The top 3,000 most varying genes were used for consensus clustering with the hierarchical clustering method.

Analysis of differentially expressed transcription factors

To annotate differentially expressed transcription factors/co-factors, the differential expression analysis was performed by Cuffdiff among D0, DR30, DR35, D29, and D33 ($FDR \leq 0.05$). Then we downloaded TFs/co-factors list from AnimalTFDB 3.0, and got the up/down-regulated TFs/co-factors by screened from the differential expression analysis. The result was visualized by a volcano plot.

ChIP-seq analysis

Reads were mapped to the human genome hg19 by bowtie2 [94]. The identical aligned reads were deduplicated to avoid PCR duplicates. Peaks were called on the merged set of all ChIP-seq reads of M397 using MACS2 with the following parameters: --nomodel, --broad [95]. Peaks were assigned to the gene with closest TSS. Differential analysis between D0 and any other samples(D3, D32, DR) were performed using diffReps with a window size 1000.[96]. Differential binding regions were called if the absolute log value of the fold change was more than 1 and $FDR < 0.05$. Then the differential binding regions were compared and merged to ChIP peaks called from MACS2 To visualize peaks in each sample, bed graph file was generated using MACS2 with following parameters: --nomodel, --broad, --bdg, --SPMR. Then the generated bed graph file was converted into bigwig file by bedGraphToBigWig tool. The average of ChIP-seq signal was calculated and visualized by deepTools v3.0.2 [97]. The read counts were normalized by RPKM. $RPKM (\text{per bin}) = \text{number of reads per bin} / (\text{number of mapped reads (in millions)} * \text{bin length (kb)})$. To assess how H3K4me3 and H3K27ac signal of differential binding regions in the cyclic transition of M397 changed in multiple cell lines, we calculated the normalized read counts around the differential binding peaks($\pm 1\text{kb}$) at the window size of 10bp. The different peaks are called from the time-series ChIP-seq data we generated at this paper. To evaluate the average H3K4me3 and H3K27ac signal at *SOX10*, we slid the 10bp window size from -3Kb to +10Kb around the TSS to counts the normalized reads and calculated the average value for 520-780 bins.

ATAC-seq analysis

All experiments were performed once. First, adaptor sequences were trimmed from the reads using Cutadapt. Then Reads were aligned to hg19 with bowtie2 with standard parameters and a maximum fragment length of 2,000. [94]. The identical aligned reads were deduplicated to avoid PCR duplicates. These de-duplicated reads were then filtered for high quality ($\text{MAPQ} \geq 30$). Peaks were called on the merged set of all ATAC-seq reads of M397 using MACS2 with following parameters: --nomodel, -broad, -q 1e-5 [95] and filtered to remove putative copy number varied regions [98]. Differentially accessible regions between D0 and any other samples(D3, D32, DR) were identified using diffReps with a window size 500. (Shen et al., 2013)). Differential binding regions were called if the absolute log value of the fold change was more than 1 and $\text{FDR} < 0.05$. Then the differential binding regions were compared and merged to ChIP peaks called from MACS2. To visualize peaks in each sample, the same routine in ChIP-seq analysis was applied. ATAC-seq profile of differentially accessible region in samples of M397 were generated by using ngs.plot.r with following parameters: -G hg19 -R bed -L 1000 -GO km -KNC 4 -SC 0,3.5. The profile of unchanged ATAC-seq peaks in samples of M397 was plotted by using ngs.plot.r with following parameters; -G hg19 -R bed -L 1000 -GO total -SC 0,3.5. HOMER was used to find over-represented motifs in the set of differentially accessible peaks by using a background set of peaks that did not significantly change, and using the parameter “-size given -len 6,8,10,12 -mset vertebrates -bg” [98]. The average of ATAC-seq signal was calculated and visualized by deepTools v3.0.2 [97]. The read counts were normalized by RPKM. $\text{RPKM (per bin)} = \text{number of reads per bin} / (\text{number of mapped reads (in millions)} * \text{bin length (kb)})$. For the calculation of the average ATAC-seq signal, we constructed the meaningful value around the different peaks ($\pm 1\text{Kb}$) at the window size of 10bp and calculated the average value for 140-160 bins. The different peaks are called from the time-series ATAC-seq data we generated at this paper.

Inference of RelA downstream transcription factors

To identify RelA-binding TFs/co-factors in the M_{late} process, we downloaded TF/co-factor list from AnimalTFDB 3.0. HOMER was used to annotate RelA-binding motif (HOMER Motif 208) at the whole genome level with the following parameters: annotatePeaks.pl tss hg19 -size -1800,400. Then, TF/co-factors containing RelA-binding-motif were selected out. Within this list of TF/co-factors, RelA-motif overlapped H3K4me3, H3K27ac and ATAC-seq peaks were analyzed by bedtools v2.27.1. Thirty-six TFs showed changes in the RelA-motif overlapped peaks across the adaptive transition (D32 vs D0). However, only two TFs, *SOX10* and *DNAJC1*, displayed significant changes ($p < 0.05$) for all three epigenome alterations (Table S5).

Surprisal analysis and SOM visualization

In order to analyze the dynamic transcriptome changes across all time points, we assume that many of them are coordinately changing together as a group (or gene module). Surprisal analysis has been well documented in deconvoluting the change of thousands of genes into the change of a couple of gene modules and one unchanged gene expression baseline [46,51,52,99].

When applied here, surprisal analysis simplified the transcriptome dynamics into two major gene modules and one unchanged gene expression baseline. Briefly, the natural logarithm of the measured level of a transcript i at a specific time point t , $\ln X_i(t)$, is expressed as a sum of a log-transformed gene expression baseline, term $\ln X_i^0$, and several gene modules $\lambda_j(t) \times G_{ij}$, representing deviations from the common expression baseline. Each deviation term is a product of a time-dependent module score $\lambda_j(t)$, and the time-independent module-specific contribution score G_{ij} of the gene i . Gene i that displays large positive or negative contribution to a module j (high positive or negative G_{ij} value) represents a gene that is functionally positively or negatively correlated with the module j . In other words, the biological function of the module j could be inferred by functional enrichment analysis of genes with positive and negative G_{ij} values.

To implement surprisal analysis, we first computed the singular value decomposition (SVD) of the matrix $\ln X(t)$. As described previously [51], the SVD factored this matrix in a way that determined the two sets of parameters that are required in the surprisal analysis: the Lagrange multipliers ($\lambda_j(t)$) for all gene modules at a given time point and for all times, as well as the module-specific contribution scores (G_{ij}) for all transcripts i at each gene module j . Further enrichment analysis of the functions associated with each module were performed based on the module-specific contribution scores of the genes associated with that module. The module-1 and module-2 scores of other published datasets on melanoma cell lines [25] or melanoma patients' biospecimens [9,41] were calculated as $\sum_i (\ln X_i) \cdot G_{ij}$ which considered the both the gene expression as well as the respective gene contribution towards each gene module.

Natural log-transformed transcriptome dataset and contributions from each gene module ($\lambda_j(t)G_{ij}$) calculated from surprisal analysis were visualized using self-organized maps (SOMs). Here, the SOMs plotted individual sample as a single 2-dimensional heatmap and, at the same time, displayed high-resolution patterns. Thousands of input genes were assigned to 625 rectangular "tiles" (SOM nodes), each of which represented a mini-cluster of genes, arranged to form a pattern within a 2-dimensional mosaic map on the SOM grid. Each mini-

cluster of genes was mapped onto the same tiles in each map, and the color of each tile represented the relative average expression of the gene mini-cluster within that tile. Most similar clusters were placed adjacent to each other in the mosaic map. Tiles at the same location represented the same group of genes across different conditions. Gene Expression Dynamics Inspector (GEDI) package was utilized to implement the SOM visualization [100].

Dynamic system modeling of two gene modules

In order to more precisely infer the mathematical inter-regulation relationship between two gene modules, we performed dynamic systems modeling with regards to the average gene expression of the top 500 genes that have the highest positive or negative G values (weights). More specifically, for drug treatment condition, we have G1 positive genes and G1 negative genes (genes that are positive or negatively correlated with M_{late}), which are paired with G2 positive and G2 negative genes (genes that are positive or negatively correlated with M_{early}) respectively. Therefore, we have 4 different scenarios for drug treatment condition. Similarly, we also have 4 different scenarios for the drug removal condition.

We started with a system of first-order mass equations that can consider all possible interaction relationships between the two modules. This system initially included terms for baseline, constant basal regulation (B_1 and B_e) on each gene module, first-order autoregulation from itself (M_{e-e} and M_{l-l}), and first-order regulation by the genes from the other module (M_{e-l} and M_{l-e}). We simultaneously fitted all coefficients through unbiased search using Markov Chain Monte Carlo (MCMC) in Python 3.0 and Gaussian distribution of coefficient probability. Initial coefficients were set on random uniform distributions. We also constrained coefficients such that the resulting fit would not lead to artificial oscillations with a frequency beyond the Nyquist frequency of our experimental sampling. Using the fitted parameters, our simulated trajectories of module1 (M_{late}) and module2 (M_{early}) can recapitulate the original experimental data.

Gene set enrichment analysis

Gene Set Enrichment Analysis (GSEA) was conducted based on GSEA v2.2.3 software with 1000 permutations and weighted enrichment statistics. Normalized enrichment score (NES) was assessed across the curated Molecular-Signatures Database (MSigDB) Hallmark, C2 curated gene sets, and MITF signature [34]. To calculate the single-sample gene set enrichment, we used the GSVA program [101] to derive the absolute enrichment scores of previously experimentally validated gene signatures. The normalized log₂ RPKM values were utilized as input for GSVA in the RNA-seq mode. The patient transcriptomic data was

based on the patient transcriptomic data was obtained from [64]. GSEA v3.0 was used with the same parameters described above.

Transcription factor target and motif enrichment analysis

Two different approaches were utilized to identify driving transcription factor in module2 (M_{early}) process. For the first approach, we filtered the TF that are associated with module2 (Pearson correlation with module2 amplitude (λ_2) bigger than 0.8 or less than -0.8) and define them as module2 associated TFs. We then acquired the downstream targets genes for all module2 associated TFs using public database TFtargets (<https://github.com/slowkow/tftargets>). The KDM5B gene targets were manually verified by ChIP-seq data (GSE101045). We then further filter the module2-associated TFs based on the overlap of their downstream target gene with certain module1 (M_{late}). More specifically, for a certain TF in module2 (M_{early}), if its' downstream-targeted genes are over-represented in module1 (M_{late}) process (Hypergeometric test with Bonferroni correction, $\text{FDR} \leq 0.05$), then this TF is selected as a candidate for driving TF in module2. For the second approach, we use HOMER to find enriched motifs in the promoter sequence of module1 associated gene set (Pearson correlation with module2 amplitude (λ_2) bigger than 0.8 or less than -0.8) with following parameters: -len 6,8,10,12 -start -1800 -end 100 -b -mset vertebrates. Then, we infer the potential TFs based on the enriched motif information.

GDSC data analysis

Cell lines from skin cutaneous melanoma (SKCM) samples, containing the *BRAF*^{V600E} genetic mutation from the GDSC project, were selected to analyze the association between the transcriptional states before drug treatment and their drug responses [102]. Gene expression levels of the selected cell lines were projected to two gene modules (M_{early} and M_{late}). BRAF inhibitors Dabrafenib is selected to analyze the association of transcriptome state and drug response. Pearson correlation analysis and linear regression modeling for the two gene modules and the log-transformed IC50 values (Drug concentration that reduces viability by 50%) or AUC (area under the dose-response curve) values were carried out.

CCLE and TCGA analysis

GSVA analysis was utilized to analyze the pathway enrichment scores across RNA-seq data of melanoma patient from TCGA database [103] and from melanoma cell line data from CCLE [104] database. The enrichment score of M_{early} and M_{late} associated genesets across all samples within the (patient or cell line) dataset were utilized as input to calculate pairwise

Pearson correlations, and the average Pearson values of all possible pairwise correlations are used as co-occurrence score of M_{early} and M_{late} genesets within each dataset.

Patient data analysis

Paired patient data before and after the MAPKi treatments were used to evaluate relevant gene expression levels and gene sets enrichment. These data were collected from two published papers. The gene expression levels and associated patient identification numbers in the original papers were provided in Table S6. Patient survival analysis was performed with high expression vs. low expression of selected genes from the TCGA melanoma (SKCM) data set including all stage III and IV patients. Kaplan-Meier method was used to estimate the survival rate, along with a log-rank statistical test comparing the survival distribution. All tests were two-sided, and p values less than 0.05 were considered statistically significant.

Data and Software Availability

The accession number for the gene expression, ATAC-seq and ChIP-seq data reported in this paper is GEO: GSE134459.

Figures.

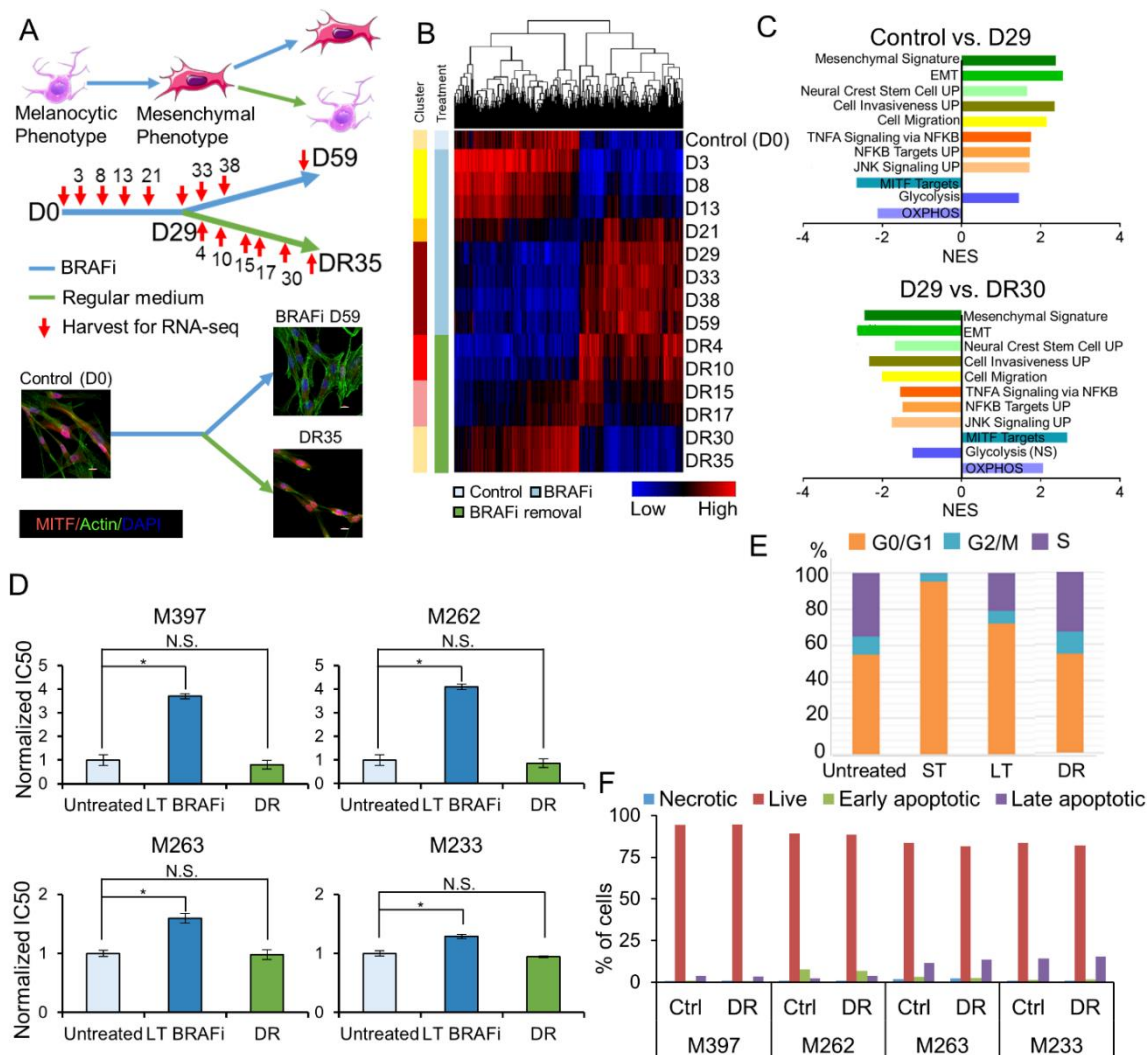


Figure 1. Adaptive drug resistance and reversibility across a panel of melanoma cell lines. (A) An illustration of the melanocyte-to-mesenchymal transition and the experimental timeline. Cells were treated with BRAF inhibitor (BRAFi) vemurafenib for 29 days (D29). BRAFi treatment continued for some cells up to D59, while other cells were followed over a 35 day period of drug removal (DR35). Cells were harvested for RNA-seq at the time points specified. (B) Heatmap of differential expressed genes (DEGs) at a series of time points of drug treatment and drug removal for M397 cells. Sidebars denote consensus clustering results of the variated genes from the samples (6 clusters) and their treatment conditions. DR30 and DR35 fall into the same cluster with the control sample. (C) Enriched molecular signatures associated with the adaptive transition in M397 cells. (D) Increased drug tolerance and reversed drug sensitivity across multiple melanoma cell lines with varying baseline sensitivities to BRAF inhibition evaluated by IC50 values of vemurafenib. LT: long-term;

DR: drug release. Mean \pm SD. (E) Cell cycle distribution across the reversible transition of M397 cells. (F) Cell viability and apoptotic profiles of untreated cells (Ctrl) and reverted cells (upon 30 days drug removal) after 3-day BRAFi exposure. DR: drug removal. See also Figure S1 and Table S1

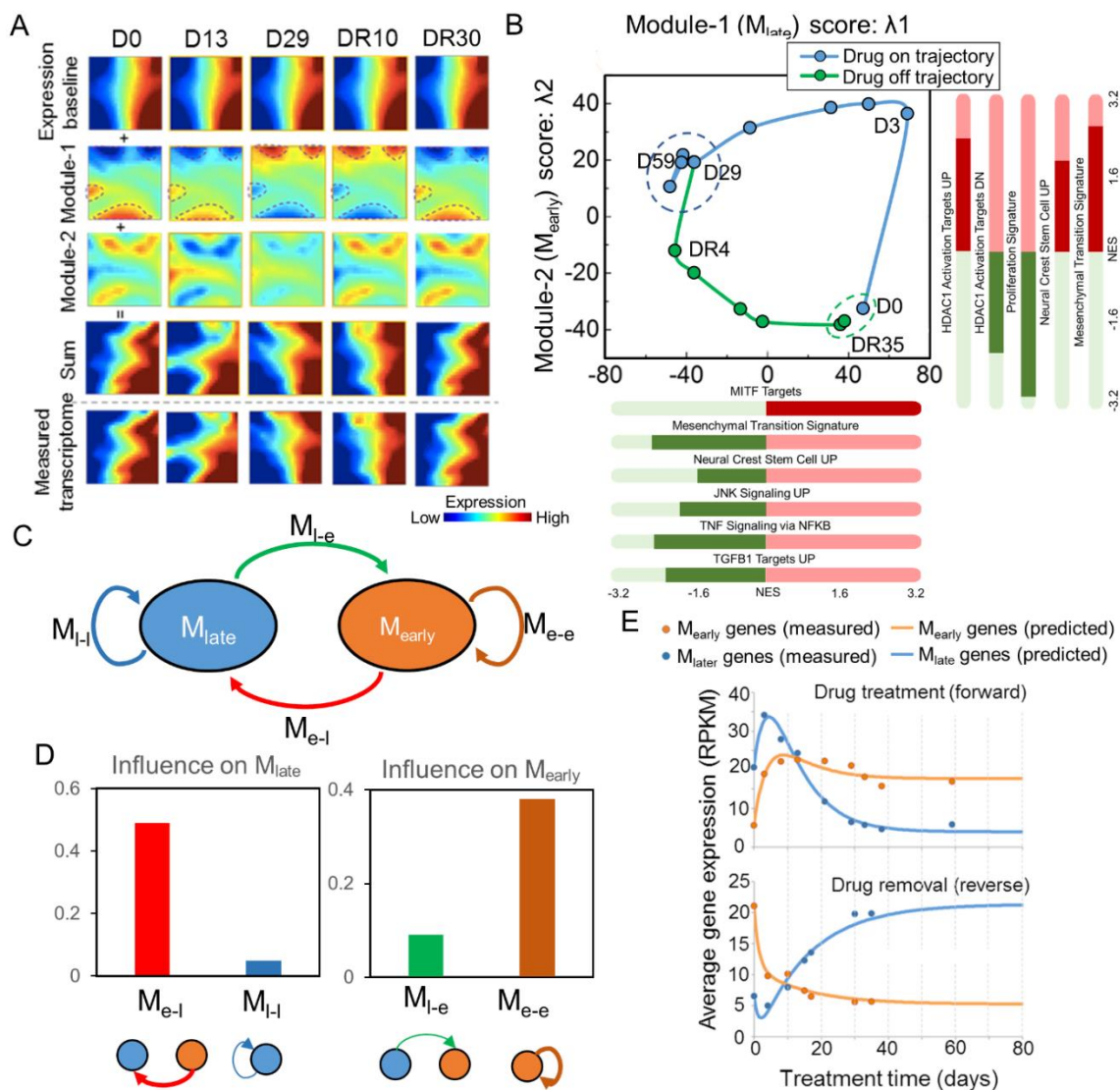


Figure 2. Information theoretic analysis and dynamic systems modeling of the reversible adaptive transition in M397 cells. (A) Application of surprisal analysis to the time-series transcriptome data over the transition. The transcriptome data, decomposed into a time invariant gene expression baseline plus two time-dependent gene modules, are illustrated as self-organizing maps (SOMs). Adding the baseline and first 2 gene modules recapitulates the experimentally measured transcriptome profiles. (B) The cyclic trajectory of the reversible transition plotted in the landscape defined by the first two gene modules. The blue and green dash lines circled the milieu of the mesenchymal-like drug-resistant state and drug naïve state, respectively. Selected enriched molecular processes (nominal $p < 0.05$) associated with each gene module are listed. NES: normalized enrichment score. (C) Schematic illustration of the simplified model for two gene module interactions. (D) The module-module interaction coefficient in the ordinary differential equations (ODEs) determined by fitting the model to the average expression level of the top 500 genes associated with each gene module. (E) Experimentally measured and ODE fitted average

expression levels of genes associated with the two modules in the forward and reverse directions of the cyclic transition. See also Figures S2, S3 and Tables S2, S3, S4.

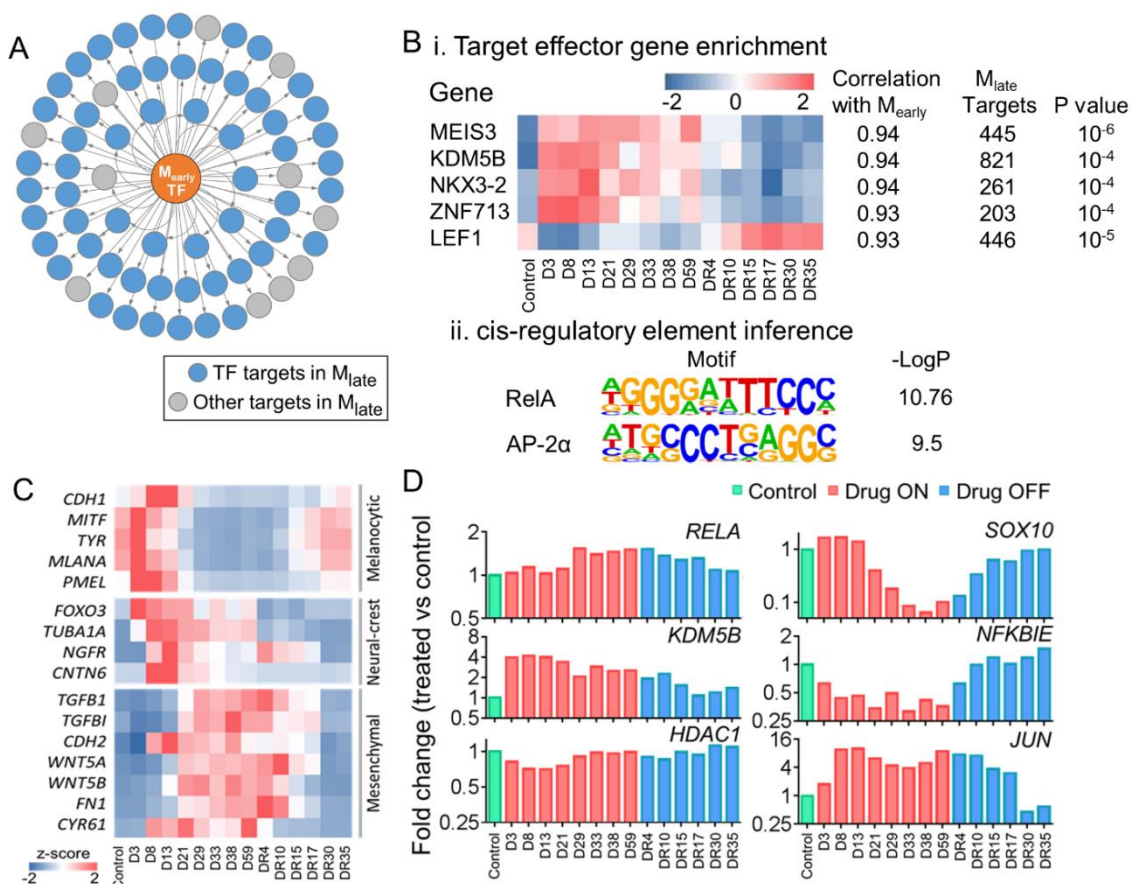


Figure 3. Bioinformatic inference of the critical regulators that drive the initiation of the reversible adaptive transition. (A) A scheme showing the target gene inferences. (B) Bioinformatic inferences based on the dynamic relationships between the two gene modules. (i) The list of enriched transcription factors (TF) and co-factors from target gene enrichment are ranked according to their absolute correlation coefficients with M_{early} scores with relative expression levels (z-score) shown as a heatmap. The target gene number and statistical significance (p values) for each enriched element are listed to the right. (ii) Enriched motifs from the cis-regulatory elements of genes highly correlated ($\rho > 0.8$) with M_{late} . Top two significantly enriched motifs are listed. $-\text{Log}_2$ p values are shown to the right. (C) Relative expression levels of cell-state specific genes over the course of the adaptive cyclic transition (D) Gene expression levels, normalized to D0, of the critical TFs/co-factors involved in the adaptive transition. See also Figure S4.

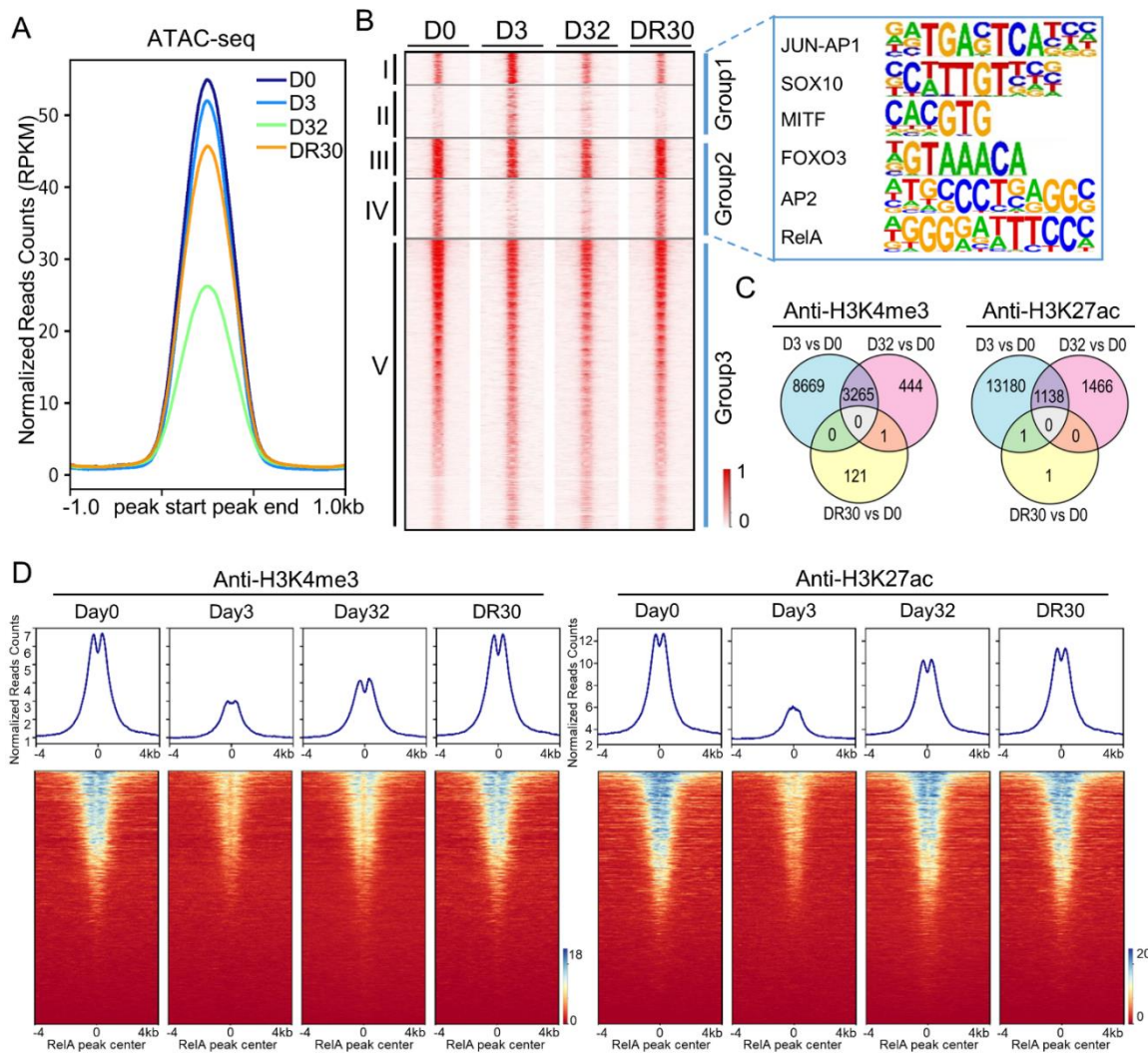


Figure 4. Epigenetic reversibility of the adaptive transition. (A) Chromatin accessibility change assessed by average peak signal of ATAC-seq across the entire genome. The x-axis shows flanking regions of ± 1 kb around the peak center. (B) Heatmap of chromatin accessibility changes assessed by average ATAC-seq peak signal across all peaks, at selected time points over the transition. K-mean clustering of rows identifies five chromatin regions that grouped into D3 enriched (group 1), D0/DR30 enriched (group 2), and independent of drug treatment (group 3). Color corresponds to the normalized ATAC-seq signal. Relevant transcription factor binding motifs are indicated for cluster groups 1 and 2. (C) Venn diagrams showing the numbers and overlaps of differential ChIP-seq peaks for H3K4me3 and H3K27ac. Each circle represents changes in those peaks between two time points, while the intersection of the circles represent changes that are shared between circles. (D) ChIP-seq profile plots show the average H3K4me3 (left) and H3K27ac (right) ChIP-seq signal across peaks identified by RelA ChIP-seq, with heatmap representation of each peak shown

below. The x-axis shows flanking regions of +/- 4kb around the peak center. See also Figure S5 and Table S5.

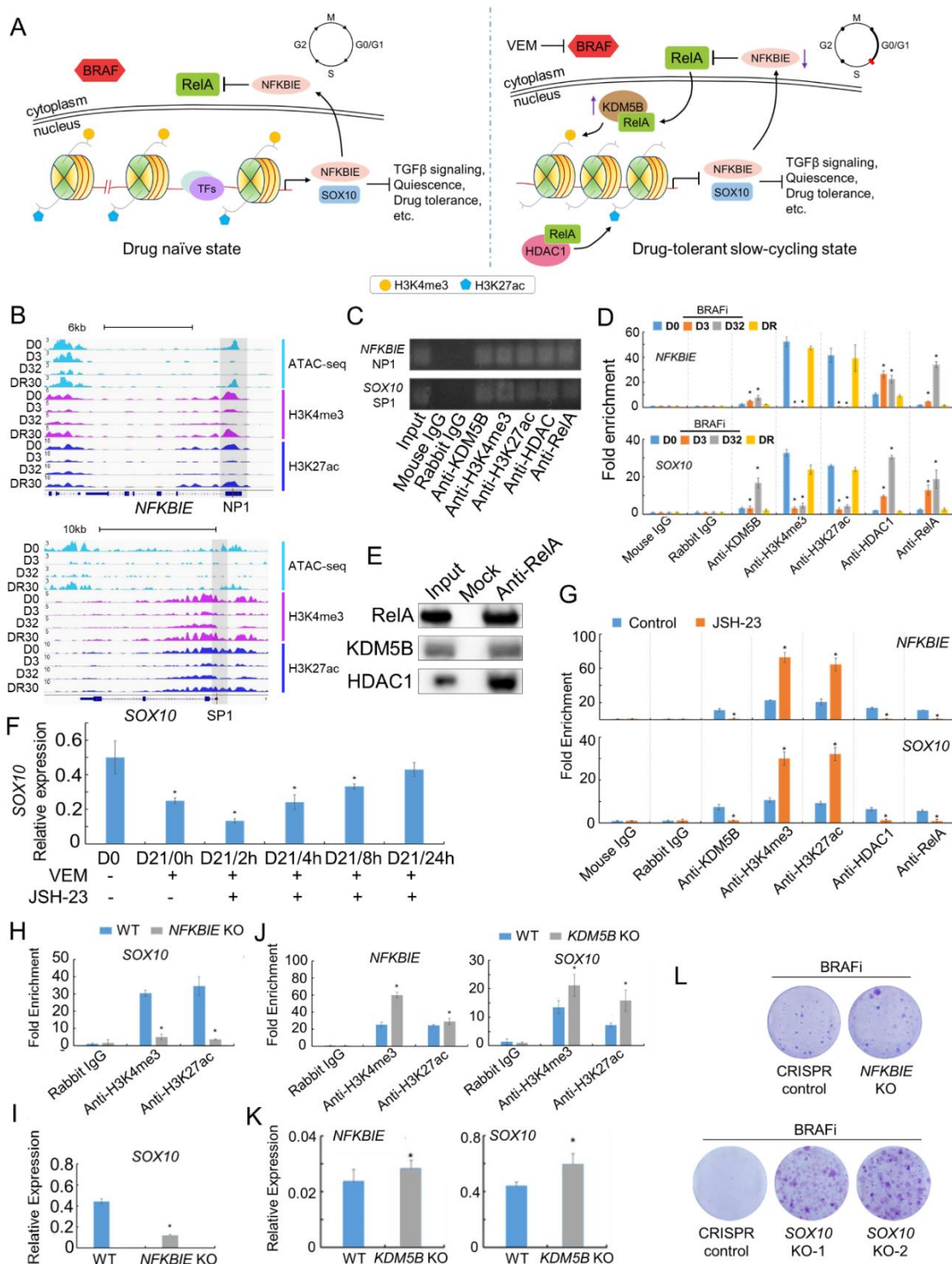


Figure 5. Molecular mechanism that underlies the reversible adaptive transition. (A) Illustration of the mechanism of epigenetic regulation before and after BRAF inhibition. Left

panel: retention of RelA in the cytoplasm and open chromatin at the promoter regions of *SOX10* and *NFKBIE*. Right panel: BRAFi induces translocation of RelA into the nucleus, allowing RelA to recruit histone modifiers KDM5B and HDAC1 to the target genes to reduce chromatin accessibility and epigenetically repress of *SOX10* and *NFKBIE* expression. Functional consequences, such as increased TGF β signaling and adaptive drug resistance, result in turn. The illustrations of the cell cycle reflect the measured cell cycle arrest observed upon short-term BRAF inhibition. (B) ATAC-seq and ChIP-seq profiles at the promoter regions of *NFKBIE* and *SOX10*, at selected time points across the reversible transition. (C) ChIP-PCR data illustrates the binding and co-localization of RelA, KDM5B, HDAC1, H3K4me3, and H3K27ac to promoter regions of *SOX10* and *NFKBIE* (labeled NP1 and SP1, respectively). (D) ChIP-qPCR assessment of the binding profiles of RelA, KDM5B, HDAC1, H3K4me3, and H3K27ac on the promoter regions of *NFKBIE* and *SOX10* at a series of time points across the reversible transition. (E) Co-immunoprecipitation of RelA with KDM5B and HDAC1, confirming the binding between RelA and the two histone modifiers (*P<0.05 compared to respective D0). (F) The recovery of *SOX10* gene expression levels of M397 cells pretreated with BRAFi for 21 days (D21), and then co-treated for 0-24 hours with BRAFi and JSH-23 (*P<0.05 compared to D0) (G) ChIP-qPCR assessment of the binding profiles of RelA, KDM5B, HDAC1, H3K4me3, and H3K27ac on the promoter regions of *NFKBIE* and *SOX10* for control and JSH-23 24h-treated cells (*P<0.05 compared to respective control). (H) ChIP-qPCR of the binding profiles of H3K4me3 and H3K27ac on the promoter region of *SOX10* from *NFKBIE* KO M397 cells (*P<0.05 compared to respective WT). (I) *SOX10* expression levels after *NFKBIE* KO compared to wild type (WT) (*P<0.05 compared to WT) (J) ChIP-qPCR of the binding profiles of H3K4me3 and H3K27ac on the promoter regions of *NFKBIE* and *SOX10* from *KDM5B* KO M397 cells (*P<0.05 compared to WT) (K) Expression levels of *SOX10* and *NFKBIE* after *KDM5B* KO compared to WT (*P<0.05 compared to WT). (L) Clonogenic assays of *NFKBIE* KO or *SOX10* KO cells related to respective controls.

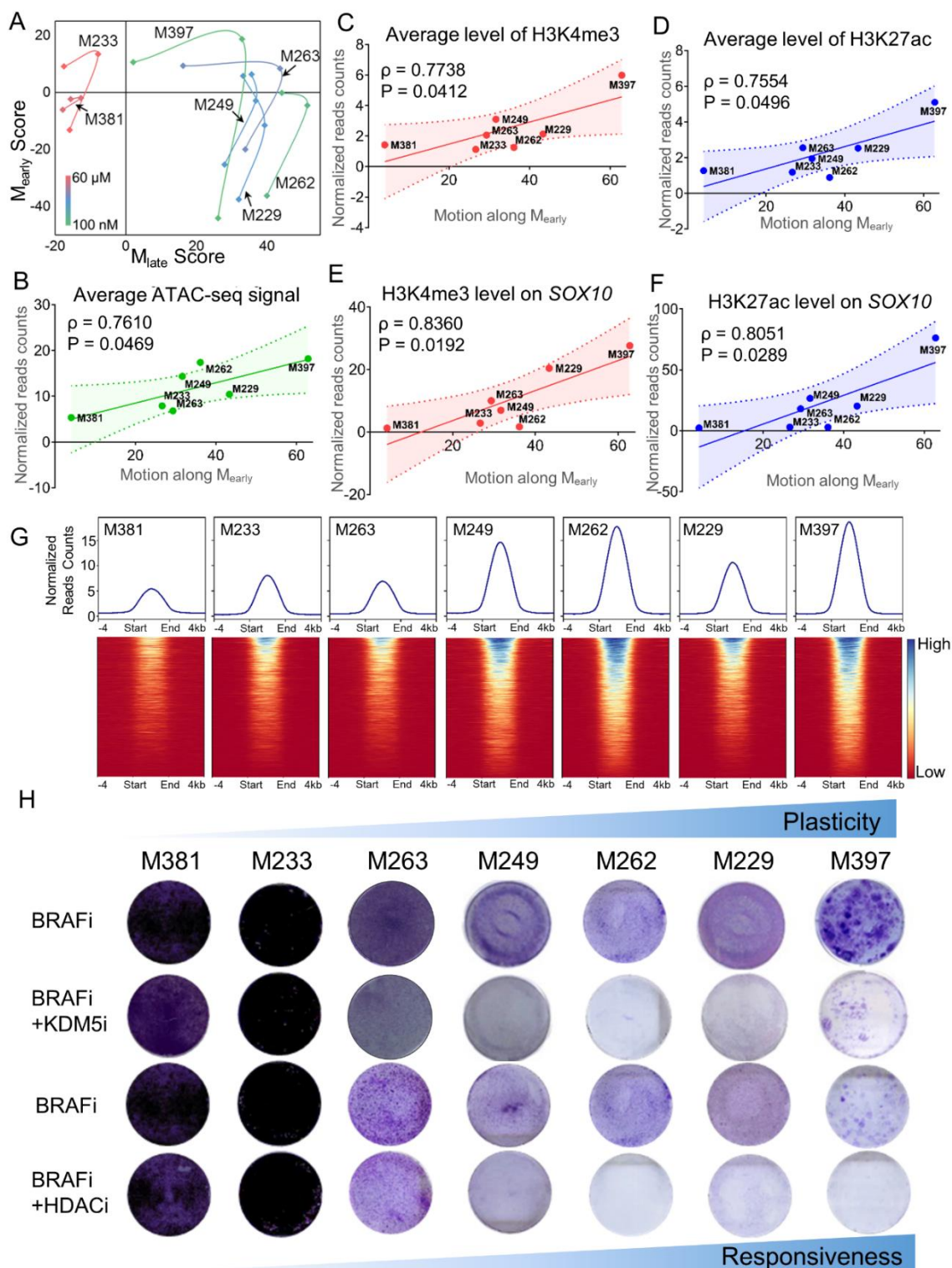


Figure 6. The generality and molecular underpinning of the phenotypic plasticity of patient-derived melanoma cell lines in response to BRAF inhibition. (A) Quantification

of phenotypic plasticity upon BRAF inhibition across a panel of melanoma cell lines. The transcriptome data are projected to the 2D plane defined by the two gene modules (M_{early} and M_{late}) and connected by smooth lines. The data points denote 0-day (D0), D3, and D21 BRAFi treatment in counterclockwise order, respectively. The color of the line encodes the baseline IC50 value of the cell line. (B-F) The correlation between short-term plasticity (motion along M_{early}) and the (B) average ATAC-seq signal, (C) average H3K4me3 (D) and H3K27ac ChIP-seq signal across all peaks, as well as (E) average H3K4me3 and (F) H3K27ac ChIP-seq signal on the transcription start site (TSS) region of *SOX10* across all cell lines with Pearson correlation coefficients and p-values as shown. The shaded regions of panels B-F denote 95% CIs of each linear fitting. (G) The chromatin accessibility of a panel of melanoma cell lines quantified by the average ATAC-seq signal across all peaks with heatmap view of each peak shown below. The x-axis includes flanking regions of +/- 4kb around the peak center. (H) Clonogenic assays for BRAFi monotherapy and combination therapies simultaneously targeting the driver oncogene BRAF and histone modifiers KDM5B and HDAC1. The cell lines are ordered from left to right with increased plasticity. See also Figure S6.

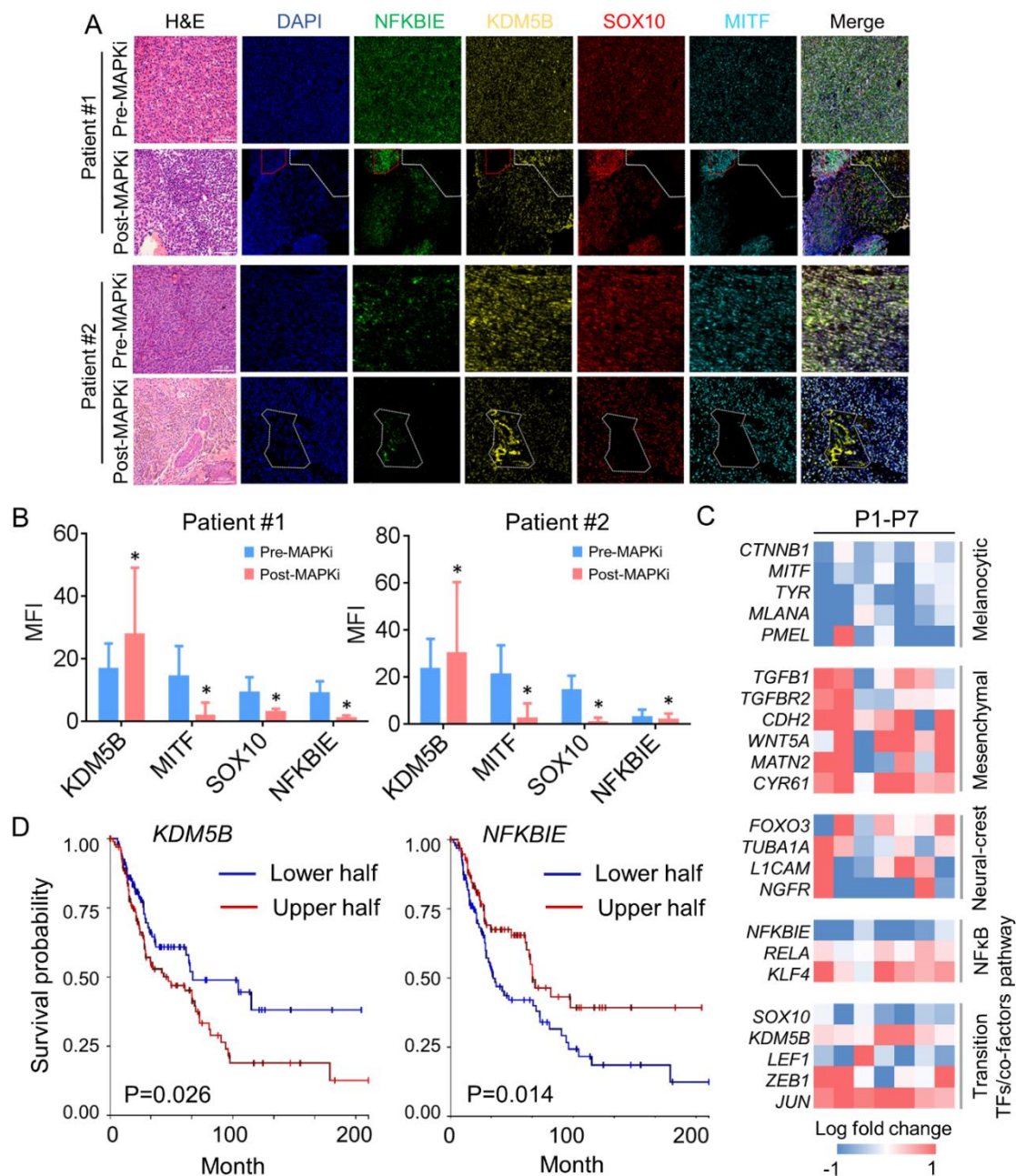


Figure 7. The clinical relevance of the drug-induced chromatin remodeling mechanism.

(A) Immunohistochemical (IHC) staining of melanoma tissue biopsies from two patients bearing *BRAF*-mutant melanoma before and after MAPKi treatment. Hematoxylin and eosin (H&E) staining shown in left column followed by a staining panel from pre-treatment or post-treatment biopsies. Post-treatment tissue was collected at the onset of tumor recurrence. The stains are DAPI nuclear stain (blue), NFKBIE (green), KDM5B (yellow), SOX10 (red), MITF (cyan), and merge. The region highlighted by white dashed lines in the post-MAPKi

tissues display reduced MITF, NFKBIE, and SOX10 expression and elevated KDM5B expression, consistent with the adaptive resistance mechanism. The region highlighted by red dashed lines retained the MITF, NFKBIE, and SOX10 expressions but with loss of KDM5B after treatment. (B) Digitized mean fluorescence intensity (MFI) of the areas highlighted by white dashed lines for the selected markers in two patients. Data are represented as mean \pm SD (*P<0.05 compared to respective pre-MAPKi). (C) Log-fold change in the expression of relevant genes (post-treatment vs baseline), collated from published datasets of *BRAF*-mutant melanoma patients treated with MAPK inhibitors (STAR Method). (D) Kaplan-Meier plots assembled using TCGA data sets of tumors from patients with stages III and IV melanomas with log-rank P values shown. See also Figure S7 and Table S6.

Supplementary Information

Supplementary figures

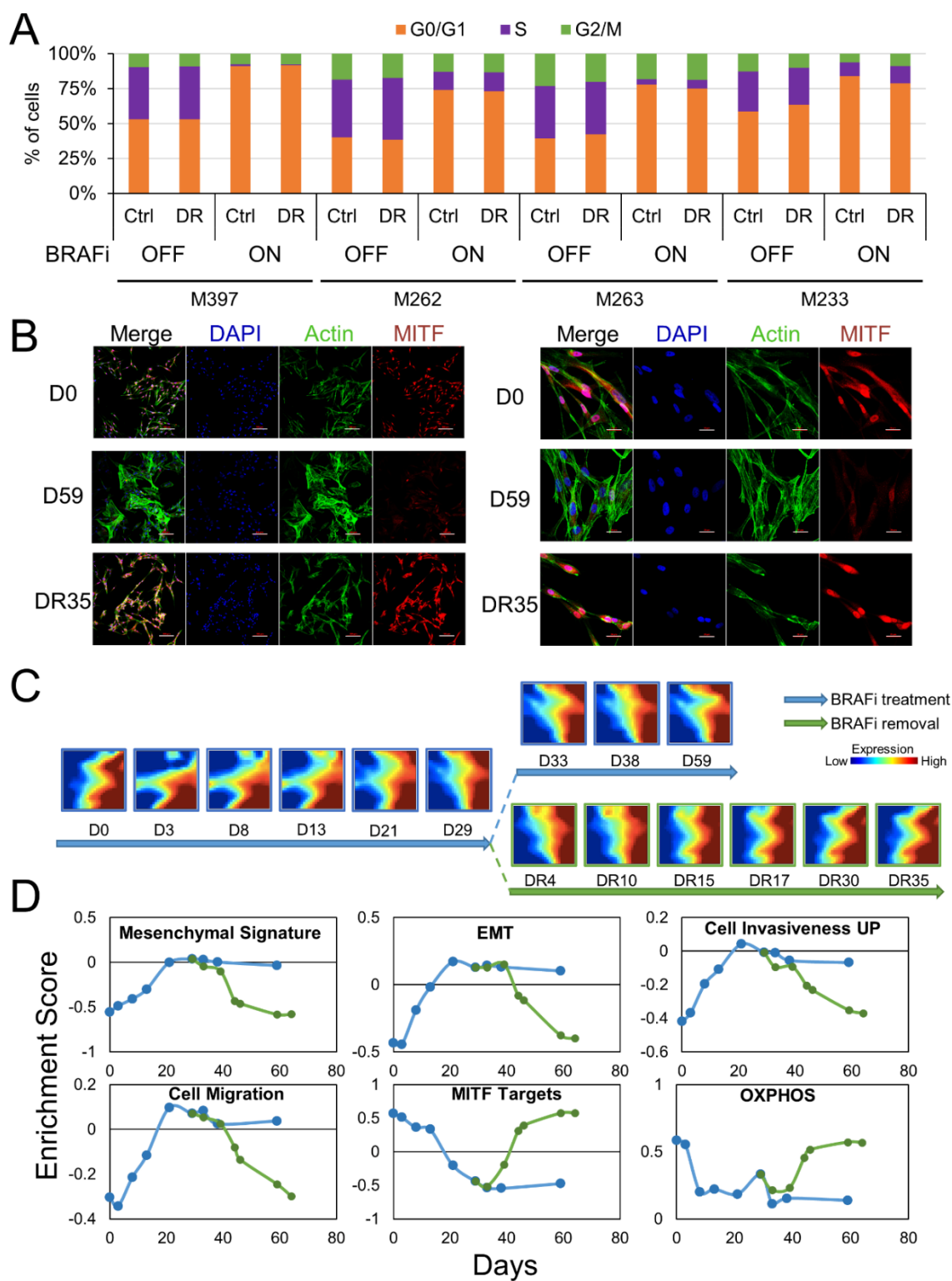


Figure S1. Reversible adaptive resistance across melanoma cell lines. Related to Figure 1.

- A. Stacked bar plot shows the fraction of cells viable in G0/G1, S, and G2/M phases (y-axis) for different melanoma cell lines. Each cell line has two different assay conditions: observed either before treatment, or after pretreated with BRAFi for 30 days and drug removal in normal medium for another 30 days. Cells in both conditions underwent cell cycle analysis at both drug-naïve condition and retreatment with BRAFi for another 3 days. Cells that have gone through drug treatment and drug removal have the same cell cycle distribution as cells that never receive drug treatment.
- B. Immunostaining of M397 cells at different stages of reversible adaptive drug resistance. M397 cells before treatment (D0, first row), after treatment with BRAFi for 59 days (D59, second row), and pretreated with BRAFi for 29 days and then cultured with normal medium for another 35 days (DR35, third row) were used for immunostaining of MITF (red), actin (green), and DAPI (blue). The cell morphology at D0 is very similar to that at DR35. Cell morphology at D59 is very different from the ones at the other two conditions. Left panel scale bar 100um, right panel scale bar 20um.
- C. Two-dimensional self-organizing maps (SOMs) of overall transcriptome profiles of cells collected at different stages across the reversible adaptive drug response.
- D. Enrichment scores of representative gene sets across different stages of the reversible adaptive response. Enrichment scores at different time points are shown as dots connected with solid lines. The scores stabilize after prolonged drug treatment (after 21 days of BRAFi, blue line) and return to the enrichment score of day 0 after long-term drug removal (green line).

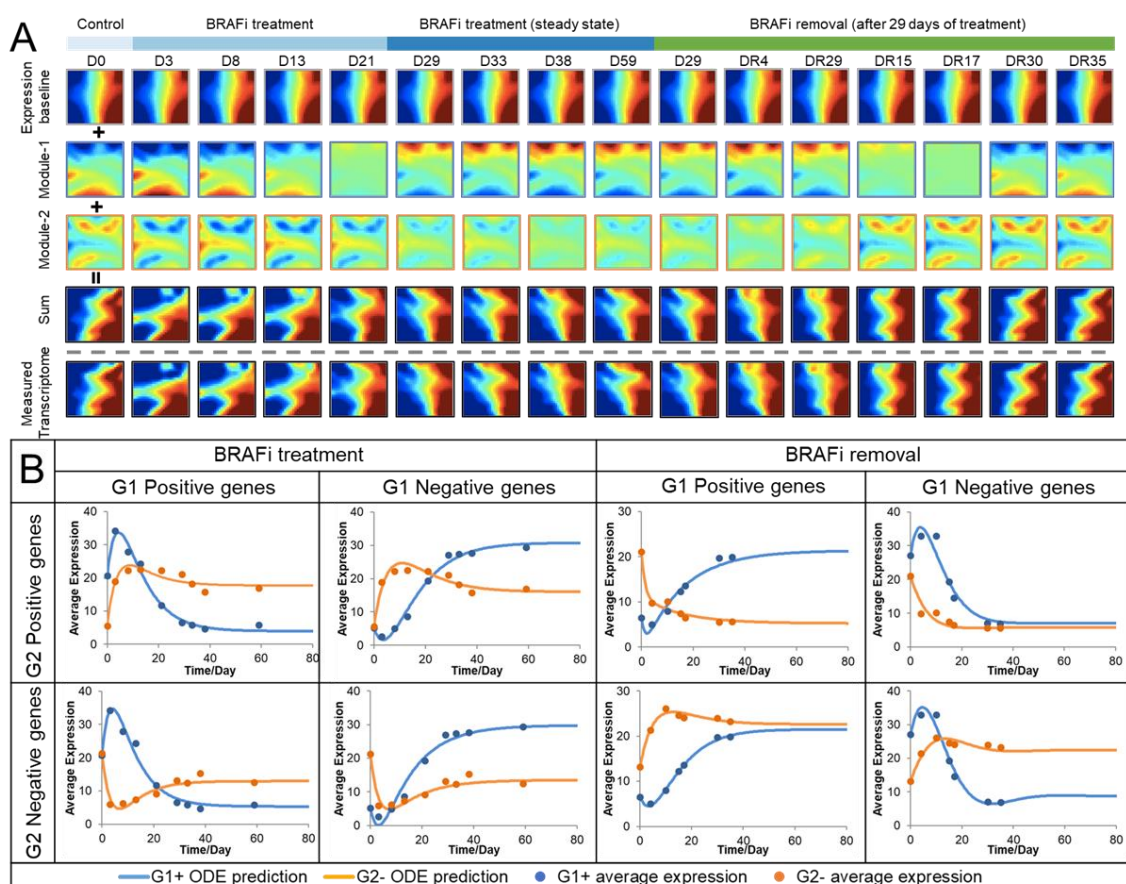


Figure S2. Surprisal analysis of the reversible adaptive transition in M397. Related to Figure 2.

(A) Application of surprisal analysis to the kinetic transcriptome profile with respect to the reversible adaptive transition. The transcriptome data, decomposed into a time-invariant gene expression baseline plus two time-dependent gene modules, are illustrated as self-organizing maps (SOMs). Adding the expressions of the baseline gene module and time-dependent module-1 and module-2 recapitulates the experimentally measured transcriptome profiles visualized by the fact that the patterns of the SOMs in the last row (experimentally measured transcriptome profiles) are almost identical to those at second last row (predicted transcriptome profiles from surprisal analysis by adding first three rows).

(B) ODE predictions (smooth line) are consistent with the average expression levels of genes associated with module-1 and module-2 from experimental measurements (dots) in the forward and reverse directions of the adaptive transition. More specifically, for drug treatment conditions, we have G1 positive genes (genes that positively contribute to module-1 or M_{late}) and G1 negative genes (genes that negatively contribute to module-1 or M_{late}), which are paired with G2 positive and G2 negative genes (genes that positively and negatively contribute to module-2 or M_{early}) respectively. Therefore, we have four different scenarios for drug treatment and four different scenarios for drug removal.

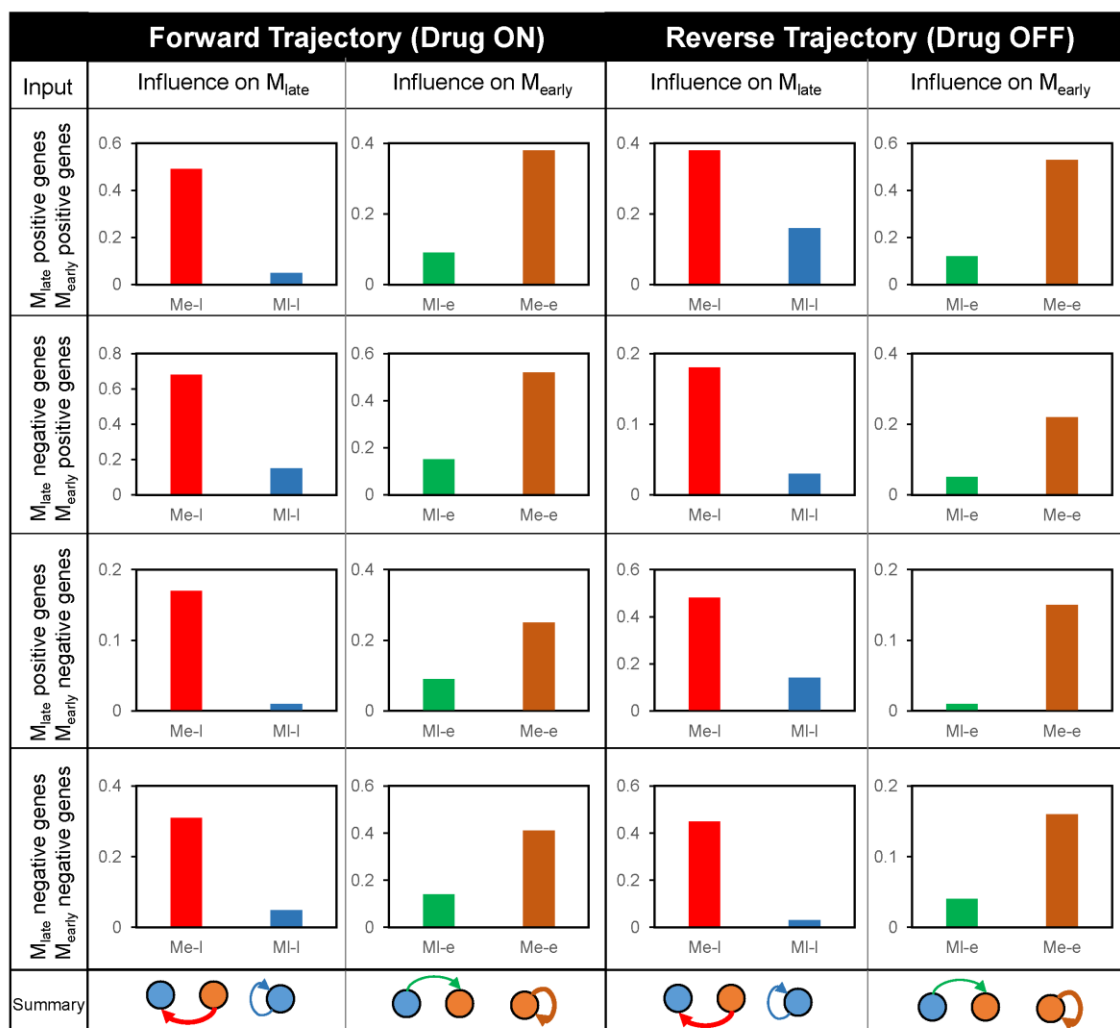


Figure S3. Best fitted parameters from dynamic system modeling of the reversible adaptive transition in M397. Related to Figure 2. The module-module interaction coefficients in the ordinary differential equations (ODEs) determined from fitting the ODE model to the average expression level of the top 500 genes associated with each gene module. More specifically, for drug treatment condition, we have G1 positive genes (genes that positively contribute to module-1 or M_{late}) and G1 negative genes (genes that negatively contribute to module-1 or M_{late}), which are paired with G2 positive and G2 negative genes (genes that positively and negatively contribute to module-2 or M_{early}), respectively. Therefore, we have four different scenarios for drug treatment. Similarly, we also have another four different scenarios for the drug removal.

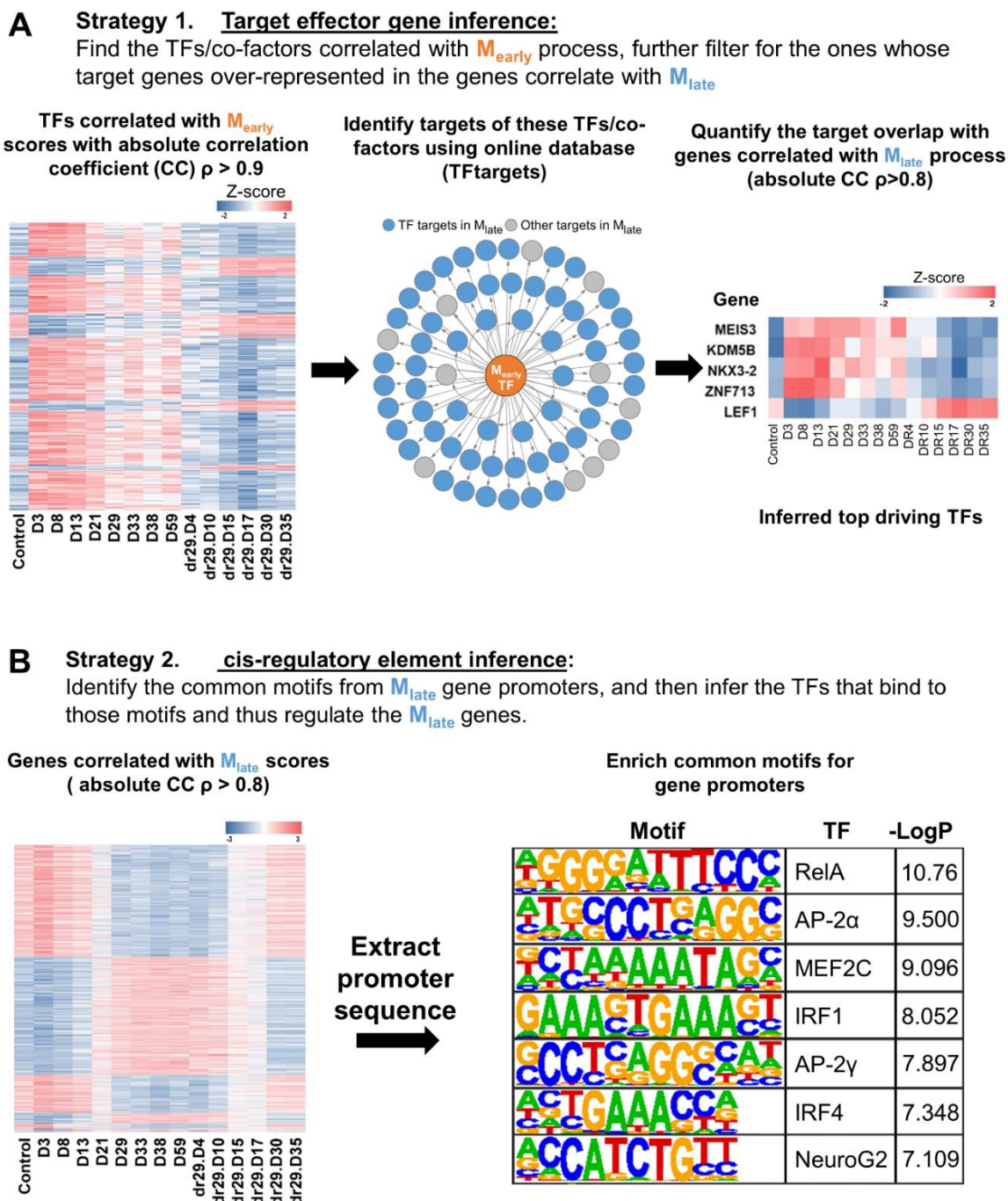


Figure S4. Strategies for inference of the critical regulators that drive the initiation of the reversible adaptive transition. Related to Figure 3.

(A) Target gene inference based on the dynamic relationships between the two gene modules. The TFs/co-factors whose expression kinetics are correlated with the module scores of M_{early} (left panel) are mapped to their target genes, followed by

assessing the target gene enrichments in the genes correlated with M_{late} scores (middle panel). The inferred transition-driving TFs/co-factors whose target genes are significantly overrepresented in M_{late} are ranked by their absolute correlation coefficients with M_{early} scores. The top-5 elements were listed.

- (B) Common motif inference to extract enriched motifs from genes highly correlated with M_{late} (left panel) and to identify the TFs that bind to these motifs and regulate cell state regression (right panel). Seven significantly enriched motifs with $p < 0.01$ (i.e. $-\log_2 P > 6.64$) were identified and listed.

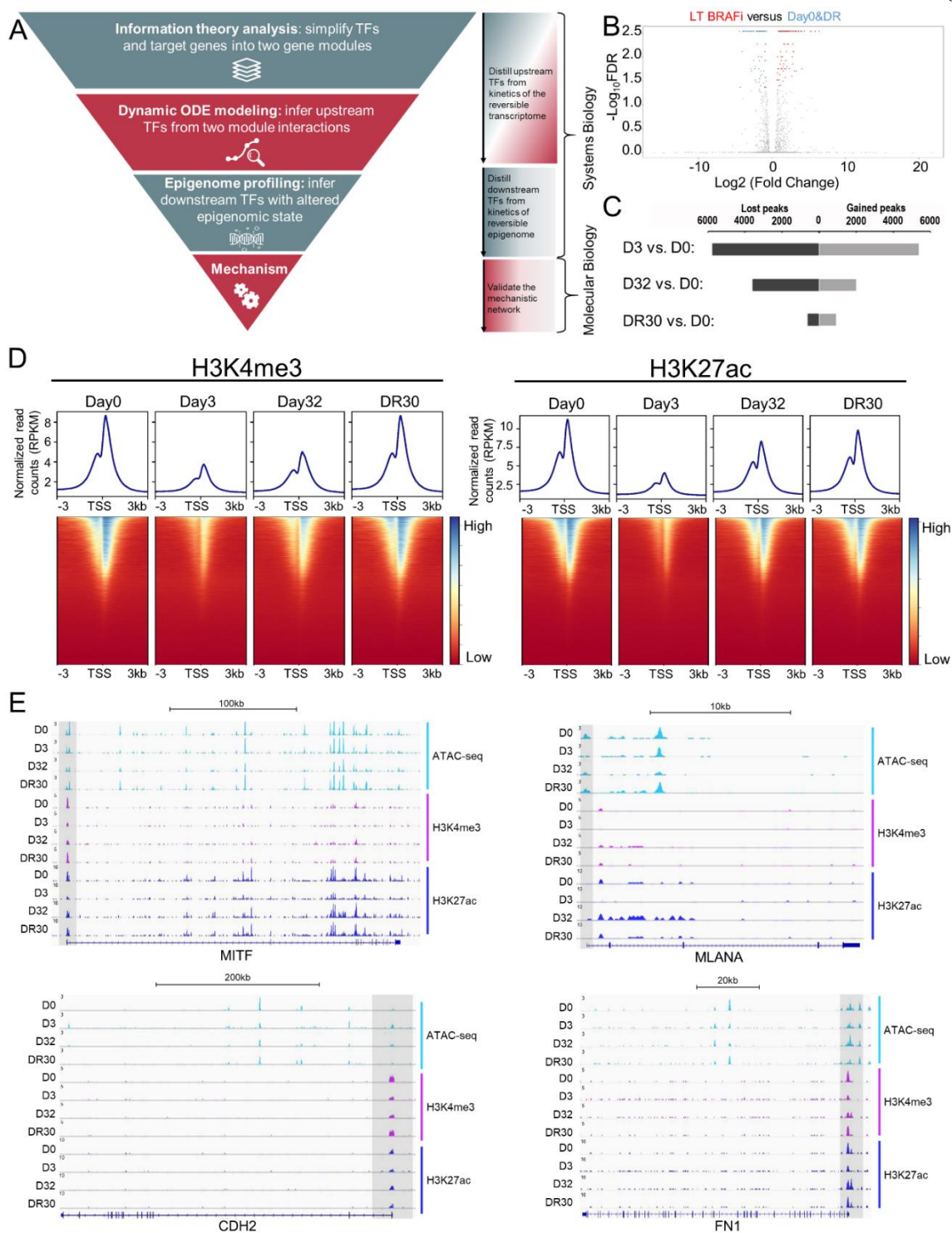


Figure S5. Epigenetic reversibility of the adaptive transition. Related to Figure 4.

- (A) Graphical illustration of our methodology that integrates systems biology, bioinformatics and molecular biology approaches for investigating the molecular mechanism of the adaptive resistance.
- (B) A volcano plot showing the transcription factors/co-factors that display significant alterations between the drug-resistant state and the drug-sensitive state.
- (C) Differential peaks of the ATAC-seq profiles between two different time points. D0, D3, D32, and DR30 denote day-0, day-3, day-32, and drug removal day-30 across the adaptive transition, respectively.
- (D) Average H3K4me3 (left) and H3K27ac (right) ChIP-seq signal at the transcription start sites (TSS) across all genes with heatmap representation of each peak shown below. The x-axis shows flanking regions of +/- 3kb around the TSS.
- (E) ATAC-seq and ChIP-seq profiles at the promoter regions of some representative cell state marker genes, at selected time points across the reversible transition

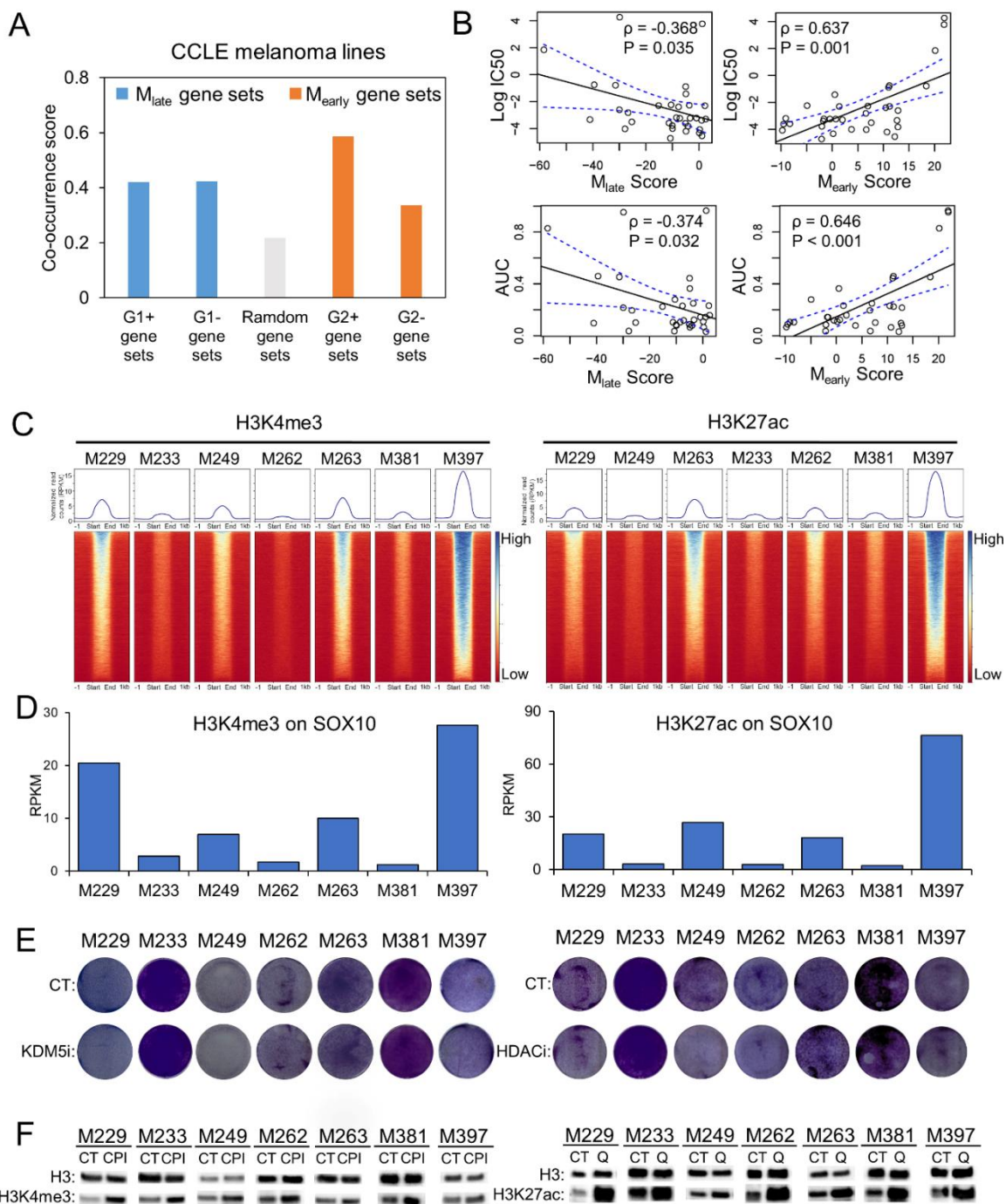


Figure S6. The generality and molecular underpinning of the phenotypic plasticity of patient-derived melanoma cell lines in response to BRAF inhibition. Related to Figure 6.

- (A) Co-occurrence score of M_{early} -related gene sets (G2+ and G2- gene sets) and M_{late} -related gene sets (G1+ and G1- gene sets) in comparison with randomly selected gene sets calculated from the transcriptome data across all melanoma cells from the CCLE database.
- (B) Correlations between M_{early} or M_{late} module scores and BRAFi resistance levels across $BRAF^{V600E}$ -mutant melanoma cell lines in the GDSC database. The BRAFi resistance levels are quantified by natural log-transformed IC50 (μM) values and AUC.
- (C) Average H3K4me3 (left) and H3K27ac (right) ChIP-seq signal across promoter regions of all genes for a panel of melanoma cell lines, with heatmap view around TSS shown below. The x-axis shows flanking regions of +/- 1kb around each peak center. The y-axis of the top panel represents the read counts normalized by RPKM.
- (D) Average H3K4me3 (left) and H3K27ac (right) ChIP-seq signal at the transcription start site (TSS) region of *SOX10*.
- (E) Short-term clonogenic assay of KDM5 inhibitor (left) and HDAC inhibitor (right) across a panel of melanoma cell lines showing no significant toxicity to the cells at the dose used.
- (F) Left, western blot of lysates from melanoma either untreated control (CT) or treated with KDM5B inhibitor (CPI) and HDAC inhibitor (Q). H3 is used as loading control.

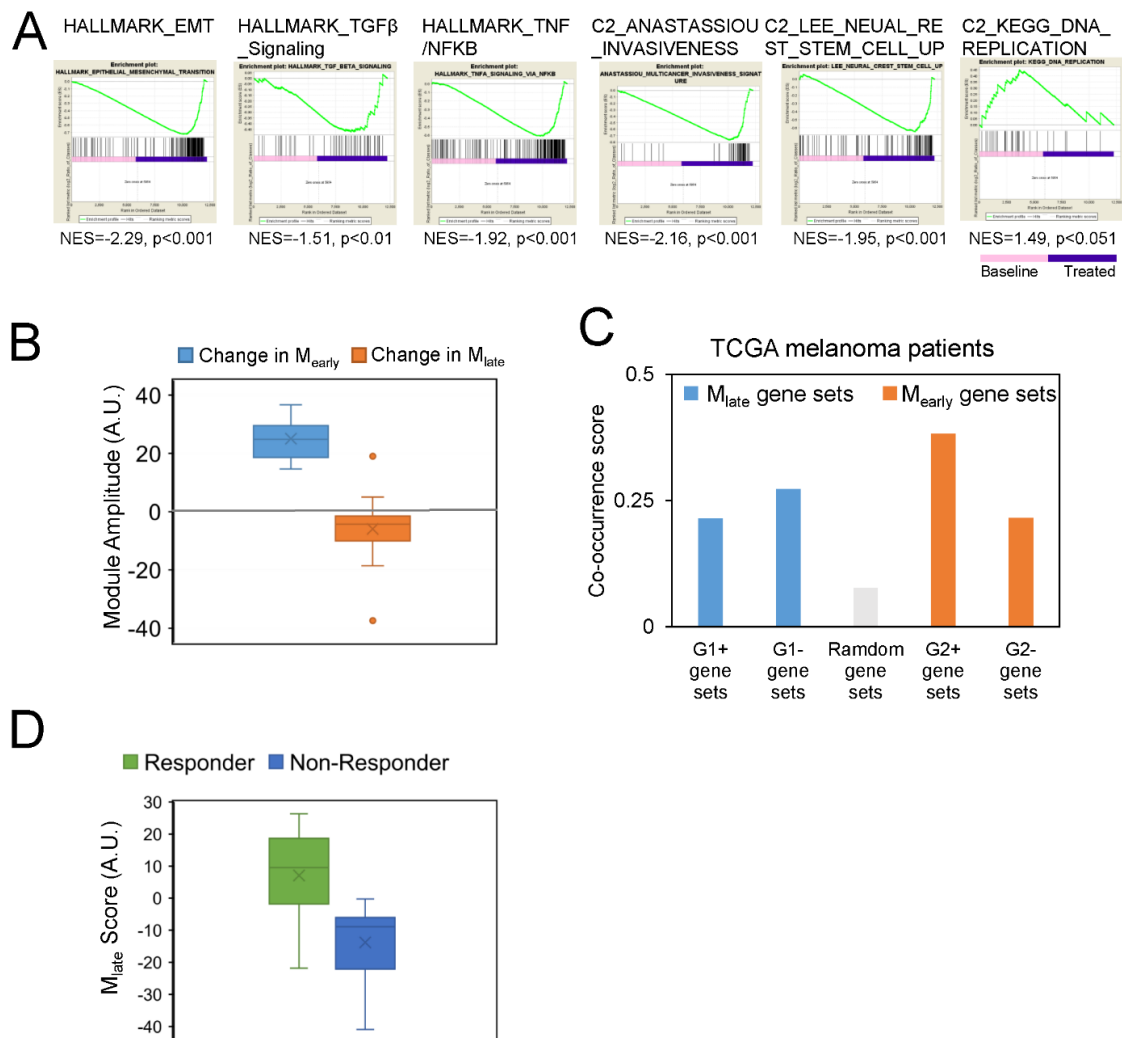


Figure S7. Generality and clinical relevance of adaptive epigenetic mechanism in melanoma patients. Related to Figure 7.

- (A) Gene set enrichment analysis (GSEA) on published transcriptome data from a melanoma patient (P2 in Table S6) before and after MAPKi treatment for selected gene sets relevant to the reversible transition observed in our system. NES, normalized enrichment score.
- (B) The change in M_{early} and M_{late} module scores calculated by published transcriptome data from melanoma patients before and after MAPKi treatment.
- (C) Co-occurrence scores of M_{early} -related gene sets (G2+ and G2- gene sets) and M_{late} -related gene sets (G1+ and G1- gene sets) relative to randomly selected gene sets calculated from transcriptome data across all melanoma patients from the TCGA database.

(D) Average M_{late} module scores of responders and non-responders to PD-1 checkpoint blockade calculated by published transcriptome data of melanoma patients under PD-1 checkpoint inhibitor treatment (see STAR Methods)

Supplemental Tables

Table S1: RNA-seq data (in RPKM) for time-course experiments of M397 and relevant gene module scores from information theory analysis. Data are provided as Excel spreadsheets. (<https://www.biorxiv.org/content/10.1101/724740v1>)

Table S2. GSEA analysis for selected gene sets between different time points. Statistically significant positive enrichments are highlighted in yellow and negative enrichments in blue.

Gene Set	MsigDB Category	Gene Number	D3 vs. D0			D13 vs. D0			D21 vs. D0			D29 vs. D0			D59 vs. D0			D21 vs. dr29.D15			dr29.D15 vs. dr29.D30			dr29.D30 vs. D29		
			NES	p-value	q-value	NES	p-value	q-value	NES	p-value	q-value	NES	p-value	q-value	NES	p-value	q-value	NES	p-value	q-value	NES	p-value	q-value	NES	p-value	q-value
Oxidative Phosphorylation	HALLMARK	198	-0.84	0.854	0.856	-2.22	0.000	0	-2.31	0.000	0.000	-2.12	0.000	0.000	-2.25	0.000	0.000	-1.77	0.000	0.005	-2.30	0.000	0.000	2.06	0.000	0.000
Glycolysis	HALLMARK	198	N/A			N/A			1.28	0.034	0.187	1.45	0.007	0.083	1.16	0.123	0.316	N/A			1.4	0.009	0.104	-1.24	0.065	0.261
MITF targets*	N/A	102	1.28	0.058	0.500	-1.79	0.000	0.002	-2.49	0.000	0.000	-2.65	0.000	0.000	-2.65	0.000	0.000	-1.79	0.000	0.003	-2.66	0.000	0.000	2.87	0.000	0.000
HAN_JNK_Signaling_UP	C2:CGP	35	N/A			1.82	0.000	0.002	1.96	0.000	0.000	1.72	0.000	0.006	1.84	0.000	0.001	1.40	0.043	0.189	1.72	0.000	0.003	-1.76	0.004	0.004
PHONG_TNF_Response_via_P38_Complete	C2:CGP	222	N/A			1.40	0.003	0.115	1.47	0.000	0.060	1.15	0.123	0.353	1.36	0.012	0.135	1.08	0.212	0.525	1.56	0.000	0.025	-1.18	0.090	0.327
HINATA_NFKB_Targets_Keratinocyte_Up	C2:CGP	90	N/A			1.57	0.000	0.039	1.71	0.000	0.006	1.73	0.000	0.005	1.72	0.000	0.006	N/A			2.01	0.000	0.000	-1.49	0.007	0.069
TNFA_Signaling_via_NFKB	HALLMARK	198	N/A			1.74	0.000	0.006	1.92	0.000	0.000	1.78	0.000	0.003	1.95	0.000	0.000	N/A			1.74	0.000	0.006	-1.55	0.000	0.043
WU_Cell_Migration	C2:CGP	181	N/A			1.87	0.000	0.015	2.10	0.000	0.000	2.15	0.000	0.000	2.14	0.000	0.000	N/A			2.19	0.000	0.000	-2.01	0.000	0.000
SCHUETZ_Breast_Cancer_Ductal_Invasive_Up	C2:CGP	338	N/A			2.07	0.000	0	2.38	0.000	0.000	2.38	0.000	0.000	2.26	0.000	0.000	1.72	0.000	0.021	2.10	0.000	0.000	-2.33	0.000	0.000
LEE_Neural_Crest_Stem_Cell_Up	C2:CGP	142	1.13	0.151	0.627	1.98	0.000	0	1.89	0.000	0.000	1.68	0.000	0.013	1.46	0.007	0.076	1.68	0.000	0.032	1.57	0.000	0.024	-1.58	0.000	0.012
Epithelial_Mesenchymal_Transition	HALLMARK	196	N/A			2.42	0.000	0	2.54	0.000	0.000	2.58	0.000	0.000	2.45	0.000	0.000	2.02	0.000	0.000	2.25	0.000	0.000	-2.83	0.000	0.000

Table S3. GSEA analysis of the genes associated with M_{early} (G2) and M_{late} (G1) gene modules for selected gene sets. Statistically significant positive enrichments are highlighted in yellow and negative enrichments in blue.

Gene Set	MsigDB Category	Gene Number	G1			G2		
			NES	p-value	q-value	NES	p-value	q-value
Oxidative Phosphorylation	HALLMARK	198	2.26	0.000	0.000	-1.51	0.005	0.082
Glycolysis	HALLMARK	198	-1.59	0.000	0.031	1.16	0.123	0.316
MITF targets*	N/A	102	3.19	0.000	0.000	-1.99	0.000	0.002
HAN_JNK_Signaling_UP	C2:CGP	35	-1.45	0.002	0.085	1.42	0.047	0.183
PHONG_TNF_Response_via_P38_Complete	C2:CGP	222	-1.18	0.090	0.327	0.87	0.783	0.869
HINATA_NFKB_Targets_Keratinocyte_Up	C2:CGP	90	-2.12	0.000	0.000	N/A		
TNFA_Signaling_via_NFKB	HALLMARK	198	-2.31	0.000	0.000	N/A		
WU_Cell_Migration	C2:CGP	181	-2.33	0.000	0.000	N/A		
SCHUETZ_Breast_Cancer_Ductal_Invasive_Up	C2:CGP	338	-2.36	0.000	0.000	1.87	0.000	0.007
LEE_Neural_Crest_Stem_Cell_Up	C2:CGP	142	-1.42	0.023	0.104	1.85	0.000	0.008
Epithelial_Mesenchymal_Transition	HALLMARK	196	-2.56	0.000	0.000	2.45	0.000	0.000

Table S4. Fitting parameters used in the ODE modeling.

	Input genes for ODE parameter fitting		Basal term		Influence on M_{late}		Influence on M_{early}	
	M_{early} input	M_{late} input	B_l	B_e	M_{e-l}	M_{l-l}	M_{l-e}	M_{e-e}
Drug ON	$M_{early_positive_genes}$	$M_{late_positive_genes}$	8.39	6.33	0.49	-0.05	0.09	0.38
	$M_{early_negative_genes}$	$M_{late_positive_genes}$	-9.6	7.59	-0.68	-0.15	-0.15	0.52
	$M_{early_positive_genes}$	$M_{late_negative_genes}$	-3.12	6.83	-0.17	-0.01	-0.09	0.25
	$M_{early_negative_genes}$	$M_{late_negative_genes}$	2.75	1.49	0.31	-0.048	0.14	0.41
Drug OFF	$M_{early_positive_genes}$	$M_{late_positive_genes}$	5.47	5.35	0.38	0.16	-0.12	0.53
	$M_{early_negative_genes}$	$M_{late_positive_genes}$	-3.46	6.2	-0.18	0.03	-0.05	0.22
	$M_{early_positive_genes}$	$M_{late_negative_genes}$	-1.83	0.93	-0.48	0.14	-0.01	0.15
	$M_{early_negative_genes}$	$M_{late_negative_genes}$	10.23	3.23	0.45	0.03	0.04	0.16

Table S5. The statistical significance of the alterations of chromatin accessibility and histone marks across the adaptive transition. The epigenetic alterations were evaluated in the RelA binding regions of a list of TFs and co-factors that are strongly associated with M_{late} and contain RelA binding motifs. The TFs/co-factors that show statistically significant changes across all three epigenome alterations are shown in black.

TF name	H3K4me3	H3K27ac	ATAC-seq
	P values		
SOX10	3.2×10^{-11}	1.7×10^{-4}	5.9×10^{-5}
DNAJC1	5.9×10^{-5}	1.2×10^{-3}	9.5×10^{-3}
ACTN1	3.4×10^{-9}	4.0×10^{-5}	0.13
MMS19	3.0×10^{-9}	1.2×10^{-4}	6.1×10^{-2}
REPIN1	7.0×10^{-9}	7.3×10^{-4}	0.18
IKZF5	7.0×10^{-7}	1.2×10^{-4}	0.15
SIX4	5.1×10^{-8}	6.9×10^{-4}	0.42
VEGFA	5.8×10^{-7}	5.5×10^{-4}	0.48
KLF10	1.1×10^{-6}	8.8×10^{-4}	0.73
E2F3	5.4×10^{-6}	1.3×10^{-3}	0.16
HIVEP2	2.1×10^{-6}	6.5×10^{-4}	0.95
IRX3	1.9×10^{-6}	1.4×10^{-3}	0.60
SGK1	4.1×10^{-5}	3.1×10^{-4}	0.14
TADA3	1.1×10^{-6}	4.0×10^{-3}	0.97
SERTAD3	7.0×10^{-5}	3.8×10^{-4}	0.44
MAF	3.1×10^{-5}	5.8×10^{-3}	0.17
SOX5	3.1×10^{-6}	1.3×10^{-2}	0.89
PHTF1	3.2×10^{-5}	4.2×10^{-3}	0.32
SATB2	6.3×10^{-5}	2.6×10^{-3}	0.49
HOXA13	5.3×10^{-5}	2.8×10^{-3}	0.68
ZBTB24	3.5×10^{-5}	9.4×10^{-3}	0.32
FHIT	3.5×10^{-5}	8.5×10^{-3}	0.53
IRF1	4.9×10^{-5}	1.3×10^{-2}	0.58
ZNF670	3.2×10^{-4}	2.6×10^{-3}	0.53
VDR	9.8×10^{-5}	1.5×10^{-2}	0.79
YAF2	9.5×10^{-5}	2.9×10^{-2}	0.47
RNF25	4.7×10^{-4}	2.1×10^{-2}	0.67

ZNF280B	1.3×10^{-2}	3.4×10^{-3}	0.55
ETS1	1.9×10^{-2}	4.1×10^{-3}	0.36
CTDSP1	4.5×10^{-3}	1.7×10^{-2}	0.85
TAF10	2.0×10^{-2}	7.5×10^{-3}	0.89
RFX2	6.1×10^{-3}	0.12	0.53
FOXP1	4.0×10^{-3}	0.37	0.53
STAT1	9.4×10^{-2}	0.22	0.75
TARBP1	0.18	0.14	0.94
ZNF280A	0.16	0.61	0.53

Table S6. Relevant gene expression levels (RPKM) of selected patients before and after the MAPKi treatments from published data. Data are provided as Excel spreadsheets.

References

1. Salgia R, Kulkarni P. The Genetic/Non-genetic Duality of Drug 'Resistance' in Cancer. *Trends in Cancer*. 2018. pp. 110–118. doi:10.1016/j.trecan.2018.01.001
2. Brock A, Chang H, Huang S. Non-genetic heterogeneity a mutation-independent driving force for the somatic evolution of tumours. *Nature Reviews Genetics*. 2009. pp. 336–342. doi:10.1038/nrg2556
3. Arkenau HT, Kefford R, Long G V. Targeting BRAF for patients with melanoma. *British Journal of Cancer*. 2011. pp. 392–398. doi:10.1038/sj.bjc.6606030
4. Pritchard JR, Lauffenburger DA, Hemann MT. Understanding resistance to combination chemotherapy. *Drug Resistance Updates*. 2012. doi:10.1016/j.drug.2012.10.003
5. Nazarian R, Shi H, Wang Q, Kong X, Koya RC, Lee H, et al. Melanomas acquire resistance to B-RAF(V600E) inhibition by RTK or N-RAS upregulation. *Nature*. 2010;468: 973–977. doi:10.1038/nature09626
6. Wagle N, Emery C, Berger MF, Davis MJ, Sawyer A, Pochanard P, et al. Dissecting therapeutic resistance to RAF inhibition in melanoma by tumor genomic profiling. *J Clin Oncol*. 2011;29: 3085–3096. doi:10.1200/JCO.2010.33.2312
7. Pisco AO, Brock A, Zhou J, Moor A, Mojtahedi M, Jackson D, et al. Non-Darwinian dynamics in therapy-induced cancer drug resistance. *Nat Commun*. 2013;4. doi:10.1038/ncomms3467
8. Ramirez M, Rajaram S, Steininger RJ, Osipchuk D, Roth MA, Morinishi LS, et al. Diverse drug-resistance mechanisms can emerge from drug-tolerant cancer persister cells. *Nat Commun*. 2016;7. doi:10.1038/ncomms10690
9. Hugo W, Shi H, Sun L, Piva M, Song C, Kong X, et al. Non-genomic and Immune Evolution of Melanoma Acquiring MAPKi Resistance. *Cell*. 2015;162: 1271–1285. doi:10.1016/j.cell.2015.07.061
10. Sharma S V., Lee DY, Li B, Quinlan MP, Takahashi F, Maheswaran S, et al. A Chromatin-Mediated Reversible Drug-Tolerant State in Cancer Cell Subpopulations. *Cell*. 2010;141: 69–80. doi:10.1016/j.cell.2010.02.027
11. Wang L, Leite de Oliveira R, Huijberts S, Bosdriesz E, Pencheva N, Brunen D, et al. An Acquired Vulnerability of Drug-Resistant Melanoma with Therapeutic Potential. *Cell*. 2018;173: 1413–1425.e14. doi:10.1016/j.cell.2018.04.012
12. Hata AN, Niederst MJ, Archibald HL, Gomez-Caraballo M, Siddiqui FM, Mulvey HE, et al. Tumor cells can follow distinct evolutionary paths to become resistant to epidermal growth factor receptor inhibition. *Nat Med*. 2016;22: 262–269. doi:10.1038/nm.4040
13. Rambow F, Rogiers A, Marin-Bejar O, Aibar S, Femel J, Dewaele M, et al. Toward Minimal Residual Disease-Directed Therapy in Melanoma. *Cell*. 2018;174: 843–855.e19. doi:10.1016/j.cell.2018.06.025
14. Bai X, Fisher DE, Flaherty KT. Cell-state dynamics and therapeutic resistance in melanoma from the perspective of MITF and IFN γ pathways. *Nature Reviews Clinical Oncology*. Nature Publishing Group; 2019. p. 1. doi:10.1038/s41571-019-0204-6

15. Flavahan WA, Gaskell E, Bernstein BE. Epigenetic plasticity and the hallmarks of cancer. *Science*. American Association for the Advancement of Science; 2017. doi:10.1126/science.aal2380
16. Suvà ML, Rheinbay E, Gillespie SM, Patel AP, Wakimoto H, Rabkin SD, et al. Reconstructing and reprogramming the tumor-propagating potential of glioblastoma stem-like cells. *Cell*. 2014;157: 580–594. doi:10.1016/j.cell.2014.02.030
17. Brown R, Curry E, Magnani L, Wilhelm-Benartzi CS, Borley J. Poised epigenetic states and acquired drug resistance in cancer. *Nature Reviews Cancer*. Nature Publishing Group; 2014. pp. 747–753. doi:10.1038/nrc3819
18. Knoechel B, Roderick JE, Williamson KE, Zhu J, Lohr JG, Cotton MJ, et al. An epigenetic mechanism of resistance to targeted therapy in T cell acute lymphoblastic leukemia. *Nat Genet*. 2014;46: 364–370. doi:10.1038/ng.2913
19. Kelly TK, De Carvalho DD, Jones PA. Epigenetic modifications as therapeutic targets. *Nature Biotechnology*. 2010. pp. 1069–1078. doi:10.1038/nbt.1678
20. Strub T, Ghiraldini FG, Carcamo S, Li M, Wroblewska A, Singh R, et al. SIRT6 haploinsufficiency induces BRAF V600E melanoma cell resistance to MAPK inhibitors via IGF signalling. *Nat Commun*. 2018;9. doi:10.1038/s41467-018-05966-z
21. Shaffer SM, Dunagin MC, Torborg SR, Torre EA, Emert B, Krepler C, et al. Rare cell variability and drug-induced reprogramming as a mode of cancer drug resistance. *Nature*. 2017;546: 431–435. doi:10.1038/nature22794
22. Fang M, Hutchinson L, Deng A, Green MR. Common BRAF(V600E)-directed pathway mediates widespread epigenetic silencing in colorectal cancer and melanoma. *Proc Natl Acad Sci*. 2016;113: 1250–1255. doi:10.1073/pnas.1525619113
23. Liao BB, Sievers C, Donohue LK, Gillespie SM, Flavahan WA, Miller TE, et al. Adaptive Chromatin Remodeling Drives Glioblastoma Stem Cell Plasticity and Drug Tolerance. *Cell Stem Cell*. 2017;20: 233-246.e7. doi:10.1016/j.stem.2016.11.003
24. Dawson MA, Kouzarides T. Cancer epigenetics: From mechanism to therapy. *Cell*. 2012. pp. 12–27. doi:10.1016/j.cell.2012.06.013
25. Su Y, Wei W, Robert L, Xue M, Tsoi J, Garcia-Diaz A, et al. Single-cell analysis resolves the cell state transition and signaling dynamics associated with melanoma drug-induced resistance. *Proc Natl Acad Sci U S A*. 2017;114. doi:10.1073/pnas.1712064115
26. Sun C, Wang L, Huang S, Heynen GJJE, Prahallad A, Robert C, et al. Reversible and adaptive resistance to BRAF(V600E) inhibition in melanoma. *Nature*. 2014;508: 118–122. doi:10.1038/nature13121
27. Das Thakur M, Salangsang F, Landman AS, Sellers WR, Pryer NK, Levesque MP, et al. Modelling vemurafenib resistance in melanoma reveals a strategy to forestall drug resistance. *Nature*. 2013;494: 251–255. doi:10.1038/nature11814
28. Roesch A, Fukunaga-Kalabis M, Schmidt EC, Zabierowski SE, Brafford PA, Vultur A, et al. A Temporarily Distinct Subpopulation of Slow-Cycling Melanoma Cells Is Required for Continuous Tumor Growth. *Cell*. 2010;141: 583–594. doi:10.1016/j.cell.2010.04.020
29. Kurata T, Tamura K, Kaneda H, Nogami T, Uejima H, Asai G, et al. Effect of re-treatment with gefitinib (“Iressa”, ZD1839) after acquisition of resistance. *Annals of*

- Oncology. 2004. p. 173. doi:10.1093/annonc/mdh006
30. Lee. Remarkable Effect of Gefitinib Retreatment in a Lung Cancer Patient With Lepidic Predominant Adenocarcinoma Who Had Experienced Favorable Results From Initial Treatment With Gefitinib: A Case Report. *J Clin Med Res*. 2012. doi:10.4021/jocmr816e
 31. Cara S, Tannock IF. Retreatment of patients with the same chemotherapy: Implications for clinical mechanisms of drug resistance. *Annals of Oncology*. 2001. pp. 23–27. doi:10.1023/A:1008389706725
 32. Mackiewicz-Wysocka M, Krokowicz Ł, Kocur J, Mackiewicz J. Resistance to vemurafenib can be reversible after treatment interruption. *Med (United States)*. 2014;93. doi:10.1097/MD.0000000000000157
 33. Landsberg J, Kohlmeyer J, Renn M, Bald T, Rogava M, Cron M, et al. Melanomas resist T-cell therapy through inflammation-induced reversible dedifferentiation. *Nature*. 2012;490: 412–416. doi:10.1038/nature11538
 34. Hoek KS, Eichhoff OM, Schlegel NC, Döbbeling U, Kobert N, Schaerer L, et al. In vivo switching of human melanoma cells between proliferative and invasive states. *Cancer Res*. 2008;68: 650–656. doi:10.1158/0008-5472.CAN-07-2491
 35. Kemper K, De Goeje PL, Peeper DS, Van Amerongen R. Phenotype switching: Tumor cell plasticity as a resistance mechanism and target for therapy. *Cancer Research*. 2014. pp. 5937–5941. doi:10.1158/0008-5472.CAN-14-1174
 36. Kochanowski K, Morinishi L, Altschuler SJ, Wu LF. Drug persistence – From antibiotics to cancer therapies. *Current Opinion in Systems Biology*. 2018. pp. 1–8. doi:10.1016/j.coisb.2018.03.003
 37. Fallahi-Sichani M, Becker V, Izar B, Baker GJ, Lin J, Boswell SA, et al. Adaptive resistance of melanoma cells to RAF inhibition via reversible induction of a slowly dividing de-differentiated state. *Mol Syst Biol*. 2017;13: 905. doi:10.15252/msb.20166796
 38. Müller J, Krijgsman O, Tsoi J, Robert L, Hugo W, Song C, et al. Low MITF/AXL ratio predicts early resistance to multiple targeted drugs in melanoma. *Nat Commun*. 2014;5. doi:10.1038/ncomms6712
 39. Tsoi J, Robert L, Paraiso K, Galvan C, Sheu KM, Lay J, et al. Multi-stage Differentiation Defines Melanoma Subtypes with Differential Vulnerability to Drug-Induced Iron-Dependent Oxidative Stress. *Cancer Cell*. 2018;33: 890-904.e5. doi:10.1016/j.ccell.2018.03.017
 40. Ramsdale R, Jorissen RN, Li FZ, Al-Obaidi S, Ward T, Sheppard KE, et al. The transcription cofactor c-JUN mediates phenotype switching and BRAF inhibitor resistance in melanoma. *Sci Signal*. 2015;8: ra82. doi:10.1126/scisignal.aab1111
 41. Hugo W, Zaretsky JM, Sun L, Song C, Moreno BH, Hu-Lieskovan S, et al. Genomic and Transcriptomic Features of Response to Anti-PD-1 Therapy in Metastatic Melanoma. *Cell*. 2016;165: 35–44. doi:10.1016/j.cell.2016.02.065
 42. Fallahi-Sichani M, Moerke NJ, Niepel M, Zhang T, Gray NS, Sorger PK. Systematic analysis of BRAFV600E melanomas reveals a role for JNK/c-Jun pathway in adaptive resistance to drug-induced apoptosis. *Mol Syst Biol*. 2015;11: 797–797. doi:10.15252/msb.20145877
 43. Roesch A, Vultur A, Bogeski I, Wang H, Zimmermann KM, Speicher D, et al.

- Overcoming intrinsic multidrug resistance in melanoma by blocking the mitochondrial respiratory chain of slow-cycling JARID1B^{high} cells. *Cancer Cell*. 2013;23: 811–825. doi:10.1016/j.ccr.2013.05.003
44. Levine RD. Information Theory Approach to Molecular Reaction Dynamics. *Annu Rev Phys Chem*. 2003;29: 59–92. doi:10.1146/annurev.pc.29.100178.000423
 45. Poovathingal SK, Kravchenko-Balasha N, Shin YS, Levine RD, Heath JR. Critical Points in Tumorigenesis: A Carcinogen-Initiated Phase Transition Analyzed via Single-Cell Proteomics. *Small*. 2016;12: 1425–1431. doi:10.1002/smll.201501178
 46. Zadran S, Arumugam R, Herschman H, Phelps ME, Levine RD. Surprisal analysis characterizes the free energy time course of cancer cells undergoing epithelial-to-mesenchymal transition. *Proc Natl Acad Sci U S A*. 2014;111: 13235–40. doi:10.1073/pnas.1414714111
 47. Kravchenko-Balasha N, Levitzki A, Goldstein A, Rotter V, Gross A, Remacle F, et al. On a fundamental structure of gene networks in living cells. *Proc Natl Acad Sci*. 2012;109: 4702–4707. doi:10.1073/pnas.1200790109
 48. Kravchenko-Balasha N, Wang J, Remacle F, Levine RD, Heath JR. Glioblastoma cellular architectures are predicted through the characterization of two-cell interactions. *Proc Natl Acad Sci*. 2014;111: 6521–6526. doi:10.1073/pnas.1404462111
 49. Kravchenko-Balasha N, Shin YS, Sutherland A, Levine RD, Heath JR. Intercellular signaling through secreted proteins induces free-energy gradient-directed cell movement. *Proc Natl Acad Sci*. 2016;113: 5520–5525. doi:10.1073/pnas.1602171113
 50. Kravchenko-Balasha N, Johnson H, White FM, Heath JR, Levine RD. A thermodynamic-based interpretation of protein expression heterogeneity in different glioblastoma multiforme tumors identifies tumor-specific unbalanced processes. *J Phys Chem B*. 2016;120: 5990–5997. doi:10.1021/acs.jpcc.6b01692
 51. Remacle F, Kravchenko-Balasha N, Levitzki A, Levine RD. Information-theoretic analysis of phenotype changes in early stages of carcinogenesis. *Proc Natl Acad Sci*. 2010;107: 10324–10329. doi:10.1073/pnas.1005283107
 52. Zadran S, Remacle F, Levine RD. miRNA and mRNA cancer signatures determined by analysis of expression levels in large cohorts of patients. *Proc Natl Acad Sci*. 2013;110: 19160–19165. doi:10.1073/pnas.1316991110
 53. Uribe RA, Bronner ME. Meis3 is required for neural crest invasion of the gut during zebrafish enteric nervous system development. *Mol Biol Cell*. 2015;26: 3728–3740. doi:10.1091/mbc.e15-02-0112
 54. Lim J, Thiery JP. Epithelial-mesenchymal transitions: insights from development. *Development*. 2012;139: 3471–3486. doi:10.1242/dev.071209
 55. Hinohara K, Wu HJ, Vigneau S, McDonald TO, Igarashi KJ, Yamamoto KN, et al. KDM5 Histone Demethylase Activity Links Cellular Transcriptomic Heterogeneity to Therapeutic Resistance. *Cancer Cell*. 2018;34: 939–953.e9. doi:10.1016/j.ccell.2018.10.014
 56. Berger AJ, Davis DW, Tellez C, Prieto VG, Gershenwald JE, Johnson MM, et al. Automated quantitative analysis of activator protein-2 α subcellular expression in melanoma tissue microarrays correlates with survival prediction. *Cancer Res*. 2005;65: 11185–11192. doi:10.1158/0008-5472.CAN-05-2300

57. Sáez-Ayala M, Montenegro MF, Sánchez-del-Campo L, Fernández-Pérez MP, Chazarra S, Freter R, et al. Directed Phenotype Switching as an Effective Antimelanoma Strategy. *Cancer Cell*. 2013;24: 105–119. doi:10.1016/j.ccr.2013.05.009
58. Verfaillie A, Imrichova H, Atak ZK, Dewaele M, Rambow F, Hulselmans G, et al. Decoding the regulatory landscape of melanoma reveals TEADS as regulators of the invasive cell state. *Nat Commun*. 2015;6. doi:10.1038/ncomms7683
59. Whiteside ST, Epinat JC, Rice NR, Israël A. I kappa B epsilon, a novel member of the IκB family, controls RelA and cRel NF-κB activity. *EMBO J*. 1997;16: 1413–1426. doi:10.1093/emboj/16.6.1413
60. Shin HM, Kim MH, Kim BH, Jung SH, Kim YS, Park HJ, et al. Inhibitory action of novel aromatic diamine compound on lipopolysaccharide-induced nuclear translocation of NF-κB without affecting IκB degradation. *FEBS Lett*. 2004;571: 50–54. doi:10.1016/j.febslet.2004.06.056
61. Spiecker M, Darius H, Liao JK. A Functional Role of IκB-ε in Endothelial Cell Activation. *J Immunol*. 2000;164: 3316–3322. doi:10.4049/jimmunol.164.6.3316
62. Vinogradova M, Gehling VS, Gustafson A, Arora S, Tindell CA, Wilson C, et al. An inhibitor of KDM5 demethylases reduces survival of drug-tolerant cancer cells. *Nat Chem Biol*. 2016;12: 531–538. doi:10.1038/nchembio.2085
63. Arts J, King P, Mariën A, Floren W, Beliën A, Janssen L, et al. JNJ-26481585, a novel “second-generation” oral histone deacetylase inhibitor, shows broad-spectrum preclinical antitumoral activity. *Clin Cancer Res*. 2009;15: 6841–6851. doi:10.1158/1078-0432.CCR-09-0547
64. Kwong LN, Boland GM, Frederick DT, Helms TL, Akid AT, Miller JP, et al. Co-clinical assessment identifies patterns of BRAF inhibitor resistance in melanoma. *J Clin Invest*. 2015;125: 1459–1470. doi:10.1172/JCI78954
65. Li E. Chromatin modification and epigenetic reprogramming in mammalian development. *Nature Reviews Genetics*. 2002. pp. 662–673. doi:10.1038/nrg887
66. Wainwright EN, Scaffidi P. Epigenetics and Cancer Stem Cells: Unleashing, Hijacking, and Restricting Cellular Plasticity. *Trends in Cancer*. 2017. pp. 372–386. doi:10.1016/j.trecan.2017.04.004
67. Lindroth AM, Park YJ, Plass C. Epigenetic reprogramming in cancer. *Epigenetics Hum Heal*. 2015;4: 193–223. doi:10.1007/978-3-642-31974-7_9
68. Easwaran H, Tsai HC, Baylin SB. Cancer Epigenetics: Tumor Heterogeneity, Plasticity of Stem-like States, and Drug Resistance. *Molecular Cell*. 2014. pp. 716–727. doi:10.1016/j.molcel.2014.05.015
69. Jordan NV, Bardia A, Wittner BS, Benes C, Ligorio M, Zheng Y, et al. HER2 expression identifies dynamic functional states within circulating breast cancer cells. *Nature*. 2016;537: 102–106. doi:10.1038/nature19328
70. Sharma S V., Lee DY, Li B, Quinlan MP, Takahashi F, Maheswaran S, et al. A chromatin-mediated reversible drug tolerant state in cancer cell subpopulations. *Cell*. 2010;141: 69–80. doi:10.1016/j.cell.2010.02.027.A
71. Alter O, Brown PO, Botstein D. Singular value decomposition for genome-wide expression data processing and modeling. *Proc Natl Acad Sci*. 2000;97: 10101–10106. doi:10.1073/pnas.97.18.10101

72. Mutambara AGO, Mutambara AGO. Modeling of Dynamic Systems. Design and Analysis of Control Systems. 2018. pp. 49–148. doi:10.1201/9781315140940-2
73. Yosef N, Shalek AK, Gaublomme JT, Jin H, Lee Y, Awasthi A, et al. Dynamic regulatory network controlling TH 17 cell differentiation. *Nature*. 2013;496: 461–468. doi:10.1038/nature11981
74. Telley L, Govindan S, Prados J, Stevant I, Nef S, Dermitzakis E, et al. Sequential transcriptional waves direct the differentiation of newborn neurons in the mouse neocortex. *Science* (80-). 2016;351: 1443–1446. doi:10.1126/science.aad8361
75. Zhang K, Wang M, Zhao Y, Wang W. Taiji: System-level identification of key transcription factors reveals transcriptional waves in mouse embryonic development. *Sci Adv*. 2019;5. doi:10.1126/sciadv.aav3262
76. Hnisz D, Shrinivas K, Young RA, Chakraborty AK, Sharp PA. A Phase Separation Model for Transcriptional Control. *Cell*. 2017. doi:10.1016/j.cell.2017.02.007
77. Gloire G, Legrand-Poels S, Piette J. NF- κ B activation by reactive oxygen species: Fifteen years later. *Biochem Pharmacol*. 2006;72: 1493–1505. doi:10.1016/j.bcp.2006.04.011
78. Wolf-Yadlin A, Hautaniemi S, Lauffenburger DA, White FM. Multiple reaction monitoring for robust quantitative proteomic analysis of cellular signaling networks. *Proc Natl Acad Sci*. 2007;104: 5860–5865. doi:10.1073/pnas.0608638104
79. Lee MJ, Ye AS, Gardino AK, Heijink AM, Sorger PK, MacBeath G, et al. Sequential application of anticancer drugs enhances cell death by rewiring apoptotic signaling networks. *Cell*. 2012;149: 780–794. doi:10.1016/j.cell.2012.03.031
80. Ellis L, Atadja PW, Johnstone RW. Epigenetics in cancer: Targeting chromatin modifications. *Mol Cancer Ther*. 2009;8: 1409–1420. doi:10.1158/1535-7163.mct-08-0860
81. Mehta A, Kim YJ, Robert L, Tsoi J, Comin-Anduix B, Berent-Maoz B, et al. Immunotherapy resistance by inflammation-induced dedifferentiation. *Cancer Discov*. 2018;8: 935–943. doi:10.1158/2159-8290.CD-17-1178
82. Buenrostro JD, Wu B, Chang HY, Greenleaf WJ. ATAC-seq: A method for assaying chromatin accessibility genome-wide. *Curr Protoc Mol Biol*. 2015;2015: 21.29.1-21.29.9. doi:10.1002/0471142727.mb2129s109
83. Li G, Bethune MT, Wong S, Joglekar A V., Leonard MT, Wang JK, et al. T cell antigen discovery via trogocytosis. *Nat Methods*. 2019;16: 183–190. doi:10.1038/s41592-018-0305-7
84. Li G, So AYL, Sookram R, Wong S, Wang JK, Ouyang Y, et al. Epigenetic silencing of miR-125b is required for normal B-cell development. *Blood*. 2018;131: 1920–1930. doi:10.1182/blood-2018-01-824540
85. Forde PM, Chaft JE, Sloan M, Cancer K, Smith KN, Anagnostou V, et al. Neoadjuvant PD-1 Blockade in Resectable Lung Cancer. *N Engl J Med*. 2018;378: 1976–1986. doi:10.1056/NEJMoa1716078.Neoadjuvant
86. Kim D, Pertea G, Trapnell C, Pimentel H, Kelley R, Salzberg SL. TopHat2: Accurate alignment of transcriptomes in the presence of insertions, deletions and gene fusions. *Genome Biol*. 2013;14. doi:10.1186/gb-2013-14-4-r36
87. Anders S, Pyl PT, Huber W. HTSeq-A Python framework to work with high-throughput sequencing data. *Bioinformatics*. 2015;31: 166–169.

- doi:10.1093/bioinformatics/btu638
88. Hsu F, Kent JW, Clawson H, Kuhn RM, Diekhans M, Haussler D. The UCSC known genes. *Bioinformatics*. 2006;22: 1036–1046. doi:10.1093/bioinformatics/btl048
 89. Warden CD, Yuan Y-C, Wu X. Optimal Calculation of RNA-Seq Fold-Change Values. *Int J Comput Bioinforma Silico Model*. 2013;2: 285–292. Available: <http://bioinfo.aizeonpublishers.net/content/2013/6/bioinfo285-292.pdf>
 90. Lawrence M, Huber W, Pagès H, Aboyoun P, Carlson M, Gentleman R, et al. Software for Computing and Annotating Genomic Ranges. *PLoS Comput Biol*. 2013;9. doi:10.1371/journal.pcbi.1003118
 91. Law CW, Chen Y, Shi W, Smyth GK. Voom: Precision weights unlock linear model analysis tools for RNA-seq read counts. *Genome Biol*. 2014;15. doi:10.1186/gb-2014-15-2-r29
 92. Benjamini Y, Hochberg Y. Controlling the False Discovery Rate: A Practical and Powerful Approach to Multiple Testing. *J R Stat Soc Ser B*. 1995;57: 289–300. doi:10.1111/j.2517-6161.1995.tb02031.x
 93. Wilkerson MD, Hayes DN. ConsensusClusterPlus: A class discovery tool with confidence assessments and item tracking. *Bioinformatics*. 2010;26: 1572–1573. doi:10.1093/bioinformatics/btq170
 94. Langmead B, Salzberg SL. Fast gapped-read alignment with Bowtie 2. *Nat Methods*. 2012;9: 357–359. doi:10.1038/nmeth.1923
 95. Zhang Y, Liu T, Meyer CA, Eeckhoute J, Johnson DS, Bernstein BE, et al. Model-based analysis of ChIP-Seq (MACS). *Genome Biol*. 2008;9. doi:10.1186/gb-2008-9-9-r137
 96. Love MI, Huber W, Anders S. Moderated estimation of fold change and dispersion for RNA-seq data with DESeq2. *Genome Biol*. 2014;15. doi:10.1186/s13059-014-0550-8
 97. Ramírez F, Dündar F, Diehl S, Grüning BA, Manke T. DeepTools: A flexible platform for exploring deep-sequencing data. *Nucleic Acids Res*. 2014;42. doi:10.1093/nar/gku365
 98. Denny SK, Yang D, Chuang CH, Brady JJ, Lim JSS, Grüner BM, et al. Nfib Promotes Metastasis through a Widespread Increase in Chromatin Accessibility. *Cell*. 2016;166: 328–342. doi:10.1016/j.cell.2016.05.052
 99. Vasudevan S, Flashner-Abramson E, Remacle F, Levine RD, Kravchenko-Balasha N. Personalized disease signatures through information-theoretic compaction of big cancer data. *Proc Natl Acad Sci*. 2018;115: 7694–7699. doi:10.1073/pnas.1804214115
 100. Eichler GS, Huang S, Ingber DE. Gene Expression Dynamics Inspector (GEDI): for integrative analysis of expression profiles. *Bioinformatics*. 2003;19: 2321–2322. doi:10.1093/bioinformatics/btg307
 101. Hänzelmann S, Castelo R, Guinney J. GSVA: Gene set variation analysis for microarray and RNA-Seq data. *BMC Bioinformatics*. 2013;14. doi:10.1186/1471-2105-14-7
 102. Iorio F, Knijnenburg TA, Vis DJ, Bignell GR, Menden MP, Schubert M, et al. A Landscape of Pharmacogenomic Interactions in Cancer. *Cell*. 2016;166: 740–754. doi:10.1016/j.cell.2016.06.017

103. Akbani R, Akdemir KC, Aksoy BA, Albert M, Ally A, Amin SB, et al. Genomic Classification of Cutaneous Melanoma. *Cell*. 2015;161: 1681–1696. doi:10.1016/j.cell.2015.05.044
104. Barretina J, Caponigro G, Stransky N, Venkatesan K, Margolin AA, Kim S, et al. The Cancer Cell Line Encyclopedia enables predictive modelling of anticancer drug sensitivity. *Nature*. 2012;483: 603–607. doi:10.1038/nature11003

SINGLE CELL ANALYSIS RESOLVES THE CELL STATE TRANSITION AND SIGNALING DYNAMICS ASSOCIATED WITH MELANOMA DRUG-INDUCED RESISTANCE

Continuous BRAF inhibition of BRAF mutant melanomas triggers a series of cell state changes that lead to therapy resistance, and escape from immune control, prior to establishing acquired resistance genetically. We used genome-wide transcriptomics and single-cell phenotyping to explore the response kinetics to BRAF inhibition for a panel of patient-derived BRAFV600-mutant melanoma cell lines. A subset of plastic cell lines, which followed a trajectory covering multiple known cell-state transitions, provided models for more detailed biophysical investigations. Markov modeling revealed that the cell state transitions were reversible and mediated by both Lamarckian induction and non-genomic Darwinian selection of drug tolerant states. Single cell functional proteomics revealed activation of certain signaling networks shortly following BRAF inhibition, and prior to the appearance of drug resistant phenotypes. Drug targeting those networks, in combination with BRAF inhibition, halted the adaptive transition and led to prolonged growth inhibition in multiple patient derived cell lines.

This chapter includes content from our previously published article:

- [1] Su, Yapeng, Wei Wei, Lidia Robert, Min Xue, Jennifer Tsoi, Angel Garcia-Diaz, Blanca Homet Moreno et al. "Single-cell analysis resolves the cell state transition and signaling dynamics associated with melanoma drug-induced resistance." *Proceedings of the National Academy of Sciences* 114, no. 52 (2017): 13679-13684. doi:10.1073/pnas.1712064115

Introduction

The high rate of both response and resistance to BRAF inhibitors (BRAFi) has made *BRAF* mutant melanomas and derived cell lines into paradigmatic models for exploring the challenges of targeted inhibitors. Epigenetic alterations and associated cell state transitions along the melanocytic lineage towards drug tolerant states appear to precede the emergence of clones that are genetically resistant to BRAF inhibition [1-5]. Specifically, brief BRAFi exposure (1-3 days) can trigger melanocytic differentiation in certain cell lines. This is accompanied by increased MITF (a melanocytic transcription factor) and upregulation of downstream melanosomal antigens MART-1 and gp100 [1, 2]. Slightly longer exposure (2-9 days) can induce de-differentiation towards a slow-cycling neural crest-like phenotype, with a characteristic increase of Nerve Growth Factor Receptor (NGFR) and loss of MART-1 [5]. Extended exposure (>2 weeks) can yield an invasive mesenchymal-like state with both MART-1 and NGFR loss [3]. The kinetics and molecular details of these cell state changes depend upon the drug treatment duration and dose, and the plasticity of the cancer cells [3-5]. For some patient-derived cell lines, these drug-induced cell state transitions are reversed upon drug release [5, 6]. Observations on patient-derived cells have been shown to correlate with what is seen in patient tumors [3-5].

Several studies have explored the biology of non-genetic BRAFi resistance in *BRAF* mutant melanomas [1-5], but the biophysical picture of this process is less resolved. Biophysical studies can yield predictive insights, but may lack the mechanistic detail of a biological investigation. Of particular interest here are the nature of the cell-state changes observed over the course of drug resistance development. We consider two scenarios. The first involves the enrichment of drug resistant cancer cell genotypes, or epigenotypes, with growth advantage upon drug exposure, akin to the Darwinian-type selection [7]. The second, Lamarckian induction [8], is when the drug treatment itself induces cell state changes towards a more drug tolerant state that can persist across cell generations through transcriptional reprogramming and signaling network rewiring. The second scenario is often loosely (and imprecisely) termed as an adaptive response to drugging.

In principle, experimental measures of the trajectories of many single melanoma cells would discriminate between the different scenarios for drug resistance development. However, such trajectories are not feasible for the full, few month, reversible melanocyte to mesenchymal transition, although sub-regions of this cell state space may be so mapped [5]. Here, we utilize whole transcriptome analysis and single cell phenotype profiling to investigate the responses of a series of patient-derived *BRAF* mutant melanoma cell lines to BRAFi. Certain cell lines exhibit the full range of adaptive responses, and data from those cells is computationally modeled to investigate the transition kinetics and the nature of the

BRAFi-triggered cell-state changes. We further explore the signaling pathways associated with the induction of various sub-phenotypes via a kinetic single cell functional proteomic study [9]. These single cell assays uncover the emergence of drug-activated signaling, prior to the appearance of drug-tolerant phenotypes, and identify strategies for arresting the cell-state transitions and prolonging cell growth inhibition. We demonstrate that our findings extend to less-plastic cell lines.

Results

The cellular transition trajectories of phenotypically plastic melanoma cells in adaptation to BRAFi.

We interrogated 18 patient-derived *BRAF*^{V600E} mutant melanoma cell lines by exposing them to BRAFi (vemurafenib) for periods of 3 days and 3 weeks at a concentration of $2 \times IC_{50}$ for each cell line (*SI Appendix*, Table S1). Phenotypic changes were characterized by flow cytometry using well-established markers for melanocytic (MART-1) and neural crest-like cells (NGFR), respectively (*SI Appendix*, Figs. S1 and S2, and Table S2) [5, 6, 10]. Clustering of flow cytometry data classified the 18 cell lines into 4 clusters according to their phenotypic plasticity to BRAFi. Cluster C cells exhibited the highest plasticity upon drug treatment (*SI Appendix*, Fig. S1A).

We further characterized these phenotypic changes at the whole transcriptome level. We randomly selected 9 cell lines from the 4 clusters for RNA-seq analysis at baseline, plus after 3 days and 3 weeks of drug exposure (Fig. 1 and *SI Appendix*, Fig. S1B). Consistent with previous findings, the most drug resistant cell lines (defined by $IC_{50} > 1 \mu M$) showed a relatively low melanocytic signature, elevated expression of neural crest and mesenchymal related genes, and activated signaling in JNK and NF κ B pathways [3, 5]. *AXL* and *c-JUN* strongly correlate with the IC_{50} values while *LEF1* and *MITF* are anti-correlated [3, 11, 12]. A clustering analysis of genome-wide expression of the 9 cell lines yielded partitions identical to those generated from two-marker flow cytometry data (*SI Appendix*, Fig. S1B). This confirmed NGFR and MART-1 as robust markers for characterizing the BRAFi-induced phenotypic transitions. The differentially expressed genes (DEGs) upon BRAFi treatment, as analyzed using Gene Expression Dynamic Inspector (GEDI) [13], pointed to cluster C again that exhibited the largest transcriptional alterations upon drugging (Fig. 1C). A common group of proliferation-related genes showed varying degrees of down-regulation in all clusters (*SI Appendix*, Fig. S3).

We selected the highly plastic Cluster C cell lines (M397, M229, and M263) for a time-course analysis for either a brief (3 days) to a prolonged (71-90 days) BRAF inhibition. The

three lines followed similar trajectories on the flow cytometry plots (Fig. 1B), starting with transient melanocytic differentiation (increased MITF/MART-1 expression) for 3 day treatment (Figs. 1B and *SI Appendix*, Table S2), followed by the appearance of the slow cycling neural crest-like (NGFR^{high}/MART-1^{neg}) state after 1-3 weeks of drug treatment. Prolonged BRAF inhibition yielded a double negative (NGFR^{low}/MART-1^{neg}) state characterized by a sharp increase in cell proliferation [5]. The interpretation of these trajectories (Fig. 1B) was validated at the transcriptional level by scoring MITF activity [14] and neural crest signatures [15] of each cell line using curated gene sets (Fig. 1D and *SI Appendix*, Fig. S4 and Table S3). The trajectories also correlated with the development of adaptive resistance (*SI Appendix*, Fig. S5). Similarly, Gene Set Enrichment Analysis (GSEA) on the averaged gene expression of the three cell lines revealed significant enrichment in neural crest stem cell and EMT related genes with elevated invasiveness and migration signatures. Meanwhile, TNF/NFκB, JNK, and p38 MAPK signaling related genes were significantly enriched upon continuous BRAFi exposure (Fig. 1E), with down-regulation of MITF signature (Fig. 1E and *SI Appendix*, Fig. S6). These findings were confirmed by inspecting the expression levels (*SI Appendix*, Fig. S7A) and mining the GO terms of these DEGs (*SI Appendix*, Fig. S7B). The enrichment of neural crest-related genes was insignificant after prolonged drug exposure while the enrichment of EMT-associated genes held steady (Fig. 1E). Thus, the double negative state carried mesenchymal signatures, and exhibited the loss of neural crest state signatures. Analysis of other clusters showed similar enrichment in neural crest and mesenchymal signatures except for Cluster A, which contained innately resistant cells with MART-1^{neg}/NGFR^{neg} baseline expression (*SI Appendix*, Fig. S8). Similar enrichment patterns of the transcriptional programs were also found in published transcriptomic datasets involving 39 patient samples from pre-treatment, on-treatment, and/or emergence of acquired resistance to RAF/MEK inhibitors [16]. This suggests similar adaptive resistance in these BRAFi-treated patient tumors (*SI Appendix*, Fig. S9). Moreover, when cells were treated with BRAFi for 3 weeks or longer, we identified significant enrichment in most innate anti-PD-1 resistance (IPRES) signatures [17] (*SI Appendix*, Table S4), pointing to a potential rise of resistance to PD-1 blockade for cells adapted to the run-in BRAFi therapy. The BRAFi-induced cell state changes in Cluster C cells reflected a summation of the various types of adaptive transitions reported for melanomas in response to BRAFi [3-6]. Thus, Cluster C cell lines were carried forward for a detailed biophysical investigation of BRAFi-induced cell state transitions.

Adaptive transition proceeds through drug-mediated cell state interconversion and phenotypic selection.

Three factors can account for the drug-induced cell-state transition kinetics. The first is a deterministic factor that arises from cell state changes determined by the underlying

causative gene regulatory networks. The second factor arises from the stochastic nature of gene expression. Stochastic cell-state changes may be considered as a random walk diffusion process across the epigenetic landscape [18]. The third factor accounts for phenotype-specific cell proliferation and survival upon drug exposure. To account for all three factors, we modified a published Markov kinetic framework [19] to model the BRAFi-induced cell state transitions (Fig. 2). Our model assumed that the cell population is comprised of four discrete cell states (Fig. 2A), and contains a non-symmetric cell state interconversion matrix to account for both deterministic (Lamarckian induction) and stochastic cell state transitions. For drug treated cells, a drug susceptibility matrix is introduced to quantify the third factor (See *SI Appendix*, Materials and Methods). Experimental inputs into the model are short-time measures of the cell-state composition dynamics. Computational outputs are state-to-state transition probabilities (Fig. 2B), and, for drug treated samples, state-dependent drug susceptibility (Fig. 2C).

We sorted NGFR^{pos} and NGFR^{neg} subpopulations of two Cluster C cell lines (M397 and M229) at baseline, and seeded them separately in petri-dishes for in vitro expansion (Fig. 2A and *SI Appendix*, Figs. S10-S12), with and without BRAFi, thus providing 4 initial conditions for each cell line. For untreated samples, flow cytometry analysis of the phenotype compositions over the first 3 cycles of expansion provided input into the Markov model. The fitted Markov model parameters (Fig. 2C) were then used to predict longer-term phenotypic evolution. Without BRAFi, the NGFR^{pos} and NGFR^{neg} subpopulations of both cell lines were predicted and experimentally shown to return to their original unsorted phenotypic composition after several cell cycles (*SI Appendix*, Fig. S10B) [5, 18-20].

BRAFi clearly altered the cell-state interconversion probabilities (Figs. 2B and *SI Appendix*, Fig. S13). The Markov model fits from phenotype dynamics of sorted populations (Fig. 2B) under BRAFi were used to predict the drug susceptibility of each cell state. The neural crest-like and double negative states were predicted, and experimentally shown, to be more resistant to drug treatment compared to melanocytic and double positive states (Fig. 2C). We further used the interconversion and drug susceptibility matrices inferred from the cell-state kinetics of segregated populations to predict the phenotypic evolution of unsorted cells upon prolonged BRAFi exposure. The model predictions were in good agreement with the experiments (Fig. 2D and *SI Appendix*, Fig. S13C, Tables S5 and S6). Furthermore, the Markov model suggests that, upon drug removal, the cells should return to the original phenotypic compositions characteristic of drug naive cells. In fact, such a reversible transition was observed in both the Cluster C cells and the less plastic Cluster B cells (*SI Appendix*, Fig. S14A), and the reverted cells also exhibited a similar IC₅₀ to BRAFi as the untreated cells (*SI Appendix*, Fig. S14B).

The Markov model predictions provide evidence for Lamarckian induction, since they show that BRAFi influences the specific rates of cell-state interconversion. The predictions also provide evidence of phenotype-dependent Darwinian selection, since cell states with the lowest drug susceptibility eventually win out. If only the drug susceptibility matrix is included in the Markov model, the resultant prediction is in poor agreement with the experiments (*SI Appendix*, Fig. S13D). Therefore, the combined actions of both cell state interconversion and drug selection contribute to the observed phenotypic kinetics.

Single cell functional proteomics reveals the emergence of drug-activated signaling at the initiation of the adaptive transition.

We utilized the microfluidics based SCBC technology to carry out single cell analysis of the M397 cells so as to interrogate those signaling pathways directly targeted by BRAFi [9]. Guided by the transcriptional analysis, we designed a protein panel that covers critical phenotypic markers, transcription factors and signaling effectors involved in the adaptive transition (*SI Appendix*, Tables S7 and S8). Each SCBC has 320 microchambers (1.5 nanoliter volume) engineered for cell lysis, and each equipped with an antibody array for protein capture. Following cell lysis, specific proteins are captured, and each array element is developed as a sandwich immunofluorescent assay (*SI Appendix*, Fig. S15).

Scatter plots of single cell data are shown in Fig. 3A with averaged protein abundance indicated by the black horizontal lines. The time-series data are projected onto a two-dimensional plane using the t-SNE algorithm (Fig. 3B) [21]. SCBC assays from different time points cluster into different groups. The dispersion within a group and the distance between groups provide functional measures of how different the single cells are. Such dispersion can be quantified by the functional heterogeneity index (FHI) defined in our previous study [9]. Notably, BRAFi treatment increases the cellular heterogeneity in days 3 and 6, indicating an elevated plasticity (Fig. 3C). This is reflected in the sharply increased dispersion of day-6 cells in the t-SNE plane. This increase in heterogeneity between days 3 and 6 is reminiscent of the attractor destabilization and bifurcation prior to a cell-state transition in other systems [22, 23].

We used the SCBC data to assess protein-protein correlations at each time point (*SI Appendix*, Fig. S16). The emergence of strong negative correlations between NGFR and MITF/MART-1 at day-3 points to the initiation of the cell state transition towards the neural crest-like phenotype with elevated NGFR and loss of MITF/MART-1. The overall activity of the network may be quantified by the signaling network activity index (SNAI) that accounts for both the numbers and strengths of statistically significant correlations (See *SI Appendix*, Materials and Methods). The SNAI is highest at day-6 (Fig. 3D), with particularly

strong signaling participation of p-ERK and p-NFκB p65 (*SI Appendix*, Fig. S16), suggesting a potential gain of function through MEK/ERK and NFκB p65 signaling that might lead to BRAFi drug tolerance by promoting the adaptive transition. The SNAI drops sharply between day 6 and day 10, but then recovers to an activity similar to that seen for untreated cells (Fig. 3D), albeit with altered active network components (*SI Appendix*, Fig. S16). This general behavior is reminiscent of cell-state transitions seen in other model systems [23], and indicates a possible cell-state switch between days 6 and 10.

To quantify the influence of the functional proteins on the overall signaling coordination at the initiation of the transition, we performed Principal Component Analysis (PCA), using an analytical approach previously reported [9]. We calculated the correlations between the assayed proteins and first principal component (PC1) for untreated and 6 days BRAFi treated samples. PC1 captures the most essential feature of the signaling network, and thus identifies those proteins that participate most strongly in the signaling coordination. For the untreated sample, PC1 is populated by p-ERK, p-NFκB p65, p-JNK, and p-P38α (Fig. 3E). At day 6, these four proteins bifurcate into 2 groups, with the influence of p-JNK and p-P38α (blue group) signaling repressed, and MEK/ERK and NFκB p65 signaling (red group) elevated (Fig. 3E). This behavior suggests that combining BRAFi with MEK and NFκB p65 inhibition that might arrest the adaptive cell-state transition towards drug resistant phenotypes.

Combined MEK/ERK and NFκB p65 inhibition with BRAFi arrests the adaptive transition and induced a sustained growth inhibition.

The single cell analysis suggests that inhibiting the NFκB p65 and MEK/ERK signaling axes might keep the cells in the BRAFi sensitive state. To test this hypothesis, we used trametinib (T, MEK inhibitor) and JSH-23 (J, NFκB p65 translocation inhibitor) [24] in combination with vemurafenib (V) to treat the M397 cells *in vitro*, and compared the results against mono-therapies (V, T, and J) or dual combinations (V+T and V+J) over 23 days. Consistent with our prediction, all combination therapies induced considerable cell growth inhibition (Fig. 4A). The monotherapies T and J were much less potent compared to V, but both dual combinations and the triple combination significantly outperformed the monotherapies. Consistent with previous finding [5], while V+T yielded enhanced therapeutic effect relative to V, it did not halt the phenotypic transition towards the neural crest-like drug tolerant state (Figs. 4B, and *SI Appendix*, Fig. S17), and therapy resistance emerged after prolonged treatment (Fig. 4C, *SI Appendix*, Fig. S19A). However, both V+J and V+T+J successfully arrested the transition and kept the cells in the drug sensitive state (MART-1^{POS}) (Figs. 4B), indicating NFκB p65 nuclear translocation is necessary for the adaptive transition towards the drug tolerant phenotypes. Drug dose-response assay under the Bliss independence assumption further confirmed that the sustained growth inhibition of

the triple combination was not simply a result of drug synergy, but due to the arrest of cell state transition (*SI Appendix*, Fig. S18). We further performed colonogenic assays to assess if the combination can induce sustained growth inhibition on four other $BRAF^{V600E}$ mutated melanoma cell lines. The results indicated that the V+T+J combination outperforms V+T over prolonged periods for all cell lines tested, while treatment with J alone showed no significant cytotoxicity (Fig. 4C and *SI Appendix*, Fig. S19).

Discussion

Adaptive resistance resulting from transcriptomic reprogramming permits BRAF mutant melanoma cells to survive BRAF inhibition. BRAFi exposure triggers a transient melanocytic differentiation program, followed by multiple de-differentiation programs that terminate in a drug-resistant mesenchymal-like state. Cells with distinct innate drug sensitivities may follow all or part of this transition trajectory upon BRAFi exposure (*SI Appendix*, Fig. S2). The full transition trajectory was observed within a highly plastic set of patient derived cells (*SI Appendix*, Fig. S1A, Cluster C), accompanied by an elevated IPRES gene signature associated with anti-PD-1 therapy-resistant melanomas [17]. These results challenge the notion of protocols with a run-in period of targeted BRAFi therapy followed by immune checkpoint therapy, as the adaptive response to BRAFi may also create a less friendly environment to immunotherapies in certain BRAFi sensitive tumors [25].

The kinetics of the cell state transitions that occur from the drug naïve, melanocytic state to the drug resistant mesenchymal state was well-captured by a Markov model. This analysis revealed the critical role of drug induction, relative to the selection of drug tolerant phenotypes, in the adaptive response to BRAFi. Drug induction can enable the *de novo* generation of new cell states, while selection accelerates the enrichment of the drug tolerant states. The cell state interconversion probabilities over long periods of drug treatment were inferred from snapshots of flow cytometry data. However, the Markov model does have limitations. For example, the phenotype-dependent drug susceptibility determined from the Markov model is incomplete, as it groups the net effect of cell proliferation and cell death of each phenotype into a single diagonal term in the matrix. The relative contribution of each factor is not distinguished [20, 26]. Similarly, upon drug removal, the relative contribution of the cell state reversion versus regrowth of specific cellular phenotypes is also not resolved. Additionally, the Markov model oversimplifies the continuous cell state transitions by categorizing cells into discrete phenotypes based on their marker expression levels. Continuous kinetic models [18], coupled with experimental measures of single cell trajectories [26], may prove attractive for investigating these transitions at finer resolution.

Transcriptional analysis revealed several critical signaling pathways associated with cellular adaptation to BRAFi. This, in turn, informed the design of a second kinetic investigation of the transition via single cell functional proteomics. That study unveiled the BRAFi-induced activation of MEK/ERK and NF κ B p65 signaling, prior to the emergence of the drug-resistant phenotype. NF κ B can synergize with c-Jun in the transcriptional response to TNF- α [12]. Further, the c-Jun/JNK signaling axis has been reported to play a critical role in melanoma adaptive resistance to BRAFi [3, 4], and was also found here to be associated with the emergence of adaptive resistance when the cells were transitioning to the neural crest or mesenchymal-like states (*SI Appendix*, Fig. S20). However, TNF/NF κ B signaling was activated at the beginning of the adaptive transition (prior to the c-Jun/JNK activation), implying that TNF/NF κ B signaling might enable the neural crest transition program. This is further supported by the report that neural crest de-differentiation can be triggered by pro-inflammatory cytokine TNF- α secreted from tumor infiltrating lymphocytes [10]. It echoes the observation that the MITF^{low}/NF κ B^{high} transcriptional state of melanomas is resistant to inhibition of BRAF and MEK, singly or in combination [11]. NF κ B inhibitors are normally used as adjuvant to chemo- or targeted-therapies in clinical trials [27]. However, due to the host toxicity, identifying more clinically actionable targets downstream of the NF κ B pathway may be an appealing option [28] for arresting BRAFi adaptive resistance. As similar enrichment patterns were recurrent in more than half of the on-treatment patient biopsies (*SI Appendix*, Fig. S9), we anticipate that combined therapy with inhibitors of this pathway may improve the durability of BRAFi therapy.

Materials and Methods

Human melanoma cell lines (M series) were established from patient's biopsies under UCLA IRB approval # 11-003254. Please refer to *SI Appendix, SI Materials and Methods* for cell lines and reagents used, experimental protocols and statistical analysis.

Figures.

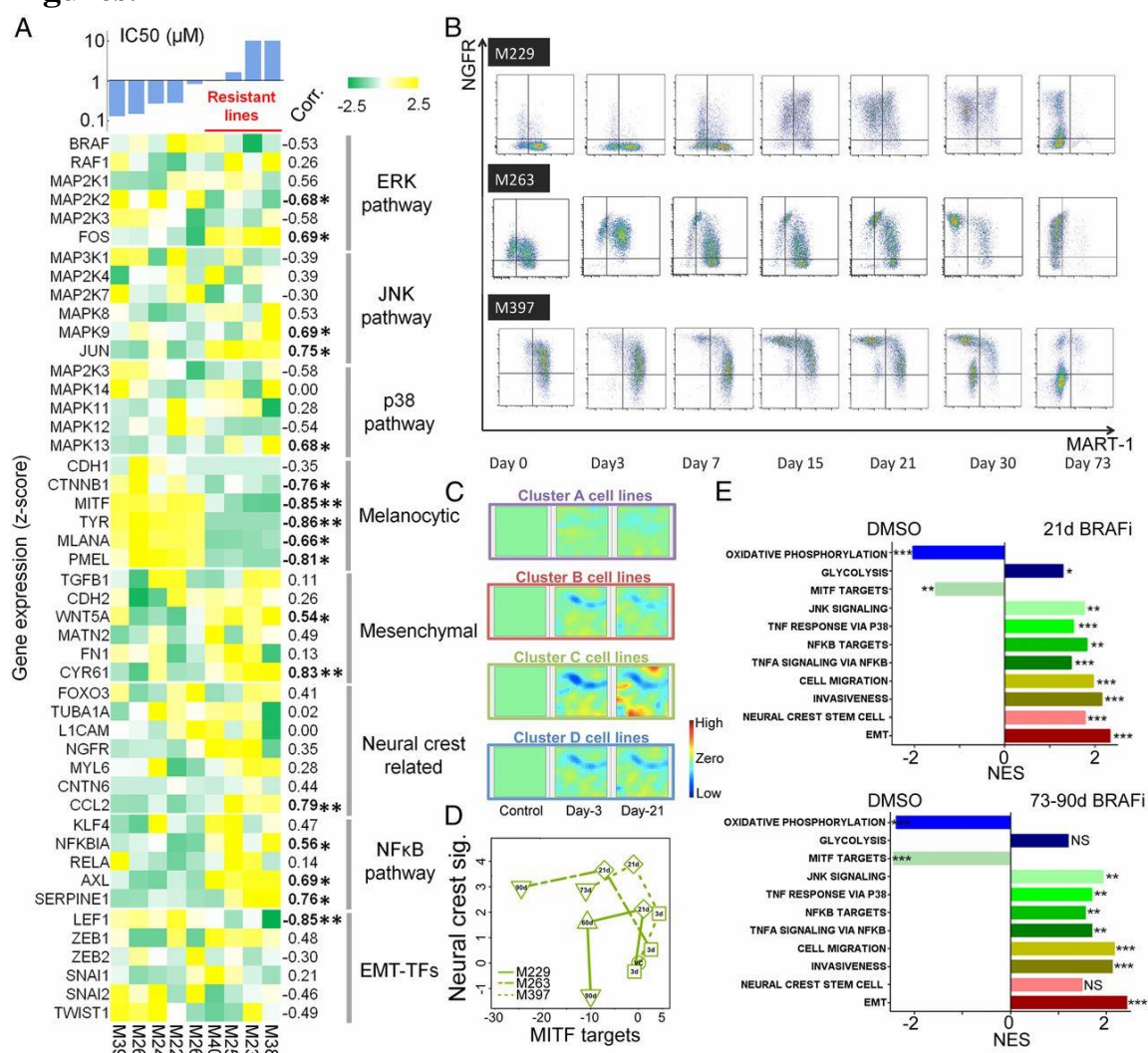


Fig. 1. Phenotypic and transcriptomic characterization of a panel of patient-derived melanoma cell lines while adapting to BRAF inhibition. (A) Heat map of baseline expression levels for critical genes involved in the adaptive BRAFi resistance across a panel of melanoma cell lines, ordered by averaged IC₅₀ to BRAFi. An IC₅₀ of 1 μM was set to be the threshold for resistant lines. Correlation coefficients between each gene's expression and IC₅₀ across cell lines were evaluated with statistically significant correlations listed in bold font (* $p < 0.05$ and ** $p < 0.005$). (B) Phenotypic kinetics screened by flow cytometry shows how the three plastic cell lines from Cluster C experienced a phenotypic transition following a counter-clockwise trajectory over a 73 days BRAF inhibition. (C) Visualization of differentially expressed genes for all the cell line clusters relative to control by GEDI. Each mosaic map represents averaged genome-wide expression profile for a specific cluster of cell lines at a time point as labeled. Each pixel

in the same location within the mosaic maps represents the same minicluster of genes (red: up-regulation, blue: down-regulation, green: no change). (D) Plot of signature scores of MITF and neural crest for the 3 plastic cell lines across different time points upon BRAFi treatment. Counter-clockwise trajectories appear for all three lines (VC: DMSO control). (E) GSEA normalized enrichment scores (NES) show significant enrichment of curated gene sets in the relevant categories associated melanoma adaptive cell state transition for 21 days and 73-90 days (NOM p values: $*p < 0.05$, $**p < 0.005$, $***p < 0.0005$, *NS: not significant*).

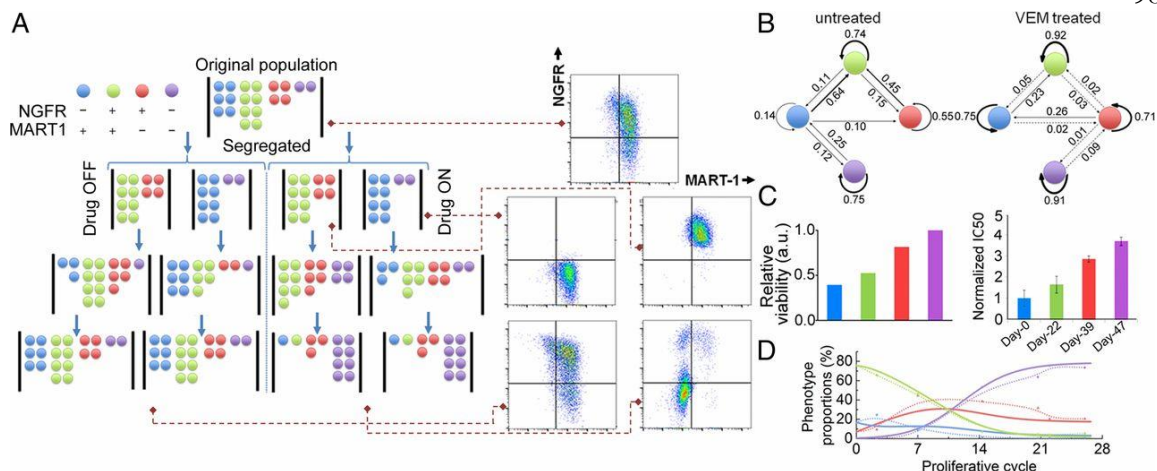


Fig. 2. Markov model of cell state transition predicts phenotypic evolution of melanoma cells upon BRAF inhibition. (A) Schematic illustration of phenotypic segregation and treatment conditions in Markov model. The cells were sorted to NGFR+ and NGFR- subpopulations and treated with or without vemurafenib. (B) Cell state transition probabilities of M397 at untreated and vemurafenib treated conditions. (C) Relative viability of different phenotypes for M397 inferred by the model (up), and measured IC₅₀ values (normalized to control) at different time points (down) across the transition at which one phenotype is enriched as indicated by its respective color code (error bars: \pm SD). (D) Model prediction of the phenotypic kinetics (solid lines) versus experimental data (dots connected with dash lines) for M397 with continuous exposure to vemurafenib.

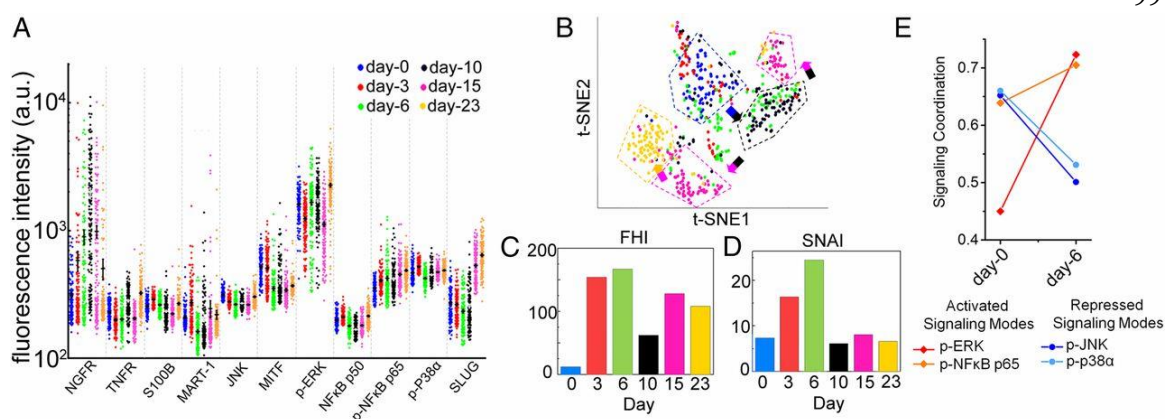


Fig. 3. Single cell proteomic profiling of the M397 cell line during the course of adaptive cell state transition. (A) Background subtracted SCBC data represented as one-dimensional scatter plot (mean \pm SEM was overlaid for each protein by the black horizontal bar). Statistical uniqueness is evaluated by Kruskal-Wallis test comparison among multiple time points. All 13 markers are statistically significant with $P < 0.0005$. (B). Application of t-SNE algorithm to the single cell data separates the cells into spatially distinct clusters based on their proteomic profiles. Each point in the t-SNE plane represents a single cell measurement and its color is coded by a time point. (C) Quantification of the functional heterogeneity (FHI) of M397 cells across different time points along with the transition. (D) The Signaling Network Activity Index (SNAI) across different time points along with the transition, extracted from single cell proteomic measurements of M397 cells. (E) Change in signaling coordination quantified as correlations between key functional proteins and the first principal component for control and day-6 in which a bifurcation of signaling proteins is identified.

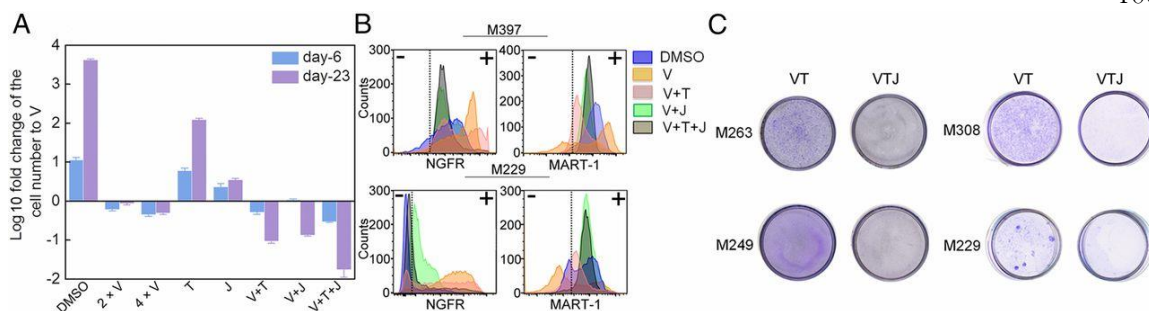


Fig. 4. In vitro validation of the mono- and combination therapies predicted by SCBC analysis. (A) In vitro cell proliferation assay of M397 for the mono- and combination therapies based upon the predictions from the SCBC data analysis. At each time point, cell number of each test condition is normalized to the number of vemurafenib monotherapy and plotted as Log 10 fold change (Error bars: \pm SD). (B) Flow cytometry analysis of MART-1 and NGFR levels at single cell resolution for mono- and combination therapies on both M397 (23 days treatment) and M229 (28 days treatment). (C) Clonogenic assays of long-term drug treated samples confirm V+T+J induced a sustained growth inhibition.

References

1. Boni A, Cogdill AP, Dang P, Udayakumar D, Njauw CNJ, Sloss CM, et al. Selective BRAFV600E inhibition enhances T-cell recognition of melanoma without affecting lymphocyte function. *Cancer Res.* 2010. doi:10.1158/0008-5472.CAN-10-0118
2. Frederick DT, Piris A, Cogdill AP, Cooper ZA, Lezcano C, Ferrone CR, et al. BRAF inhibition is associated with enhanced melanoma antigen expression and a more favorable tumor microenvironment in patients with metastatic melanoma. *Clin Cancer Res.* 2013. doi:10.1158/1078-0432.CCR-12-1630
3. Hill TL. Thermodynamics of small systems. *AIP Conference Proceedings.* Courier Corporation; 1962. doi:10.1063/1.2839115
4. Ramsdale R, Jorissen RN, Li FZ, Al-Obaidi S, Ward T, Sheppard KE, et al. The transcription cofactor c-JUN mediates phenotype switching and BRAF inhibitor resistance in melanoma. *Sci Signal.* 2015;8: ra82. doi:10.1126/scisignal.aab1111
5. Titz B, Lomova A, Le A, Hugo W, Kong X, Ten Hoeve J, et al. JUN dependency in distinct early and late BRAF inhibition adaptation states of melanoma. *Cell Discov.* 2016;2. doi:10.1038/celldisc.2016.28
6. Fallahi-Sichani M, Becker V, Izar B, Baker GJ, Lin J, Boswell SA, et al. Adaptive resistance of melanoma cells to RAF inhibition via reversible induction of a slowly dividing de-differentiated state. *Mol Syst Biol.* 2017;13: 905. doi:10.15252/msb.20166796
7. Sun C, Wang L, Huang S, Heynen GJJE, Prahallad A, Robert C, et al. Reversible and adaptive resistance to BRAF(V600E) inhibition in melanoma. *Nature.* 2014;508: 118–122. doi:10.1038/nature13121
8. Huang S. Tumor progression: Chance and necessity in Darwinian and Lamarckian somatic (mutationless) evolution. *Prog Biophys Mol Biol.* 2012. doi:10.1016/j.pbiomolbio.2012.05.001
9. Pisco AO, Huang S. Non-genetic cancer cell plasticity and therapy-induced stemness in tumour relapse: “What does not kill me strengthens me.” *British Journal of Cancer.* 2015. doi:10.1038/bjc.2015.146
10. Wei W, Shin YS, Xue M, Matsutani T, Masui K, Yang H, et al. Single-Cell Phosphoproteomics Resolves Adaptive Signaling Dynamics and Informs Targeted Combination Therapy in Glioblastoma. *Cancer Cell.* 2016;29: 563–573. doi:10.1016/j.ccell.2016.03.012
11. Landsberg J, Kohlmeyer J, Renn M, Bald T, Rogava M, Cron M, et al. Melanomas resist T-cell therapy through inflammation-induced reversible dedifferentiation. *Nature.* 2012;490: 412–416. doi:10.1038/nature11538

12. Riesenbergs S, Groetchen A, Siddaway R, Bald T, Reinhardt J, Smorra D, et al. MITF and c-Jun antagonism interconnects melanoma dedifferentiation with pro-inflammatory cytokine responsiveness and myeloid cell recruitment. *Nat Commun*. 2015. doi:10.1038/ncomms9755
13. Eichler GS, Huang S, Ingber DE. Gene Expression Dynamics Inspector (GEDI): for integrative analysis of expression profiles. *Bioinformatics*. 2003;19: 2321–2322. doi:10.1093/bioinformatics/btg307
14. Hoek KS, Eichhoff OM, Schlegel NC, Döbbling U, Kobert N, Schaerer L, et al. In vivo switching of human melanoma cells between proliferative and invasive states. *Cancer Res*. 2008;68: 650–656. doi:10.1158/0008-5472.CAN-07-2491
15. Bell GW, Yatskievych TA, Antin PB. GEISHA, a Whole-Mount in Situ Hybridization Gene Expression Screen in Chicken Embryos. *Dev Dyn*. 2004. doi:10.1002/dvdy.10503
16. Kwong LN, Boland GM, Frederick DT, Helms TL, Akid AT, Miller JP, et al. Co-clinical assessment identifies patterns of BRAF inhibitor resistance in melanoma. *J Clin Invest*. 2015;125: 1459–1470. doi:10.1172/JCI78954
17. Hugo W, Zaretsky JM, Sun L, Song C, Moreno BH, Hu-Lieskovan S, et al. Genomic and Transcriptomic Features of Response to Anti-PD-1 Therapy in Metastatic Melanoma. *Cell*. 2016;165: 35–44. doi:10.1016/j.cell.2016.02.065
18. Sisan DR, Halter M, Hubbard JB, Plant AL. Predicting rates of cell state change caused by stochastic fluctuations using a data-driven landscape model. *Proc Natl Acad Sci*. 2012;109: 19262–19267. doi:10.1073/pnas.1207544109
19. Gupta PB, Fillmore CM, Jiang G, Shapira SD, Tao K, Kuperwasser C, et al. Stochastic state transitions give rise to phenotypic equilibrium in populations of cancer cells. *Cell*. 2011;146: 633–644. doi:10.1016/j.cell.2011.07.026
20. Zhou JX, Pisco AO, Qian H, Huang S. Nonequilibrium population dynamics of phenotype conversion of cancer cells. *PLoS One*. 2014;9. doi:10.1371/journal.pone.0110714
21. Amir EAD, Davis KL, Tadmor MD, Simonds EF, Levine JH, Bendall SC, et al. ViSNE enables visualization of high dimensional single-cell data and reveals phenotypic heterogeneity of leukemia. *Nat Biotechnol*. 2013;31: 545–552. doi:10.1038/nbt.2594
22. Mojtahedi M, Skupin A, Zhou J, Castaño IG, Leong-Quong RYY, Chang H, et al. Cell Fate Decision as High-Dimensional Critical State Transition. *PLoS Biol*. 2016;14: 1–13. doi:10.1371/journal.pbio.2000640
23. Bargaje R, Trachana K, Shelton MN, McGinnis CS, Zhou JX, Chadick C, et al. Cell population structure prior to bifurcation predicts efficiency of directed differentiation in human induced pluripotent cells. *Proc Natl Acad Sci*. 2017;114:

2271–2276. doi:10.1073/pnas.1621412114

24. Shin HM, Kim MH, Kim BH, Jung SH, Kim YS, Park HJ, et al. Inhibitory action of novel aromatic diamine compound on lipopolysaccharide-induced nuclear translocation of NF- κ B without affecting I κ B degradation. *FEBS Lett.* 2004;571: 50–54. doi:10.1016/j.febslet.2004.06.056
25. Cooper ZA, Frederick DT, Ahmed Z, Wargo JA. Combining checkpoint inhibitors and BRAF-targeted agents against metastatic melanoma. *Oncoimmunology.* 2013;2. doi:10.4161/onci.24320
26. Pisco AO, Brock A, Zhou J, Moor A, Mojtahedi M, Jackson D, et al. Non-Darwinian dynamics in therapy-induced cancer drug resistance. *Nat Commun.* 2013;4. doi:10.1038/ncomms3467
27. Lin Y, Bai L, Chen W, Xu S. The NF- κ B activation pathways, emerging molecular targets for cancer prevention and therapy. *Expert Opinion on Therapeutic Targets.* 2010. doi:10.1517/14728220903431069
28. Tornatore L, Sandomenico A, Raimondo D, Low C, Rocci A, Tralau-Stewart C, et al. Cancer-Selective Targeting of the Nf-KB Survival Pathway With Gadd45B/Mkk7 Inhibitors. *Cancer Cell.* 2014. doi:10.1016/j.ccr.2014.07.027

SI Appendix

Supplementary Materials and Methods

Cell lines, reagents and cell culture

Human melanoma cell lines (M series) were established from patient's biopsies under UCLA IRB approval # 11-003254. Cells were cultured in RPMI 1640 with L-glutamine (Mediatech, Inc, Manassas, VA), 10% fetal bovine serum (Omega Scientific Tarzana, CA), and 1% penicillin, streptomycin and fungizone (Omega Scientific Tarzana, CA). Cultures were incubated in a water-saturated incubator at 37°C with 5% CO₂. Cells were maintained and tested for mycoplasma as described before [1, 2]. Cell lines were periodically authenticated to their early passages using GenePrint® 10 System (Promega, Madison, WI). Presence of mutations in the genes of interest was checked by OncoMap 3 or Iontrone, and was confirmed by PCR and Sanger sequencing as previously described [1, 2].

Vemurafenib (NC0621949, Selleck Chemicals LLC), trametinib (NC0592237, Selleck Chemicals LLC), and JSH-23 (S7351, Selleck Chemicals LLC) were dissolved in DMSO at designated concentrations before applying to cell culture media. All cell lines were plated in T-75 plates at 60% confluency and treated with vemurafenib at twice the 50% inhibition concentration ($2 \times IC_{50}$) of each cell line using their previously described IC_{50} (Table S1). The DNA-antibody conjugates were synthesized with previous protocols reported [3]. The list of ssDNA and antibodies used in this work is shown in Tables S6 and S7.

Phenotype tracking by flow cytometry.

Cell suspensions were stained for flow cytometry with PE conjugated anti human NGFR antibody from Biolegend (San Diego, CA). All cells were then fixed with Fix-Perm buffer from BD Bioscience (San Jose, CA) and stained for intracellular FITC conjugated anti human Melan-A antibody from Santa Cruz (Dallas, TX). Isotypes for mouse IgG1k and mouse IgG1 respectively were used to enable correct gating and to confirm antibody specificity. Blue live-dead staining from Life technologies (Waltham, MA) was used to discriminate alive. 10000 alive events were collected for each sample. Flow cytometry analysis was conducted using LSR-II from BD Biosciences (San Jose, CA), and the data was analyzed using FlowJo software (Tree Star, Inc., San Carlos, CA). The hierarchical clustering from the 18 cell lines, was performed using the expression levels in flow cytometry, with complete linkage and Euclidean distance metric. Gating of NGFR and Mart1 for defining cell states are all based on the staining of isotype controls.

MITF Reporter Cell Line

The human *Tyrosinase Promoter* (TP) was subcloned from pLightSwitch Prom S700747 (SwitchGear Genomics, Carlsbad, CA), which was first digested with MluI (New England Biolabs; Ipswich, MA). Blunt ends were generated using T4 Polymerase (New England Biolabs) and the resulting fragment was digested again with Bgl II (New England Biolabs). Resulting 1057 bp Tyrosinase promoter insert was then cloned by standard methods [4] into

the BamH1 and HpaI sites of the lentiviral vector backbone Lenti-D-EN-fLUC, driving the expression of the firefly luciferase gene.

Lentivirus particles were generated as previously described [5] to stably transduce M229, M263 and M397. Generated stable reporter cell lines M229TP, M263TP and M397TP from different conditions were trypsinized and seeded at a density of 100.000 cells per well in 96-well white-bottomed plates. Luciferase activity was read out from white-bottomed plates using luciferin directly (1:10 Final dilution) and signal was normalized according to viability calculated using CellTiter-Glo (Promega, San Luis Obispo, CA) (1:2 final dilution), also plated in white-bottomed plates. Bioluminescence imaging was carried out with a Xenogen IVIS 200 Imaging System (Xenogen/Caliper Life Sciences).

RNA-Seq

RNA extraction was performed using AllPrep DNA/RNA Mini kit from Qiagen in 18 human melanoma cell lines samples and also in samples from M229, M263 and M397 treated under different conditions. Bioanalyzer confirmed correct integrity, library was constructed and Illumina 50 bp single-end RNA-seq data was collected for the samples described. RNA sequencing was performed using 50 bps single end sequencing on the Illumina HiSeq 2500 platform. Libraries were prepared using the IlluminaTruSeq RNA sample preparation kit per the manufacturer's instructions. Reads were mapped and aligned to the Homo sapiens NCBI build 37.2 reference genome using TopHat2 v2.0.9 [6]. Expression values in fragments per kilobase of exon per million fragments mapped (FPKM) were generated using Cufflinks v2.2.1 program and Cuffnorm to quantify and normalize aligned reads using the geometric library size normalization method [7].

The stochastic cell transition model

The stochastic cell-state transition model is built by assuming a time-homogeneous Markov chain process as described in a previous publication [8]. Two basic assumptions are made for the model: First, cells at four designated subpopulations transition randomly between states per certain unit time. Second, the transition probabilities depend only on a cell's current state, regardless of its prior states. The governing equations are listed below.

$$\begin{bmatrix} \text{original} \\ \text{proportions} \end{bmatrix} \begin{bmatrix} \text{treatment} \\ \text{sensitivity matrix} \end{bmatrix} \begin{bmatrix} \text{State transition} \\ \text{probability matrix} \end{bmatrix}^{\text{Time}} = \begin{bmatrix} \text{new} \\ \text{proportions} \end{bmatrix}$$

Proportions of various states are listed as column vectors. The 4×4 state transition probability matrix with each element denoting the transition probability from one cell state to other states per unit time is pre-multiplied with a diagonal drug sensitivity matrix. The four diagonal elements of this matrix encode the relative viability of the two melanocyte, neural crest and double negative states in the presence of drug treatment. The calculated 4-element vector is normalized to have a summation of 1 to generate the new proportions vector.

Kinetic flow cytometry data (Table S5) of segregated cell populations at different time points are used as input. Monte Carlo simulation is performed by random sampling differential transition probability and viability vectors to quantitatively infer the most probable values in the matrices that best recapitulate the experimental observations of sorted cells. The values

inferred from sorted cells are then utilized to predict the cell state dynamics and final steady-state composition of unsorted cells under drug treatment (Fig. 2D).

Transcriptomic data analysis

Heatmap and clustering analysis of transcriptomic dataset for all 9 cell lines was performed via MATLAB. Genes are pre-filtered by RPKM value with criteria of average value greater than 1 and coefficient of variance greater than 0.3. Filtered gene expression values were standardized across each row (normalized for each individual gene) and represented by redblue colormap. Hierarchical clustering was performed with average linkage and Euclidean distance metric. Whole transcriptomic dataset for each cell line upon drug treatment was also plotted as self-organized mosaic maps with respect to its control via Gene Expression Dynamics Inspector (GEDI) [9]. Each tile in the maps represents a minicluster of genes with similar expression kinetics. Gene clusters with related expression kinetics are placed close together, while clusters exhibiting very different kinetic trajectories are placed far apart. The tile color encodes the average expression level of the genes in that minicluster at a given time point. By extracting genes in interesting regions (e.g. common regions that are changing in the same direction across all cell line clusters or unique regions that are only changing in only one cluster, *etc.*), one could further investigate their biological functions. Genes in regions of interest are further enriched in the Gene Ontology Biology Process database using Enricher [10].

For generating the phenotypic trajectory in Figs. 1D and S4, the MITF activity and neural crest signature scores were determined by using genes identified as MITF targets [11] and chicken embryo neural crest genes from Gallus EST in situ hybridization analysis – GEISHA- [12] (Table S3) respectively. Signature scores were calculated by taking the sum of all log₂ fold changes from DMSO control for all signature genes and divided by the square root of the total number of genes.

Gene Set Enrichment Analysis (GSEA) was performed using GSEA v2.2.3 software with 1000 permutations and weighted enrichment statistics. For correlation enrichment, we used Pearson correlation of relevant pathways with *MITF*, *LICAM*, *NGFR*, *NFκB1*, *CCL2*, and *AXL* expression across patient samples. For the pre-ranked option with log₂ fold changes were used as the ranking metric. Normalized enrichment score (NES) was assessed across the curated Molecular Signatures Database (MSigDB) Hallmark, C2 curated gene sets, and MITF signature [11].

Using Database for Annotation, Visualization and Integrated Discovery (DAVID) 6.8, we looked at relevant Gene ontology (GO) terms for differentially expressed genes for M229, M263 and M397 at 21 days and 73-90 days of drug treatment with respect to DMSO control (Fig. S7).

Microchip fabrication and single cell proteomic assay

The fabrication of the SCBC devices and the protocol of the single cell proteomic assays were extensively discussed in our previous publications [13, 14]. Briefly, the DNA

microarrays at each microchamber were converted to antibody microarrays by flowing the DNA-antibody conjugate cocktail solution immediately prior to use. Cells were randomly loaded into the 310 microchambers of the SCBC. Each microchamber has an assay component, and a separate reservoir of lysis buffer, and was photographed after cell loading. The SCBC was then cooled on ice for cell lysis. Following a 2-hour protein capture period at room temperature, the microchambers were flushed and the antibody arrays were developed using a cocktail of detection antibodies. The developed antibody barcode arrays were digitized by a Genepix scanner. Each array is matched with the micrograph of that array for preparing a table that contains the microchamber address, the numbers of cells, and the measured fluorescence levels of each assayed protein.

Clonogenic assay

Clonogenic assays were performed by plating melanoma cells in six-well plates with fresh media at an optimal confluence. The media (with drug or DMSO) were replenished every 2 days. Upon the time of staining, 4% paraformaldehyde was applied onto colonies to fix the cells and 0.05% crystal violet solution was used for staining the colonies.

Drug dose-response SRB assay

The 3 cell lines were pre-seeded into 96-well plates for 48 hours before the addition of drug. After that, cells were treated with drug for 72 hours, and cell viability was determined using In Vitro Toxicology Assay Kit (TOX6, SIGMA-ALDRICH) following the manufacturer's instruction. A Bliss independence model was used to evaluate the effect of drug combination [15].

Statistical analysis of SCBC data

The SCBC readouts from the microchambers with a single cell were collected to form a data table. Each row of the table corresponds to a measurement of a panel of functional proteins from a single cell and each column contains digitized fluorescence intensities that provide readout of the levels of each of the assayed proteins. Protein-protein Spearman's rank correlation coefficients can be directly calculated from single cell data. Protein correlation networks were generated by running the calculation through all the protein pairs in panel (Fig. S12). Bonferroni corrected p-value was used to define the statistical significance level for the entire panel and only those significant correlations were shown in the networks.

The t-SNE dimensionality reduction analysis was performed on SCBC dataset following a previous published algorithm [16].

A normalized PCA was used to peel off layer after layer of systematic co-variations from the data, in terms of principal components (PCs). The correlations between functional protein levels and PCs were calculated to quantify the dominative protein pattern of the signaling network coordination and its response to external perturbations such as drug treatment. The signaling network activity index (SNAI) is a metric of the overall strength of the protein signaling coordination at a given condition, and is defined as the reciprocal of the determinant of the protein-protein correlations

Supplementary References

1. Wong DJL, Robert L, Atefi MS, Lassen A, Avarappatt G, Cerniglia M, et al. Antitumor activity of the ERK inhibitor SCH722984 against BRAF mutant, NRAS mutant and wild-type melanoma. *Mol Cancer*. 2014. doi:10.1186/1476-4598-13-194
2. Atefi M, Avramis E, Lassen A, Wong DJL, Robert L, Foulad D, et al. Effects of MAPK and PI3K pathways on PD-L1 expression in melanoma. *Clin Cancer Res*. 2014;20: 3446–3457. doi:10.1158/1078-0432.CCR-13-2797
3. Bailey RC, Kwong GA, Radu CG, Witte ON, Heath JR. DNA-encoded antibody libraries: A unified platform for multiplexed cell sorting and detection of genes and proteins. *J Am Chem Soc*. 2007;129: 1959–1967. doi:10.1021/ja065930i
4. Wood E. *Molecular Cloning. A Laboratory Manual*. Biochem Educ. 1983. doi:10.1016/0307-4412(83)90068-7
5. Koya RC, Mok S, Comin-Anduix B, Chodon T, Radu CG, Nishimura MI, et al. Kinetic phases of distribution and tumor targeting by T cell receptor engineered lymphocytes inducing robust antitumor responses. *Proc Natl Acad Sci U S A*. 2010. doi:10.1073/pnas.1008300107
6. Kim D, Pertea G, Trapnell C, Pimentel H, Kelley R, Salzberg SL. TopHat2: Accurate alignment of transcriptomes in the presence of insertions, deletions and gene fusions. *Genome Biol*. 2013;14. doi:10.1186/gb-2013-14-4-r36
7. Borisy AA, Elliott PJ, Hurst NW, Lee MS, Lehár J, Price ER, et al. Systematic discovery of multicomponent therapeutics. *Proc Natl Acad Sci U S A*. 2003. doi:10.1073/pnas.1337088100
8. Trapnell C, Williams BA, Pertea G, Mortazavi A, Kwan G, Van Baren MJ, et al. Transcript assembly and quantification by RNA-Seq reveals unannotated transcripts and isoform switching during cell differentiation. *Nat Biotechnol*. 2010;28: 511–515. doi:10.1038/nbt.1621
9. Gupta PB, Fillmore CM, Jiang G, Shapira SD, Tao K, Kuperwasser C, et al. Stochastic state transitions give rise to phenotypic equilibrium in populations of cancer cells. *Cell*. 2011;146: 633–644. doi:10.1016/j.cell.2011.07.026
10. Eichler GS, Huang S, Ingber DE. Gene Expression Dynamics Inspector (GEDDI): for integrative analysis of expression profiles. *Bioinformatics*. 2003;19: 2321–2322. doi:10.1093/bioinformatics/btg307
11. Chen EY, Tan CM, Kou Y, Duan Q, Wang Z, Meirelles G V., et al. Enrichr: Interactive and collaborative HTML5 gene list enrichment analysis tool. *BMC Bioinformatics*. 2013. doi:10.1186/1471-2105-14-128
12. Hoek KS, Eichhoff OM, Schlegel NC, Döbbeling U, Kobert N, Schaerer L, et al. In vivo switching of human melanoma cells between proliferative and invasive states.

Cancer Res. 2008;68: 650–656. doi:10.1158/0008-5472.CAN-07-2491

13. Bell GW, Yatskievych TA, Antin PB. GEISHA, a Whole-Mount in Situ Hybridization Gene Expression Screen in Chicken Embryos. *Dev Dyn*. 2004. doi:10.1002/dvdy.10503
14. Shi Q, Qin L, Wei W, Geng F, Fan R, Shik Shin Y, et al. Single-cell proteomic chip for profiling intracellular signaling pathways in single tumor cells. *Proc Natl Acad Sci*. 2012;109: 419–424. doi:10.1073/pnas.1110865109
15. Xue M, Wei W, Su Y, Kim J, Shin YSYS, Mai WXWX, et al. Chemical methods for the simultaneous quantitation of metabolites and proteins from single cells. *J Am Chem Soc*. 2015;137. doi:10.1021/jacs.5b00944
16. Amir EAD, Davis KL, Tadmor MD, Simonds EF, Levine JH, Bendall SC, et al. ViSNE enables visualization of high dimensional single-cell data and reveals phenotypic heterogeneity of leukemia. *Nat Biotechnol*. 2013;31: 545–552. doi:10.1038/nbt.2594

Supplementary Figures

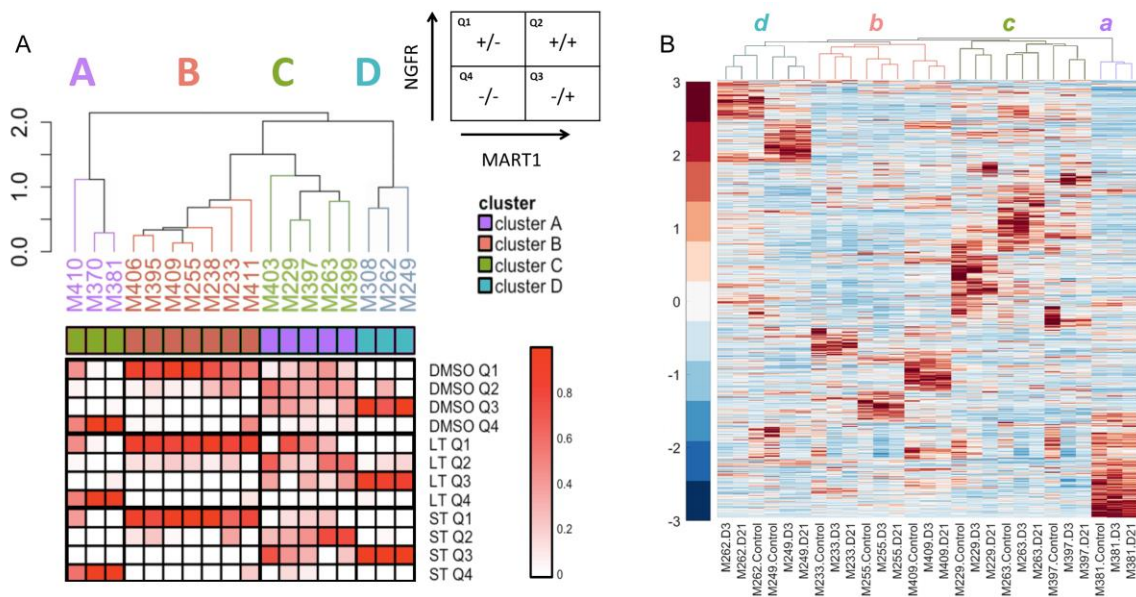
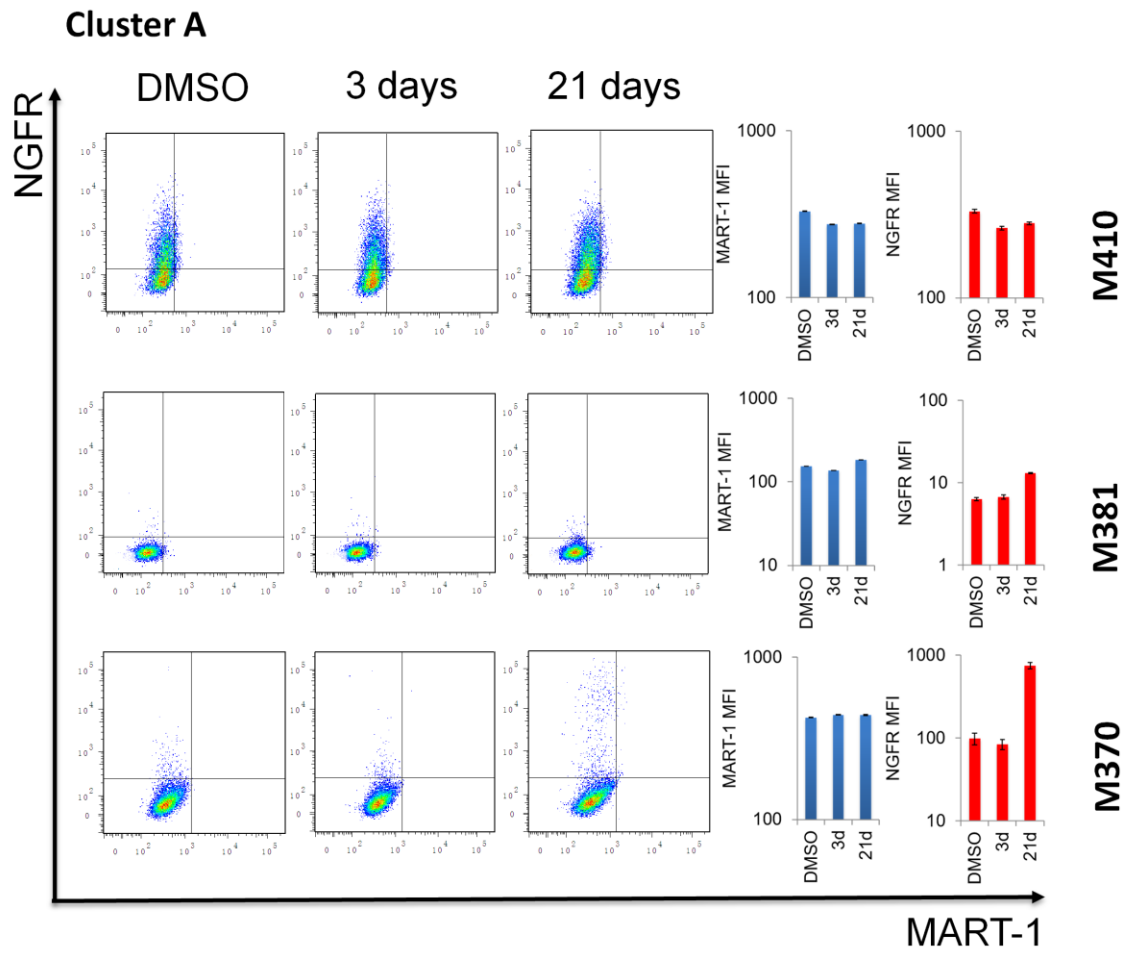
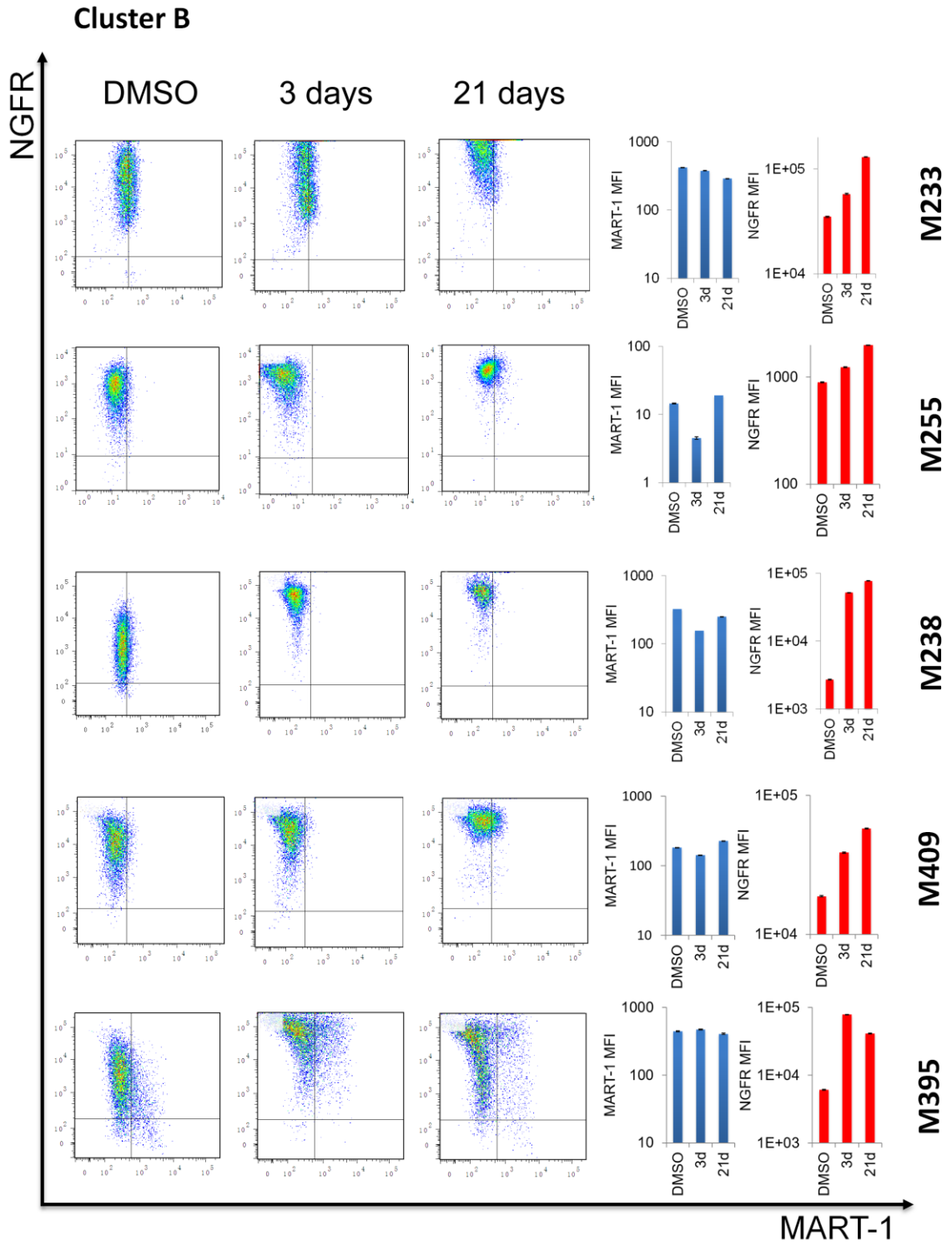
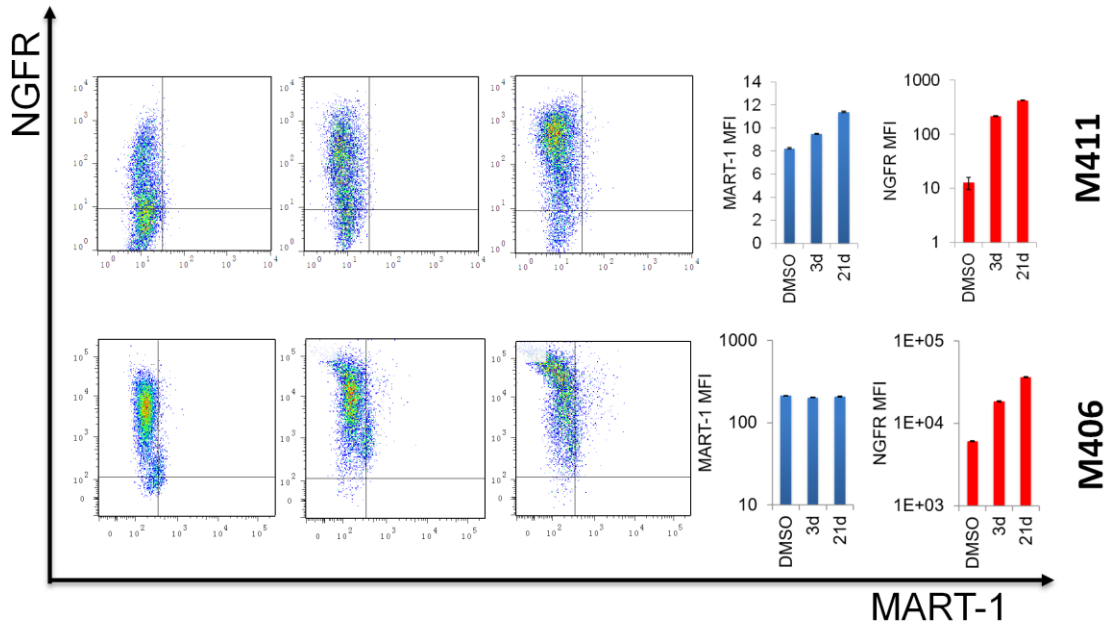
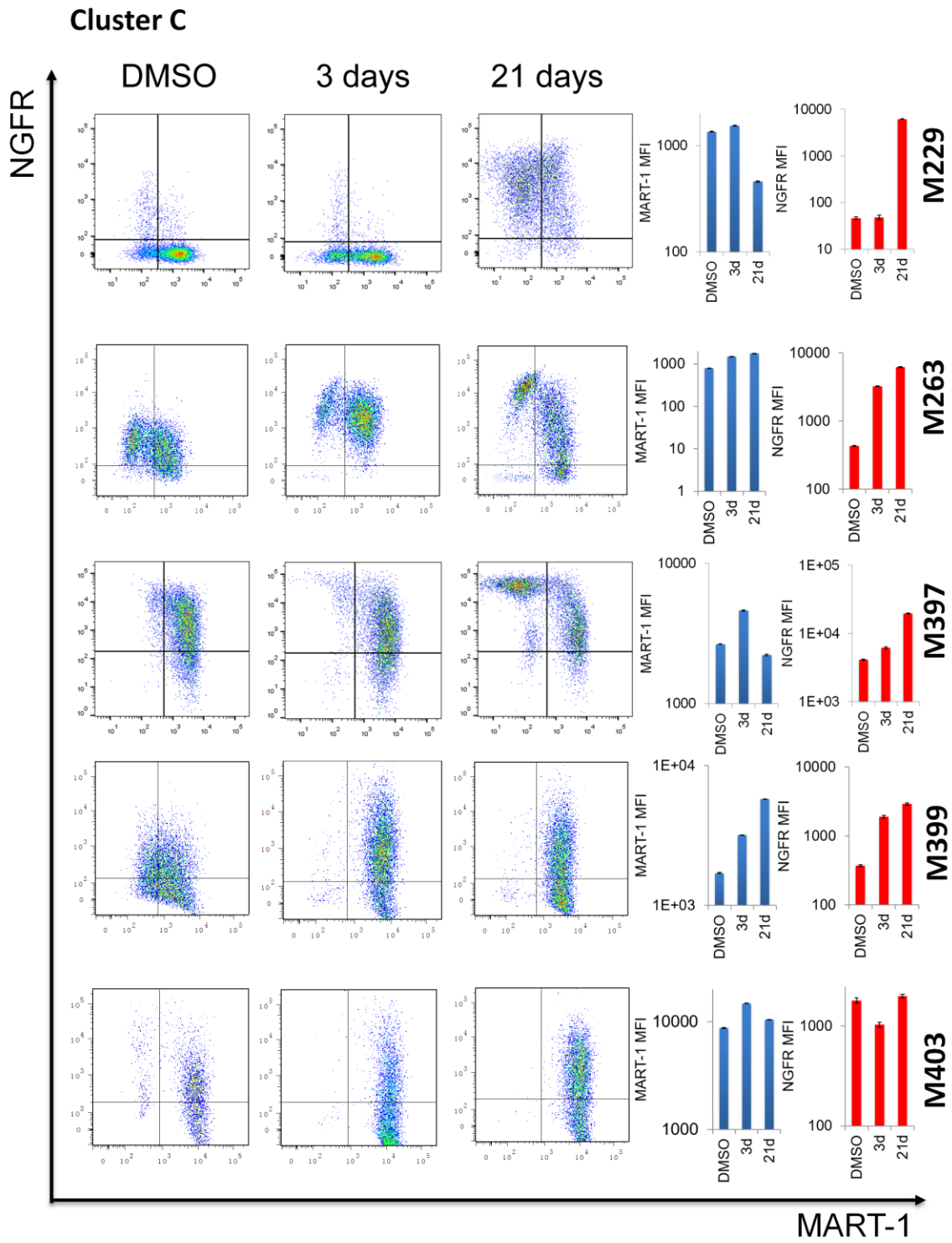


Fig. S1. Phenotypic clustering of 18 BRAFV600 mutant melanoma cell lines upon BRAF inhibition. (A) Clustering of 18 cell lines based upon their partition percentages (color coded in red) in four phenotypic quadrants (inset) at baseline and upon BRAFi response identifies 4 groups. The quadrants are defined by the gate setting of NGFR and MART-1 expression levels for each cell line in the flow cytometry analysis. Cluster C cells show highest phenotypic plasticity upon BRAF inhibition. Hierarchical clustering is performed with complete linkage and Euclidean distance metric (ST: 3 days vemurafenib treatment, LT: 3 weeks vemurafenib treatment). (B) Heat map of the genome-wide expression levels of 9 cell lines randomly selected from each cluster at control, 3 days, and 3 weeks vemurafenib treatment. Clustering is performed with average linkage by Euclidean distance metric. Four clusters are identified to be wholly consistent with the clustering results using MART-1 and NGFR markers in panel A. The clusters are labeled in lower case font, indicating that these cells represent a subset of those analyzed in panel A. Up-regulated genes are colored in red and down-regulated genes in blue.









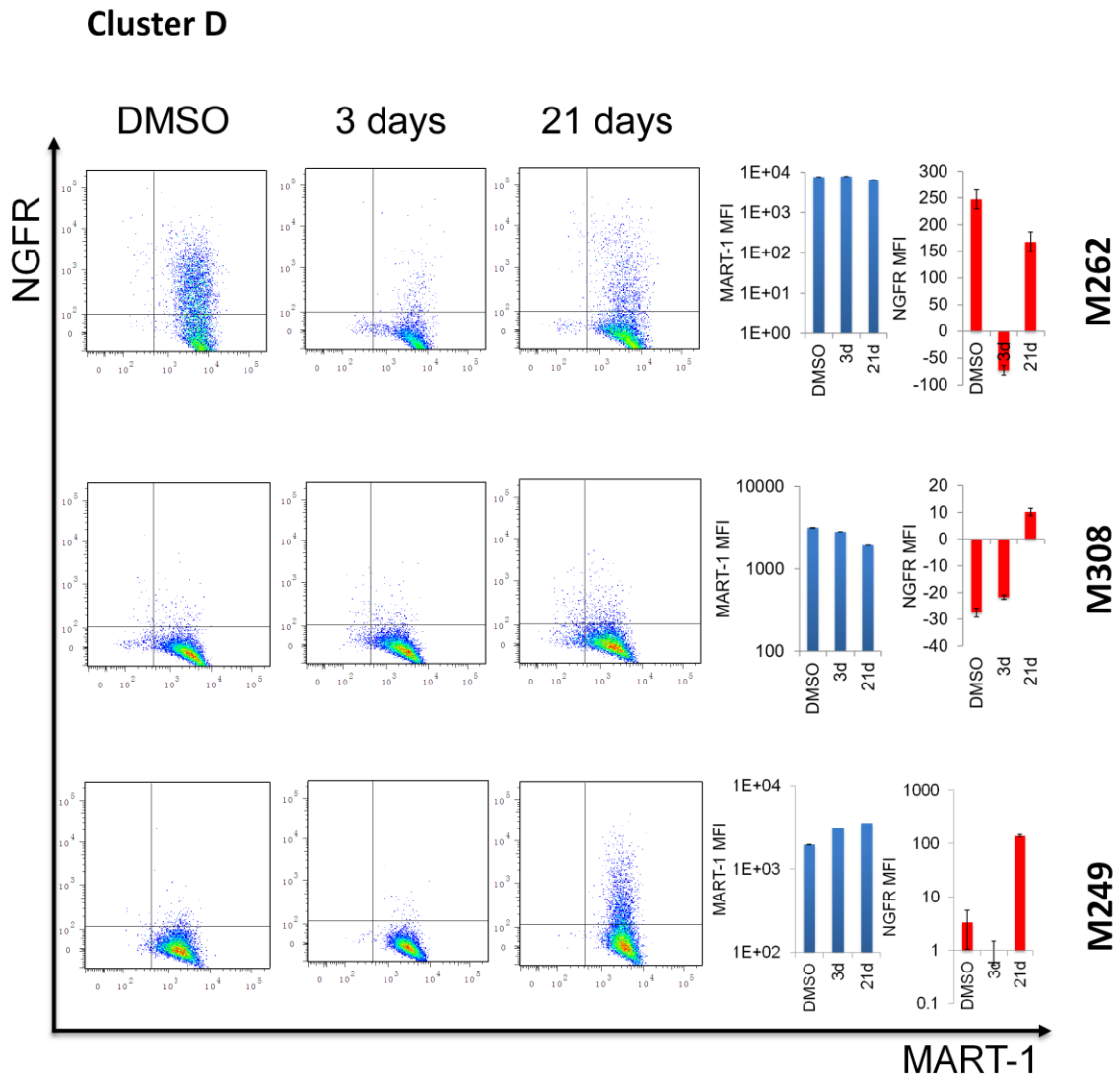


Fig. S2. Flow cytometry analysis of NGFR and MART-1 expression levels for 18 BRAFV600 mutant melanoma cell lines treated with DMSO control and vemurafenib for 3 days and 21 days. The average NGFR and MART-1 levels across treatment conditions are as bar graphs on the right (mean \pm SEM). The cell lines are ordered according to their respective clusters identified in Fig. S1A.

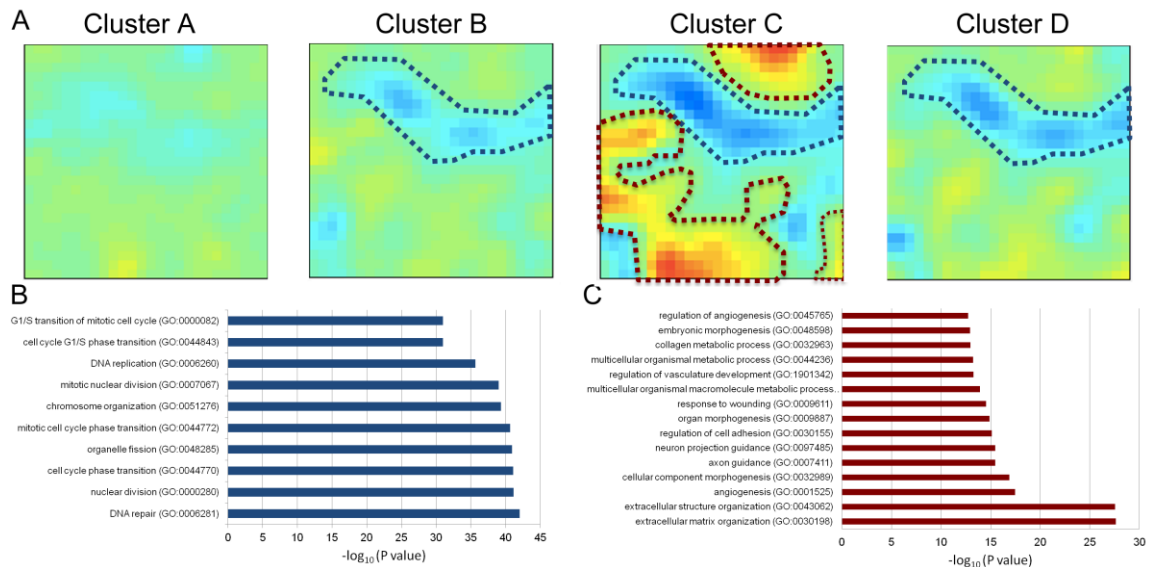


Fig. S3. Enrichment analysis of commonly down-regulated genes across all the cell line clusters and uniquely up-regulated genes in cluster C upon BRAFi exposure. (A) GEDI visualization of differentially expression genes relative to control for all the cell line clusters upon 21 days of vemurafenib treatment. Gene miniclusters circled in blue denote commonly down-regulated genes across all the cell line clusters at varying degrees. Gene miniclusters circled in red denote genes that are uniquely up-regulated in Cluster C cells. (B and C) Gene Ontology enrichment using Enricher for genes circled in blue (or red). The top 10 ontology terms with highest enrichment scores are listed from top to bottom with decreasing p values.

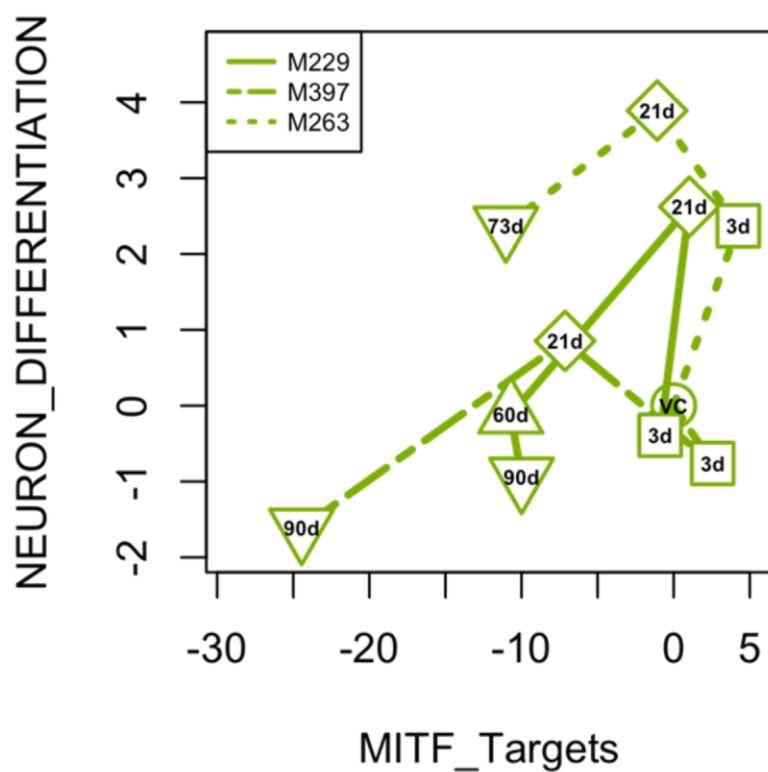


Fig. S4. Plot of MITF activity signature scores vs neuron differentiation (Molecular Signatures Database C5 Collection) signature scores for the 3 plastic cell lines across different time points upon vemurafenib treatment. Counterclockwise trajectories appear for all three lines (VC: DMSO control).

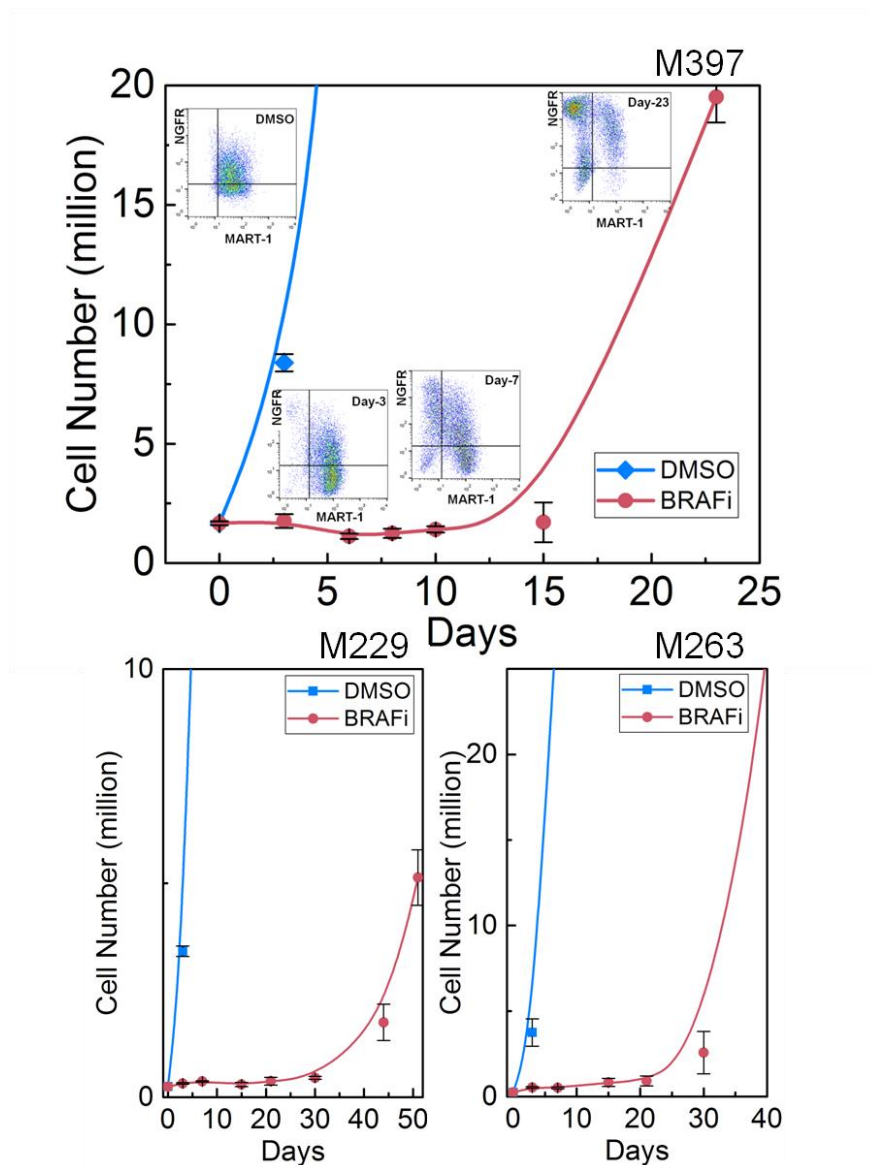


Fig. S5. Cell growth kinetics of M397, M229 and M263 under DMSO control or BRAFi treatment overlaid with phenotypic profiles (M397 only). BRAFi exposure moderately inhibited the cell growth for a short-term followed by a drug tolerant exponential growth phase characteristic of the adaptive resistance to BRAFi (data are shown as mean \pm SD).

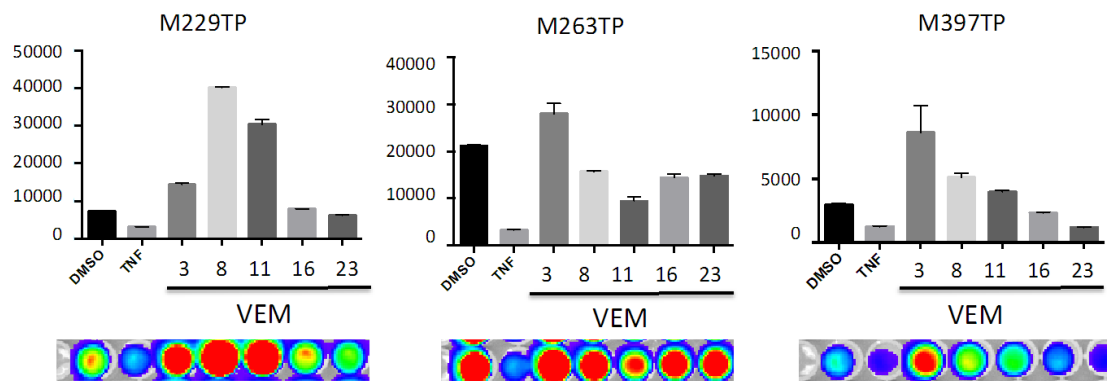


Fig. S6. MITF activity analyzed using a bioluminescence tyrosinase promoter (TP) reporter system through different time points of vemurafenib for M229TP, M263TP and M397TP. Each condition is normalized for 100,000 cells and viability. Data is representative of duplicate wells, and representative of an experiment done in two independent experiments. Error bars are standard deviation of the two wells. Luciferase representative images are shown underneath.

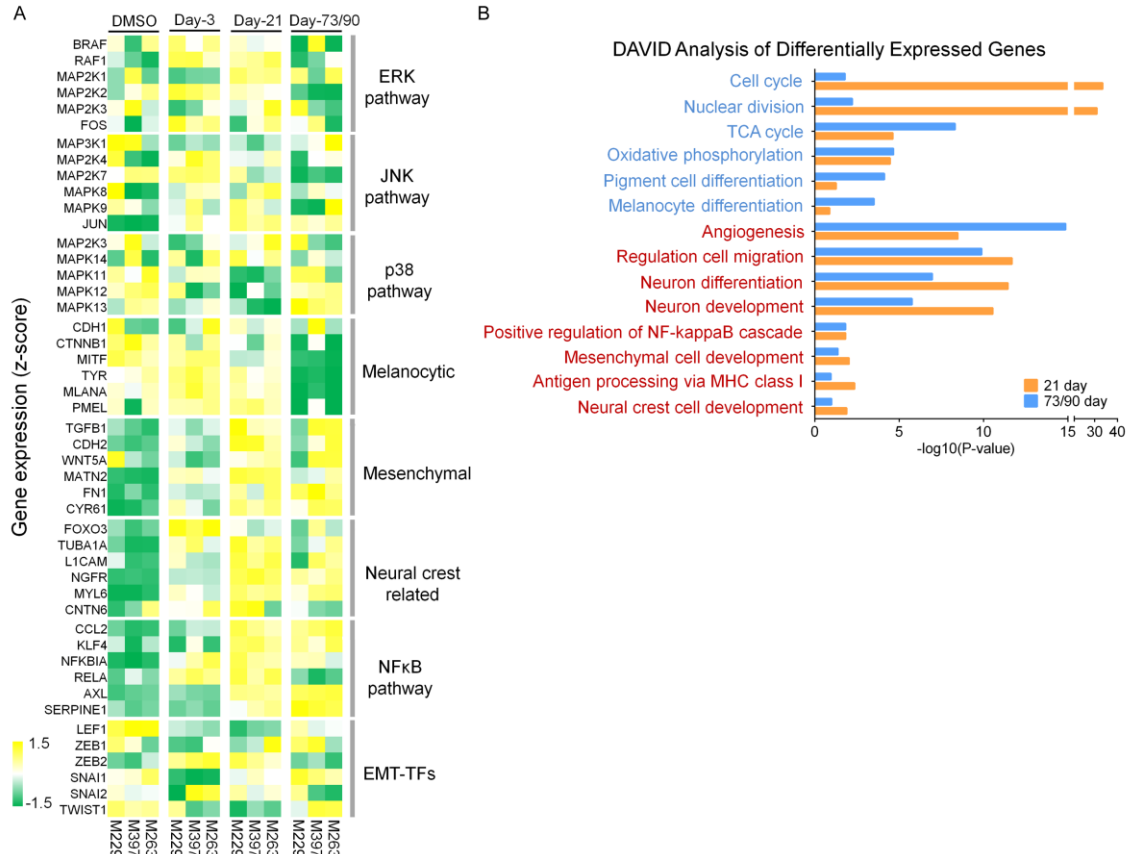


Fig. S7. Transcriptional signatures of three plastic cell lines in Cluster C. (A) Heat map of expression levels for critical genes involved in the adaptive BRAFi resistance at baseline (DMSO) as well as upon 3 days, 21 days, and 73-90 days of vemurafenib exposure. (B) Gene Ontology analysis of differentially expressed genes for the three plastic cell lines following 21 days and 73-90 days drug treatment with respect to DMSO control. Relevant GO terms are listed with respective p-values, analyzed by DAVID. Blue terms denote GO term enrichment for down-regulated genes and red terms denote GO term enrichment for up-regulated genes.

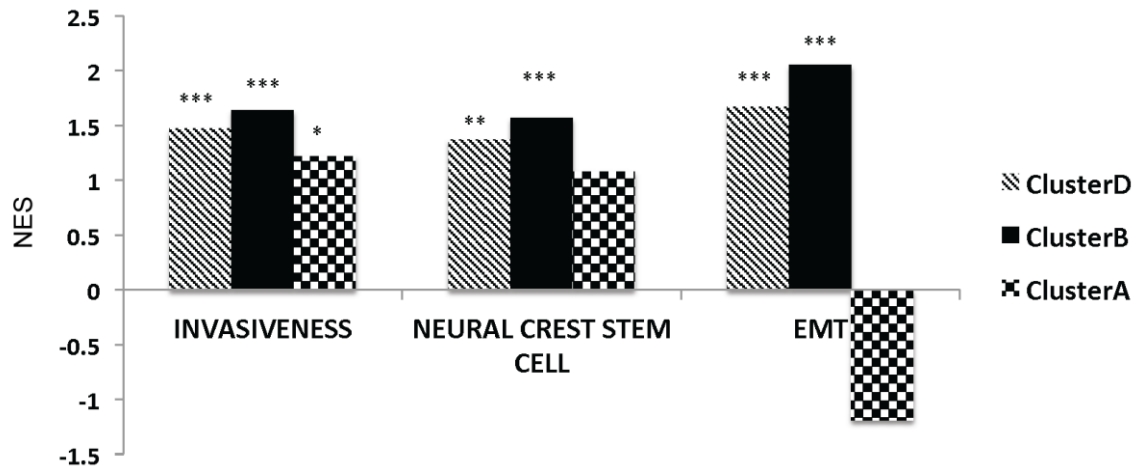


Fig. S8. GSEA shows enrichment of curated gene sets associated with the cell state regression towards neural-crest like and mesenchymal-like states upon 21 days vemurafenib exposure in other cell line clusters (NOM p values: * $p < 0.05$; ** $p < 0.005$, *** $p < 0.0005$).

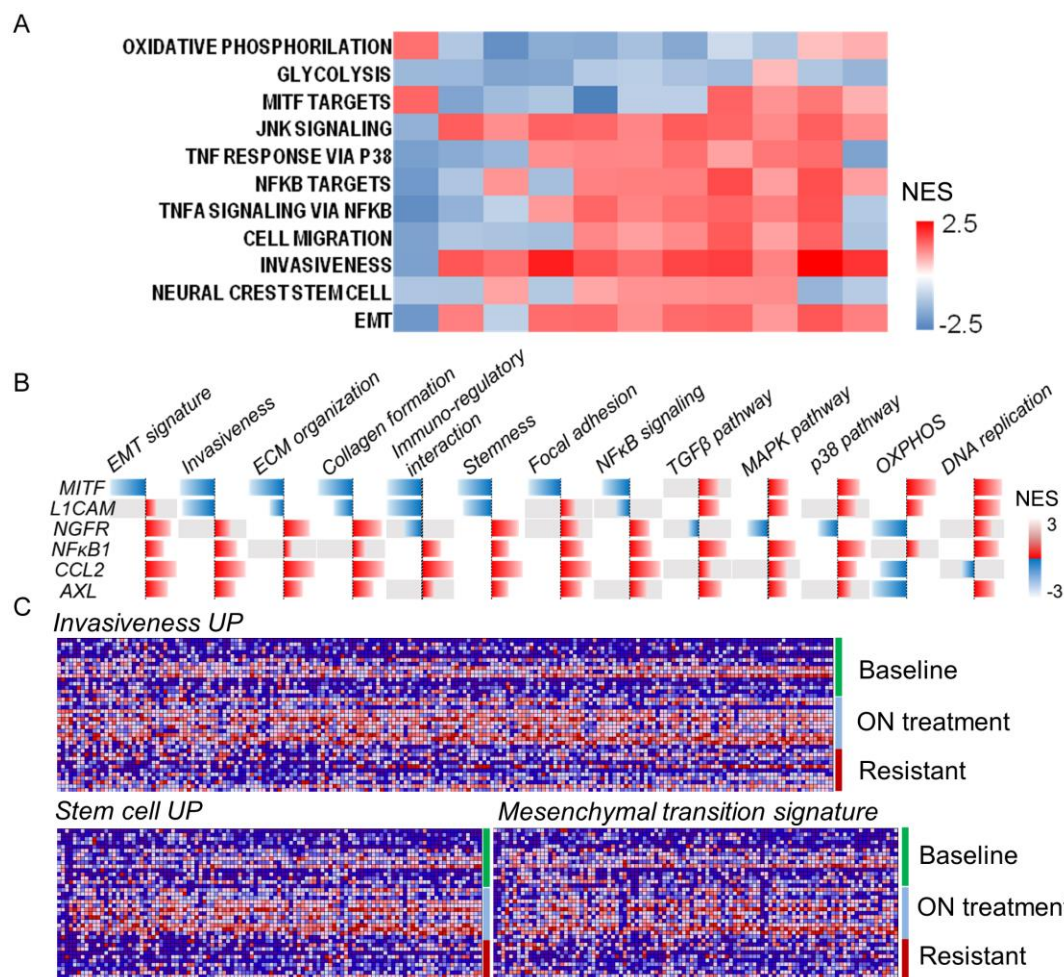


Fig. S9. Transcriptional signatures of the cell state transition associated with the adaptive resistance in melanoma patient biopsies (transcriptomes from ref. 16 in the main text). (A) Heat map of GSEA normalized enrichment scores (NES) of relevant curated gene sets involved in the adaptive transition for 11 paired pre-treatment and on-treatment patient biopsies. More than half of patient samples show acquisition of neural crest-like and mesenchymal phenotype signatures with up-regulated NFκB and JNK signaling as identified in the cell line studies. (B) Correlation of critical regulatory genes with relevant transcriptional signatures associated with the adaptive resistance across 39 melanoma patient biopsy samples. Genes involved in the ECM reprogramming, focal adhesion, collagen formation, stemness, EMT signatures were negatively correlated with *MITF* and positively correlated with *NGFR*, *NFκB*, *CCL2* and *AXL*. Gray shadow denotes an insignificant enrichment with a p value > 0.05. (C) Gene expression levels of patient samples at baseline (pre-treatment), on-treatment and resistant stages for three curated gene sets for invasiveness, stem cell and mesenchymal transition signatures. It revealed that the genes involved in cellular invasiveness, stem cell signature and EMT were consistently up-regulated at on-treatment stage and descending at acquired resistant stage, implying the existence of cellular

regression towards neural crest-like and mesenchymal-like phenotypes as a non-genomic adaptive response in these on-treatment patient biopsies prior to the disappearance of these signatures when cells acquired robust therapy resistance potentially genetically.

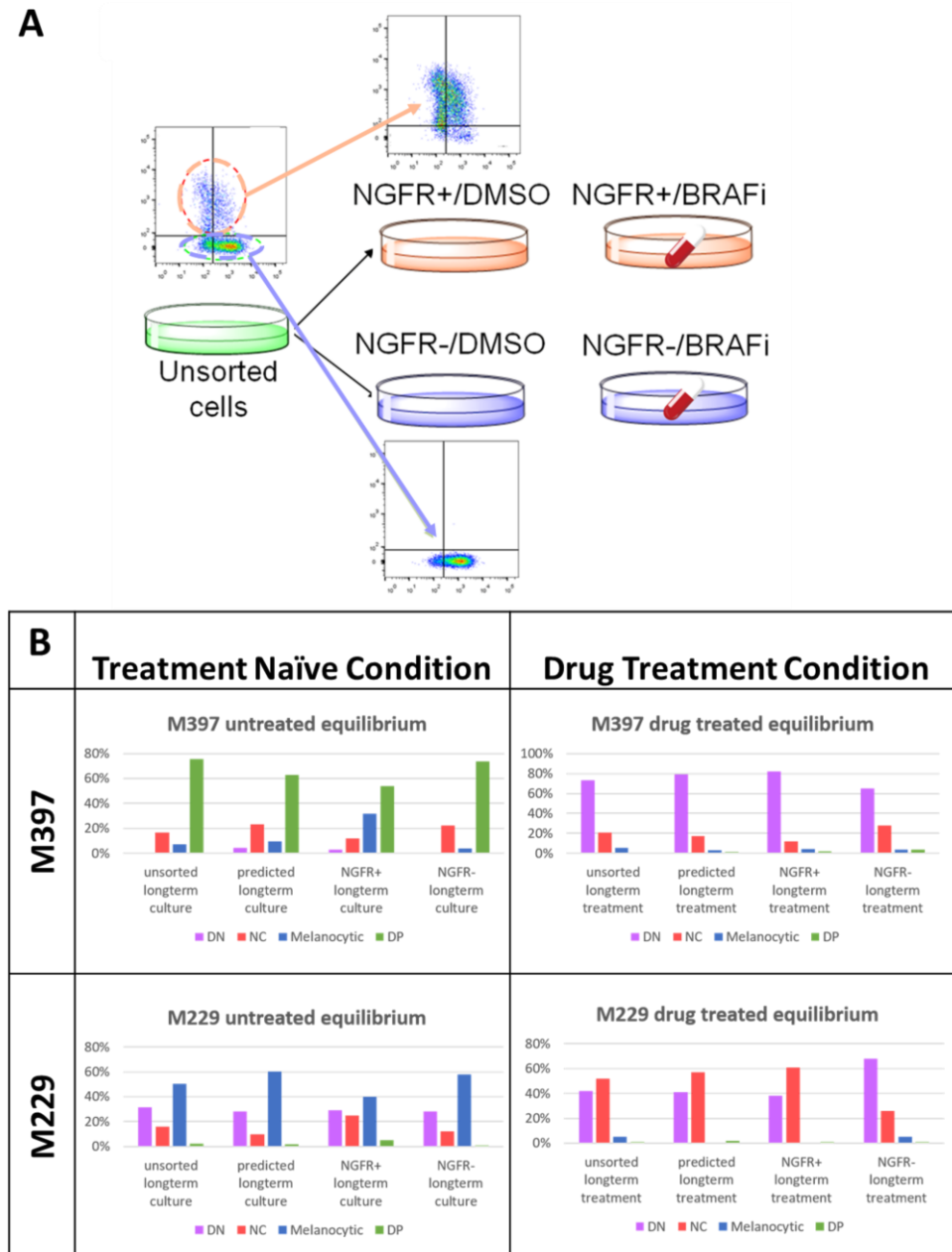


Fig. S10. The Markov model prediction and the experimental validation of cell state kinetics for segregated M229 and M397 cells. (A) Experimental flow for sorting cells to obtain NGFR+ and NGFR- subpopulations, and culturing each subpopulation in fresh growth media with or without BRAFi treatment. **(B)** For both M397 and M229 cell lines, unsorted cells or sorted NGFR+ or NGFR- subpopulations are cultured with or without drug,

and their phenotype composition are monitored using flow cytometry until they reach to an equilibrium composition. The final equilibrium composition from unsorted, NGFR^{+/-} subpopulations and model prediction are presented as bargraphs. DN – double negative mesenchymal-like state (NGFR⁻/MART-1⁻), NC – neural crest-like state (NGFR⁺/MART-1⁻), DP – double positive plastic state (NGFR⁺/MART-1⁺), melanocytic state (NGFR⁻/MART-1⁺).

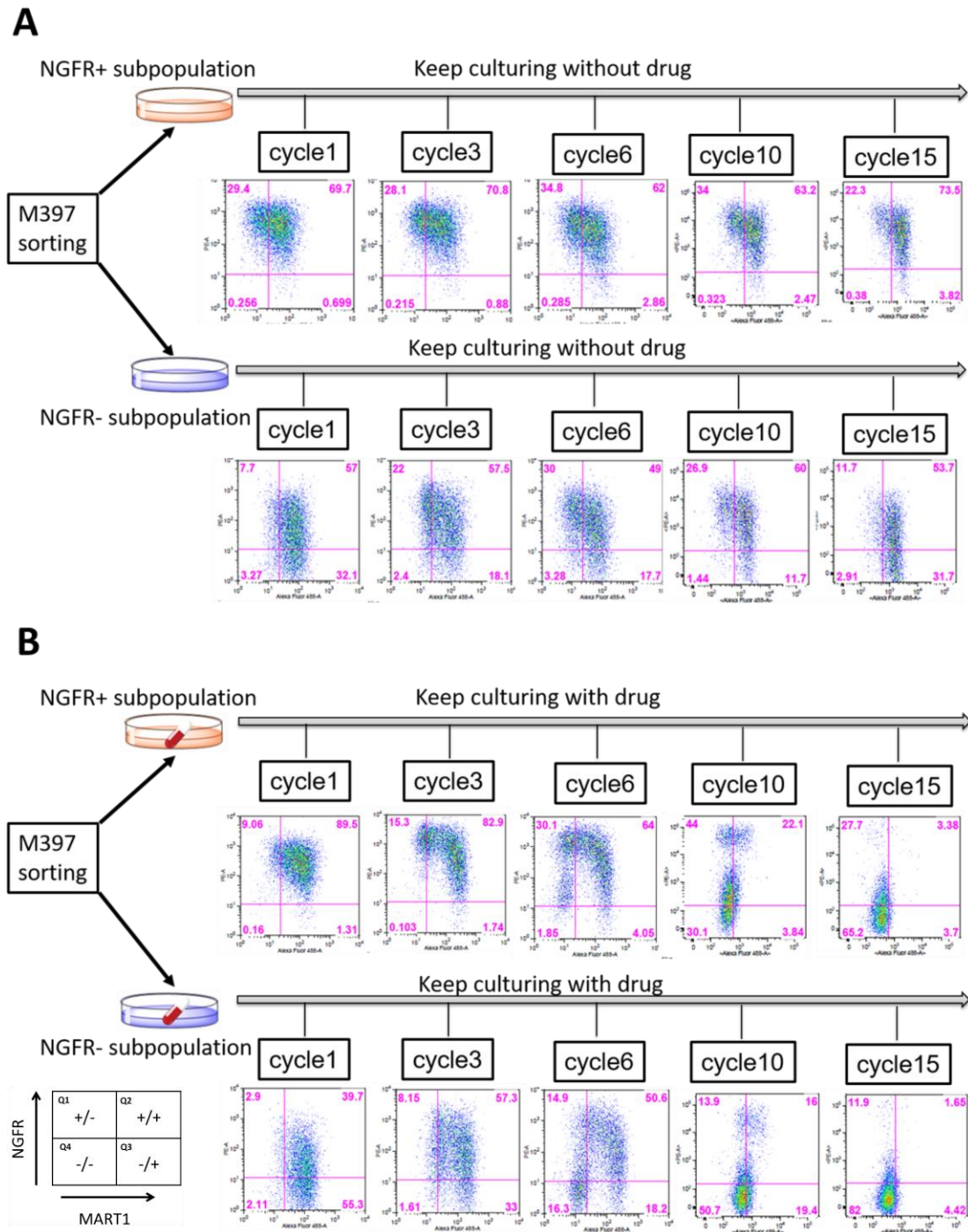


Fig. S11 Experiments setting and flow cytometry plots of sorted M397 NGFR+ and NGFR- subpopulations under treatment naïve and drug treatment conditions. Time-

series flow cytometry phenotyping of M397 sorted subpopulations cultured without BRAFi (A) and with BRAFi (B) treatment. The cell cycle for M397 is 3 days.

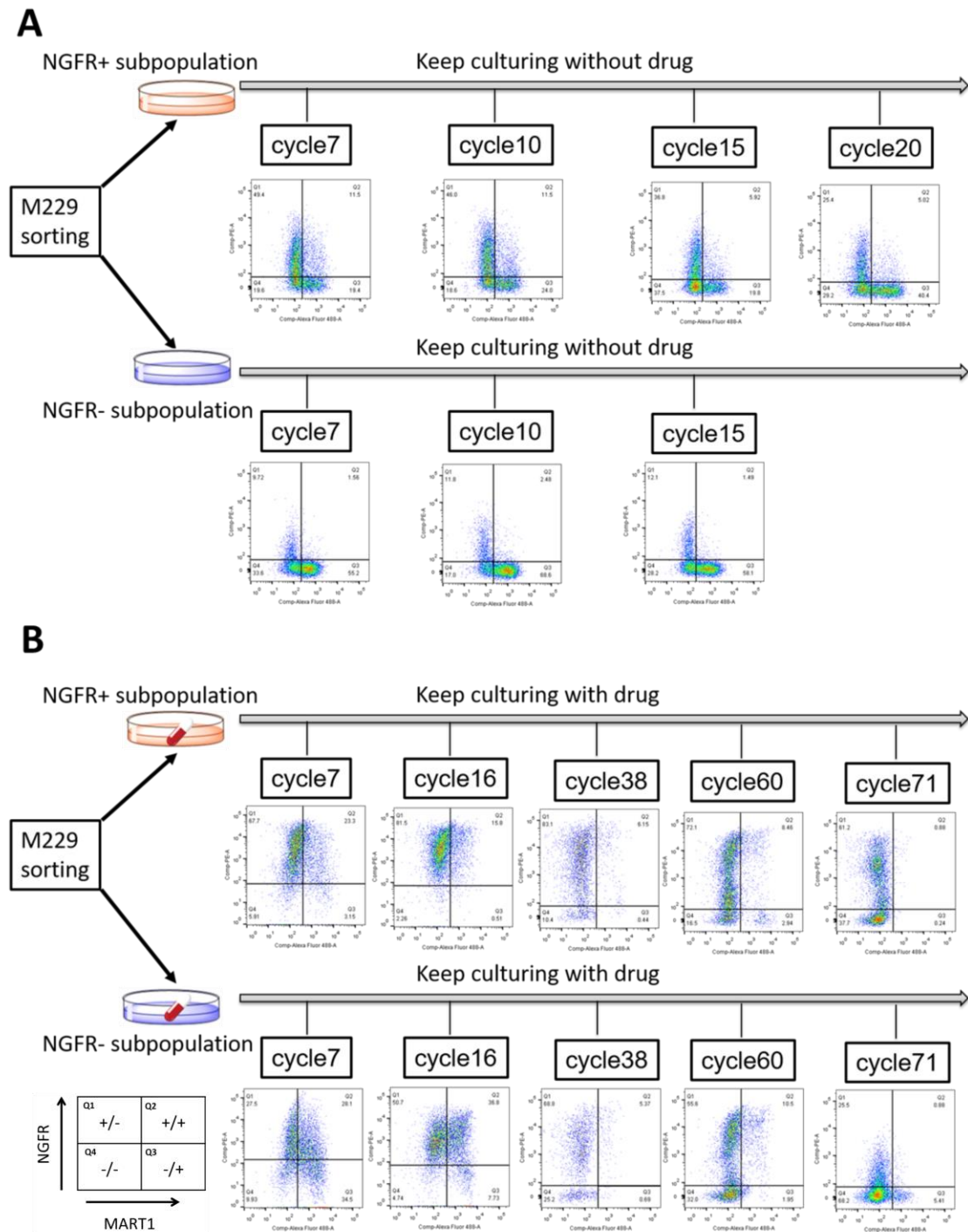


Fig. S12. Experiments setting and flow cytometry plots of sorted M229 NGFR+ and NGFR- subpopulations under treatment naïve and drug treatment conditions. Time-

series flow cytometry phenotyping of M229 sorted subpopulations cultured without BRAFi (A) and with BRAFi (B) treatment. The cell cycle for M229 is 1 day.

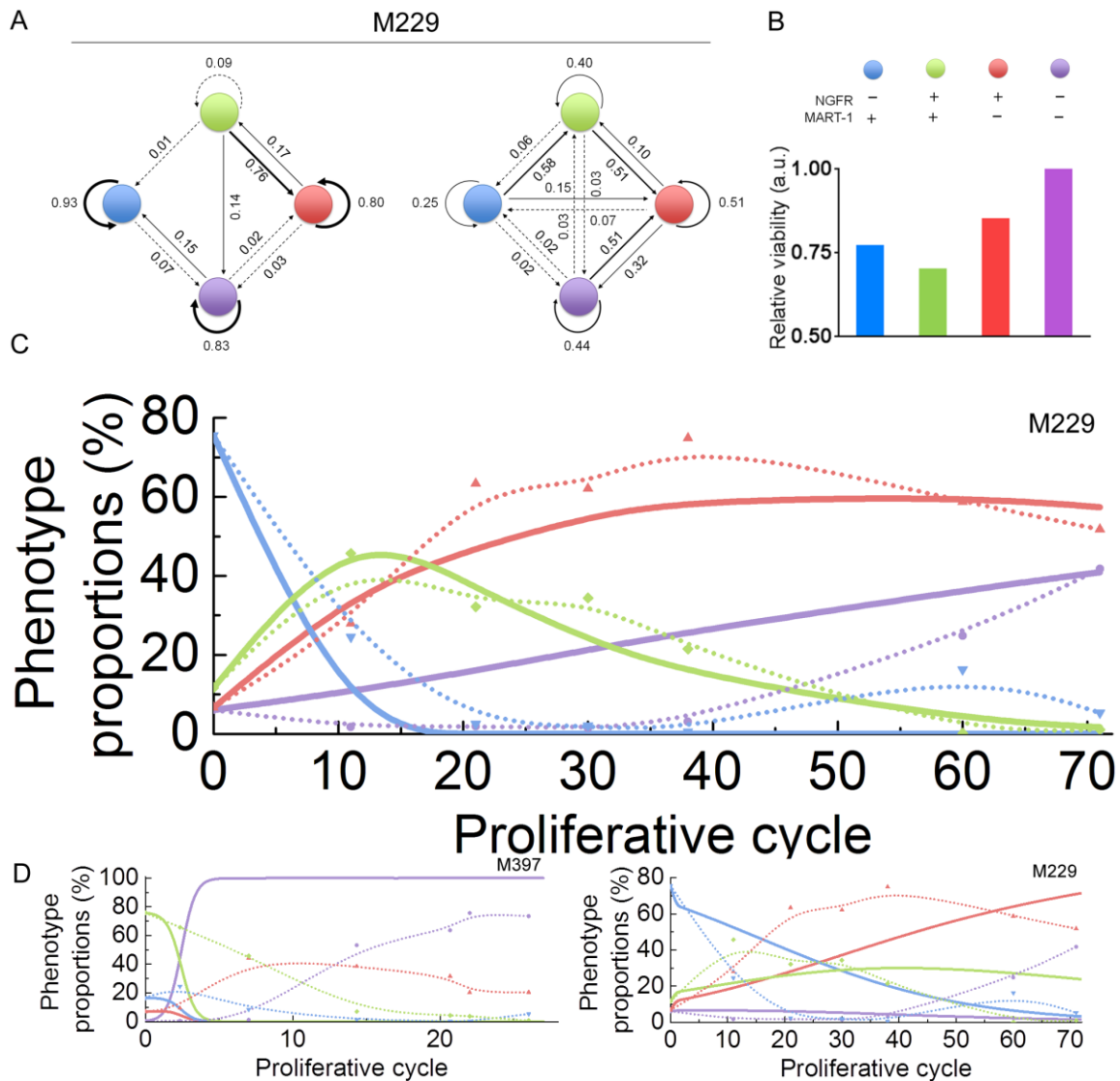


Fig. S13. Markov model of stochastic cell state transition predicts phenotypic evolution of melanoma cells upon BRAF inhibition. (A) Cell state transition probabilities of M229 at untreated and vemurafenib treated conditions. (B) Treatment sensitivity of different phenotypes for M229 inferred by the model. (C) Model prediction of the phenotypic kinetics (solid lines) versus experimental data (dots connected with dash lines) for M229 with continuous exposure to vemurafenib. (D) Model prediction of the phenotypic kinetics (solid lines) versus experimental data (dots connected with dash lines) for M397 and M229 when only drug selection is considered.

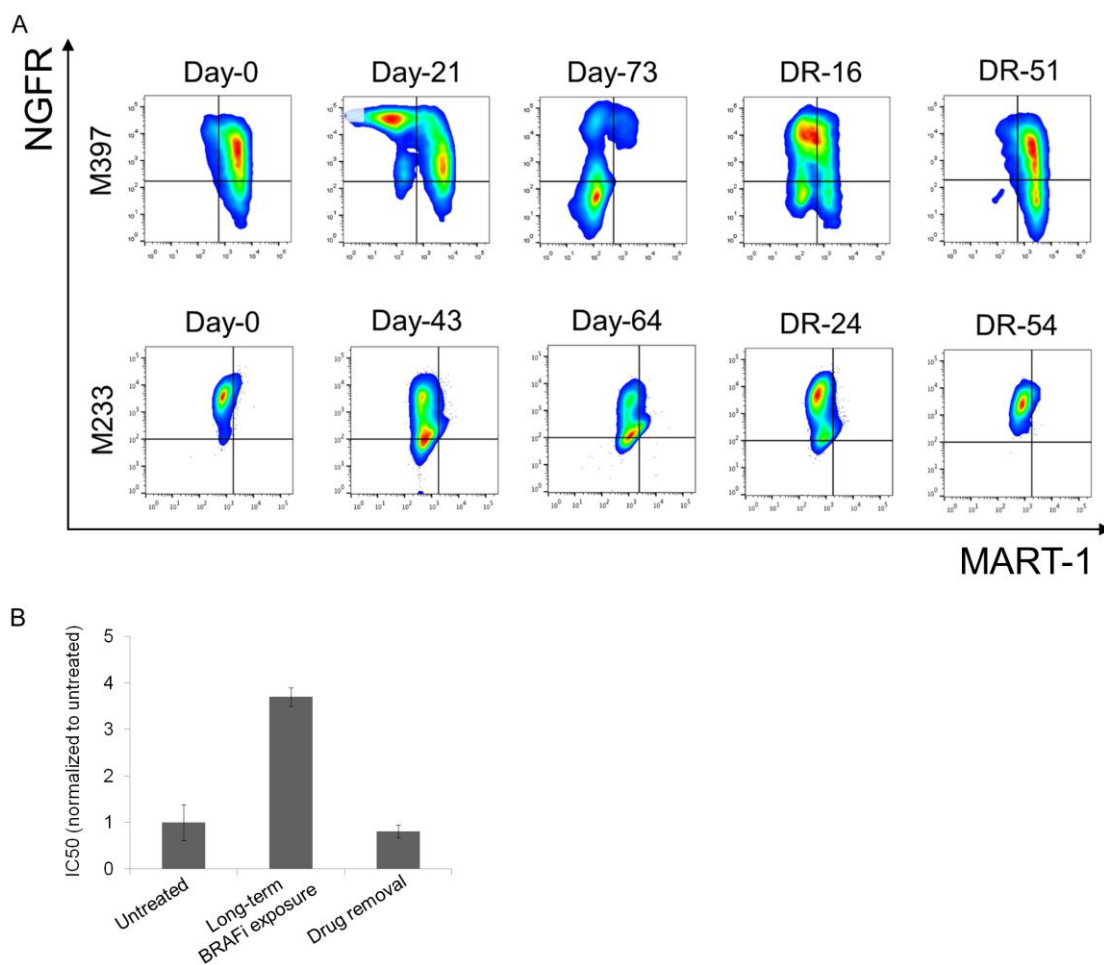


Fig. S14. Reversibility of the adaptive transition upon drug removal (A) Phenotypic reversibility for the plastic M397 cell line in Cluster C and less plastic M233 cell line in Cluster B. While starting at different baseline phenotypic composition, both M397 and M233 cell lines follow the transition trajectory towards double negative state (NGFR-/MART-1-) upon drug exposure and return to their original composition upon drug removal. DR: drug removal. (B) The IC50 values for M397 cells at untreated, upon long-term drug exposure (46 days), and after long-term drug removal (treatment discontinued for 33 days), confirming the reverted cells are re-sensitized to BRAF inhibition.

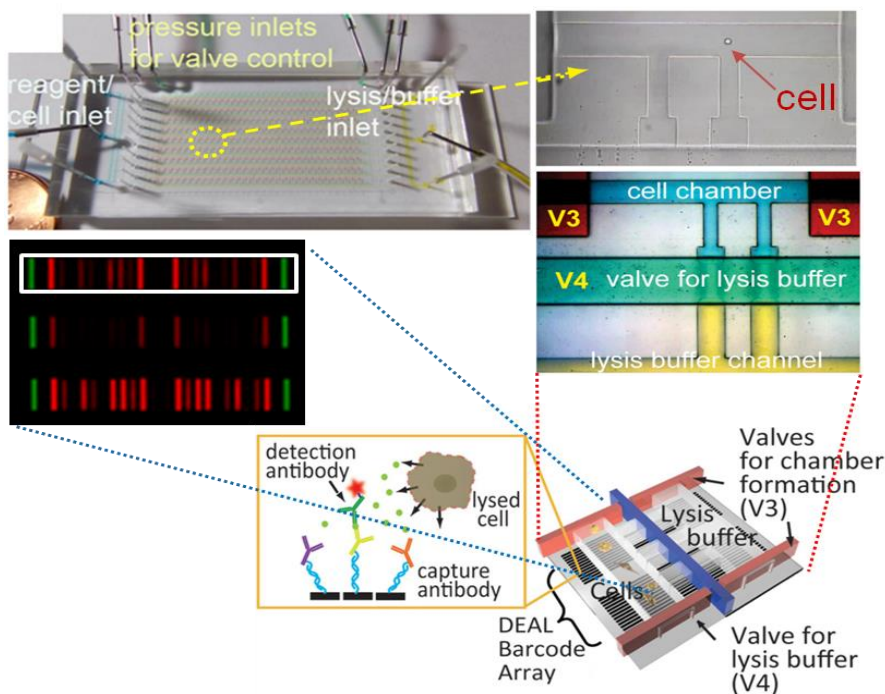


Fig. S15. The optical pictures of SCBC and its microchamber units: valves for chamber formation (red), valves for lysis buffer control (green), cell chamber compartment (blue), and lysis buffer reservoir (yellow) are delineated by food dyes. The sandwich immunofluorescence detection scheme with a scanned image is listed below the optical images. In the scanned image, the green stripes are used as alignment markers of a microchamber; each red stripe represents a functional protein measured and the fluorescence signal denotes the protein level from the single cells.

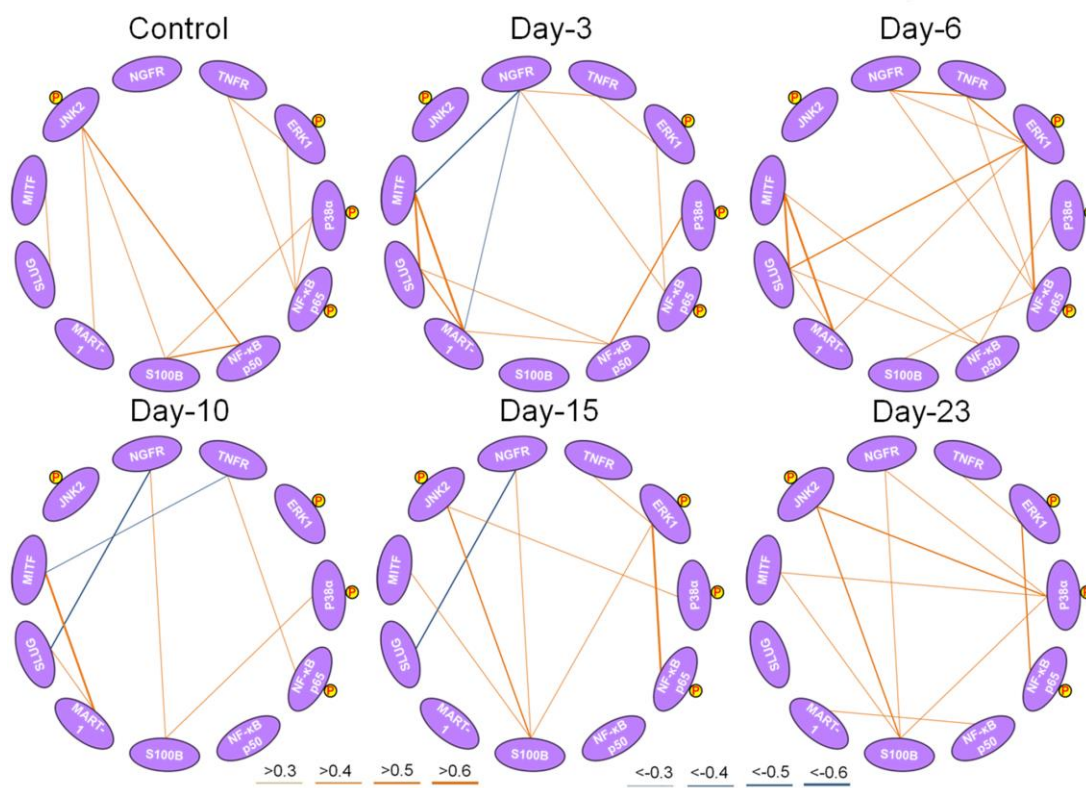


Fig. S16. Protein-protein correlation networks of M397 cells at different time points, extracted from SCBC data. The correlation (orange) / anti-correlation (blue) strength were reflected in the thickness of the edges (see keys).

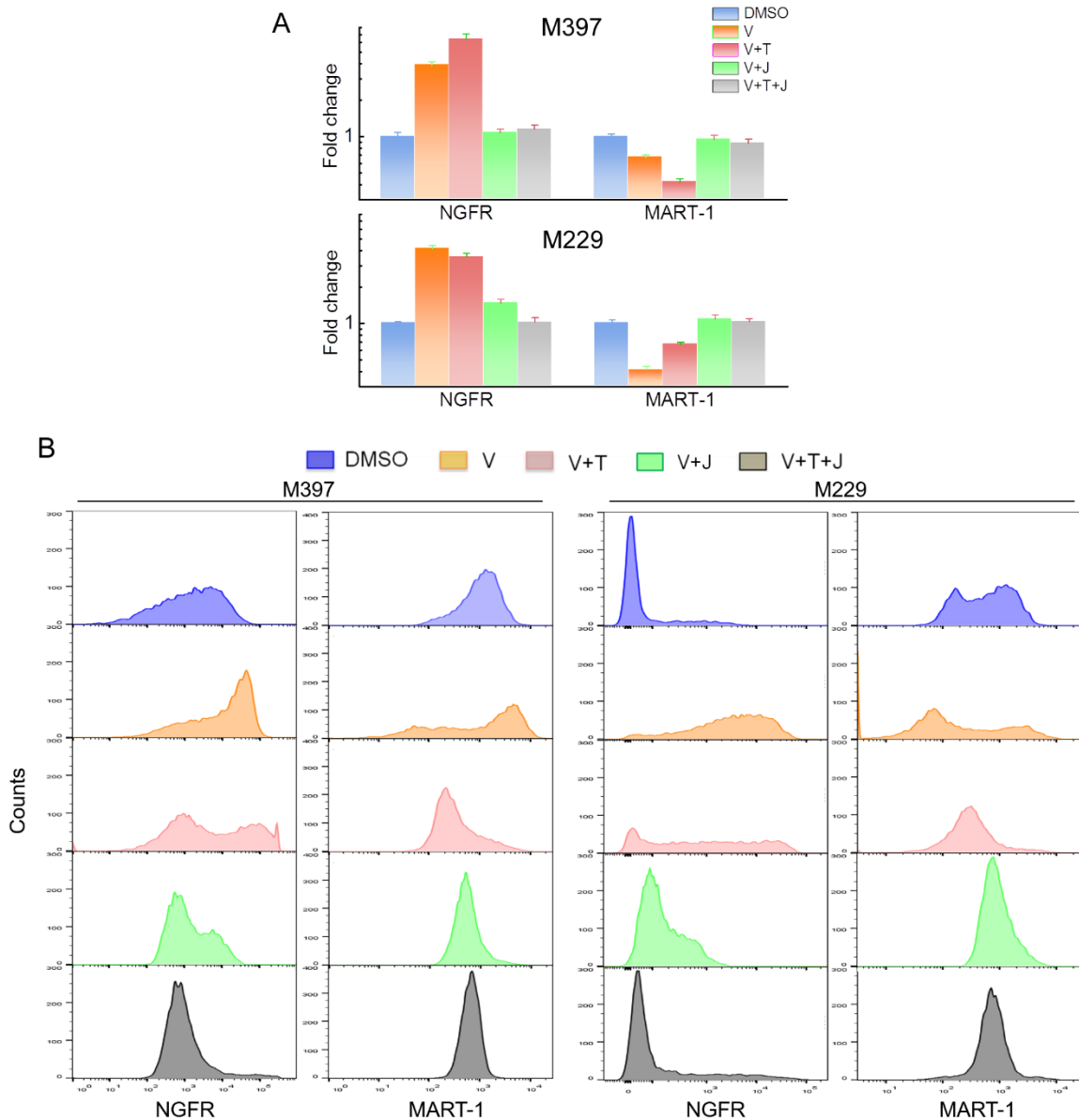


Fig. S17. Immunofluorescence and flow cytometry analyses of NGFR and MART-1 markers to BRAF inhibition. (A) Fold change of NGFR and MART-1 levels for mono- and combination therapies (23 days treatment) with respect to DMSO control on bulk M397 and M229 populations quantified by sandwich immunofluorescence assay. The predicted effective combinations (V+J and V+T+J) keep the MART-1 and NGFR levels unchanged, while V or V+T induces significant NGFR up-regulation and loss of MART-1 (error bars: \pm SD). (B) Cell phenotype marker histograms from flow cytometry analysis of MART-1 and NGFR levels for mono- and combination therapies on both M397 (23 days drug treatment) and M229 (28 days drug treatment).

	M229					M263					M397				
1	-9*	-15*	-22*	-3*	1*	22	5*	-1	2	4*	-2	-17*	-7	-8*	-2*
5	-9	-10*	-24*	-5*	2	6	-10	-6	-5	4*	-20	-21	-3	-7	-6
15	-5	-20*	-7*	-8*	-10*	8	-5	-4	-5	3*	-7	-7	0	5*	-16*
25	0	-13*	-13*	-12*	3	-8*	-15*	-12*	-3*	2*	-3*	-20*	5*	-11*	-31*
50	4	-12*	-9*	-12*	-14*	-4*	4	0	-1	0*	6*	-8*	-2*	-12*	-1
	0.1	0.2	1	2	10	0.1	0.2	1	2	10	0.05	0.1	0.5	1	5
	V+T (500:1) (μ M)					V+T (200:1) (μ M)					V+T (1000:1) (μ M)				

Fig. S18. Synergy effects of combining vemurafenib (V) and trametinib (T) with JSH-23 (J). Percentage of excess activity over that expected under the Bliss independence assumption for each of the various dose combinations. Red indicates synergy; blue indicates antagonism. The red boxes outline the concentration ranges used in the long-term clonogenic assays in Fig. 4. * $p < 0.05$ under Student's t-test.

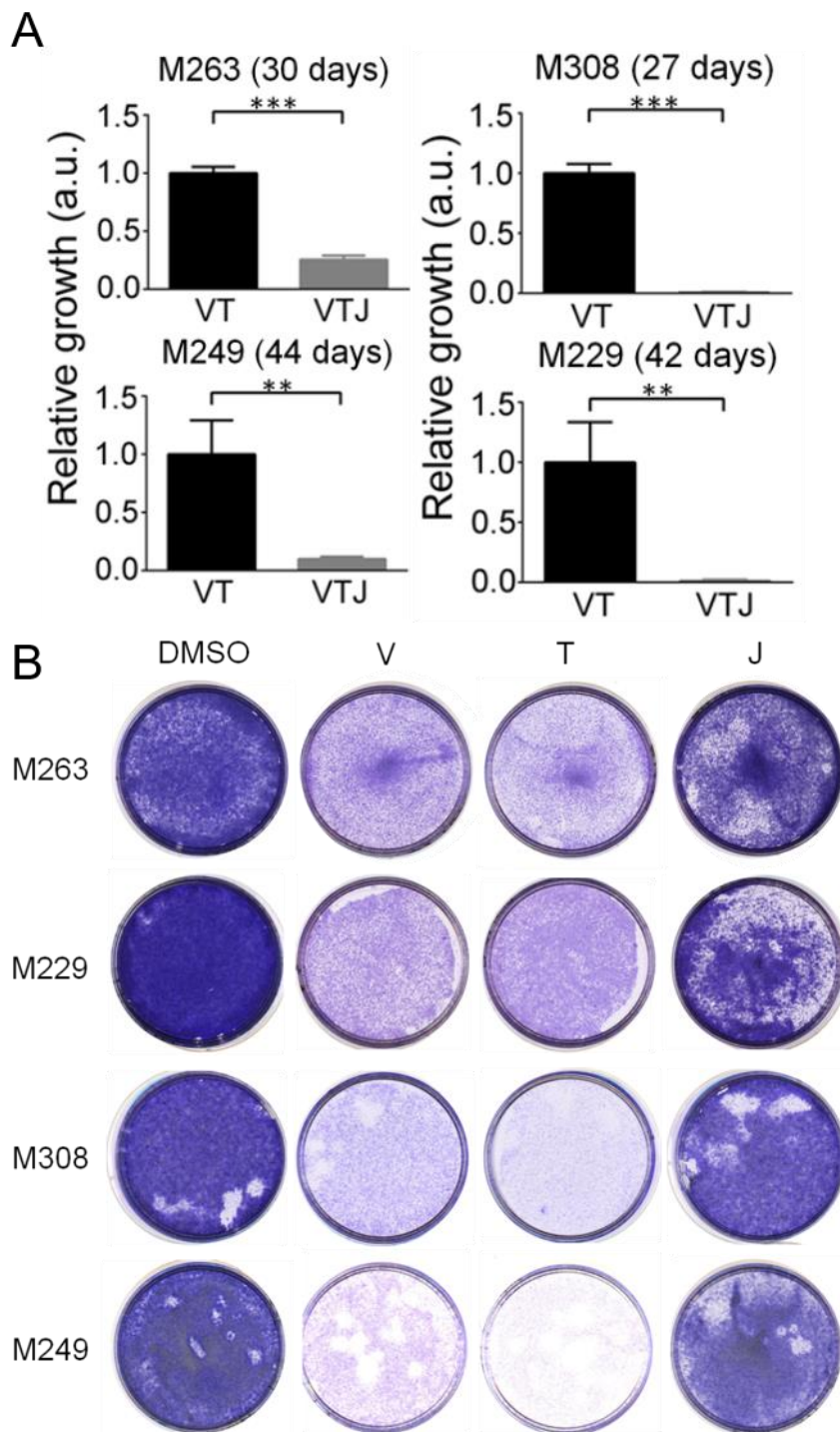


Fig. S19. Clonogenic assays for long-term combination therapy and short-term monotherapies in a cohort of melanoma cell lines. (A) Clonogenic assays of long-term drug treated samples were quantified using ImageJ software and normalized to V+T. The statistical significance is evaluated by Student's t-test. ** $p < 0.005$, *** $p < 0.0005$. Error bars:

\pm SD). (B) The same doses used in long-term combination treatments were used for monotherapies here. No significant toxicity to the cells was observed for using JSH-23 alone (treatment time: M263, 7 days; M229: 11 days; M308: 10 days; M249: 7 days).

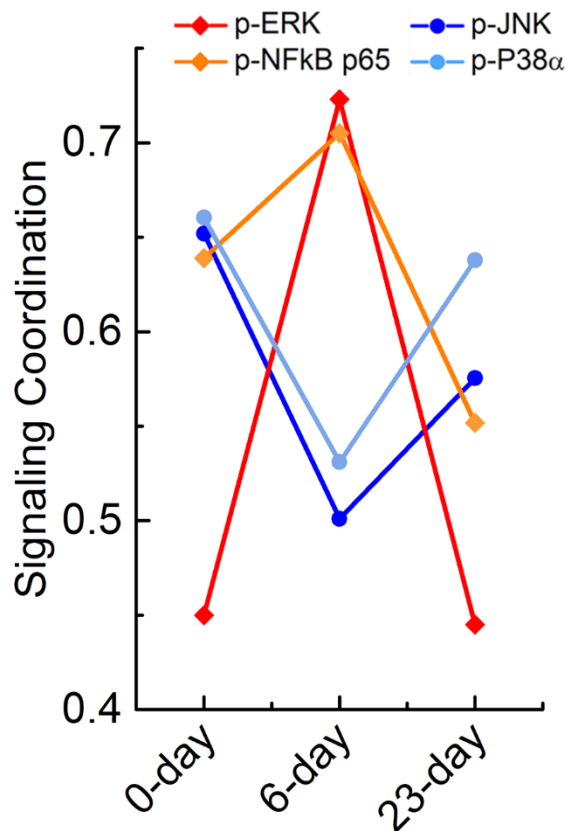


Fig. S20. Change in signaling coordination quantified as correlations between key functional proteins and the first principal component for control, day-6 (initiation of the adaptive transition), and day-23 (establishment of adaptive resistance). The up-regulation of JNK and p38 α signaling axes is identified when the cells develop adaptive resistance to BRAFi.

Supplementary Tables**Table S1. Characterization of 18 melanoma cell lines used in this study, where 9 randomly selected cell lines from each cluster for transcriptomic studies are shadowed in red.**

Cell line	Sensitivity	IC50 (nM)	Mutational Status	
M370	R	>10000	BRAFV600E mutant	Cluster A
M381	R	>10000	BRAFV600E mutant	
M410	R	3510	BRAFV600E mutant	
M233	R	>10000	BRAFV600E mutant 3 copies BRAF AKT1 amplification CCN31 amplification EGFR amplification CDKN2A deletion PTEN deletion	Cluster B
M238	S	243	BRAFV600E mutant 2 copies BRAF CDKN2A deletion PTEN deletion	
M255	I	1625	BRAFV600E mutant 2 copies BRAF AKT2 amplification CCND1 amplification EGFR amplification CDKN2A deletion	
M395	S	131	BRAFV600E mutant	
M406	S	645	BRAFV600E mutant	
M409	I	1018	BRAFV600E mutant	
M411	S	171	BRAFV600E mutant	
M229	S	282	BRAFV600E mutant 4 copies BRAF MITF amplification AKT1 amplification PTEN deletion	
M263	I	839	BRAFV600E mutant 2 copies BRAF CDKN2A deletion	Cluster C
M397	S	132	BRAFV600E mutant	
M399	I	1155	BRAFV600E mutant	
M403	S	450	BRAFV600E mutant	

M249	S	273	BRAFV600E mutant 3 copies BRAF MITF amplification AKT2 amplification PTEN deletion	Cluster D
M262	S	150	BRAFV600E mutant 2 copies BRAF AKT1 mutation& CDKN2A deletion	
M308	R	>10000	BRAFV600E mutant 3 copies BRAF MITF amplification AKT2 amplification EGFR amplification CDKN2A deletion	

Table S2. Color coded table comparing normalized median fluorescence intensity values for MART-1 and NGFR upon 3 days and 21 days of vemurafenib exposure with respect to DMSO control. The data are extracted from flow cytometry analysis (Fig. S2) across 18 cell lines. Fold changes are listed and color coded (red: increase, blue: decrease).

Cell lines	MART1		NGFR	
	Vem 3d	Vem 21d	Vem 3d	Vem 21d
M370	1.05	1.01	0.90	1.13
M381	0.89	1.07	1.04	1.56
M410	0.85	0.84	0.82	0.96
M233	0.94	0.66	1.05	7.20
M238	0.47	0.67	33.89	47.89
M255	0.29	1.13	1.51	2.07
M395	0.84	0.64	27.70	11.20
M406	0.87	0.87	2.04	4.85
M409	0.77	1.16	2.52	4.66
M411	0.70	0.77	5.98	26.00
M229	2.10	0.16	0.48	127.17
M263	2.15	2.25	7.38	6.10
M397	1.71	0.33	0.82	4.42
M399	5.04	2.79	4.04	1.54
M403	1.77	1.25	0.00	1.47
M249	1.61	1.88	0.05	1.82
M262	1.01	0.77	0.02	0.89
M308	0.89	0.60	6.50	27.03

Table S3. Complete chicken neural crest gene set list from Gallus Expression in situ Hybridization Analysis (GEISHA) (12).

Chick_neural_crest(GEISHA)		
AARS	HDAC2	PDGFD
ABCF2	HES1	PDGFRA
ACVR2B	HES5	PEBP1
ADAM12	HES6	PENK
ADAM33	HEY1	PGK1
ADAMTS1	HEY2	PITX2
ADAMTS3	HK2	PLEKHG1
AGR2	HNRNP	POU3F4
AHCYL1	HOXA3	PTK7
ALK	HOXB7	RAC1
ALX1	HS2ST1	RARA
ANGPTL4	HS3ST3A1	RARB
ANK3	HTRA1	RAR-GAMMA2
ANKRD6	ID2	RCC2
ANXA6	IPO9	RELT
AP2A2	IREB2	RERE
ARHGAP15	ISL1	RET
ARHGAP28	KDM4A	RHOB
ASCL1	KIF4A	RHOU
AUTS2	KLF10	RND3
B-G	KTN1	ROBO1
BLNK	LAMA5	ROBO2
BMP4	LECT1	RSPO3
BMP7	LFNG	RXRA
BMPER	LGR4	SALL4
BTBD11	LIMS1	SEMA3D
BTG2	LMNB2	SEMA7A
CADM3	LMO4	SIX1
CDH11	LOC100858038	SIX4
CDH6	LOC420041	SLC7A3
CRABP1	LZTS1	SLIT1
CXCL14	MAFA	SMO
CXCR4	MAFB	SNAI1
CYP26C1	MAFK	SNAI2
DACH1	MAP3K5	SOX10
DACT2	MATN4	SOX2
DAD1	MCAM	SOX8
DKC1	MECOM	SOX9
DLL1	MEF2C	SPRY2
DLL4	MKRN1	SREBF2
DLX3	MMP2	STOX1
DLX5	MOXD1	TBX1
DRGX	MSX1	TBX3
DSC2	MSX2	TCF3
DSG2	MXI1	TFAP2A
EBF2	MYC	TIAM1
EDNRB	MYCN	TIAM2
EFNB2	NCOA1	TIMP2
EGR4	NES	TPD52L2
ELK3	NET1	TRIO
ENAH	NEUROD4	TSHZ2
EPCAM	NEUROG1	VSX1
ETS1	NHLH1	WIF1
EYA2	NKX2-5	WNT-1
FGF13	NOG	WNT16
FGF3	NOLC1	WNT8A
FGFR2	NR6A1	ZEB2
FGFR3	NRP2	ZIC1
FLT4	OLFM1	ZRANB1
FOXD3	OSBP2	
FRZB	PALLD	
FZD1	PAX3	
GATA1	PAX7	
GFRA2	PCDH15	
GLG1	PCDH18	
GTF2E2	PCDH8	

Table S4. GSEA enrichment across innate anti-PD-1 resistance (IPRES) signature at 3 days and 21 days of BRAFi exposure using averaged gene expression levels of the 3 plastic cell lines. NES stands for normalized enrichment score.

IPRES (M229_M263_M397)	3days			21 days			73days		
	NES	p-value	q-value	NES	p-value	q-value	NES	p-value	q-value
ANASTASSIOU_CANCER_MESENCHYMAL_TRANSITION_SIGNATURE	1.66	0	0.056	2.18	0.0001	0.0001	2.37	0.0001	0.0001
VECCHI_GASTRIC_CANCER_ADVANCED_VS_EARLY_UP	1.22	0.072	0.368	1.8	0.0001	0.002	1.73	0.0001	0.01
MAPKi_INDUCED_EMT	-1.1	0.301	0.301	1.61	0.003	0.003	1.93	0.0001	0.0001
LU_TUMOR_ENDOTHELIAL_MARKERS_UP	-1.36	0.097	0.17	0.99	0.471	0.626	1.33	0.102	0.214
LU_TUMOR_VASCULATURE_UP	-1.01	0.43	0.637	1	0.465	0.615	1.35	0.076	0.193
ROY_WOUND_BLOOD_VESSEL_UP	1.17	0.189	0.431	1.78	0.0001	0.003	1.98	0.0001	0.0001
post_op_woundhealing	-1.38	0.01	0.01	1.34	0.028	0.028	1.82	0.0001	0.0001
lef1_up.v1_up	-1.1	0.203	0.371	1.6	0.0001	0.005	1.53	0.001	0.019
MAPKi_INDUCED_ANGIOGENESIS	1.1	0.308	0.308	1.79	0.0001	0.0001	1.97	0.0001	0.0001
EP_BLOOD_VESS_DEVEL_DN_IN_R	-0.84	0.737	0.737	1.64	0.006	0.006	1.85	0.002	0.002
MISHRA_CARCINOMA_ASSOCIATED_FIBROBLAST_UP	-1.04	0.405	0.597	1.59	0.01	0.03	1.67	0.007	0.021
LIEN_BREAST_CARCINOMA_METAPLASTIC	1.19	0.18	0.392	1.76	0.0001	0.004	1.88	0.0001	0.001
CHARAFE_BREAST_CANCER_BASAL_VS_MESENCHYMAL_UP	-0.91	0.652	0.78	0.89	0.715	0.786	-1.18	0.111	0.399
MAHADEVAN_GIST_MORPHOLOGICAL_SWITCH	1.64	0.004	0.057	1.55	0.021	0.045	1.77	0.0001	0.006
WESTON_VEGFA_TARGETS_6HR	1.42	0.024	0.21	1.86	0.0001	0.001	2.07	0.0001	0.0001
WESTON_VEGFA_TARGETS_12HR	1.76	0.0001	0.021	1.91	0.0001	0.0001	2.01	0.0001	0.0001
MS_RESP_TO_WOUNDING_UP_IN_MAPKi_aPDL1_NR	-1.53	0.004	0.004	1.1	0.304	0.304	1.41	0.042	0.042
POOLA_INVASIVE_BREAST_CANCER_UP	-2.04	0.0001	0.0001	-1.17	0.058	0.402	1.3	0.02	0.238
YE_METASTATIC_LIVER_CANCER	-1.17	0.219	0.391	-1	0.419	0.658	0.85	0.687	0.856
KARAKAS_TGFB1_SIGNALING	-0.92	0.579	0.772	1.19	0.208	0.327	1.3	0.134	0.237
JAEGER_METASTASIS_DN	1.23	0.047	0.351	1.83	0.0001	0.001	1.58	0.0001	0.049
MS_RESP_TO_HYPOXIA_UP_IN_MAPKi_aPDL1_NR	-0.94	0.541	0.541	1.45	0.033	0.033	1.53	0.027	0.027
LU_TUMOR_ANGIOGENESIS_UP	-0.78	0.803	0.938	1.2	0.2	0.311	1.14	0.257	0.436
MAINA_VHL_TARGETS_DN	-0.87	0.668	0.839	1.26	0.183	0.251	1.49	0.032	0.088
HARRIS_HYPOXIA	-1.04	0.363	0.591	1.62	0.0001	0.023	2.01	0.0001	0.0001
JEON_SMAD6_TARGETS_UP	1.74	0.0001	0.026	1.79	0.0001	0.002	1.68	0.003	0.018

Table S5. Cell state composition measured by flow cytometry across time, while being with or without BRAF inhibition. DN – double negative mesenchymal-like state (NGFR-/MART-1-), NC – neural crest-like state (NGFR+/MART-1-), DP – double positive plastic state (NGFR+/MART-1+), melanocytic state (NGFR-/MART-1+).

		NGFR+					NGFR-				
		Cycle	DN	NC	Melanocytic	DP	Cycle	DN	NC	Melanocytic	DP
M397	treatment naïve condition	0	0.0%	2.4%	0.0%	97.6%	0	0.5%	0.0%	99.5%	0.0%
		1	0.3%	29.4%	0.7%	69.7%	1	3.3%	7.7%	32.1%	57.0%
		3	0.2%	28.1%	0.9%	70.8%	3	2.4%	22.0%	18.1%	57.5%
		6	0.3%	34.8%	2.9%	62.0%	6	3.3%	30.0%	17.7%	49.0%
		10	0.3%	34.0%	2.5%	63.2%	10	1.4%	26.9%	11.7%	60.0%
		15	0.4%	22.3%	3.8%	73.5%	15	2.9%	11.7%	31.7%	53.7%
	drug treatment condition	0	0.0%	2.4%	0.0%	97.6%	0	0.5%	0.0%	99.5%	0.0%
		1	0.2%	9.1%	1.3%	89.6%	1	2.1%	2.9%	55.3%	39.7%
		3	0.1%	15.3%	1.7%	82.9%	3	1.6%	8.2%	33.0%	57.3%
		6	0.2%	30.1%	4.1%	64.0%	6	16.3%	14.9%	18.2%	50.6%
		10	30.1%	44.0%	3.8%	22.1%	10	50.7%	13.9%	19.4%	16.0%
		15	65.2%	27.7%	3.7%	3.4%	15	82.0%	11.9%	4.4%	1.7%
M229	treatment naïve condition	0	0%	59%	0%	41%	0	39%	0%	61%	0%
		7	20%	49%	19%	12%	7	34%	10%	55%	2%
		10	19%	46%	24%	12%	10	17%	12%	69%	2%
		15	38%	37%	20%	6%	15	28%	12%	58%	1%
		20	29%	25%	40%	5%					
	drug treatment condition	7	6%	68%	3%	23%	7	10%	27%	35%	28%
		16	2%	82%	1%	16%	16	5%	51%	8%	37%
		38	10%	83%	0%	6%	38	25%	69%	1%	5%
		60	17%	72%	3%	8%	60	32%	56%	2%	11%
		71	38%	61%	0%	1%	71	68%	26%	5%	1%

Table S6. Phenotype proportion for M397 and M229 unsorted cells under drug treatment condition.

	Cell Line	Cycle	DN	NC	Melanocytic	DP
M397		0	0%	7%	17%	76%
		2.3	0%	9%	25%	66%
		7	1%	44%	8%	46%
		14.3	53%	39%	1%	7%
		20.6	64%	32%	0%	4%
		22	76%	20%	0%	4%
		26	74%	21%	5%	1%
M229		0	6%	7%	76%	12%
		11	2%	28%	25%	46%
		21	2%	63%	2%	32%
		30	1%	62%	2%	34%
		38	3%	75%	1%	22%
		60	25%	59%	16%	0%
		71	42%	52%	5%	1%

Table S7. The sequences of the oligonucleotides used in the protein immunoassays. All oligonucleotides were synthesized by Integrated DNA Technology (IDT) and purified via high performance liquid chromatography (HPLC). The DNA coding oligomers were pre-tested for orthogonality to ensure that cross-hybridization between non-complementary oligomer strands was negligible (<1% in photon counts).

	DNA sequence used for patterning ssDNA microarray
A	5'-AAAAAAAAAAAAAAAAATCCTGGAGCTAAGTCCGTA-3'
B	5'-AAAAAAAAAAAAAAAAAGCCTCATTGAATCATGCCTA-3'
C	5'-AAAAAAAAAAAAAAAAAGCACTCGTCTACTATCGCTA-3'
D	5'-AAAAAAAAAAAAAAAAATGGTCGAGATGTCAGAGTA-3'
E	5'-AAAAAAAAAAAAAAAAATGTGAAGTGGCAGTATCTA-3'
F	5'-AAAAAAAAAAAAAAAAATCAGGTAAGGTTACGGTA-3'
G	5'-AAAAAAAAAAAAAAAAAGAGTAGCCTTCCCGAGCATT-3'
H	5'-AAAAAAAAAAAAAAAAATTGACCAAAGTGGTGGCG-3'
I	5'-AAAAAAAAAAAAAAAAATGCCCTATTGTTGCGTCGGA-3'
K	5'-AAAAAAAAAAAAAAAAATAATCTAATTCTGGTCGCGG-3'
L	5'-AAAAAAAAAAAAAAAAAGTGATTAAGTCTGCTTCGGC-3'
M	5'-AAAAAAAAAAAAAAAAAGTCGAGGATTCTGAACCTGT-3'
N	5'-AAAAAAAAAAAAAAAAAGTCCTCGCTTCGTCTATGAG-3'
	Complementary ssDNA Sequence for antibody conjugation
A'	5'NH3-AAAAAAAAAAAAAAAAATACGGACTTAGCTCCAGGAT-3'
B'	5'NH3-AAAAAAAAAAAAAAAAATAGGCATGATTCAATGAGGC-3'
C'	5'NH3-AAAAAAAAAAAAAAAAATAGCGATAGTAGACGAGTGC-3'
D'	5'NH3-AAAAAAAAAAAAAAAAATACTCTGACATCTCGACCAT-3'
E'	5'NH3-AAAAAAAAAAAAAAAAATAGATACTGCCACTTCACAT-3'
F'	5'NH3-AAAAAAAAAAAAAAAAATACCGTGAACCTTACCTGAT-3'
G'	5'NH3-AAAAAAAAAAAAAAAAATGCTCGGGAAGGCTACTC-3'
H'	5'NH3-AAAAAAAAAAAAAAAAACGCACCGCAGTTTGGTCAAT-3'
I'	5'NH3-AAAAAAAAAAAAAAAAATCCGACGCAACAATAGGGCA-3'
J'	5'NH3-AAAAAAAAAAAAAAAAACCTGCTCGACAACACTAGAAGA-3'
K'	5'NH3-AAAAAAAAAAAAAAAAACCGCGACCAGAATTAGATTA-3'
L'	5'NH3-AAAAAAAAAAAAAAAAAGCCGAAGCAGACTTAATCAC-3'
M'	5'Cy3-AAAAAAAAAAAAAAAAACAGGTTCAGAATCCTCGAC-3'
N'	5'NH3-AAAAAAAAAAAAAAAAACTCATAGACGAAGCGAGGAC-3'

Table S8. List of antibodies used for the SCBC multiplex protein assays.

Antibody	Manufacture
Human NGFR DuoSet	R&D DY367
Human sTNF DuoSet	R&D DY225
Human S100B Mab Mouse IgG2A	R&D MAB1820
S100B Rabbit mAb	Cell Signaling 9550
Melan-A Monoclonal	Sigma-Aldrich M6570
Human Melan-A/MART-1 Sheep IgG	R&D AF8008
Human Phospho-JNK2 DuoSet	R&D DYC2236
Human MITF Goat IgG	R&D AF5769
MITF	abcam ab80651
Human/Mouse/Rat Phospho-ERK1	R&D DYC1825
Human NFκB1 Mouse IgG	R&D MAB2697
NFκB1 p105/p50	Cell Signaling 3035
Human/Mouse NFκB p65 Mouse IgG2B	R&D MAB5078
Phospho-NFκB p65 Rabbit mAb	Cell Signaling 4025
Phospho-IκB alpha (Ser32) ELISA Kit	Cell Signaling 7343
Phospho-p38 alpha DuoSet	R&D DYC869B
Slug (SNAI2) mouse IgG	Sigma-Aldrich SAB1412527
Slug Rabbit mAb	Cell Signaling 9585

Dataset S1. Kinetic RNA-seq data of the 9 randomly selected melanoma cell lines.
(See “Dataset_S01 (XLSX)” from
<https://www.pnas.org/content/suppl/2017/12/06/1712064115.DCSupplemental>).

PHENOTYPIC HETEROGENEITY AND EVOLUTION OF MELANOMA CELLS ASSOCIATED WITH TARGETED THERAPY RESISTANCE

Phenotypic plasticity is associated with non-genetic drug tolerance in several cancers. Such plasticity can arise from chromatin remodeling, transcriptomic reprogramming, and/or protein signaling rewiring, and is characterized as a cell state transition in response to molecular or physical perturbations. This, in turn, can confound interpretations of drug responses and resistance development. Using BRAF-mutant melanoma cell lines as the prototype, we report on a joint theoretical and experimental investigation of the cell-state transition dynamics associated with BRAF inhibitor drug tolerance. Thermodynamically motivated surprisal analysis of transcriptome data was used to treat the cell population as an entropy maximizing system under the influence of time-dependent constraints. This permits the extraction of an epigenetic potential landscape for drug-induced phenotypic evolution. Single-cell flow cytometry data of the same system were modeled with a modified Fokker-Planck-type kinetic model. The two approaches yield a consistent picture that accounts for the phenotypic heterogeneity observed over the course of drug tolerance development. The results reveal that, in certain plastic cancers, the population heterogeneity and evolution of cell phenotypes may be understood by accounting for the competing interactions of the epigenetic potential landscape and state-dependent cell proliferation. Accounting for such competition permits accurate, experimentally verifiable predictions that can potentially guide the design of effective treatment strategies.

This chapter includes content from our previously published article:

- [1] Su, Yapeng, Marcus Bintz, Yezi Yang, Lidia Robert, Alphonsus HC Ng, Victoria Liu, Antoni Ribas, James R. Heath, and Wei Wei. "Phenotypic heterogeneity and evolution of melanoma cells associated with targeted therapy resistance." *PLoS computational biology* 15, no. 6 (2019): e1007034. doi: 10.1371/journal.pcbi.1007034.

Introduction

The phenotypic plasticity of many tumors can confound the identification of effective therapeutic strategies [1-4]. For such tumors, even if the cancer cells are isogenic, the cellular composition can be a heterogeneous mix of different cell states (phenotypes) that exhibit the capacity for dynamic interconversion. Each phenotype can have a characteristic gene expression profile, drug susceptibility, proliferation rate, and metastatic potential [5]. When this heterogeneous population is challenged with a physical or molecular perturbation, the cell states can rapidly evolve [6] to form a new population distribution better suited to survive the challenge. This adaptation may proceed without genetic changes [7-9]. Removal of the challenge can lead to recovery of the original population distribution [5, 10, 11]. This behavior bears similarities to that of ‘phenotypic equilibria’ [1, 12, 13]. In those systems, if a subset of this population of microstates is physically separated from a stable, heterogeneous population and allowed to expand in culture, the phenotypic heterogeneity of the original culture will recover. This facile adaptability makes plastic tumors challenging to drug-target, and it highlights the importance of quantitative models that can provide predictive and mechanistic insights into the underlying driving force controlling such behaviors.

Similarities between steady states in nonequilibrium biological systems and perturbation/relaxation scenarios in classical thermodynamics equilibria have prompted investigations into applying physicochemical models for describing phenotype dynamics within an epigenetic landscape [13-16]. Qualitative descriptive models have been explored for many years, but quantitative and predictive models have only been recently explored [14-20]. In one class of studies, epigenetic landscape models are explored, wherein stable cell states are described as local minima (attractors) within a metaphoric energy (or potential) cell-state landscape. In such models, the driving forces that influence the cellular composition and population dynamics are the gradients on that surface. As a result, cells tend to gravitate and remain in the local minima of such landscapes. However, in many other cases, this potential landscape does not predict the observed phenotypic heterogeneity [16], implicating other important factors that can influence the population dynamics are at play.

To address this puzzle, we studied highly plastic patient-derived *BRAF*^{V600E} mutant melanoma cell lines as models of cancer cell phenotypic plasticity. The high rate of both response [21] and resistance development [10] of *BRAF*-mutant melanoma patients to BRAF inhibitor (BRAFi) treatment has made such cell lines important models for understanding challenges associated with targeted inhibitors [9, 10]. BRAFi can trigger a series of nongenetic cell state changes along the melanocytic lineage towards drug-tolerant and eventually drug resistant states through epigenetic reprogramming. These include the

transition of drug-sensitive melanocytic cancer cells into a drug-tolerant neural crest-like phenotype, which, under continued BRAF inhibition, can eventually transition into a fully drug-resistant, invasive mesenchymal-like phenotype [5, 9-11]. The cell biology of this BRAFi-induced phenotypic evolution has been extensively characterized [5, 22], and shown to correlate with what is observed in patient biopsies [9-11, 22]. However, a quantitative biophysical understanding of this type of epigenetic plasticity has not been fully explored.

To this end, we carried out two sets of experiments, integrated with two theoretic approaches, on phenotypically plastic $BRAF^{V600E}$ mutant melanoma cell lines. At the macroscopic level, we measured a kinetic series of bulk transcriptomes over a 2.5-month course of low dose BRAF inhibition, during which time the cells evolve from a mostly melanocytic, drug-sensitive phenotype to a mesenchymal, drug-tolerant phenotype. This data set provides input into an information-theoretic surprisal analysis [23], which is used to identify the relative free energy-like potential over the entire course of cell state transition from drug response to drug tolerance. We also utilized microscopic inputs from flow cytometry to profile, at the single-cell level, the phenotypic evolution of the same system. These phenotypic evolution dynamic data cannot be described with conventional Fokker-Planck equation but can be well recapitulated using a modified Fokker-Planck-type (FP-type) kinetic model [17, 18, 24] which considered cell-state dependent proliferation differences. The model resolves relative cell state potential and cell-state proliferation differences were quantitatively validated through experiment. We further show that both approaches provide a self-consistent picture in which the combined effects from the relative stability of cellular phenotypes, together with the phenotype-specific net-proliferative rate, act as the drivers to predictably influence the cell population dynamics of drug-induced phenotypic evolution over time. The results provide conceptual guidance for considering effective therapy combinations [5].

Results

Surprisal analysis of bulk transcriptome data resolves steady state and time-dependent constraints in the melanocytic to mesenchymal transition

We used two patient-derived $BRAF^{V600E}$ mutant cell lines (M397 and M229) with a prominent melanocytic to mesenchymal phenotypic evolution induced upon BRAF inhibition (Fig 1A and S1 Fig) [5]. We characterized this process by both a bulk transcriptome profiling (S1 Table) and a flow cytometry phenotyping using two protein markers (MART-1 and NGFR) that are established cell phenotype markers for this system [5, 9, 25]. The transcriptome was measured at Day 0 (D0), which served as an untreated control, and at a set of time points following BRAFi (vemurafenib) treatment (S2 Fig.). Following drug exposure, the relative location of the binning of cell populations expressing

different levels of the two markers followed a counterclockwise transition trajectory around the flow cytometry plots (S1(A) Fig), moving from the melanocytic phenotype (MART-1^{POS}) towards a transiently enriched slow-cycling neural crest (MART1^{neg}/NGFR^{high}) population around day15 to day20 (D15–D20), and eventually terminating at a mesenchymal (MART1^{neg}/NGFR^{neg}) phenotype at around day62 (D62) with elevated expression of the mesenchymal marker N-cadherin (Fig 1A). This drug-resistant population stably persisted with extended drug treatment beyond D62 (S1(A) Fig). A similar transition trajectory was also observed for M229 (S1(B) Fig). These drug-induced phenotypic transitions agree with previous literature [5, 22].

To assess the overall stability and transcriptomic eigenpatterns associated with the cell population distributions at various time points across the drug-induced phenotypic evolution, we first applied surprisal analysis (Eq. 1) to the transcriptome time series. Surprisal analysis extends the principles of maximum entropy and was initially formulated to understand the dynamics of nonequilibrium systems [26]. Using the method of Lagrange multipliers, it seeks the maximum entropy of molecules and identifies the global steady state with minimal free energy, as well as a series of time-dependent constraints that prevent the nonequilibrium system from reaching the global steady state [16, 23, 26, 27]. Surprisal analysis has been extended to characterize biological processes in living cells, where it assesses the maximum entropy of the biomolecules within the cell ensemble through using a simplified approximation of quantum state distributions of the molecular species [23]. Consequently, for a system with kinetic transcriptome data as input, it can extract the time-independent gene expression baseline (the global steady state), as well as a series of gene expression modules (constraints) that evolve with time [16, 23, 26, 28]. A full derivation and thermodynamic interpretation of Eq. 1 is provided within the supplementary materials of previous reports [23, 28].

$$\underbrace{\ln X_i(t)}_{\substack{\text{measured expression} \\ \text{level of transcript } i \\ \text{at time } t}} = \underbrace{\ln X_i^0(t)}_{\substack{\text{global steady state} \\ \text{expression level of} \\ \text{transcript } i}} - \underbrace{\sum_j \lambda_j(t) \overbrace{G_{ij}}^{\substack{\text{state variable of} \\ \text{constraint } j \text{ at} \\ \text{time } t} \text{ contribution} \\ \text{of transcript } i \\ \text{to constraint } j}}}_{\substack{\text{deviation terms from} \\ \text{the global steady state} \\ \text{of transcript } i \text{ (constraints)}}} \quad (1)$$

In Eq. 1, $X_i(t)$ is the measured level of transcript i at time t . This is considered to be the global steady-state level of transcript i ($\ln(X_i^0(t)) = -\lambda_0 G_{i0}$), modified by the sum of the contributions arising from the constrained processes. The global steady state resolved by surprisal analysis is the cellular state with maximum entropy. If there were no constraints acting upon the cells, then Eq.1 predicts that the cells would be in the global steady state. However, there are non-zero constraints (with amplitudes given by the λ_j values), which are

biological processes that move the system away from the global steady state. Transcripts associated with a constraint are identified through Eq. 1 as lowering the entropy of the system, presumably to maintain one or more biological functions. Data mining the set of transcripts associated with a given constraint can provide insight into those biological functions. Although we do not impose the condition that λ_0 is time-independent, we neither expect nor find time-dependence (the λ_0 variation is $<0.7\%$) (Fig 1B).

To capture the time evolution of the drug-treated cells, each constrained process is represented by a time-dependent amplitude $\lambda_j(t)$ and constraint-specific contributions from each transcript G_{ij} . In principle, analysis of the transcriptomic data across the time series from D0 to D73 could resolve several constraints, but we resolve only three for M397 (S3 and S4 Figs). This is illustrated in Fig 1C, where we represent the whole transcriptome data as a self-organized map (SOM) [29]. The map structure is determined using all data sets. Each tile represents a minicluster of genes with similar expression kinetics. Gene clusters with related expression kinetics are placed close together, while clusters exhibiting very different kinetics are placed far apart. The tile color encodes the average expression level of the genes in that minicluster at a given time point. For SOMs representing a specific constraint, that average gene expression level is also weighted by the participation of the genes in the constraint, as determined from Eq. 1. The gene expression profile for the global steady state remains unchanged throughout the transition, while the differentially expressed genes (termed eigengenes elsewhere [30]) specific to constraints λ_1 , λ_2 and λ_3 vary with time. Summing the global steady state and the three constraints reproduces the map of the measured transcriptome, indicating that, within the noise level of the data, the three major constraints are sufficient to accurately recapitulate gene expression levels globally across the transition. (Fig 1C and S5 Fig).

The major biological processes involved in each constraint, at a given time point, can be inferred by enrichment on the gene lists ranked by the constraint-specific contributions from each gene G_{ij} (Fig 2A, S4 Fig and S2 Table), and by the time-dependent amplitude $\lambda_j(t)$ of that constraint. The first constraint shows monotonically increased amplitude (λ_1) along the course of the transition (Fig 1B), with up-regulated mesenchymal signatures, migration, invasiveness and metastasis features, as well as NF κ B signaling (G_1 positive processes). It also reflects reduced glucose uptake and metabolism, MITF activity, and oxidative phosphorylation (G_1 negative processes) (Fig 2A). Constraint 2 contains similar transcriptional signatures, but its amplitude (λ_2) drops after 3 days of BRAFi exposure and slowly increases at later times (Fig 1B). It points to an elevated MITF activity (G_2 negative process) and reduced cellular proliferation (G_2 positive process) at day-3. This is consistent with previous observations that a brief BRAFi exposure can induce melanocytic differentiation and increased BRAFi sensitivity [31, 32]. The third constraint mainly involves oxidative phosphorylation and the TCA cycle, and has a near zero amplitude except for day

3 (Fig 1B), implying that initial BRAFi exposure leads to a sharply altered metabolic program. The three major constraints associated with M229 displayed similar dynamics and are functionally similar to those in M397 (S4 Fig), confirming the robustness of the BRAFi induced melanocytic to mesenchymal transition. To get a comprehensive view of the enriched transcriptional program, we plotted the enrichment maps of the GSEA results with respect to relevant gene function categories and highlighted representative gene sets in these categories (Fig 2B and S6 Fig). Overall, these transcriptional signatures are wholly consistent with previous reports [5, 9-11, 33], testifying the validity of our cell line model for recapitulating the known biology of the transition and confirming the power of surprisal analysis for dissecting the underlying biology of the transition.

Fokker-Planck modeling of phenotypic evolution with single-cell flow cytometry phenotyping failed in recapitulating the evolution dynamics

The same biological system was further characterized at the single-cell level using flow cytometry analysis of the established cell-state markers: NGFR and MART-1. The temporal transcriptomic signatures resolved by surprisal analysis result from the dynamics of the BRAFi-induced phenotypic evolution that can be characterized by MART-1 and NGFR marker proteins [5, 9, 25]. As shown in our previous report, these two marker proteins can yield the identical phenotypic classification to that of the whole transcriptome data [5]. Therefore, they can be used as robust phenotype markers during the course of the drug-induced transition (Fig 1A and S1 Fig).

To model the single cell data, we conceptualize cell population distributions as single cells moving on a configuration space delineated by the marker proteins. In this space, cell states correspond to stable or metastable attractors of a hypothetical potential landscape [34]. The dynamics of the protein markers for a single cell can be described by the Langevin type equation $d\mathbf{z}/dt = \boldsymbol{\mu}(\mathbf{z}) + \zeta$, where \mathbf{z} is the concentration vector of the protein markers (z_1, \dots, z_N) , $\boldsymbol{\mu}(\mathbf{z})$ is a drift vector in concentration space that describes all of the deterministic (non-random) dynamics and can be determined by the gradient of the potential landscape. The term ζ is the white noise term from random fluctuations in protein expression: $\langle \zeta(t)\zeta(t') \rangle = 2\mathbf{D}\delta(t-t')$ where \mathbf{D} is the diffusivity tensor measuring the amplitude of those fluctuations [18].

The potential landscape of a cellular system is context-specific. We hypothesized that drug treatment altered the original drug naïve landscape into a new landscape, which in turn yielded relaxation dynamics as each cell adjusts to this new drift field, potentially with motions towards new attractor states.

Analyzing the dynamics arising from a multi-dimensional drift field is, in general, an intractable problem. However, the flow cytometry trajectory (Fig 1A and S1 Fig) upon

BRAF inhibition suggested the simplification that cell populations may be considered to evolve along a linear chain of a limited number of cell states. Therefore, for computational convenience, we projected the protein concentration vectors of the two dimensional (2D) flow cytometry data into a one-dimensional (1D) representation where the cell populations were constrained to move along in this characteristic 1D trajectory (Fig 3A). The distance along the trajectory $x=x(\mathbf{z})$ serves as an effective reaction coordinate of the phenotypic evolution (see Methods).

The flow cytometry data do not track an individual cell stochastic trajectory, but rather give statistical snapshots of marker protein expression levels across single cells. Thus, it is natural to transform the single-cell Langevin equation into the Fokker-Planck equation for resolving the time-dependent probability distribution $p(x,t)$ along the reaction coordinate [35]:

$$\frac{\partial p(x,t)}{\partial t} = -\frac{\partial}{\partial x}[\mu(x)p(x,t)] + \frac{\partial^2}{\partial x^2}[Dp(x,t)] \quad (2)$$

Here, drift term $\mu(x)$ implies that motion along x is influenced by a potential landscape. D is a diffusivity that is assumed, for simplicity, to be a constant independent of x or drug treatment. Even in cases where the diffusivity depends on the reaction coordinate x , a Fokker-Planck (FP) equation with constant diffusivity can be obtained by a simple coordinate transformation as shown in Ref. [17].

Because the dynamics under consideration are 1D, the drift $\mu(x)$ can always be presented as the derivative of a scalar potential $U(x) = -\int_0^x \mu(y)dy$. This, in turn, is exactly related to the steady state solution of Eq. 2 through a Gibbs relation as $\lim_{t \rightarrow \infty} p(x,t) = p_\infty(x) = C \exp(-2U(x)/D)$ where C is a normalization constant. Therefore, one can determine (up to proportionality to D) the potential U from measurement of the steady state distribution $p_\infty(x)$ as $U(x) = -\left(\frac{D}{2}\right) \ln p_\infty(x)$. This FP approach has been successfully applied to understanding the population heterogeneity of model biological systems [17, 18]. Here, we used a variation of this method to measure the diffusivity $D = 0.35q^2/\text{day}$ (q the unit length of the reaction coordinate) from sorting-relaxation experiments in the drug-naïve condition (S7 Fig, See Materials and methods for details). Given this D and flow cytometry measurements of the final steady state distribution $p_\infty(x)$ upon prolonged drug exposure, we inferred the potential $U(x)$, and equivalently the drift $\mu(x)$ consistent with this model.

To test the validity of the FP model, we performed direct numerical simulation of the FP equation with the inferred $\mu(x)$, the diffusivity D , and the measured initial distribution

$p(x,0)$ to calculate the cell population distribution $p(x,t)$ for subsequent days, which, as shown in Fig 3B (FP model), are in poor agreement with the experiments (green lines in Fig 3B and S8 Fig). The disagreement indicated the existence of extra factors influencing phenotypic transitions which were not considered in Eq. 2.

Modified Fokker-Planck-type kinetic model that incorporates cell-state-dependent proliferation recapitulates the phenotypic evolution and predicts cell-state proliferation rates.

We hypothesized that the disagreement with experiments arose because the drug would influence not only the cell phenotypic evolution but also the cell autonomous proliferation and survival. In other words, the cells have drug susceptibilities – as reflected by the net effect of cell proliferation and cell killing – that vary along the reaction coordinate. These factors can also influence the phenotypic compositions, but are neglected in Eq.2. Thus, we modified Eq.2 to include a self-sourcing term:

$$\frac{\partial P(x,t)}{\partial t} = -\frac{\partial}{\partial x}[\mu(x)P(x,t)] + \frac{\partial^2}{\partial x^2}[DP(x,t)] + \alpha(x)P(x,t) \quad (3)$$

Here the net growth rate $\alpha(x)$ (the net effect of cell proliferation and cell killing under drug treatment) was introduced to account for cell state-dependent drug susceptibility. As an additional ansatz, we considered $\alpha(x)$ as a double step function taking different values for the intermediate neural crest-like phenotype and late-stage mesenchymal phenotype relative to the early stage melanocytic phenotype. It is worthwhile to note that, with Eq. 3, we were no longer working with a probability distribution $p(x,t)$, but instead a non-normalized population $P(x,t)$. Both the differential drift and self-sourcing term act together to induce the cell number changes that are proportional to the population size of a specific cell state. For direct comparison between the model $P(x,t)$ and experimentally accessible $p(x,t)$ from flow cytometry data, we simply factored out the norm ($p(x,t) = P(x,t) / N(t) = P(x,t) / \int_{-\infty}^{\infty} dx P(x,t)$).

In this model, due to the addition of the self-sourcing term, the Gibbs relation between the drug-induced steady state $p_{\infty}(x)$ and the potential $U(x)$ used in our analysis of the original FP equation no longer holds. To determine the parameters for this modified model, we therefore resorted to an unbiased numerical search for $U(x)$ and $\alpha(x)$ that best fit the experimental data. The model prediction was obtained by numerically simulating Eq. 3 with the same experimentally measured diffusivity D and the initial distribution $p(x,0)$ as before, together with all possible $U(x)$ and $\alpha(x)$ values in the unbiased search. We determine goodness of fit using an un-weighted sum-of-square difference between all the predicted and

measured cell population distributions $p(x,t)$. In both cell lines, we were able to find one set of $U(x)$ and $\alpha(x)$ for the modified FP-type kinetic model that produced the best prediction of population distributions over time. When compared to original FP model, the modified model predictions are in much better agreement to experiments (red lines in Fig 3B and S8 Fig). The agreement appears to confirm the validity of the self-sourcing term in Eq. 3, but the value of that term can be put to an independent experimental test.

We treated the state-dependent net growth rate $\alpha(x)$ as a concrete prediction of the model, and found it to be in good agreement with experimentally measured cell growth rates: cell populations containing a higher fraction of the mesenchymal phenotype (day21-78) grow faster than those with a lower fraction (day0-21) (Fig 4, See Materials and Methods). The agreements between model-predicted growth rates and experiments (Fig 4) further confirmed the validity of Eq. 3 and show that differences in state-dependent growth rates are important in determining the drug-induced phenotypic evolution of the melanoma cells.

In addition to predicting proliferation rates, Eq. 3 also yielded relative values of the epigenetic potential along the reaction coordinate $U(x)$ (Fig 5A and S9(B) and S10(A) Figs), which yields an inference of the stability of different states along the coordinate. The scalar potential landscape was obtained by integration of $\mu(x)$ from Eq. 3 over the reaction coordinate x . The shape of the landscape indicates that the intermediate neural crest-like states (NGFR^{pos}/MART-1^{neg}) are more stable than both the MART-1^{pos} melanocytic state and the mesenchymal-like state (NGFR^{neg}/MART-1^{neg}), and thus the intermediate states can be considered as an attractor. However, the net growth rate of those intermediate states is relatively low (Figs. 4 and 5A), and so the cells do not naturally populate just that state over the course of long-term drug treatment.

Further confirmation of the concordance of the epigenetic potential landscapes calculated from macroscopic and microscopic inputs

As demonstrated in previous work, surprisal analysis of the bulk RNA-seq data can also define a free energy-like potential corresponding to the drug-induced phenotypic evolution [16, 28]. This potential, for the entire transcriptome of a cell state at time t , is relative to the global steady state, and is given by $F(t) = \sum_j \lambda_j(t) \langle G_j \rangle$, where $\langle G_j \rangle = \sum_i X_i G_{ij}$ (See Materials and Methods for details). It has a direct relationship to the entropy of the transcripts and thus evaluates, at a transcriptional level, the relative stability of a cell state (see Ref. [23] for theoretic details). Here we adopted the same definition to calculate the potential landscape over drug-induced phenotypic evolution in melanoma cells. For M397, this potential landscape calculated from surprisal analysis, similar to the landscape calculated by the modified Fokker-Planck-type (Eq. 3) model, indicates that the cells at D11 and D21, with mostly neural-crest like phenotypes are more stable than cells at earlier times (melanocytic

phenotypes) or D73 (predominantly mesenchymal phenotype) (Fig 5B). For M229, cells at D21 with mostly the neural-crest like phenotype are also more stable than the cells at D90 (predominantly mesenchymal phenotype) (S10 Fig). Thus, the epigenetic potentials calculated from either surprisal analysis of bulk data or the Fokker-Planck kinetic model from single-cell data yield a consistent picture.

Both analyses indicate that neural-crest like cells are more stable than the mesenchymal phenotype. This prediction was experimentally validated by sorting the mesenchymal (NGFR^{neg}/MART1^{neg}) subpopulation from the M397 D73 distribution (S11 Fig). We carried out surprisal analysis of transcriptome data from both the segregated mesenchymal subpopulation and the unsorted day-73 population (a mixture of mesenchymal phenotype and neural-crest phenotype). Free energy-like potentials were calculated and found to be consistent with the scalar potentials of both sorted and unsorted populations determined by the modified FP-type kinetic model. The pure mesenchymal phenotype displayed higher potentials than the unsorted cells (Fig. 5C). Hence, cell sorting and RNA-seq experiments confirmed the consistence between the two theoretic models, and indicated that the drug-resistant mesenchymal cells are epigenetically unstable relative to the neural crest phenotype.

Discussion

Heterogeneous cancer cell populations can often exhibit a phenotypic equilibrium and evolution behaviors, meaning that a specific composition comprised of relative abundances of distinct cancer cell phenotypes can be a characteristic of the system, and in the meantime, this characteristic composition will evolve or recover following the application or release of molecular or physical perturbations designed to alter it [2, 5, 12-14]. This can, of course, confound the interpretation of responses to drug treatment, but it also provides a compelling biophysical puzzle. Here we investigated two statistical physics models to help build a predictive picture of such phenotypic equilibria. The models respectively utilize macroscopic and microscopic inputs, and we applied them towards understanding the population dynamics of phenotypically plastic patient-derived *BRAF*-mutant melanoma cancer cells following BRAFi treatment. During a few months period of drug treatment, the cells evolve from drug naïve, drug-sensitive melanocytic-dominated composition to a fully drug-resistant mesenchymal-dominated cell population. In an interesting parallel with state transitions in physical systems, the associated cell state transitions are fully reversible: upon drug removal, the mesenchymal cells revert back to a melanocytic state that is, for all intents and purposes, identical to the initial drug naïve state [5].

The first theoretical model, surprisal analysis, utilizes a bulk transcriptome kinetic series across the drug treatment course to provide a description of the global steady state (the state of maximum entropy) and to identify specific, time-dependent constraints that keep the system from reaching that steady state. The weights of the constrained processes can be

utilized to generate a free energy-like potential of the cell-state space sampled during drug treatment [16, 28]. It is worth noting that cells are open systems far from equilibrium. While a significant body of work has demonstrated the apparent parallel between equilibrium and nonequilibrium thermodynamics [36-38], the potential landscape across the cell state evolution in our study is still a metaphor of the real free energy landscape in an equilibrium system. However, the maximum entropy methods can infer the most probable distribution of a probabilistic system regardless of whether or not it is in equilibrium [39]. Surprisal analysis further extends the principles of maximum entropy to understand particularly small systems that are not in thermodynamic equilibrium [23, 26, 40]. Therefore, in analogy to entropy in equilibrium thermodynamics, the entropy (and free energy-like potential) of the cellular transcriptome calculated from surprisal analysis can be used to evaluate the overall stability of a cell state [28, 41].

The second theoretic approach consists of a modified Fokker-Planck-type kinetic model, which takes a kinetic series of single cell flow cytometry data as input. This model considers the Langevin dynamics of self-sourcing single cells moving within a configuration space. That motion is influenced by both (random) diffusion and drift along a potential gradient, thus permitting a potential surface of the traversed cell-state space to also be extracted.

There are two primary considerations that allow results from these two theories to be directly compared. First, the flow cytometry data and the bulk transcriptome data sets capture the same essential biology. This is obviously not always true. However, for this particular case, the cell phenotypic markers NGFR and MART-1 used in the single cell assays are known surrogates for drug-induced changes across the whole transcriptome [5]. It also implies that a more selective subset of the transcriptome might equally well recapitulate the underlying biology, which may be assessed by the contribution scores (G_{ij} values) within each respective constraint. Second, the phenotypic evolution the melanoma cells proceeds stepwise from melanocytes \rightarrow neural crest \rightarrow mesenchymal phenotypes. This permits the cell response to BRAF inhibition to be considered as time-dependent motion along a linear reaction coordinate, and provides an equivalence between the Fokker-Planck reaction coordinate and the surprisal analysis time coordinate (Fig 5A and 5B).

We do not directly compare the y-axes of the two landscapes (Fig 5A and 5B), but only the slopes of the curves. The FP scalar potential and the surprisal analysis free-energy like potential have very different origins. The free energy-like potential is derived by comparing transcriptional profiles at each time point with that of the time-independent global steady state. The FP potential is derived from the drift term of Eq. 3, and is, in fact, the only term in that equation that needs to be fitted, since both cell proliferation rate and diffusion along the FP reaction coordinate can be experimentally determined. However, both theories predict that the most stable cellular population is a largely neural crest phenotype. Surprisingly, that is not the cell population that is ultimately induced by the long-term drug exposure. That population is dominated by a mesenchymal phenotype with a minor neural crest component,

and is arrived at through competing interactions. On the one hand, the neural crest phenotype serves as an attractor, but those cells only slowly proliferate. The higher potential mesenchymal cells are more proliferative and that is the dominating factor. This highlights a major difference between open biological systems and equilibrium thermodynamic systems [42].

The analyses presented here for the *BRAF*-mutant melanoma cells might suggest that identifying drug susceptibilities in each of the cancer cell phenotypes might lead to a more effective therapy. However, such highly plastic cancer cells might eventually switch into cell states that are resistant to even broad combination therapies. A more fruitful approach might be to target those biological mechanisms that underlie the plastic nature of the cells [5, 43].

Materials and Methods

Patient-derived melanoma tumor models and drug treatment conditions.

Cells were cultured at 37 °C with 5% CO₂ in RPMI 1640 with L-glutamine (Mediatech, Inc, Manassas, VA), 10% fetal bovine serum (Omega Scientific Tarzana, CA), and 1% penicillin, streptomycin and fungizone (Omega Scientific Tarzana, CA). Cells were maintained and tested for mycoplasma as previously described [44, 45]. Cell lines were periodically authenticated to their early passages using GenePrint 10 System (Promega, Madison, WI). Presence of mutations in the genes of interest was checked by OncoMap 3 or Iontrone, and was confirmed by PCR and Sanger sequencing as previously described [44, 45].

Vemurafenib (NC0621949, Selleck Chemicals LLC) was dissolved in DMSO at designated concentrations before applying to cell culture media. All cell lines were plated in 10cm dish at 60% confluency and treated with vemurafenib for the specified numbers of days at twice the 50% inhibition concentration (IC₅₀) of each cell line as reported before [5]. At different time points after drug treatment, cells were harvest for RNA-seq and flow cytometry. Cell number was also counted for determining the growth rate. Cell growth rate was fitted as the parameter α in the exponential growth curve equation $N(t) = N_0 \cdot 2^{(\alpha \cdot t)}$, where N_0 is the cell number at the starting time point, and $N(t)$ is the cell number at time t . Cell numbers counted at day 0, 7, and 21 were used to fit for the proliferation rate at day 0-21 time period, and cell numbers at day 30, 43, 66, and 78 were used to fit for the one at day 21-78 time period.

Flow cytometry analysis of cell phenotype.

At different time points, cells were trypsinized from the dish, spun down and washed with PBS. Cell suspensions were stained for flow cytometry with PE-conjugated NGFR antibody from Biolegend (San Diego, CA). All cells were fixed with Fix-Perm buffer from BD Bioscience (San Jose, CA). Cells were then stained for intracellular Melan-A using FITC conjugated antibody from Santa Cruz (Dallas, TX). Isotypes for mouse IgG1k and mouse IgG1 respectively were used to enable correct gating and to confirm antibody specificity. Blue live-dead staining from Life technologies (Waltham, MA) was used to gate live cell events. 10000 alive events were collected for each sample. Flow cytometry analysis was conducted using LSR-II from BD Biosciences (San Jose, CA), and the data were analyzed using FlowJo software (Tree Star, Inc., San Carlos, California, USA).

Immunofluorescence imaging

The standard immunofluorescent protocol was implemented using cells grown on the gelatin-coated glass surface. Briefly, 10,000 cells/well were seeded in 96-well glass bottom plates (Greiner Sensoplate Plus, Cat# 655892) coated with 0.1% gelatin solution, and

grown in culture media to ~70% confluency. Cells were washed twice in PBS and fixed in 4% paraformaldehyde (PFA) solution for 10 min. After washing twice in wash buffer (0.1% BSA in PBS), cells were blocked and permeabilized in blocking buffer (10% normal donkey serum, 0.3% Triton X-100) for 45 minutes. After removing the blocking buffer, cells were incubated in primary antibody for 4 hours at room temperature. Mouse monoclonal anti-NGFR antibody (BioLegend Cat# 345106 RRID:AB_2152647) or sheep polyclonal anti-N-Cadherin (R&D Systems Cat# AF6426 RRID:AB_10718850) was diluted to 0.25 or 10 $\mu\text{g}/\text{mL}$, respectively, in antibody diluent (1% BSA, 1% normal donkey serum, 0.3 % Triton X-100). After washing twice in wash buffer (0.1% BSA in PBS), cells were incubated in secondary antibody for 1 hour at room temperature. Donkey anti-Mouse IgG, Alexa Fluor 647 (Thermo Fisher Scientific Cat# A-31571 RRID:AB_162542) or donkey anti-Sheep IgG Alexa Fluor 594 (Thermo Fisher Scientific Cat# A-11016 RRID:AB_2534083) was diluted to 4 $\mu\text{g}/\text{mL}$ in antibody diluent. After washing twice in wash buffer, cells were counter stained for 5 min with 4',6-Diamidino-2-Phenylindole (DAPI) diluted to 1 $\mu\text{g}/\text{mL}$ in PBS. After washing twice in PBS, the wells were filled with 78% glycerol.

Fluorescent images were acquired with a Nikon C2plus confocal microscope (Ti) using Plan Apo λ 20 \times objective (Nikon Inc., Melville, NY). The microscope was controlled by NIS elements AR software (4.51.00) with the following settings: 30 μm pin hole, 12-bit acquisition, 0.62 μm pixel size, 60 gain, and laser power of 5% (405 nm), 0.3% (561 nm), or 0.6% (640 nm). Images were background and contrast adjusted using their respective control wells with no primary antibody staining.

RNA-seq and transcriptomic data analysis

Cells treated under specified conditions and time periods were trypsinized to harvest for cell pellets. RNA extraction was performed at cell pellets using AllPrep DNA/RNA Mini kit from Qiagen. Bioanalyzer confirmed correct integrity, the library was constructed and Illumina 50 bps single-end RNA-seq data was collected for the samples described. RNA sequencing was performed using 50 bps single end sequencing on the Illumina HiSeq 2500 platform. Libraries were prepared using the IlluminaTruSeq RNA sample preparation kit per the manufacturer's instructions. Reads were mapped and aligned to the Homo sapiens NCBI build 37.2 reference genome using TopHat2 v2.0.9 [46]. Expression values in fragments per kilobase of exon per million fragments mapped (FPKM) were generated using Cufflinks v2.2.1 program and Cuffnorm to quantify and normalize aligned reads using the geometric library size normalization method [47].

Heatmap and clustering analysis of transcriptomic datasets was performed via MATLAB. Genes are pre-filtered by RPKM value with criteria of average value greater than 0.5 and coefficient of variance greater than 0.15. Filtered gene expression values were

standardized across each row (normalized for each individual gene) and represented by a redblue colormap. Hierarchical clustering was performed with average linkage and Euclidean distance metric. Whole transcriptomic dataset and fractions of contributions from each constraints are visualized using self-organized mosaic maps with respect to its control via Gene Expression Dynamics Inspector (GEDI) [29]. Gene Set Enrichment Analysis (GSEA) [48] was performed using GSEA v2.2.3 software with 1000 permutations and weighted enrichment statistics. GSEA enriched gene sets were visualized as interaction networks with Cytoscape [49] and Enrichment Map [50].

Surprisal analysis and free energy-like potential

Surprisal analysis was applied as described previously [23, 28]. The measured expression level of mRNA i at time t , $\ln X_i(t)$, was expressed as a sum of a steady state term $\ln X_i^0(t)$ and several constraints $\lambda_j(t)G_{ij}$ representing deviations from the steady state. Each deviation term was a product of a time-dependent weight of the constraint $\lambda_j(t)$, and the time-independent contribution of the transcript to that constraint G_{ij} .

To implement surprisal analysis, we computed the singular value decomposition (SVD) of the matrix $\ln X_i(t)$. As well described previously [23], the SVD factored this matrix in a way that determined the two sets of parameters that are needed in surprisal analysis: the Lagrange multipliers (λ_j) for all constraints at a given time point, and for all times and the G_{ij} (time-independent) transcription patterns for all transcripts i at each constraint j .

The free energy-like potential calculation based on the surprisal analysis result was implemented as in Ref. 33. Briefly, The steady-state expression level of transcript i at time t can be linked to its actual expression level by as $X_i^0(t) = X_i(t) \exp(-\sum_j \lambda_j(t)G_{ij})$. Therefore, as shown in Ref. 33, surprisal analysis defines the free energy-like potential of a transcript i relative to the global steady state at time t as $f_i(t) = \sum_j \lambda_j(t)G_{ij}$. Taking all the transcripts into account, the free energy-like potential of the entire transcriptome of a cell state at time t relative to the global steady state is given by $F(t) = \sum_i X_i f_i(t) = \sum_j \lambda_j(t) \langle G_j \rangle$, where $\langle G_j \rangle = \sum_i X_i G_{ij}$ [16].

Natural log transformed transcriptomic dataset and fractions of contributions from each constraints ($\lambda_j(t)G_{ij}$) calculated from surprisal analysis are visualized using self-organized maps (SOM). Self-organized map visualization of high-dimensional dataset in a form appropriate for human pattern recognition without discarding the global, higher-order

information. Here, they present individual samples as a single 2-dimensional heatmap and, at the same time, display high-resolution patterns. Thousands of input genes are assigned to 625 rectangular “tiles” (SOM nodes), each of which represents a mini-cluster of genes, arranged so as to form a pattern within a 2-dimensional mosaic map on the SOM grid. Tiles represent most similar clusters will be placed adjacent to each other in the mosaic. Gene Expression Dynamics Inspector (GEDI) package is utilized to implement the SOM visualization [29].

Modified Fokker-Planck-type kinetic model

The dynamics of the protein markers for a single cell can be described by the Langevin type equation $d\mathbf{z} / dt = \boldsymbol{\mu}(\mathbf{z}) + \zeta$, where \mathbf{z} is the concentration vector of the protein markers (z_1, \dots, z_N) , $\boldsymbol{\mu}(\mathbf{z})$ is a drift vector in concentration space that describes all of the deterministic (non-random) dynamics and can be determined by the gradient of the potential landscape. The term ζ is the white noise term from random fluctuations in protein expression: $\langle \zeta(t)\zeta(t') \rangle = 2\mathbf{D}\delta(t-t')$, where \mathbf{D} is the diffusivity tensor measuring the amplitude of those fluctuations [18].

In the case of melanocytic to mesenchymal transition, for computational convenience, we projected the protein concentration vectors of the flow cytometry data into a one-dimensional (1D) representation where the cell populations were constrained to move along in this characteristic trajectory. This converted each snap-shot of cell population distribution from the 2D flow cytometry plot onto a one-dimensional distribution along the linear trajectory. More specifically, we reduced the dimensionality of the flow cytometry data by calculating the principle curve of the full set of measurements using the R package `princurve`. The data points were projected onto the curve, and the distances of these projected points along the curve were used as the one-dimensional data for the two Fokker-Planck models. These data points were converted into probability density functions (PDF) using kernel density estimation.

Consider the fact that flow cytometry data do not track an individual cell stochastic trajectory but rather give statistical snapshots of marker expression levels across many single cells. Thus, it is natural to transform the single-cell Langevin equation into the Fokker-Planck equation for resolving the probability distribution of the protein markers. The 1D coordinate (Fig 3A) is defined as a reaction coordinate $x(z)$ such that the Fokker-Planck (FP) equation for the probability distribution $p(x,t)$ has the following form:

$$\frac{\partial p(x,t)}{\partial t} = -\frac{\partial}{\partial x} [\mu(x)p(x,t)] + \frac{\partial^2}{\partial x^2} [Dp(x,t)] \quad (\text{M1})$$

Here, x is the 1D flow cytometry (FC) coordinate, D is a diffusion constant of the cells along x , and drift term $\mu(x)$ implies that motion along x is influenced by a potential

landscape. In this model, the equilibrium distribution $p_\infty(x) = \lim_{t \rightarrow \infty} p(x, t)$ and the potential $U(x) = - \int \mu(x) dx$ are connected through the Gibbs relation

$$U(x) = - \left(\frac{D}{2} \right) \ln p_\infty(x) \quad (\text{M2})$$

For the unmodified Fokker-Planck equation, this Gibbs relation was applied to the long-term drug treated cell population distribution data (day78 for M397 and day60 for M229) to infer a potential, whose gradient acted as the drift term driving the dynamic changes of the population distribution. This inferred potential and respective drift term, when coupled with diffusion constant D and the initial (day0) population distribution, generated the prediction results in Fig 3B.

With regards to calculating diffusion constant D from cell sorting and relaxation experiments, the diffusion coefficient D was assumed to be a constant value independent of trajectory position x and drug treatment condition for simplicity. Based on this assumption, when calculating the diffusion constant, we used time-series flow cytometry data of cell sorting and relaxation experiments. In these experiments, we sorted out the untreated cells into NGFR^{pos} and NGFR^{neg} subpopulations. Both sorted subpopulations were cultured without drug treatment. At different days after sorting and culturing, the cells were harvested to quantify its abundance of NGFR and MART-1 using flow cytometry as shown S6 Fig.

Consider the fact that variations of proliferation rates are small in the untreated cells, the Fokker-Planck model (Eq. M1) was considered valid and this data was used as input to fit the diffusion constant D . Varying D as a free parameter, the (drug-naïve) potential and hence drift were calculated with Eq. M2, using the original, untreated distribution as $p_\infty(x)$. The Fokker-Planck equation with these parameters was simulated, with the initial condition $p(x, 0)$ set by the sorted population distribution. The simulated data were compared to the measured time-series distributions with an unweighted sum-of-squares measure. This measure was then minimized as a function of D , and yielded the best-fit diffusion constant D to be $0.35 q^2/\text{day}$ where q represents the unit length on the flow cytometry coordinate.

For the modified Fokker-Planck-type kinetic model described in equation (3) where the same reaction coordinate (x) as the unmodified equation is applied, the state-dependent proliferation rate $\alpha(x)$ was modeled as piecewise-constant with different values for the melanocytic, neural crest, and mesenchymal cell types. The cutoff locations in terms of the reaction coordinate x were chosen as the two local minima in an observed PDF with the coexistence of all three subpopulations. One can show that the time evolution of the PDF does not depend on an overall constant shift $\alpha(x) + c$, so we set the proliferation rate of the starting melanocytic state to 0 for convenience, as the melanocytic cells were observed to

be cytostatic without significant proliferation or cell death upon drug treatment. This then left the proliferation rates of the neural crest (α_1) and mesenchymal cells (α_2) as two free parameters.

Because the Gibbs relationship between the long-time density $p_\infty(x)$ and the potential $U(x)$ no longer held with this nontrivial proliferation rate, we resorted to fitting a cubic spline interpolation for the drift $\mu(x) = -\partial U(x)/\partial x$. Twenty spline points were used, with x values uniformly spaced along the curve and μ values as free parameters.

Starting with an estimate of $\alpha_1(x) = \alpha_2(x) = 0$ and $\mu \sim x$, we calculated the prediction of this model using FiPy to numerically simulate the forward evolution with initial condition $p(x, 0)$ set by the experimentally measured distribution on day-0. To compare with the experimental data, we used the L^2 norm on the difference between the predicted and experimental probability densities $L = \sum_i \int_{-\infty}^{\infty} (p_{pred}(x, t_i) - p_{exp}(x, t_i))^2 dx$ as the goodness-of-fit metric. Gradient descent was performed on the proliferation and drift parameters to determine the best-fit values that minimize L . The calculated potential landscape results are robust to small variations in parameters for calculating the principal curve. (S12. Fig)

Figures

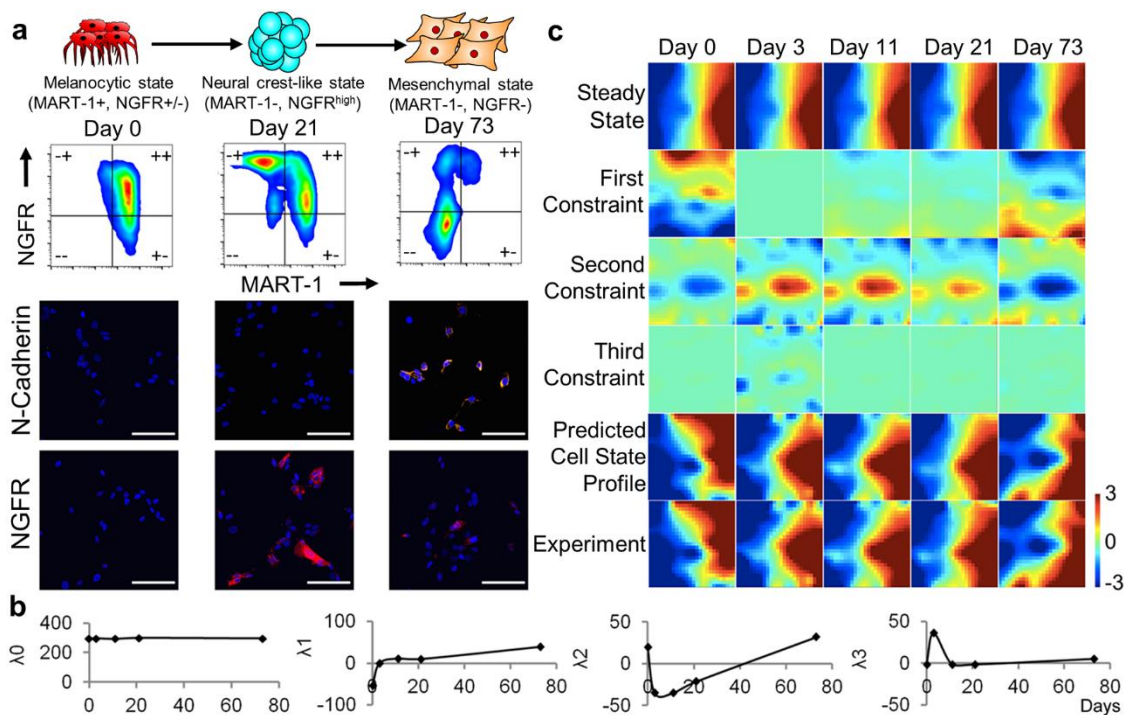


Fig 1. Information theoretic analysis of time-series transcriptome data of a patient-derived BRAF-mutant melanoma cells (M397) treated with a BRAFi. The cells responded to BRAFi by transitioning from a melanocytic to mesenchymal phenotype over the 2.5 month time course. (A) Top: Illustration of the BRAFi-induced phenotype transitions in M397. Middle: Flow cytometry profile of marker proteins MART-1 and NGFR along the course of the transition. Bottom: DAPI, NGFR and N-Cadherin staining of untreated, neural-crest like, and drug-tolerant mesenchymal cells. Scale bar: 100 μ m. (B) The amplitude of the steady state and the top three constraints as determined by surprisal analysis of the kinetic series of transcriptome data. (C) The contributions of the steady state and 3 constraints to gene expression are visualized using a self-organizing map to divide the measured transcript levels into 625 (25 \times 25) “miniclusters”. Each minicluster of genes is mapped onto the same pixel in each map. The predicted cell state profile appears as the sum of the steady state and the top three constraints.

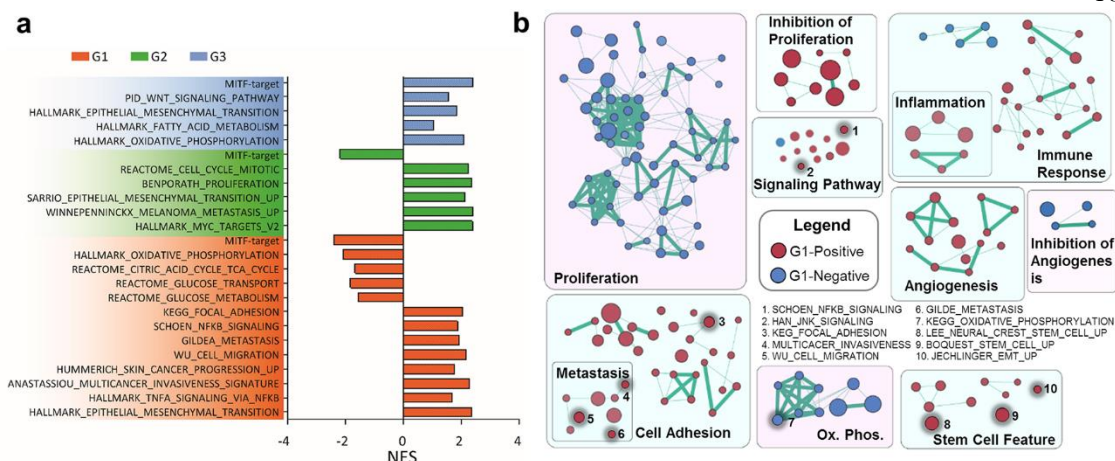


Fig 2. Gene set enrichment of the three constrained processes for the phenotypic and functional changes over the drug-induced phenotypic evolution. (A) List of relevant enriched gene sets, and their relative association with each of the top three constraints. All these gene sets exhibit a nominal p value < 0.05 . (B) Cytoscape map that annotates the enriched gene sets associated with the G1 constraint with respect to their functional categories. Enriched gene sets are represented by nodes, which are grouped and annotated based on gene similarity within each gene set. The size of each node is proportional to the total number of genes within each gene set. The edge thickness is proportional to the number of shared genes between gene sets. Red (blue) gene sets are positively (negatively) correlated with G1. Gene sets with similar functions are boxed together with the group name overlaid. Ten specific gene sets are highlighted with thicker outline, and numbered. For example, gene sets 1 and 2 are labeled within the ‘signaling pathways’ box. The corresponding names for those numbered gene sets are provided in the key.

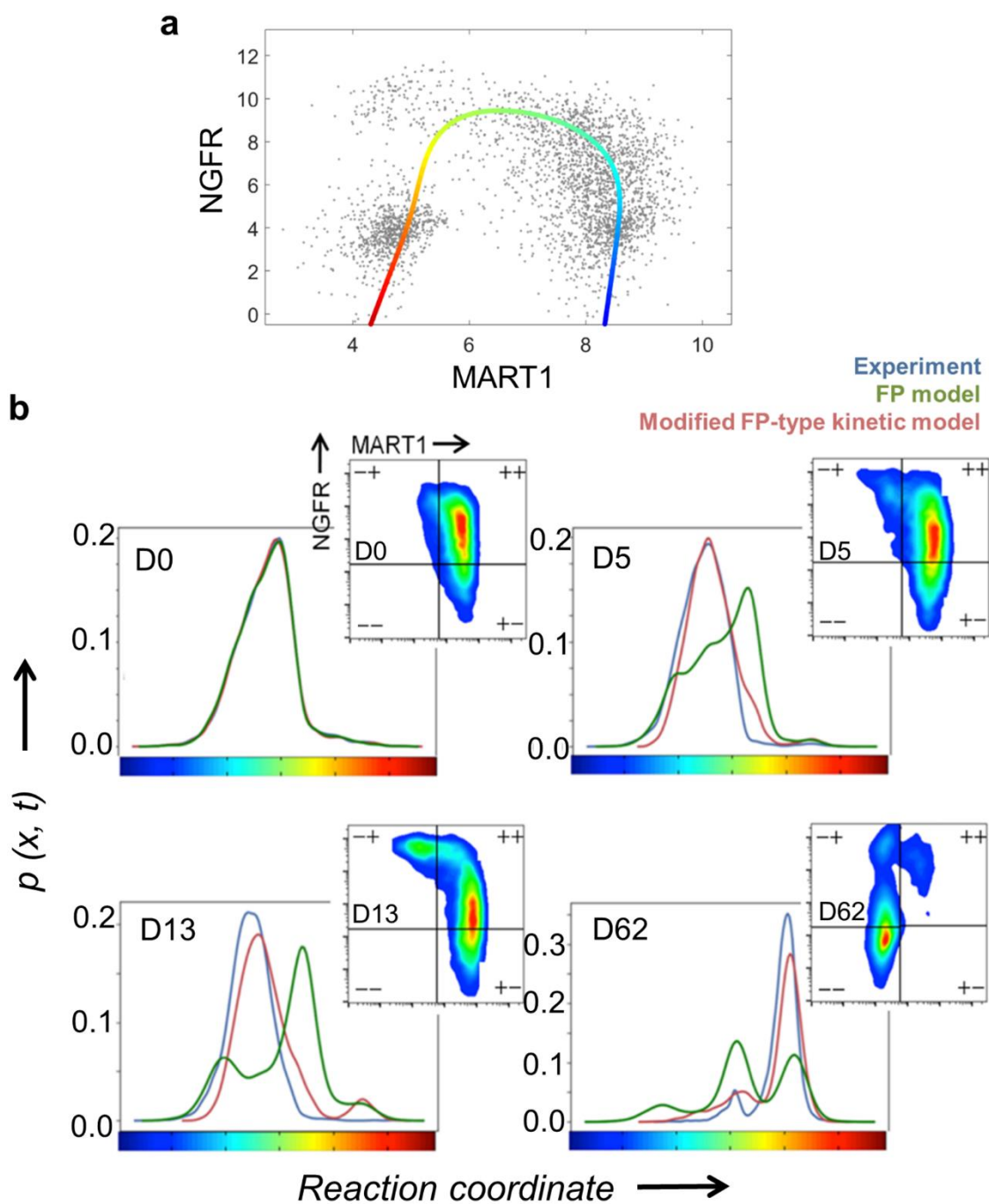


Fig 3. Single-cell flow cytometry analysis of the phenotypic evolution of the M397 cells from melanocyte to mesenchymal under BRAFi treatment, and results of Fokker-Planck-type kinetic model. (A) A reaction coordinate (x), represented as a solid line that evolves from blue (for melanocytic phenotypes) to red (mesenchymal phenotypes), is fitted to the flow cytometry data across all time points. (B) The measured and predicted cell probability density distribution along the reaction coordinate x at representative time points

over the transition. Blue line: Experimentally measured distribution of cells. Green line: predicted cell distribution using the original Fokker-Planck model. Red line: predicted distribution from the modified kinetic model that includes a state-dependent cell net growth rate.

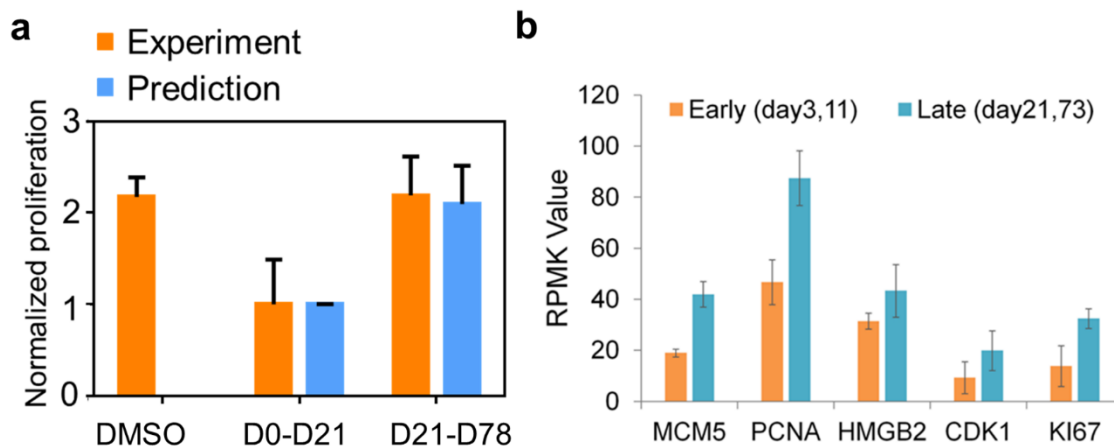


Fig 4. Cell-state-dependent relative net growth rates over the course of the phenotypic evolution for M397 cells. (A) Experimentally measured and predicted cell growth rates (bars). D0-D21 is associated with melanocytic and neural crest-like states, and D21-D78 is primarily associated with the mesenchymal state. Mean values and error bars are defined as mean and s.d., respectively. (B) Expression level of proliferation-related genes after short-term (early) or long-term (late) BRAF inhibition.

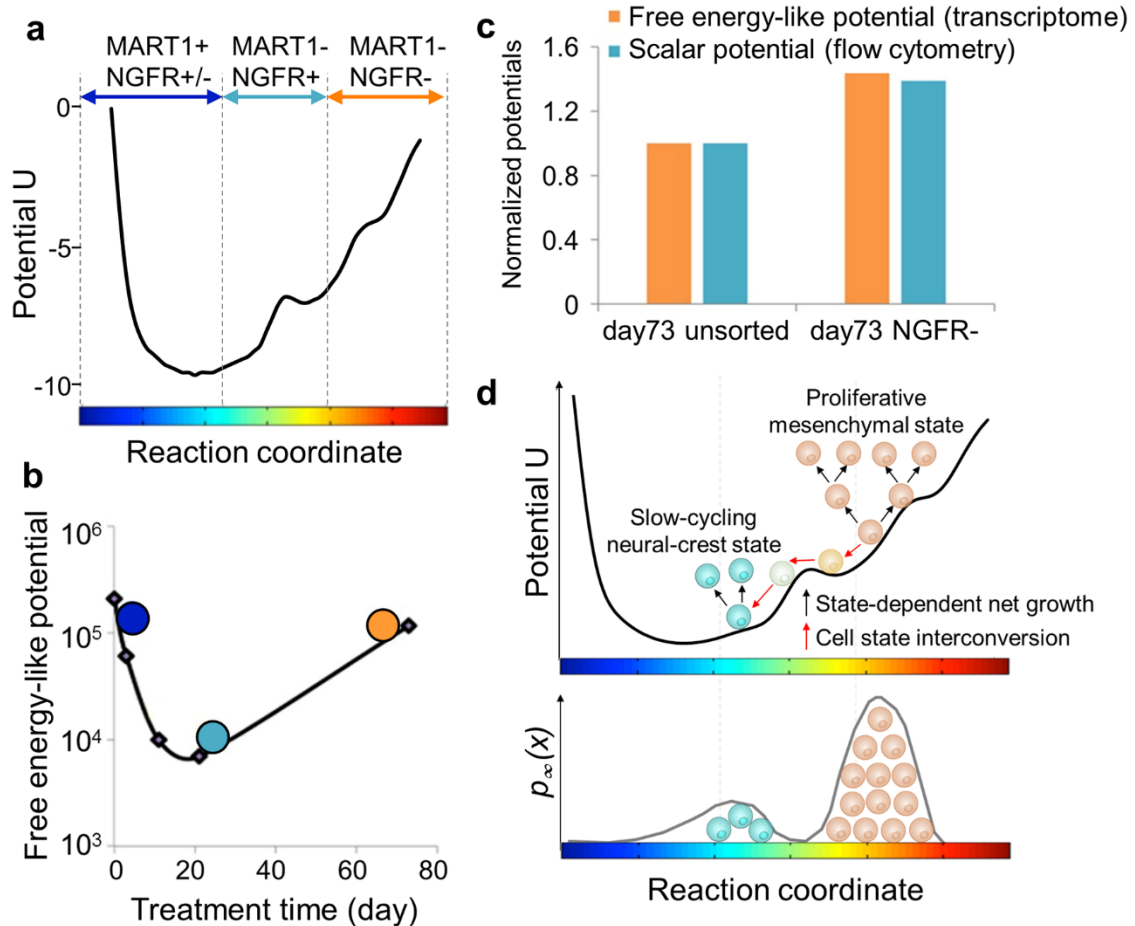
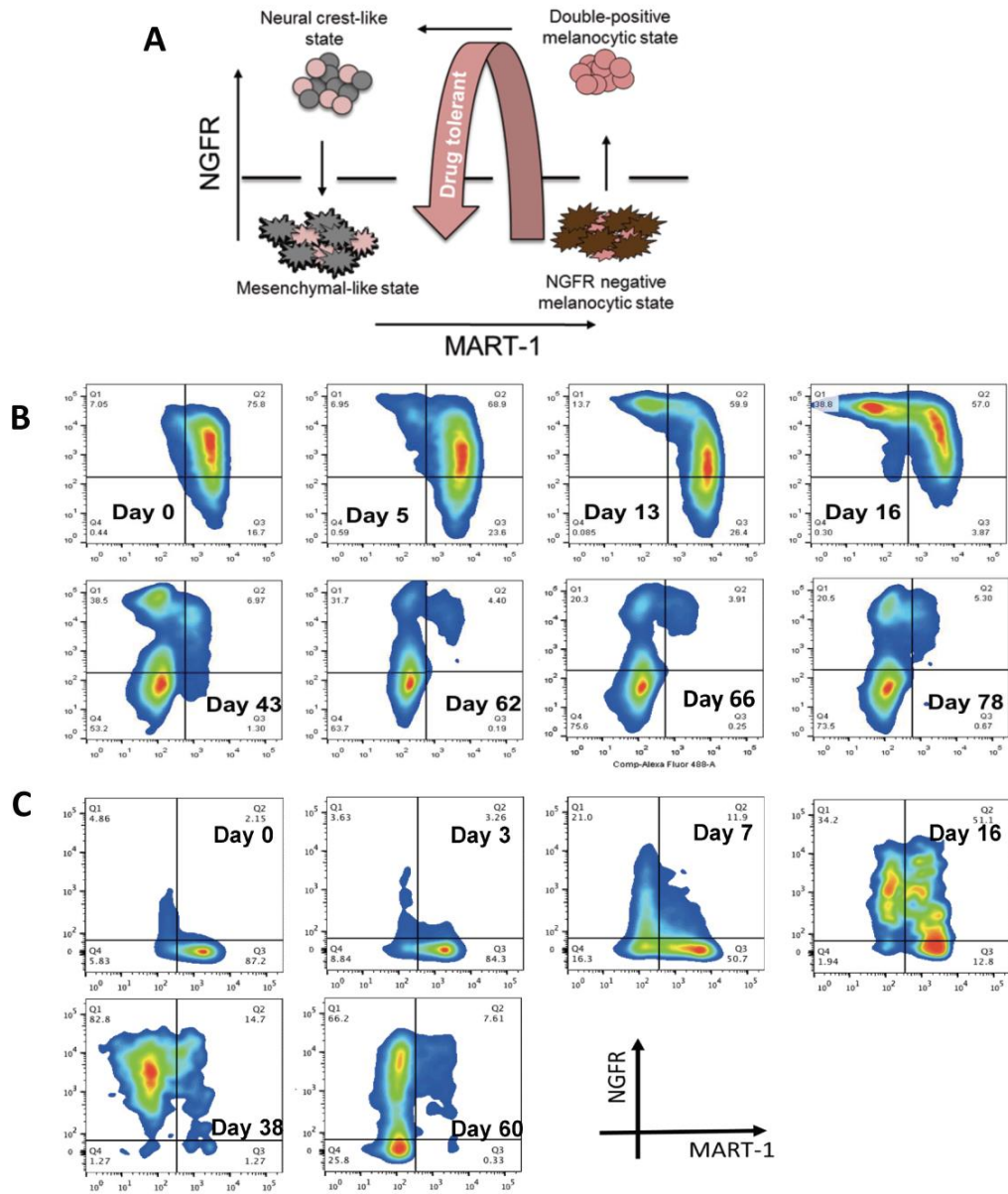


Fig 5. Potential landscapes describing the drug-induced phenotypic evolution from melanocyte to mesenchymal phenotype for M397. (A) The landscape of scalar potential extracted from the modified FP-type (Eq. 3) kinetic model. The blue, cyan, and orange arrows indicate regions dominated by melanocytic (MART1+/NGFR±), neural-crest (MART1+/NFGR-) and mesenchymal (MART1-/NGFR-) phenotypes, respectively. (B) The free energy-like potential calculated by surprisal analysis shows the relative cell state stability with respect to the global steady state across different time points. The blue, cyan, and orange circles represent cell populations primarily at melanocytic, neural-crest and mesenchymal phenotypes at the respective time points. (C) Comparison between normalized free energy-like potential (from surprisal analysis, orange bar) and scalar potential (from modified FP-type kinetic model, blue bar) for D73, calculated from transcriptional profiles of unsorted and sorted NGFR-/MART-1- mesenchymal cells. (D) Cartoon illustration of the competition between state-dependent net growth and system stabilization towards the attractor state upon drug treatment.

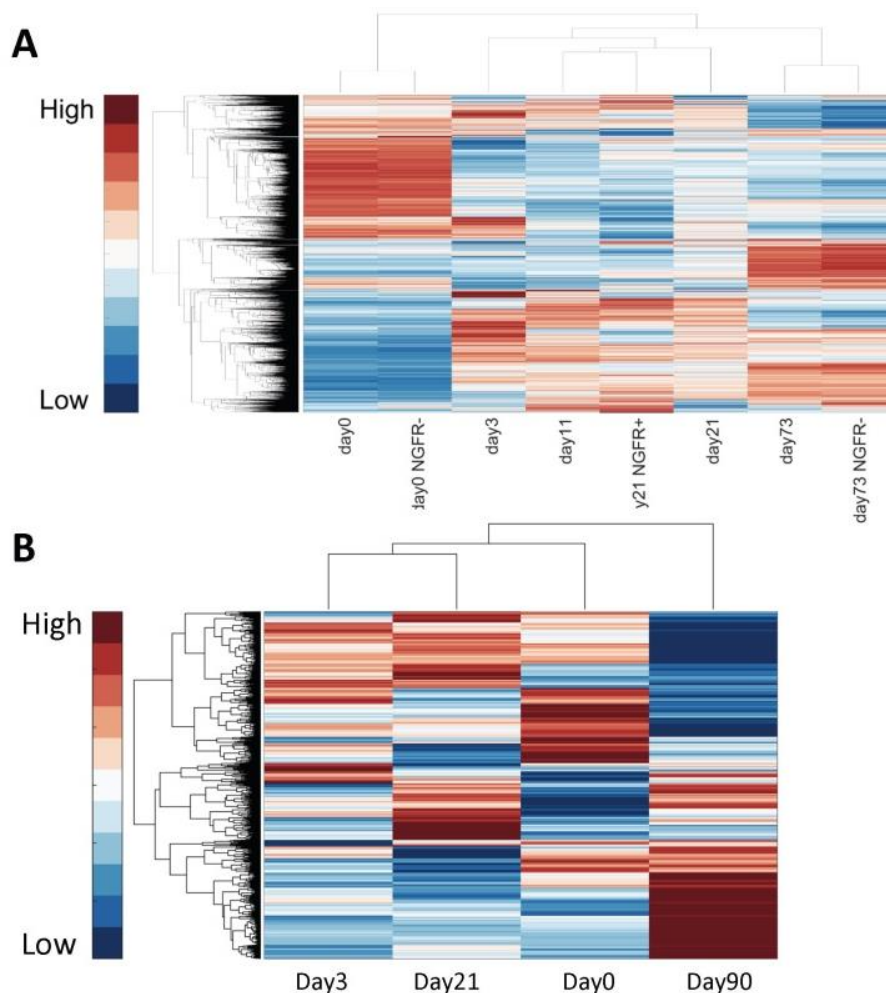
Supplementary Information

Supplementary figures

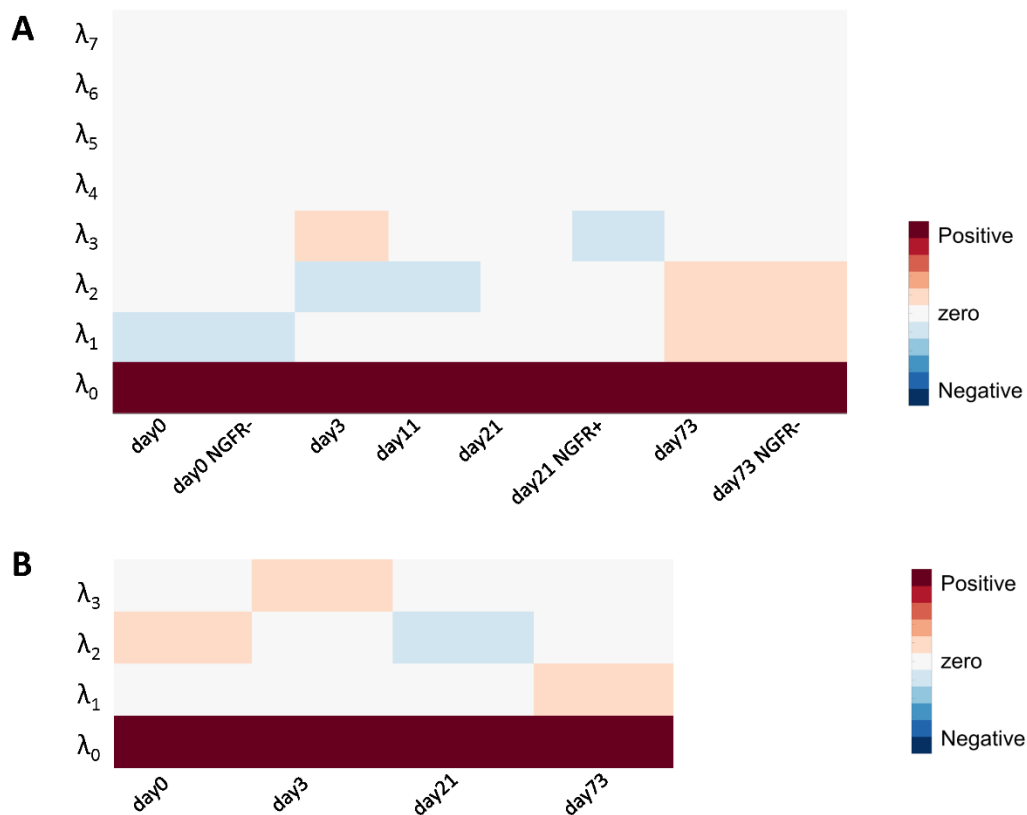


S1 Fig. Kinetic flow cytometry data of drug-induced phenotypic evolution. A. Cartoon illustration of the BRAFi-induced transition where the melanoma cells take an approximately counterclockwise trajectory around the flow cytometry plot. B. Flow cytometry plots of NGFR and MART-1 protein markers for M397 at a set of the points over the drug-induced phenotypic evolution. Data are represented as a 2-dimensional density plot for each day. As

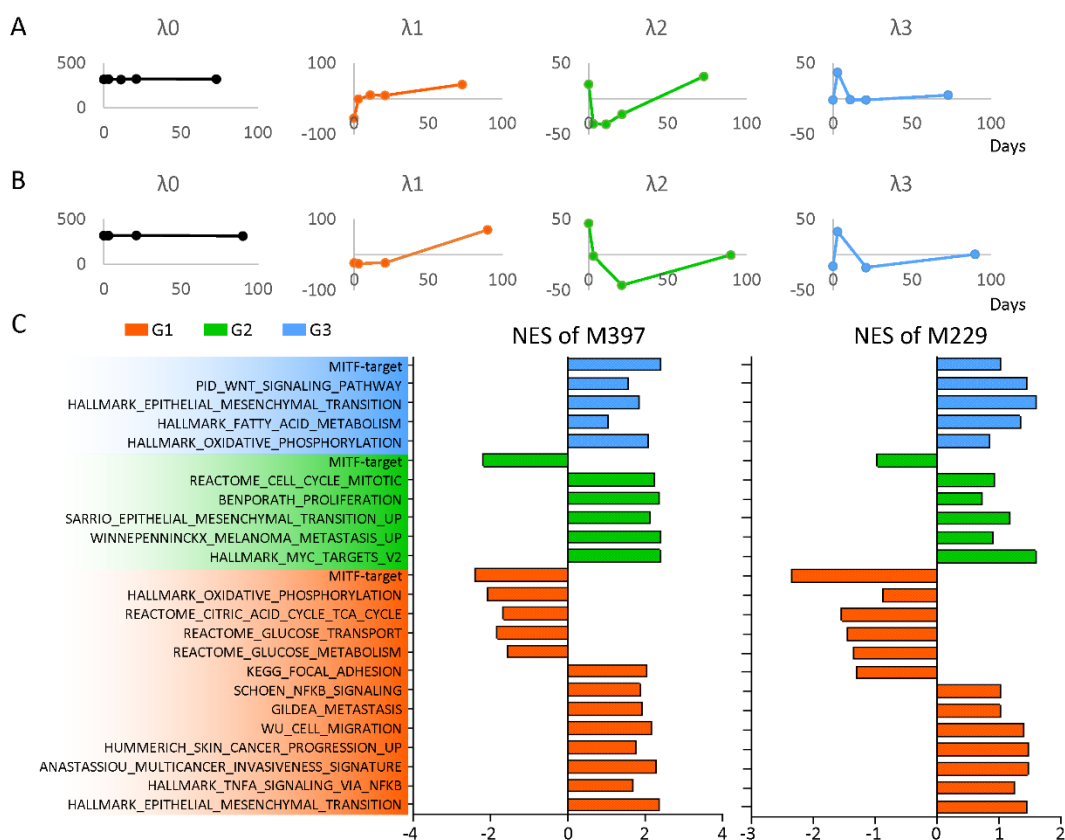
the de-differentiation transition occurs from day 0 to day 78, the cell population moves along a counterclockwise trajectory. C. Flow cytometry plots of NGFR and MART-1 protein markers for M229 at a set of the points over the drug-induced phenotypic evolution.



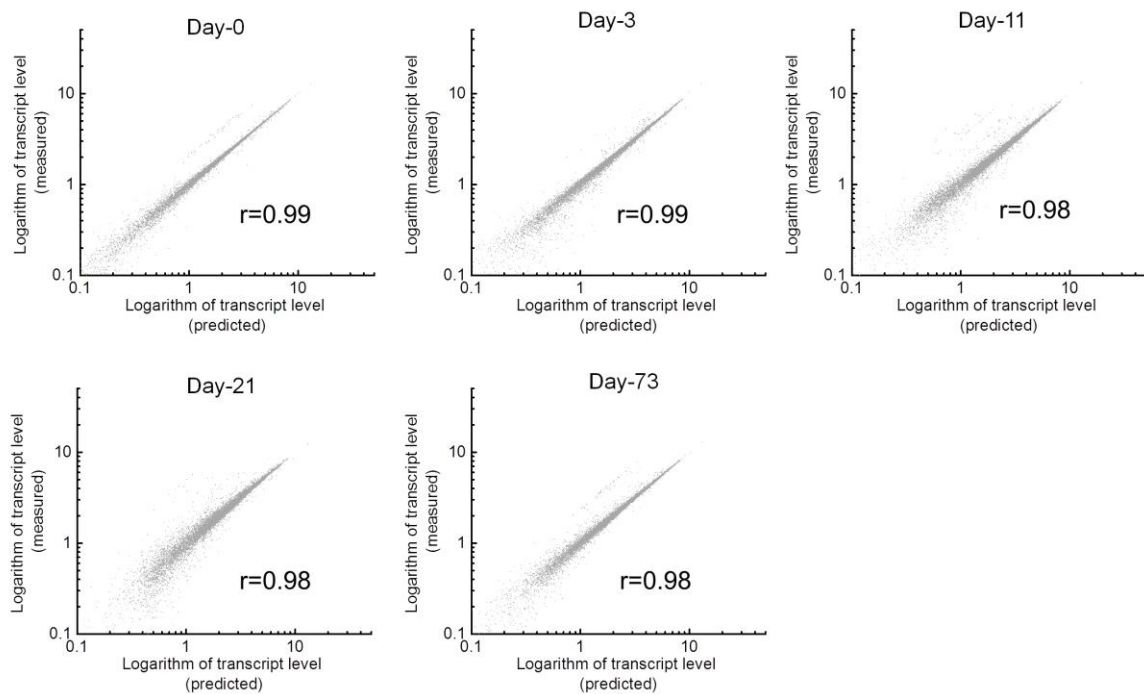
S2 Fig. Heatmap and hierarchical clustering for transcriptomic data of M397 and M229 cells under different drug treatment and/or sorting conditions. A is for M397 and B is for M229. Each Row of the heatmap indicates each gene. Each column is a sample condition, as indicated. Color represents gene expression level, with up-regulated genes colored in red and down-regulated genes colored in blue. Different molecular baselines of the two melanoma cell lines dictate distinct clustering patterns that require Surprisal analysis to resolve the altered molecular features shared by the two cell lines across the transition.



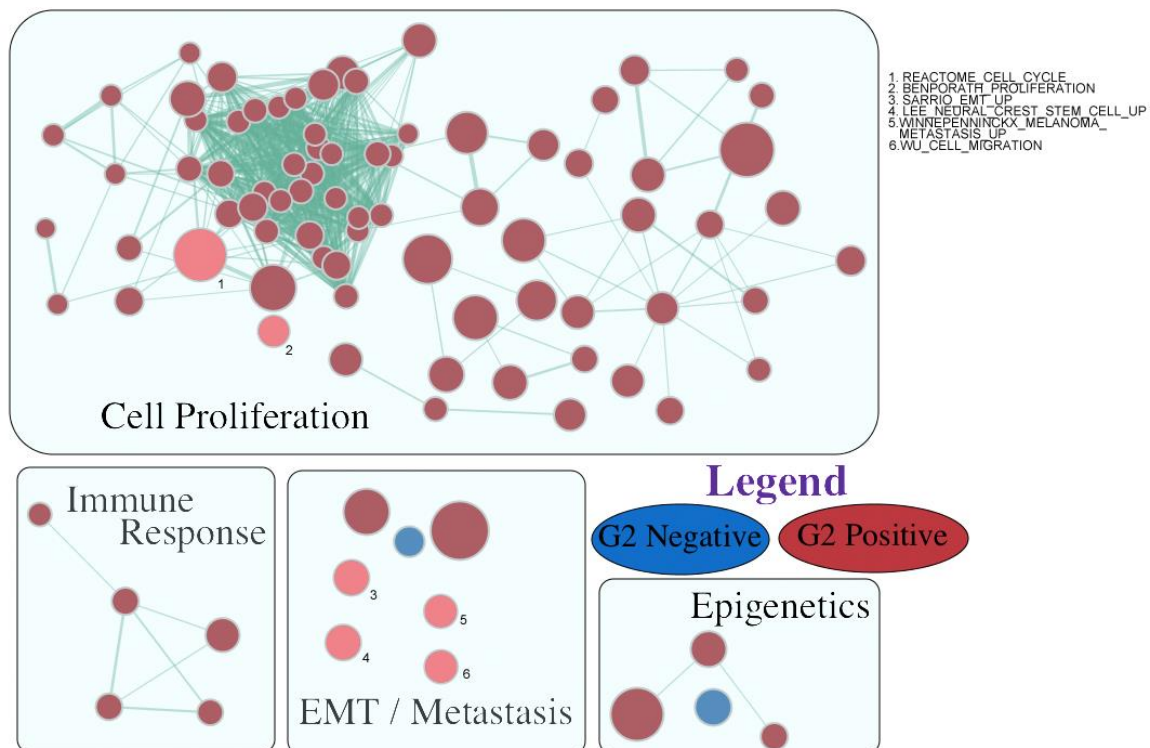
S3 Fig. Heatmap visualization of amplitudes for steady state and different constraints across different samples of M397 and M229. M397 data is shown in panel A and that of M229 is shown in panel B. Each row indicates a constraint, with λ_0 the global stable state. Each column is a sample condition, as indicated. Positive valued constraints are red, and negative are blue.



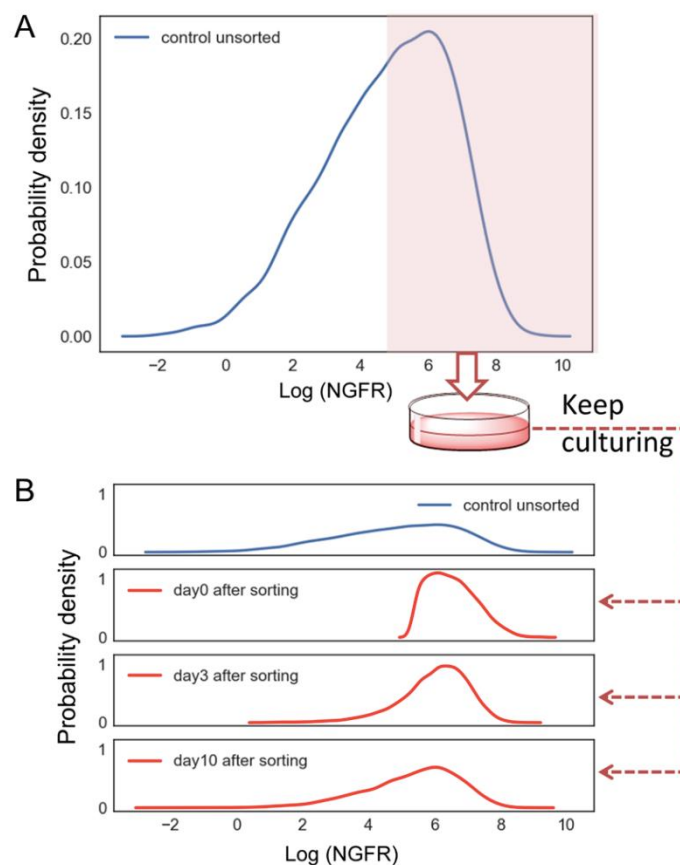
S4 Fig. Comparison of surprisal analysis result between M397 and M229. A. The amplitude of steady state and top three constraints across different time points determined by surprisal analysis of M397 cell line. B. The amplitude of steady state and top three constraints across different time points determined by surprisal analysis of M229 cell line. C. Gene set enrichment of the three constrained processes for the phenotypic and functional changes of M397 (left) and M229 (right) over the drug-induced phenotypic evolution. Each bar represents one enriched gene sets associated with the top three constraints as indicated by their respective colors. Value represents the normalized enrichment score (NES) calculated from GSEA.



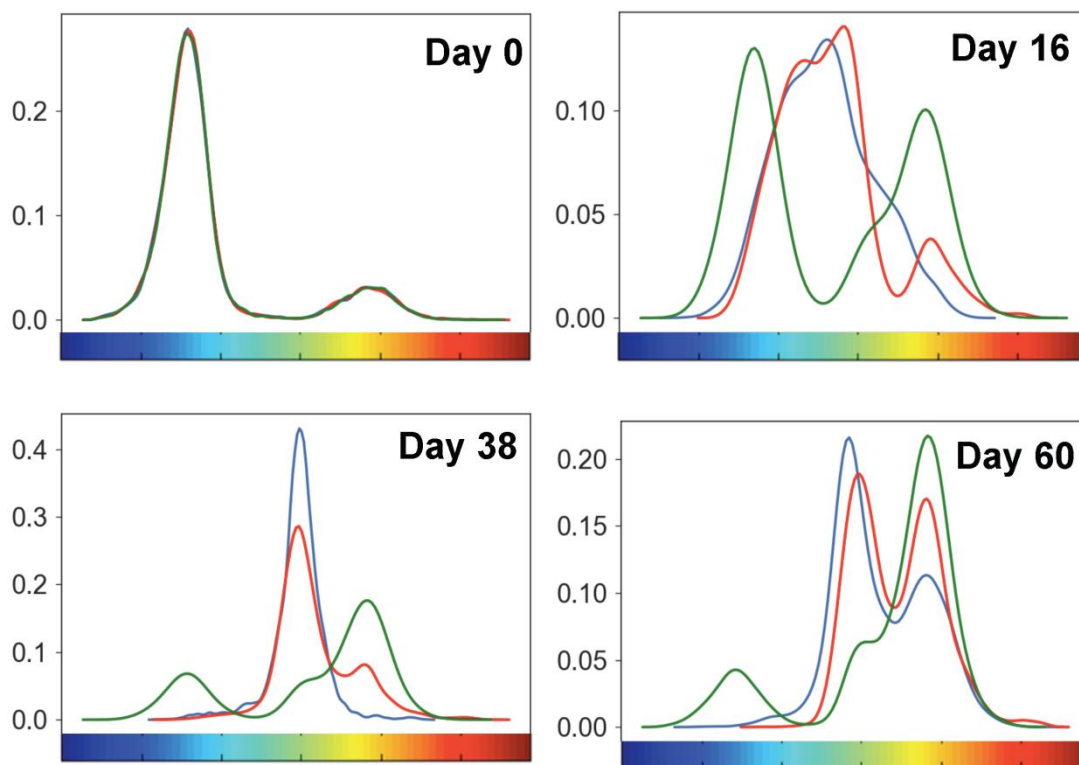
S5 Fig. Scatter plot comparison of the measured versus the predicted gene expression levels for M397 from surprisal analysis across different time points, using the global stable state and top three constraints.



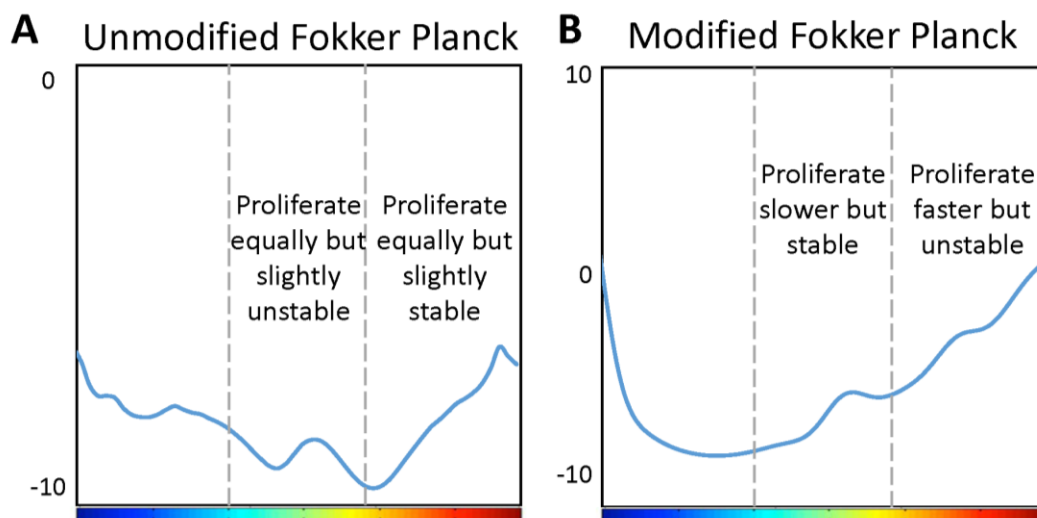
S6 Fig. Enrichment map of the enriched gene sets in the second constraint, as identified by GSEA.



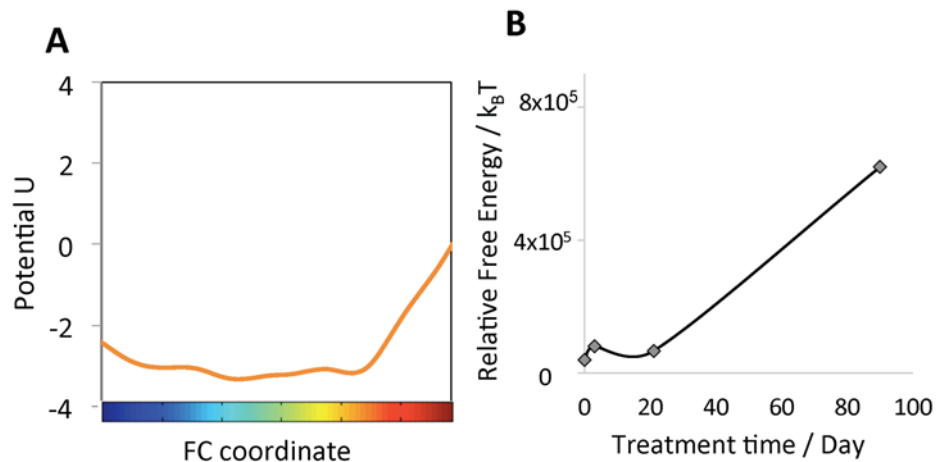
S7 Fig. Cell sorting and relaxation experiments of M397. A. Illustration of cell sorting experiments. Cells cultured without drug treatment are harvested and stained with NGFR antibody. A flow cytometer separates the NGFR+ live cell subpopulations and the sorted cells are then cultured in the same condition as before sorting. The NGFR and MART-1 (not changing) expression levels are measured for subsequent days as the population re-equilibrates towards the unsorted steady state distribution. B. Flow cytometry data of log NGFR level from cell sorting experiment. The relaxation dynamics of the sorted subpopulation is measured using flow cytometry. Dataset illustrated here was later modeled by a Fokker-Planck equation to determine the diffusion constant of the system.



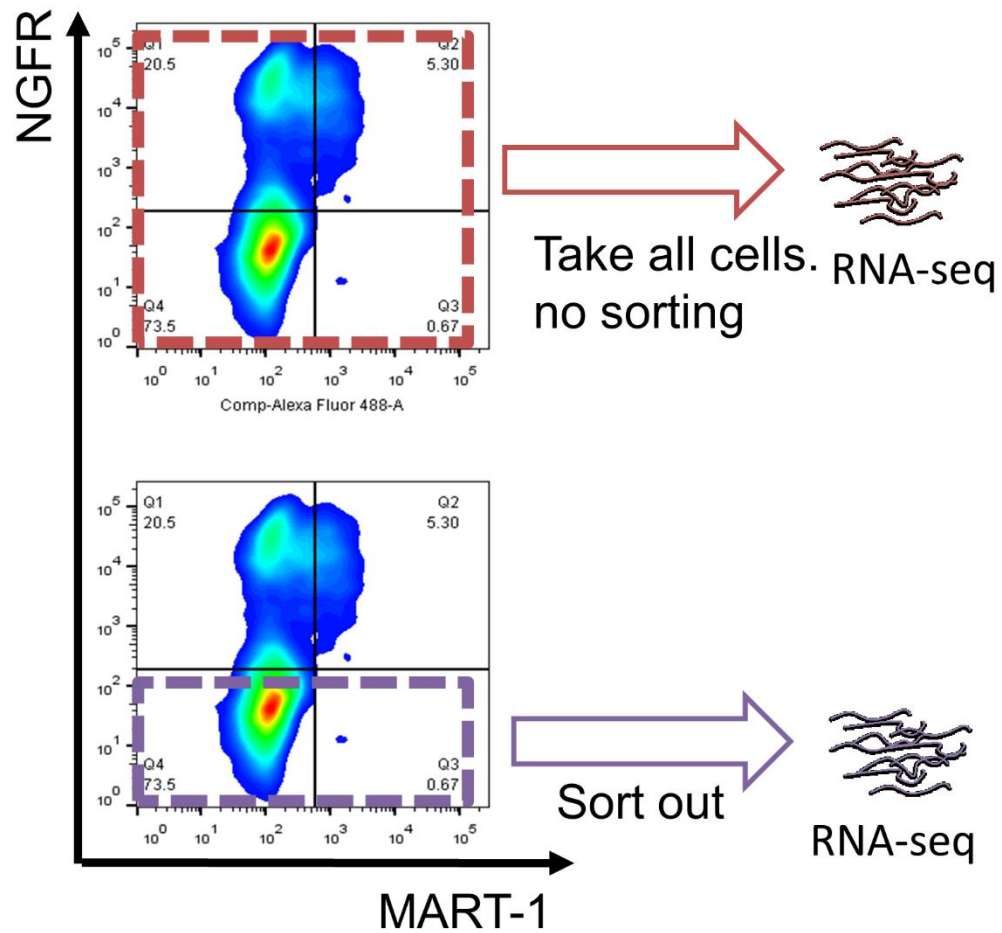
S8 Fig. The measured and predicted cell probability density distribution of M229 along reaction coordinate x at various time points. Blue line: experimental data distribution. Green line: predicted distribution using the original Fokker-Planck model (FP model). Red line: predicted distribution from the modified FP-type kinetic model that includes a state-dependent net growth rate.



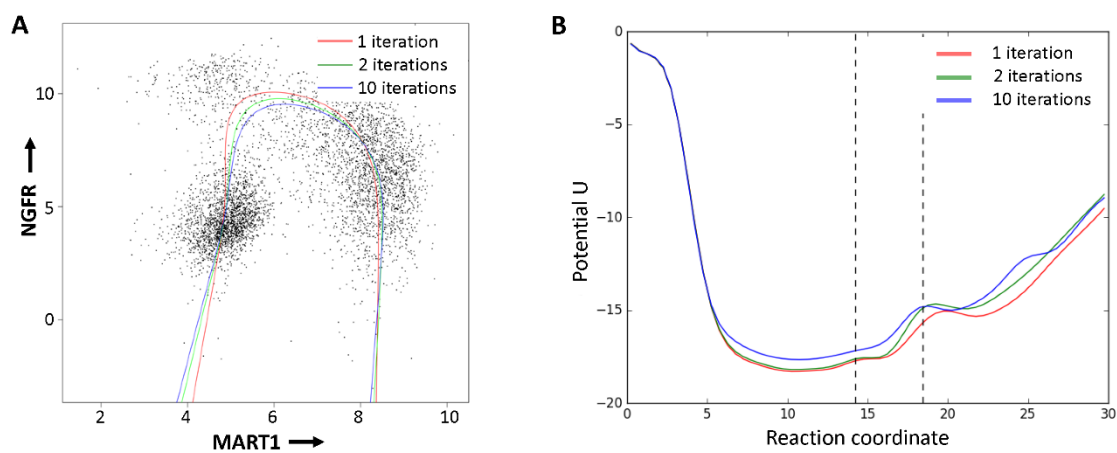
S9 Fig. Comparison of potential calculated from unmodified and modified Fokker-Planck-type kinetic models. Potential landscape calculated from unmodified Fokker-Planck model is shown in panel A and the one from modified FP-type kinetic model is shown in panel B.



S10 Fig. The potential landscapes describing the drug-induced phenotypic evolution from melanocytic to mesenchymal phenotype for M229. A. Potential landscape extracted from modified FP-type kinetic model. B. The free energy-like potential calculated by surprisal analysis shows the relative change in stability with respect to the global stable state across different time points.



S11 Fig. Illustration of cell sorting for NGFR negative phenotype of M397 at day 73. To validate the free energy calculation from the surprisal analysis, pure NGFR-/MART- subpopulation was sorted using flow cytometry for RNA sequencing and compared against RNA-seq from unsorted cells.



S12 Fig. Sensitivity analysis of “Principal Curve”. A. Three principal curves calculated with different iteration number. B. Potential U calculated for all three different principal curves.

Supplementary tables

S1 Table: Kinetic RNA-seq data for M397 and M229 cells.
(<https://doi.org/10.1371/journal.pcbi.1007034.s013>)

S2 Table: The top 100 genes that contribute positively and negatively to the top3 constraints. (<https://doi.org/10.1371/journal.pcbi.1007034.s014>)

References

1. Nathanson D, Gini B, Mottahedeh J, Visnyei K, Koga T, Gomez G, et al. Targeted therapy resistance mediated by dynamic regulation of extrachromosomal mutant EGFR DNA. *Science*. 2014;343:72-6. Epub 2013 Dec 5. doi: 10.1126/science.1241328. PubMed Central PMCID: PMC4049335.
2. Flavahan WA, Gaskell E, Bernstein BE. Epigenetic plasticity and the hallmarks of cancer. *Science*. 2017;357(6348). doi: 10.1126/science.aal2380.
3. Sharma SV, Lee DY, Li B, Quinlan MP, Takahashi F, Maheswaran S, et al. A Chromatin-Mediated Reversible Drug-Tolerant State in Cancer Cell Subpopulations. *Cell*. 141(1):69-80. doi: 10.1016/j.cell.2010.02.027.
4. Liao BB, Sievers C, Donohue LK, Gillespie SM, Flavahan WA, Miller TE, et al. Adaptive Chromatin Remodeling Drives Glioblastoma Stem Cell Plasticity and Drug Tolerance. *Cell Stem Cell*. 20(2):233-46.e7. doi: 10.1016/j.stem.2016.11.003.
5. Su Y, Wei W, Robert L, Xue M, Tsoi J, Garcia-Diaz A, et al. Single-cell analysis resolves the cell state transition and signaling dynamics associated with melanoma drug-induced resistance. *Proc Natl Acad Sci U S A*. 2017;114(52):13679-84. doi: 10.1073/pnas.1712064115. PubMed PMID: 29229836; PubMed Central PMCID: PMC5748184.
6. Meyer M, Fleming J, Ali M, Pesesky M, Ginsburg E, Vonderhaar B. Dynamic regulation of CD24 and the invasive, CD44pos CD24neg phenotype in breast cancer cell lines. *Breast Cancer Res*. 2009;11(5):R82. doi: 10.1186/bcr2449.
7. Kreso A, O'Brien CA, van Galen P, Gan OI, Notta F, Brown AMK, et al. Variable Clonal Repopulation Dynamics Influence Chemotherapy Response in Colorectal Cancer. *Science*. 2013;339(6119):543-8. doi: 10.1126/science.1227670.
8. Goldman A, Majumder B, Dhawan A, Ravi S, Goldman D, Kohandel M, et al. Temporally sequenced anticancer drugs overcome adaptive resistance by targeting a vulnerable chemotherapy-induced phenotypic transition. *Nature Communications*. 2015;6:1-13. doi: DOI: 10.1038/ncomms7139.
9. Fallahi-Sichani M, Becker V, Izar B, Baker GJ, Lin JR, Boswell SA, et al. Adaptive resistance of melanoma cells to RAF inhibition via reversible induction of a slowly dividing de-differentiated state. *Mol Syst Biol*. 2017;13(1):905. doi: 10.15252/msb.20166796. PubMed PMID: 28069687; PubMed Central PMCID: PMC5248573.
10. Sun C, Wang L, Huang S, Heynen GJ, Prahallad A, Robert C, et al. Reversible and adaptive resistance to BRAF(V600E) inhibition in melanoma. *Nature*. 2014;508(7494):118-22. doi: 10.1038/nature13121

11. Ramsdale R, Jorissen RN, Li FZ, Al-Obaidi S, Ward T, Sheppard KE, et al. The transcription cofactor c-JUN mediates phenotype switching and BRAF inhibitor resistance in melanoma. *Science Signaling*. 2015;8(390):ra82-ra. doi: 10.1126/scisignal.aab1111.
12. Gupta PB, Fillmore CM, Jiang G, Shapira SD, Tao K, Kuperwasser C, et al. Stochastic state transitions give rise to phenotypic equilibrium in populations of cancer cells. *Cell*. 2011;146(4):633-44. doi: 10.1016/j.cell.2011.07.026. PubMed PMID: 21854987.
13. Zhou JX, Pisco AO, Qian H, Huang S. Nonequilibrium population dynamics of phenotype conversion of cancer cells. *PLoS One*. 2014;9(12):e110714. doi: 10.1371/journal.pone.0110714. PubMed PMID: 25438251; PubMed Central PMCID: PMC4249833.
14. Mojtahedi M, Skupin A, Zhou J, Castano IG, Leong-Quong RY, Chang H, et al. Cell Fate Decision as High-Dimensional Critical State Transition. *PLoS Biol*. 2016;14(12):e2000640. doi: 10.1371/journal.pbio.2000640. PubMed PMID: 28027308; PubMed Central PMCID: PMC45189937.
15. Wei W, Shi Q, Remacle F, Qin L, Shackelford D, Shin YS, et al. Hypoxia Induces a Phase Transition within a Kinase Signaling Network in Cancer Cells. *Proc Natl Acad Sci*. 2013;110:e1352-e60. doi: 10.1073/pnas.1303060110.
16. Zadrán S, Arumugam R, Herschman H, Phelps ME, Levine RD. Surprisal analysis characterizes the free energy time course of cancer cells undergoing epithelial-to-mesenchymal transition. *Proc Natl Acad Sci U S A*. 2014;111(36):13235-40. doi: 10.1073/pnas.1414714111. PubMed PMID: 25157127; PubMed Central PMCID: PMC4246928.
17. Sisan DR, Halter M, Hubbard JB, Plant AL. Predicting rates of cell state change caused by stochastic fluctuations using a data-driven landscape model. *Proc Natl Acad Sci U S A*. 2012;109(47):19262-7. doi: 10.1073/pnas.1207544109. PubMed PMID: 23115330; PubMed Central PMCID: PMC3511108.
18. Ridden SJ, Chang HH, Zygalkakis KC, MacArthur BD. Entropy, Ergodicity, and Stem Cell Multipotency. *Phys Rev Lett*. 2015;115(20):208103. doi: 10.1103/PhysRevLett.115.208103. PubMed PMID: 26613476.
19. Lu M, Jolly MK, Levine H, Onuchic JN, Ben-Jacob E. MicroRNA-based regulation of epithelial-hybrid-mesenchymal fate determination. *Proc Natl Acad Sci U S A*. 2013;110(45):18144-9. doi: 10.1073/pnas.1318192110. PubMed PMID: 24154725; PubMed Central PMCID: PMC3831488.
20. MacArthur BD, Sanchez-Garcia RJ, Ma'ayan A. Microdynamics and criticality of adaptive regulatory networks. *Phys Rev Lett*. 2010;104(16):168701. doi: 10.1103/PhysRevLett.104.168701. PubMed PMID: 20482087; PubMed Central PMCID: PMC2925242.
21. Chapman PB, Hauschild A, Robert C, Haanen JB, Ascierto P, Larkin J, et al. Improved Survival with Vemurafenib in Melanoma with BRAF V600E Mutation. *New England*

- Journal of Medicine. 2011;364(26):2507-16. doi: 10.1056/NEJMoa1103782. PubMed PMID: 21639808.
22. Tsoi J, Robert L, Paraiso K, Galvan C, Sheu KM, Lay J, et al. Multi-stage Differentiation Defines Melanoma Subtypes with Differential Vulnerability to Drug-Induced Iron-Dependent Oxidative Stress. *Cancer Cell*. 2018. doi: 10.1016/j.ccell.2018.03.017. PubMed PMID: 29657129.
23. Remacle F, Kravchenko-Balasha N, Levitzki A, Levine RD. Information-theoretic analysis of phenotype changes in early stages of carcinogenesis. *Proceedings of the National Academy of Sciences*. 2010;107(22):10324-9. doi: 10.1073/pnas.1005283107.
24. Wang J, Xu L, Wang E. Potential landscape and flux framework of nonequilibrium networks: robustness, dissipation, and coherence of biochemical oscillations. *Proc Natl Acad Sci U S A*. 2008;105(34):12271-6. doi: 10.1073/pnas.0800579105. PubMed PMID: 18719111; PubMed Central PMCID: PMCPMC2527901.
25. Landsberg J, Kohlmeyer J, Renn M, Bald T, Rogava M, Cron M, et al. Melanomas resist T-cell therapy through inflammation-induced reversible dedifferentiation. *Nature*. 2012;490(7420):412-6. doi: 10.1038/nature11538. PubMed PMID: 23051752.
26. Levine RD. *Molecular reaction dynamics*. Cambridge, UK ; New York: Cambridge University Press; 2005. xiv, 554 p. p.
27. Poovathingal SK, Kravchenko-Balasha N, Shin YS, Levine RD, Heath JR. Critical Points in Tumorigenesis: A Carcinogen-Initiated Phase Transition Analyzed via Single-Cell Proteomics. *Small*. 2016;12(11):1425-31. doi: 10.1002/sml.201501178. PubMed PMID: 26780498; PubMed Central PMCID: PMCPMC4886749.
28. Kravchenko-Balasha N, Levitzki A, Goldstein A, Rotter V, Gross A, Remacle F, et al. On a fundamental structure of gene networks in living cells. *Proc Natl Acad Sci U S A*. 2012;109(12):4702-7. doi: 10.1073/pnas.1200790109. PubMed PMID: 22392990; PubMed Central PMCID: PMCPMC3311329.
29. Eichler GS, Huang S, Ingber DE. Gene Expression Dynamics Inspector (GEDI): for integrative analysis of expression profiles. *Bioinformatics*. 2003;19(17):2321-2. PubMed PMID: 14630665.
30. Alter O, Brown PO, Botstein D. Singular value decomposition for genome-wide expression data processing and modeling. *Proc Natl Acad Sci U S A*. 2000;97(18):10101-6. PubMed PMID: 10963673; PubMed Central PMCID: PMCPMC27718.
31. Frederick DT, Piris A, Cogdill AP, Cooper ZA, Lezcano C, Ferrone CR, et al. BRAF inhibition is associated with enhanced melanoma antigen expression and a more favorable tumor microenvironment in patients with metastatic melanoma. *Clin Cancer Res*. 2013;19(5):1225-31. doi: 10.1158/1078-0432.CCR-12-1630. PubMed PMID: 23307859; PubMed Central PMCID: PMCPMC3752683.
32. Boni A, Cogdill AP, Dang P, Udayakumar D, Njauw CN, Sloss CM, et al. Selective BRAFV600E inhibition enhances T-cell recognition of melanoma without affecting

- lymphocyte function. *Cancer Res.* 2010;70(13):5213-9. doi: 10.1158/0008-5472.CAN-10-0118. PubMed PMID: 20551059.
33. Titz B, Lomova A, Le A, Hugo W, Kong X, Ten Hoeve J, et al. JUN dependency in distinct early and late BRAF inhibition adaptation states of melanoma. *Cell Discov.* 2016;2:16028. doi: 10.1038/celldisc.2016.28. PubMed PMID: 27648299; PubMed Central PMCID: PMC5012007.
34. Huang S, Eichler G, Bar-Yam Y, Ingber DE. Cell fates as high-dimensional attractor states of a complex gene regulatory network. *Physical Review Letters.* 2005;94(12). doi: ARTN 128701
10.1103/PhysRevLett.94.128701. PubMed PMID: WOS:000228065600072.
35. Risken H. *The Fokker-Planck equation : methods of solution and applications.* 2nd ed. New York: Springer-Verlag; 1996. xiv, 472 p. p.
36. Hill TL. *Thermodynamics of small systems.* Dover edition 2013 . ed. Mineola, New York: Dover Publications, Inc.
Courier Corporation; 2013. 2 volumes in 1 (xii, 171 viii, 201 pages) p.
37. Niven RK. Minimization of a free-energy-like potential for non-equilibrium flow systems at steady state. *Philos T R Soc B.* 2010;365(1545):1323-31. doi: 10.1098/rstb.2009.0296. PubMed PMID: WOS:000276272200004.
38. Egolf DA. Equilibrium regained: from nonequilibrium chaos to statistical mechanics. *Science.* 2000;287(5450):101-4. PubMed PMID: 10615038.
39. Jaynes ET. Information Theory and Statistical Mechanics. *Phys Rev.* 1957;106(4):620-30. doi: DOI 10.1103/PhysRev.106.620. PubMed PMID: WOS:A1957WB72300004.
40. Levine RD. Information-Theory Approach to Molecular Reaction Dynamics. *Annu Rev Phys Chem.* 1978;29:59-92. doi: DOI 10.1146/annurev.pc.29.100178.000423. PubMed PMID: WOS:A1978FW00500003.
41. Remalec F, Graeber TG, Levine RD. Whose Entropy: A Maximal Entropy Analysis of Phosphorylation Signaling. *J Stat Phys.* 2011;144(2):429-42. doi: 10.1007/s10955-011-0215-x. PubMed PMID: WOS:000293301000012.
42. Jolly MK, Tripathi SC, Jia D, Mooney SM, Celiktas M, Hanash SM, et al. Stability of the hybrid epithelial/mesenchymal phenotype. *Oncotarget.* 2016;7(19):27067-84. doi: 10.18632/oncotarget.8166. PubMed PMID: 27008704; PubMed Central PMCID: PMC5053633.
43. Liao BB, Sievers C, Donohue LK, Gillespie SM, Flavahan WA, Miller TE, et al. Adaptive Chromatin Remodeling Drives Glioblastoma Stem Cell Plasticity and Drug Tolerance. *Cell Stem Cell.* 2017;20(2):233-46 e7. doi: 10.1016/j.stem.2016.11.003. PubMed PMID: 27989769; PubMed Central PMCID: PMC5291795.
44. Vogel CJ, Smit MA, Maddalo G, Possik PA, Sparidans RW, van der Burg SH, et al. Cooperative induction of apoptosis in NRAS mutant melanoma by inhibition of MEK and

- ROCK. *Pigment Cell Melanoma Res.* 2015;28(3):307-17. doi: 10.1111/pcmr.12364. PubMed PMID: 25728708.
45. Atefi M, Avramis E, Lassen A, Wong DJ, Robert L, Foulad D, et al. Effects of MAPK and PI3K pathways on PD-L1 expression in melanoma. *Clin Cancer Res.* 2014;20(13):3446-57. doi: 10.1158/1078-0432.CCR-13-2797. PubMed PMID: 24812408; PubMed Central PMCID: PMC4079734.
46. Kim D, Pertea G, Trapnell C, Pimentel H, Kelley R, Salzberg SL. TopHat2: accurate alignment of transcriptomes in the presence of insertions, deletions and gene fusions. *Genome Biol.* 2013;14(4):R36. doi: 10.1186/gb-2013-14-4-r36. PubMed PMID: 23618408; PubMed Central PMCID: PMC4053844.
47. Trapnell C, Williams BA, Pertea G, Mortazavi A, Kwan G, van Baren MJ, et al. Transcript assembly and quantification by RNA-Seq reveals unannotated transcripts and isoform switching during cell differentiation. *Nat Biotechnol.* 2010;28(5):511-5. doi: 10.1038/nbt.1621. PubMed PMID: 20436464; PubMed Central PMCID: PMC3146043.
48. Subramanian A, Tamayo P, Mootha VK, Mukherjee S, Ebert BL, Gillette MA, et al. Gene set enrichment analysis: a knowledge-based approach for interpreting genome-wide expression profiles. *Proc Natl Acad Sci U S A.* 2005;102(43):15545-50. doi: 10.1073/pnas.0506580102. PubMed PMID: 16199517; PubMed Central PMCID: PMC1239896.
49. Shannon P, Markiel A, Ozier O, Baliga NS, Wang JT, Ramage D, et al. Cytoscape: a software environment for integrated models of biomolecular interaction networks. *Genome Res.* 2003;13(11):2498-504. doi: 10.1101/gr.1239303. PubMed PMID: 14597658; PubMed Central PMCID: PMC403769.
50. Merico D, Isserlin R, Stueker O, Emili A, Bader GD. Enrichment map: a network-based method for gene-set enrichment visualization and interpretation. *PLoS One.* 2010;5(11):e13984. doi: 10.1371/journal.pone.0013984. PubMed PMID: 21085593; PubMed Central PMCID: PMC2981572.

TRAJECTORIES FROM SNAPSHOTS: INTEGRATED PROTEOMIC AND METABOLIC SINGLE-CELL ASSAYS REVEAL MULTIPLE INDEPENDENT ADAPTIVE RESPONSES TO DRUG TOLERANCE IN A BRAF-MUTANT MELANOMA CELL LINE

The determination of individual cell trajectories through a high-dimensional cell-state space is an outstanding challenge, with relevance towards understanding biological changes ranging from cellular differentiation to epigenetic (adaptive) responses of diseased cells to drugging. We report on a combined experimental and theoretic method for determining the trajectories that specific highly plastic BRAFV600E mutant patient-derived melanoma cancer cells take between drug-naïve and drug-tolerant states. Recent studies have implicated non-genetic, fast-acting resistance mechanisms are activated in these cells following BRAF inhibition. While single-cell highly multiplex omics tools can yield snapshots of the cell state space landscape sampled at any given time point, individual cell trajectories must be inferred from a kinetic series of snapshots, and that inference can be confounded by stochastic cell state switching. Using a microfluidic-based single-cell integrated proteomic and metabolic assay, we assayed for a panel of signaling, phenotypic, and metabolic regulators at four time points during the first five days of drug treatment. Dimensional reduction of the resultant data set, coupled with information theoretic analysis, uncovered a complex cell state landscape and identified two distinct paths connecting drug-naïve and drug-tolerant states. Cells are shown to exclusively traverse one of the two pathways depending on the level of the lineage restricted transcription factor MITF in the drug-naïve cells. The two trajectories are associated with distinct signaling and metabolic susceptibilities, and are independently druggable. Our results update the paradigm of adaptive resistance development in an isogenic cell population and offer insight into the design of more effective combination therapies.

This chapter includes content from our previously published article:

- [1] Su, Yapeng, Guideng Li, Melissa E. Ko, Hanjun Cheng, Ronghui Zhu, Min Xue, Jessica Wang et al. "Trajectories from Snapshots: Integrated proteomic and metabolic single-cell assays reveal multiple independent adaptive responses to drug tolerance in a BRAF-mutant melanoma cell line." *Nature Communications* (Under revision). doi: 10.1101/767988

Introduction

Cellular processes ranging from the development of drug-tolerant states in cancer cells to stem cell differentiation, can be described as cell state changes. Specifically, certain cancer cells that are initially responsive to targeted inhibitors that act against these oncogenic drivers[1–4] can evolve into a drug-tolerant state via non-genetic mechanisms, perhaps preceding the emergence of drug-resistant clones[5–7]. The molecular details of how the cancer cells transition between the two states can inform the use of additional drugs designed to arrest the transition[8–10]. Dating back to the epigenetic landscapes of Waddington[11], a prevalent picture is that cells take a single path that connects the initial to the final state, but this does not have to be the case. In fact, if cells can take multiple independent paths between the two states, then the challenge of finding drug combination that can arrest the unfavorable cell state transition is significantly increased. Here we investigate a highly plastic cancer cell line that, when treated with a targeted inhibitor, switches from a rapidly dividing, drug responsive state to a drug-tolerant, slow cycling state within a few days. We show that the cells can take multiple classes of trajectories between the two states. Each trajectory class is characterized by a unique signaling and metabolic networks with distinct druggable susceptibilities.

From a functional perspective, cell state changes are often accompanied by changes in gene expression[10,12–15], protein signaling[12,14,16–22] and cellular metabolism.[23–26] Highly multiplex single-cell methods[27–30] can provide powerful tools for mapping out cell-state landscapes associated with cell state changes[20,31–35]. However, capturing the trajectories that individual cells take as they traverse those landscapes is challenging, even for the case of an isogenic cell line. This is because multiplex single-cell omics methods only provide snapshots of the occupied cell state space at a given instant. Measured similarities between cells captured at successive time points can imply probable paths through the landscape[36–40]. However, cells may stochastically switch from one state to another, so an individual cell may not take a smooth trajectory between states. Time-lapse imaging methods can map individual cell trajectories, but for only a couple of analytes for each cell, and so provide a limited view of the cell state space[41–43]. Thus, the ability to extract cellular trajectories from a kinetic series of cell state space snapshots would have high value. Here we report on combined experimental and theoretical approaches towards addressing this fundamental challenge.

We utilized a patient-derived *BRAF*^{V600E} mutant melanoma cancer cell line as a model for the rapid development of drug tolerance against targeted inhibitors. Under BRAF inhibition, these highly plastic cells rapidly (and reversibly) transition from a drug-responsive state to a drug-tolerant state[12,19]. We characterized this transition using

integrated single-cell functional proteomic and metabolic assays designed to broadly sample proteins and metabolites associated with selected cancer hallmarks and cell state-specific processes. Dimensional reduction, information-theoretic analysis, and visualization of the time-series single-cell data uncovered a complex cell state space landscape, and hinted at the possibility of two distinct paths between drug-naïve and drug tolerant states. Further experiments tested whether these paths constituted independent (and thus independently druggable) cellular trajectories. In fact, we find that even isogenic tumor cells can undertake different, independent trajectories to drug tolerance. The two trajectories are associated with distinct signaling and metabolic networks, and are independently druggable. This finding challenges the current paradigm of targeted inhibitor resistance development, and also provides guidelines for assessing the value of combination therapies.

Results

Integrated single-cell proteomic and metabolic analysis characterizes early BRAFi adaptation in melanoma cells

We characterized drug adaptation in individual melanoma cells by assaying for a panel of selected proteins, plus glucose uptake, in BRAF^{V600E} mutant M397 cell cultures during the first five days of BRAFi treatment using the Single Cell Barcode Chip (SCBC)[12,20,29,44–47] (**Fig 1a**). Following 0, 1, 3, and 5 days (D0 control, D1, D3, and D5) of drug treatment, individual cells were isolated into nanoliter-volume microchambers within an SCBC. Each isolated cell was lysed *in situ* to release the cellular contents. Each microchamber within an SCBC contains a full barcode array in which each barcode element is either an antibody for specific protein capture[48] or a molecular probe designed to assay for a specific metabolite via a competition assay[46,47] (**Fig.1a**). The design of this panel was informed by transcriptomic analysis of BRAFi-treated M397 cells (**Supplementary Fig. 1**) and existing literature[12,14,16,23,49,50]. The panel broadly samples various functional and metabolic hallmarks of cancer, as well as cell state markers.

Single-cell profiling of BRAFi-naïve (D0) M397 cells revealed heterogeneous levels of many assayed markers at baseline. Referring to **Fig. 1b,c and Supplementary Fig. 2**, certain analytes exhibit high variability across the cell population. These include the melanocytic lineage transcription factor MITF and its downstream melanocytic cell state marker MART1, the metabolic regulators HIF1 α and p-AMPK α , and the proliferation marker Ki67. The variance in Ki67 implies that the population contains both rapid-cycling and slow-cycling cells. By contrast, a high glucose uptake and the expression of metabolic enzymes LDH and PKM2 were relatively uniform from cell-to-cell. Drug treatment initially (at D1) inhibits glucose uptake and represses most metabolic regulators and signaling phosphoproteins, as

well as Ki67. The repression of these cancer hallmarks reflects blockage of the key oncogenic signaling pathway upon initial BRAF inhibition. The drug also promotes transient cell differentiation followed by dedifferentiation, as evidenced by an increase of MART1 expression in D3 followed by its downregulation in D5. However, a small subpopulation of M397 cells remains Ki67-high in D1, implying a slower drug response in that subset of cells. At D3, most analytes exhibit a sharp and transitory increase in variance, which shrinks by D5. This change includes all of the metabolic regulators except p-LKB, all resistant state markers and regulators except Slug, all of the metabolic enzymes, and all of the signaling phosphoproteins. The increased magnitude of the fluctuations of many markers at D3, based upon previous reports[45,51], implies one or more cell state changes near this time point. By D5, glucose uptake has increased back to near D0 levels, but with increased variance. Ki67 is further decreased, and with sharply decreased variance relative to D0. Additionally at this day, the variance and abundance of the epithelial–mesenchymal transition (EMT)-related transcription factor, Slug, has increased, indicating the emergence of some cells that are trending towards a mesenchymal phenotype. Further, the levels of the other assayed protein markers that are associated with drug resistance (AXL, N-cadherin, NGFR, and TNFR) are all higher by D5. The upregulation of glucose uptake and many resistance marker indicates that cells have initiated drug resistance programs by D5. Thus, single-cell integrated proteomic and metabolic analysis, when viewed at the level of individual analytes, provides evidence of initial drug response at D1, a drug-induced cell state change at D3, and emerging drug tolerance at D5, prior to an increase in cell proliferation (full drug resistance) which has been shown to occur a few weeks later. These observations are all consistent with existing literature[12,14,16,52,53].

Dimensional reduction analysis implies multiple trajectories towards drug adaptation

Simultaneous visualization of the time-dependent, coordinated changes across multiple markers requires algorithms that can reduce the high-dimensionality of the dataset. We applied two such algorithms: the FLOW-MAP algorithm[54] and the t-SNE algorithm[32]. Both approaches provided an intuitive representation of the dataset (**Fig. 2 and Supplementary Figs. 3 and 4**). FLOW-MAP analysis revealed that melanoma cells clustered primarily based upon drug exposure time (**Fig. 2, upper left plot**) indicating chronological cell state trajectories. Most untreated M397 cells (in the lower left of the graph) were characterized by uniform levels of all measured analytes excepting N-cadherin, MITF, HIF1 α , Ki67 and MART1 (see analyte-specific plots of **Fig. 2 and Supplementary Fig. 3**). Most of these non-uniformly expressed proteins exhibit differences that vary gradually from left-to-right across the D0 cluster of cells, with a small subpopulation of untreated cells (right hand side of D0 cluster) exhibiting lower expression of Ki67, MITF, and MART1. These

features point to a small group of dedifferentiated, slow-cycling cells. Upon BRAFi treatment, the cells initially split to occupy two regions of the FLOW-MAP. At D1 (green points), the majority of the cells cluster to the upper right of the D0 cells, while a small subpopulation clusters directly to the right of the D0 group. This trend continues at D3, with most cells clustering above the largest D1 mass, while a small number cluster to the right of the small D1 group. By D5 (purple), all cells cluster to the right hand side of the graph. The bifurcation of cells at Day 1 and 3 implies the possibility of “upper” and “lower” trajectories towards the drug-tolerant state. The possibility of two classes of trajectories was also indicated by t-SNE analysis[32] (**Supplementary Fig.4**). Thus, both computational analyses of the single-cell data set indicate a bifurcated drug response during the early stages of BRAFi adaptation.

Surprisal analysis uncovers analyte modules of the bifurcated drug-response trajectories

To further dissect the dynamics of molecular changes associated with the bifurcated drug-response trajectories, we applied surprisal analysis[55–57] to our single-cell dataset. Surprisal analysis is a thermodynamics-inspired method that has been broadly applied to understanding large-scale bulk and single-cell omics data sets[51,55,57–59]. This approach is based on the identification of the steady state of the system (formally speaking the state of minimum free energy), and any constraints (analyte modules) that increase the free energy from this theoretical minimum[57,60]. Using this approach, we identified two main modules, each representing a set of analytes that are coordinately changing together across cells. The predicted expression of all 20 analytes based on these two modules matched well with the measured single-cell dataset (**Supplementary Figs. 5 and 6**), demonstrating that modules 1 and 2 recapitulate the overall changes of all molecular signatures across all cells over the five-day course of drug treatment.

The influence score (the lambda values defined in ref [57]) of a module in a cell represents the extent to which the module-associated analytes are enriched or repressed in that cell. Modules 1 and 2 were visualized by color-coding their influence scores onto each node in the FLOW-MAP graph (**Fig. 3a**). We found that the influence score of module 1 gradually increased from negative (blue) to positive (red) value along both the upper and lower paths, with a clear “biophysical barrier” ($\lambda_1 = 0$) in the middle time points (**Fig. 3a, left panel**). We have previously shown that such a sign change can imply a cell state transition[55]. The time-dependence of module 1 appears to reflect the transition from a drug-responsive state to a slow-cycling, drug-tolerant state between days 1 and 3. This observation is consistent with the negative correlation of Ki67 expression and positive correlation of NGFR/AXL expression with the module 1 score (**Supplementary Fig. 7**). The

module 2 projection on the FLOW-MAP also exhibits a sign change, or biophysical barrier ($\lambda_2 = 0$), which separates the upper and lower paths (**Fig. 3a, right panel**). In fact, module 2 distinguishes cell subpopulations for each of the analyzed time points. Notably, the expression of melanocytic phenotype transcription factor MITF and its downstream protein MART1 both showed negative correlations with module 2 score (**Fig 3b and Supplementary Fig. 8**), indicating that the separation of the two paths may be related to the melanocytic lineage of the cells. In summary, surprisal analysis resolves both time-dependent and path-specific modules. It also reveals that, as the cells advance from drug-naïve to drug-tolerant, they occupy a rather complex landscape of cellular states separated by multiple biophysical barriers (**Supplementary Fig. 9**).

Experimental validation supports bifurcated drug-response trajectories

Surprisal analysis provides theoretical support for the existence of both the upper and lower paths from drug-naïve to drug-tolerant cell states. However, experimental validation is required to determine whether individual cells exclusively follow a single trajectory along one path or the other, or if cells stochastically switch between paths. The map of module2 on the D0 cells data hints at biological differences that separate even the untreated D0 cells into two subpopulations (**Supplementary Fig. 9**). The expression levels of the transcription factor MITF and its direct downstream target MART1 are among the top four markers that distinguish the two D0 subpopulations (**Supplementary Fig. 10**). This finding suggests that drug-treated MITF^{low} cells might follow the lower path, while MITF^{high} cells might follow the upper path (**Supplementary Figs. 11 a**). We thus generated MITF-GFP reporter cell lines and sorted GFP^{high} (MITF^{high}) and GFP^{low} (MITF^{low}) subpopulations (**Supplementary Figs. 11 b and 12**). Consistent with our hypothesis, MITF^{high} cells displayed higher expression of Ki67 and MITF as well as a shorter doubling time relative to sorted MITF^{low} subpopulations (**Fig. 3 c-f**). This data is consistent with reported observations of melanoma phenotype switching from a melanocytic, highly proliferative state to a non-melanocytic, more invasive state[61]. It also confirmed that the two subpopulations in D0 cells can be separated using this reporter system, and further suggests that the MITF^{high} and MITF^{low} subpopulations at D0 may represent cells destined to follow the upper and lower paths, respectively, following drug treatment.

To quantify the frequency of stochastic interconversion between the sorted MITF^{high} and MITF^{low} subpopulations during the drug treatment, we monitored the MITF activity within large numbers of single-cells, over a 5-day period of BRAFi treatment. As expected, the MITF^{high} cells always displayed higher activity (quantified by the GFP-reporter) than did the MITF^{low} cells (**Fig. 3g**), with no significant stochastic switching between the two trajectories observed.

To further confirm that the sorted cells reach their respective destination states after five days of drugging, we quantified the markers that are differentially expressed between the upper and lower paths at D5. Mining of the single-cell data sets revealed that several markers, including Slug, MITF, MART1 and PFK are differentially expressed between the two paths (negative- and positive-valued module 2) at D5 (**Fig. 3h, Supplementary Figs. 9 and 13a**). By analyzing the expression of these four genes in sorted MITF^{high} and MITF^{low} D0 cells after five days of treatment (**Supplementary Fig. 13b**), we found that their expression levels in sorted MITF^{low} cells were significantly lower than those in MITF^{high} cells after five days of treatment (**Fig. 3i**). These results experimentally support that, upon drug treatment, MITF^{high} and MITF^{low} cells take distinct trajectories toward drug tolerance along the upper and lower paths respectively (**Supplementary Fig. 13a, left panel**).

MITF is the molecular driver for the two drug response trajectories

MITF is suggested to be an elicitor of intrinsic drug tolerance[62]. To investigate if MITF drives the bifurcation in drug response, we generated a M397 cell line with MITF stably knocked down. Before treatment, knockdown of MITF induced the cells to become slow-cycling with characteristic low Ki67 expression (**Supplementary Fig. 14a, b**), suggesting that downregulation of MITF will force these cells to transition along the lower path. Furthermore, upon five days of BRAFi treatment, MITF knockdown cells showed significantly lower levels of Slug, MITF, MART1 and PFK relative to control (**Supplementary Fig. 14 c**), suggesting that MITF-silenced cells did, in fact, follow a trajectory along the lower path. Thus, MITF is identified as an important molecular driver that discriminates between the two drug response trajectories we identified.

Critical point analysis identifies central regulators along both trajectories

Surprisal analysis of the single-cell data sets indicates that both the upper and lower paths are characterized by a cell state transition in the D1-D3 time window (**Fig 3a, left panel**). A critical point analysis of the single-cell data in different regions of the FLOW-MAP can provide validation of this picture, and can also help identify the tipping points at which those cell state changes take place.[51,63,64] Furthermore, network analysis of those tipping points can be used to identify key regulators that drive the transition from drug-naïve to drug-tolerant[12,51,58,63,65,66].

We first clustered the single-cell data from all time points into 14 different sub-clusters on the FLOW-MAP. Clusters 1, 6, 7, 8, 10, 11, and 12 align with the upper path, while clusters 2, 3, 9, 13, and 14 fall along the lower path (**Fig. 4a**). Two previously reported critical state transition indices, the signaling network activity index (SNAI)[12] and the critical

transition index (I_c)[64], were utilized to evaluate the tipping points associated with the lower and upper paths. We found cluster 7 in the upper path and cluster 9 in the lower path showed the highest values of these indices within their respective path (**Fig. 4 b, c and Supplementary Figs. 15, 16, and 17**), suggesting that clusters 7 and 9 are closest to the tipping points.

We next investigated the correlation networks[12,20,44] for clusters 7 and 9. These two networks are characterized by different structures (**Fig. 4d, e**), implying these transitions are regulated in different ways. We quantified the participation of each analyte (node) in the correlation networks by calculating the node degree and hub score for each node (**See Methods**). For cluster 7 (upper path), we found that several transcription factors and enzymes, including MITF, PFK, p-LKB, PKM2, LDH2 and Slug, showed high levels of network participation by both scoring metrics (**Fig. 4f and Supplementary Fig. 18**). For cluster 9 (lower path), TNFR, N-cadherin and p-NF κ B-p65 appeared dominant. An interesting observation was that the markers that exhibited a high score in cluster 7 often displayed a low score in cluster 9, and vice versa, indicating that the two paths are dissimilarly regulated.

To examine if the transitions along the two paths are driven by distinct hub regulators, we perturbed the respective hub nodes identified within clusters 7 and 9, and probed for differential influence on the two trajectories. We hypothesized that inhibition of the glycolysis enzyme PKM2 and the signaling phosphoprotein p-NF κ B-p65 would differentially influence the transitions along upper and lower paths respectively (**Fig. 4f and Supplementary Fig. 18**). Accordingly, we used a PKM2 inhibitor (PKM2i) or an NF κ B inhibitor (NF κ Bi) in combination with the BRAFi to treat sorted MITF^{high} and MITF^{low} cell subpopulations. Consistent with our hypothesis, the MITF^{low} subpopulation was more sensitive to the BRAFi + NF κ Bi combination (**Fig. 5a**), while the MITF^{high} subpopulation was more sensitive to the BRAFi + PKM2i combination (**Fig. 5b**). This hypothesis was further validated by testing the same drug combinations on the MITF-knockdown cell line relative to unmodified M397 cells (**Fig. 5c, d**). Thus, cells passing along the different trajectories displayed differential sensitivities to PKM2 and NF κ B inhibition.

Considering the differential regulator dependence of the two trajectories, we further hypothesized that co-blocking both trajectories by simultaneously inhibiting PKM2 and NF κ B signaling might show additive effects in preventing the transitions towards BRAFi tolerance. To test this hypothesis, we used the triple drug combination (BRAFi + PKM2i + NF κ Bi) to treat the M397 cells *in vitro* for five days and compared the resulting cell number against monotherapies (BRAFi only) and double-drug combinations (BRAFi + PKM2i and BRAFi + NF κ Bi) for five days. Consistent with our prediction, the triple-drug combination

significantly outperformed the double-drug combinations which in turn were superior to the monotherapy (**Fig. 5e**). Further, PKM2i or NFκBi monotherapy showed minimal growth inhibition on the M397 cells (**Supplementary Fig.19**), implying that these drugs likely function by selectively blocking the BRAFi-induced cell state transitions to the drug-tolerant state. These results demonstrate that the upper and lower paths are independent, have different regulators, and are independently druggable.

Discussion

We explored here whether cell trajectories connecting between the initial and final states of a cell-state transition could be determined from a kinetic series of static snapshots of the traversed cell-state space landscape. As a model system, we utilized a highly plastic, patient-derived M397 *BRAF*^{V600E} mutant melanoma cell line, which has been shown to reversibly transition between drug-naïve and drug-resistant states upon treatment with a BRAF inhibitor. While single-cell omics tools have proven immensely valuable for resolving the cellular heterogeneity of tissues at a single given time point, here we sought to quantitatively connect that cellular heterogeneity to dynamic heterogeneity of cell state changes.

We utilized microfluidic-based SCBC technology to characterize the cellular heterogeneity during the first five days of drug-response. Because both metabolic activity and signaling pathways display functional changes during the early drug-response, SCBC is uniquely suited here since it is capable of simultaneously capturing both metabolites and cytoplasmic proteins (and phosphoproteins) from single cells. However, unlike single-cell RNA-seq, single cell proteomics is typically limited to assaying only tens of functional proteins and metabolites. In order to accurately capture the cell state space accessed by M397 cells under BRAFi treatment, we first utilized transcriptomic analysis and literature guidance to define a panel of 20 analytes that included phenotypic markers, and markers of metabolic activity, oncogenic signaling, and cell proliferation, all of which are altered during the initial drug-response. Single cell analysis using this carefully selected panel readily resolved the complex cell-state space traversed by the cells during the first few days of BRAFi treatment. Of course, moving towards larger numbers of analytes would certainly provide for a deeper characterization.[67–69]

We utilized computational and theoretical methods[32,33,36,37,70–73], integrated with additional cell biology experiments, to translate the SCBC kinetic series of snapshots in to classes of single cell trajectories. Dimensional reduction of the dataset using the FLOW-MAP algorithm revealed suggested that the cells might take one of two paths (labeled “upper” and “lower”) through cell-state space that connected the drug-naïve cells to the drug-resistant cells. Surprisal analysis of the same data resolved both a time-dependent module

and a path-dependent module. The path-dependent module suggested that cells traveling along one path are separated from the other path by a biophysical barrier, which appeared to be associated with the transcription factor MITF and its downstream melanocytic marker MART1. These analyses further predicted that the trajectory a specific cell takes is determined by its MITF level prior to drug treatment. These predictions were verified experimentally, which supported the integration of computational visualization methods with theoretical biophysical approaches to gain insight into a complex biological system. Such an approach should be broadly applicable to other dynamic, complex biological systems, including studies of cellular differentiation, tumorigenesis, and more.

Proliferative and invasive phenotypes are well-known in melanoma[61,74]. MITF, MART1, and Ki67 have been reported as robust markers for distinguishing these two phenotypes[61,74]. We have found that these two distinct phenotypes can co-exist even in the untreated, isogenic M397 cell line used in our study. The MITF^{high} and MITF^{low} subpopulations not only displayed different doubling time without BRAFi treatment but also followed distinct drug-response trajectories upon treatment. This finding is consistent with the observations of melanoma phenotype switching from a melanocytic and highly proliferative state to a non-melanocytic and more invasive state⁶¹. In that study, proliferative or invasive cell lines displayed fixed gene expression profiles in culture, but when transplanted *in vivo*, each class generated heterogeneous tumors containing cells with both kinds of expression profile. Consistent with their observation of fixed gene expression profiles *in vitro*, we did not observe significant inter-conversion between cells traveling along different paths during the five-day treatment period. These findings suggested that these two phenotypes are relatively stable in short term period of BRAFi treatment *in vitro*. Of course, our *in vitro* study may not fully recapitulate *in vivo* melanoma biology in which the tumor microenvironment can wield a strong influence. Furthermore, we also found that transition towards MITF-low invasive-like phenotype can be easily induced by artificial knockdown of a single transcription factor: MITF. This indicates that the complex cell-state landscape is likely regulated by very few master-regulators. It also emphasizes the importance of MITF as a molecular driver in regulating melanoma phenotype determination[75]. These findings, which add significantly to our understanding of melanoma phenotype regulation, would not have been evident had it not been for single-cell analytics.

The coexistence of two distinct drug-response trajectories even in an isogenic cell line may explain the so-called “mixed-responses”, which is commonly observed during the therapeutic treatment of melanoma in clinical settings. Such alternative “escape paths” may also explain why melanomas are so refractory to BRAFi targeted therapy. Intriguingly, for each of the two paths, different drug-susceptibilities were identified by critical point analysis and network analysis: the upper path was found to be susceptible to inhibition of the

glycolysis enzyme PKM2, while the lower path is sensitive to NF κ b-p65 inhibition. These differential drug sensitivity results are consistent with previous bulk studies on invasive phenotypes of melanoma: MITF-low, invasive (or mesenchymal) melanoma cells have been reported to be more dependent on NF κ B signaling[12,76], and the single-cell resolution of our study reveals the exact molecular and cellular dynamics behind that observation. Co-inhibition of PKM2 and NF κ B pathways demonstrated superior effects in inhibiting tumor growth, however, both genes are essential regulators in normal cells and their inhibition can cause toxicity to non-malignant tissue[77,78]. Nevertheless, the resolved heterogeneous drug response trajectories update the current understanding of resistance development, and can provide a powerful methodology for identifying effective therapy combinations.

Methods

Cell lines, reagents and cell culture

Patient-derived melanoma cell line, M397, used in this study was generated under UCLA IRB approval # 11-003254. Cells were cultured at 37 °C with 5% CO₂ in RPMI 1640 with L-glutamine (Life Technologies), supplemented with 10% fetal bovine serum (Omega), and 0.2% antibiotics (MycZap™ Plus-CL from Lonza). The cell line was periodically authenticated to its early passage using GenePrint® 10 System (Promega). Presence of mutations in the genes of interest was checked by OncoMap 3 or Iontrone, and was confirmed by PCR and Sanger sequencing as previously described[79,80]. BRAF inhibitor (vemurafenib), PKM2 inhibitor (Compound 3K) and NFκB inhibitor (JSH-23), all from Selleck Chemicals LLC, were dissolved in DMSO at designated concentrations before applying to cell culture media. M397 cells were plated in 10cm tissue culture plate at 60% confluency and treated with 3 μM BRAF inhibitor for the specified numbers of days.

Microchip fabrication and integrated single-cell proteomic and metabolic assay

The fabrication of the SCBC devices and the protocol of the integrated single-cell proteomic assays were extensively discussed in our previous publications[44,46]. Briefly, the DNA microarrays within each microchamber were converted to antibody or Nano-probe microarrays by flowing the DNA-antibody or DNA-probe conjugate cocktail solution immediately before use. Cells treated with Gluc-Bio[46] were randomly loaded into microchambers within the SCBC. Each microchamber has an assay component, and a separate reservoir of lysis buffer, and was photographed after cell loading. The SCBC was then cooled on ice for cell lysis. Following a 2-hour protein and metabolite capture period at room temperature, the microchambers were flushed and the captured protein or metabolite on the arrays were converted into fluorescent readout and digitized by a Genepix scanner (Molecular Devices).

Data processing from Genepix scanner

By a custom MATLAB code, the average fluorescence signals for all bars within a given barcode were extracted and matched with the micrograph of that array to prepare a table that contains the microchamber address, the numbers of cells, and the measured fluorescence levels of each assayed protein or metabolite. The SCBC readouts from the microchambers with a single cell were collected to form an $m \times n$ matrix table where each row (m) represents a specific microchamber address and each column (n) represents the

abundance of a specific analyte. This matrix table is used for further analysis.

FLOW-MAP Visualizations

All FLOW-MAP visualizations were created with the FLOWMAPR R package available on GitHub (<https://github.com/zunderlab/FLOWMAP/>). Graphs were produced with $\text{seed.X} = 1$ and no clustering or downsampling. Final figures were produced in Gephi (<https://gephi.org/>) either using the “bluered” palette described in the FLOWMAPR package or using the “jet” rainbow palette. The code used to generate the exact FLOW-MAP graphs is available upon request.

Surprisal Analysis

Surprisal analysis was applied as previously described[57]. Briefly, the measured level of analyte i at cell c , $\ln X_i(c)$, is expressed as a sum of a steady state term $\ln X_i^0(c)$, and several constraints (modules) $\lambda_j(c) \times G_{ij}$ representing deviations from the steady state. Each deviation term is a product of a cell-dependent weight (influence score) of the constraint $\lambda_j(c)$, and the cell-independent contribution of the analyte to that constraint (module) G_{ij} . To implement surprisal analysis, we compute the singular value decomposition (SVD) of the matrix $\ln X_i(c)$. This factors this matrix in a way that determines the two sets of parameters that are needed in surprisal analysis: the Lagrange multipliers (λ_j) for all constraints (modules) at a given time point, and for all times and the G_{ij} (time-independent) analyte patterns for all analyte i at each constraint j . In figure 3, cells with the top 10% most positive module2 score are defined as Module2-High cells (M2-High cells), and the most negative 10% ones are defined as Module2-Low cells (M2-Low cells).

Time-lapse microscopy

Movies were acquired on an Olympus IX8 inverted fluorescence microscope with hardware autofocus (ZDC2) and an environmental chamber maintaining a 37C, 5% CO2 culture environment. Automated acquisition software (METAMORPH, Molecular Devices) was used to acquire differential interference contrast (DIC) and GFP images every 15 min from multiple stage positions.

Image segmentation and single-cell fluorescence calculation

Custom MATLAB code (R2017a, MathWorks) was used to pre-process the DIC images of each movie. DIC images were first corrected for uneven illuminations of the

field, then adjusted contrast to sharpen the cell edges. The processed DIC images were then segmented using image segmentation software ilastik[81] (version 1.3.2) to acquire segmented cell bodies. 6 frames (out of 474 frames) were used as the training set for image segmentation of each movie. Pixel Classification feature of ilastik 1.3.2 was used to segment pixels of all 474 frames into ‘Background’, ‘Cell edge’, and ‘Cell body’ based on the labeled 6-image training set of each movie. GFP fluorescence data was extracted from cell body segments using a custom Python code. In each movie frame, each separated ‘Cell Body’ pixel block from DIC segmentation was first labeled as separated individual single cell. Then GFP fluorescence of each single cell block was calculated by integrating fluorescence from the corresponding pixels from GFP images. Background GFP fluorescence was calculated by the median GFP values of ‘Background’ pixels, and was subtracted from GFP values of ‘Cell Body’ pixels. Mean and standard error of the mean (SEM) were calculated for each time point from ensemble single-cell GFP fluorescence.

Single-Cell Clustering

Prior to clustering, all single-cell data were separated by time point (i.e. day 0, day 1, day 3, and day 5). Rclusterpp clusters then applied which cluster the cells into 14 subpopulations. Rclusterpp clusters were produced using the Rclusterpp R package using all default settings (<https://github.com/nolanlab/Rclusterpp>). All clustering algorithms were performed with cells clustered on the following markers: Ki67, Mart1, HIF1a, LDH, AMPKA, p-ERK1, PFK, p-ACAC, Slug, and p-LKB. The code used for clustering is available upon request.

Signaling Activity Indices

The signaling network activity index (SNAI) value is defined as “the reciprocal of the determinant of the protein-protein correlations” in previous publications[12]. The I_c value or critical transition index is defined as “the ratio of the average of all pairs of protein-to-protein correlation coefficients to the average of all pairs of cell-to-cell correlation coefficients” and was calculated as described previously[64]. The code used to calculate the SNAI/ I_c indices for individual cell clusters is available upon request.

Network Analysis

Pair-wise correlation matrices were calculated on within each of the 14 clusters using the Hmisc R package (<https://cran.r-project.org/web/packages/Hmisc/index.html>). Spearman correlations were calculated. Correlation output from the Hmisc package produces the pair-wise correlation values matrix. Bonferroni corrected p-value was used to filter the

correlation network through statistical significance, and the correlation networks were drawn using a custom MATLAB code. Hub score and node degree for each marker in each correlation network were calculated using the igraph R package. Both scores were rescaled from 0 to 1 for each marker for side-by-side comparison and plotted to visualize marker-to-marker variation in hub behavior between methods of calculating correlation. The code used to perform the correlation network analysis is available upon request.

mRNA extraction and qPCR

RNA was extracted from cells using the RNeasy Mini Kit or RNeasy plus Micro Kit (Qiagen) according to the manufacturer's protocol. First-strand cDNA was synthesized from extracted total RNAs using the iScript cDNA Synthesis Kit (Bio-Rad). The expression of human Slug, MITF, MART1 and PFK transcripts were analyzed by SYBR Green-based real-time quantitative RT-PCR (qRT-PCR) using specific primers purchased from Santa Cruz. Data were normalized to the expression of RPL19 and are expressed as fold changes.

MITF knockdown cell line

Short hairpin RNA (shRNA) targeting the coding sequence of MITF and control shRNA were purchased from Santa Cruz. Lentiviruses encoding control shRNA and MITF shRNA were produced in HEK-293T cells by transient transfection of lentiviral based vectors and their packaging vectors psPAX2 and pMD2.G as previously described[82]. The virus was collected, filtered through a 0.45 μ m syringe filter after 48 hours and the M397 cells were spin-infected with viral supernatant supplemented with 10 μ g/mL polybrene at 2,500 rpm and 30°C for 90 min. The transduced cells were selected using puromycin, starting at 3 days post-transduction.

MITF Reporter Cell Line

The human *Tyrosinase Promoter* (TP) was subcloned from pLightSwitch Prom S700747 (SwitchGear Genomics, Carlsbad, CA) into the BamHI and EcoRI sites of the lentiviral vector backbone, driving the expression of the ZsGreen gene. Lentivirus particles were generated as described above to stably transduce M397 cells. A clonal cell line was further generated via single cell sorting and expansion. Cells were then sorted as GFP^{high} and GFP^{low} population by BD FACSAria Fusion Cell Sorter for further treatment and analysis.

Fluorescence microscopy

Images were acquired at 10X (Olympus, 10X FL PH, 0.3 NA) on an EVOS FL Auto

Imaging System (Fisher Scientific) in YFP and differential interference contrast (DIC) channel. Light or laser intensity, exposure and gain were set to be the same between MITF^{high} well and MITF^{low} well.

Clonogenic assay

M397 cells were plated onto six-well plates with fresh media at an optimal confluence. The media (with drug or DMSO) were replenished every two days. Upon the time of staining, 4% paraformaldehyde was applied onto colonies to fix the cells and 0.05% crystal violet solution was used for staining the colonies.

Figures

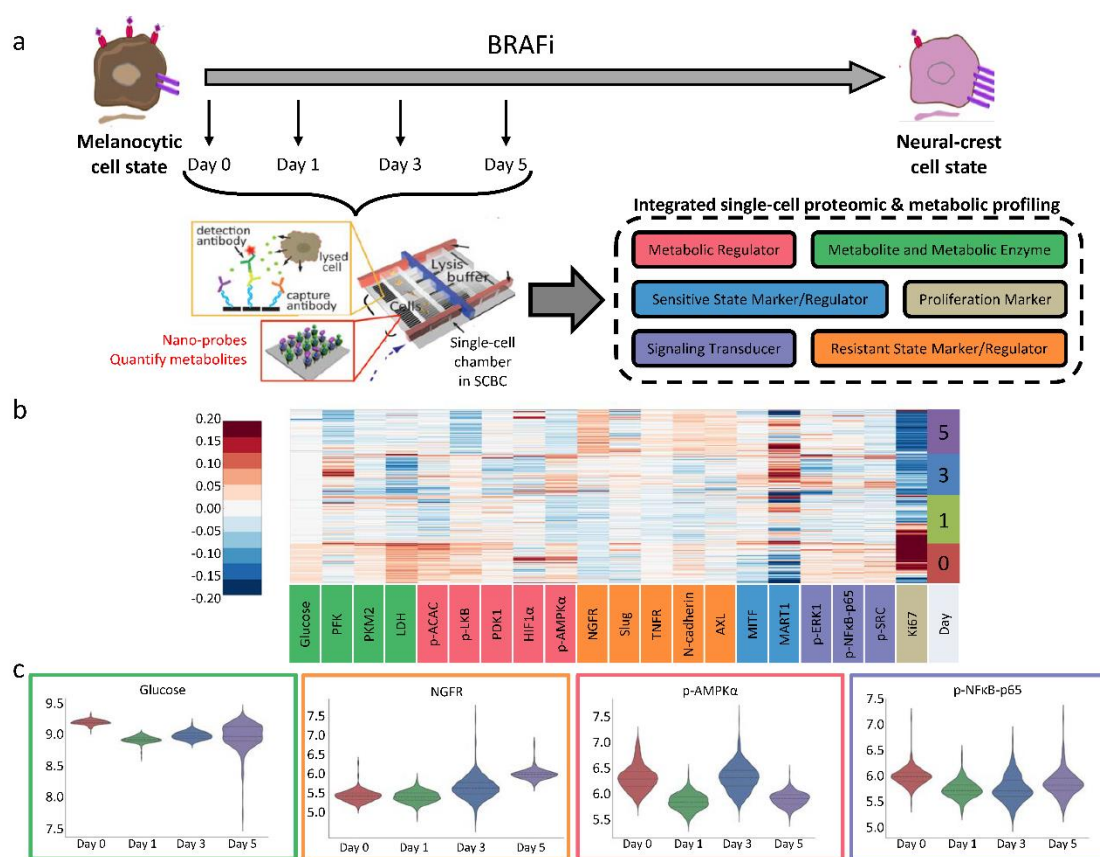


Fig. 1. Single-cell proteomic and metabolic analysis of early drug response in M397 cells. **a.** The single-cell integrated proteomic and metabolic analysis experiments design. Cells from different time points during BRAFi treatment are harvested and individually analyzed using the microfluidic based single-cell barcode (SCBC) technology. Each cell was characterized for the levels of 6 different categories of markers. **b.** Heatmap representation of integrated proteomic and metabolic analysis dataset. Each row represents an individual cell and each column (except the last column) represents an individual analyte, with the color in the heatmap representing measured level of the analyte. The last column represents the number of days after starting BRAFi treatment. On the X-axis, markers are colored corresponding to which of the six functional categories they belong to. **c.** Violin plot representation of distribution of certain representative markers across 4 time points. Y-axis represents natural log of measured marker level. Each plot is bordered by the color of the functional category of the measured marker.

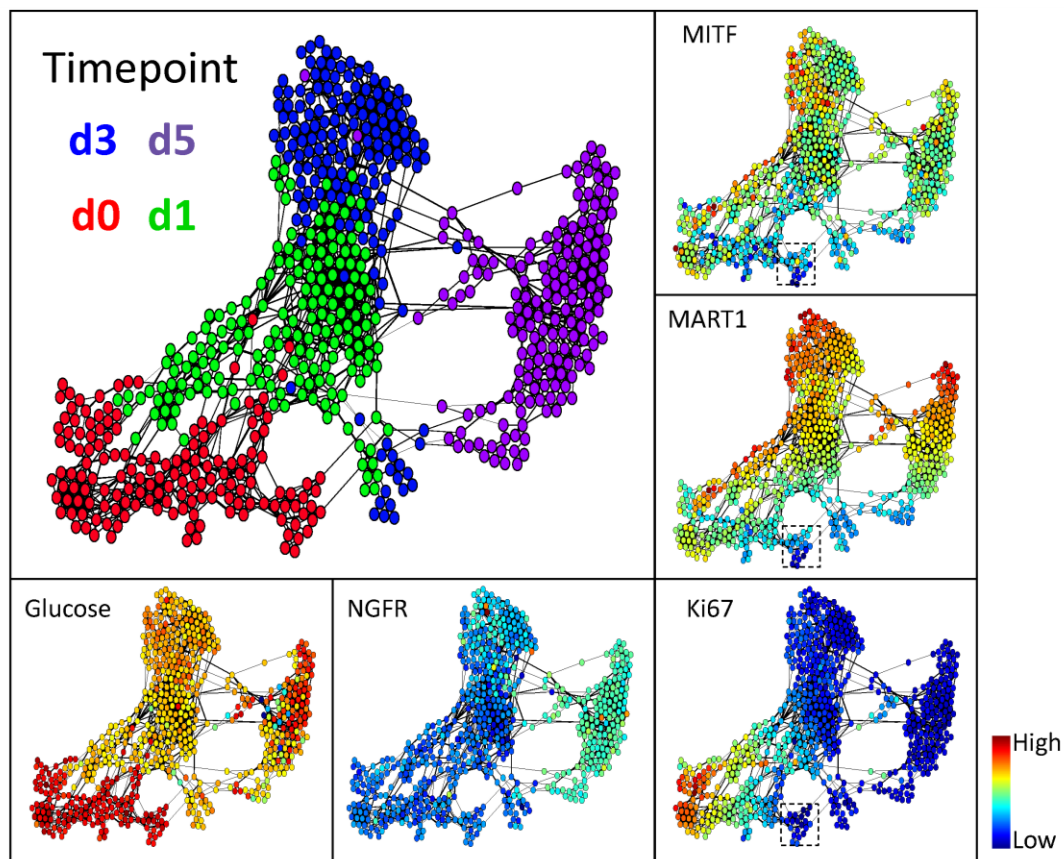


Figure.2 Visualization of single-cell data by FLOW-MAP. Each dot represents an individual cell. The distance between each pair of cells represents the overall multi-omic dissimilarity between them. Cell pairs that are close enough are linked with an edge in between. The colors of the dots in the main panel (upper-left) represent BRAFi exposure time (0, 1, 3, or 5 days) of the corresponding cells. Dot colors in the other panels represent the abundance of each marker in each cell. The dashed-line box in the panels for MITF, MART1, and Ki67 levels shows a small subpopulation of day-0 cells that are slow cycling with less melanocytic phenotype.

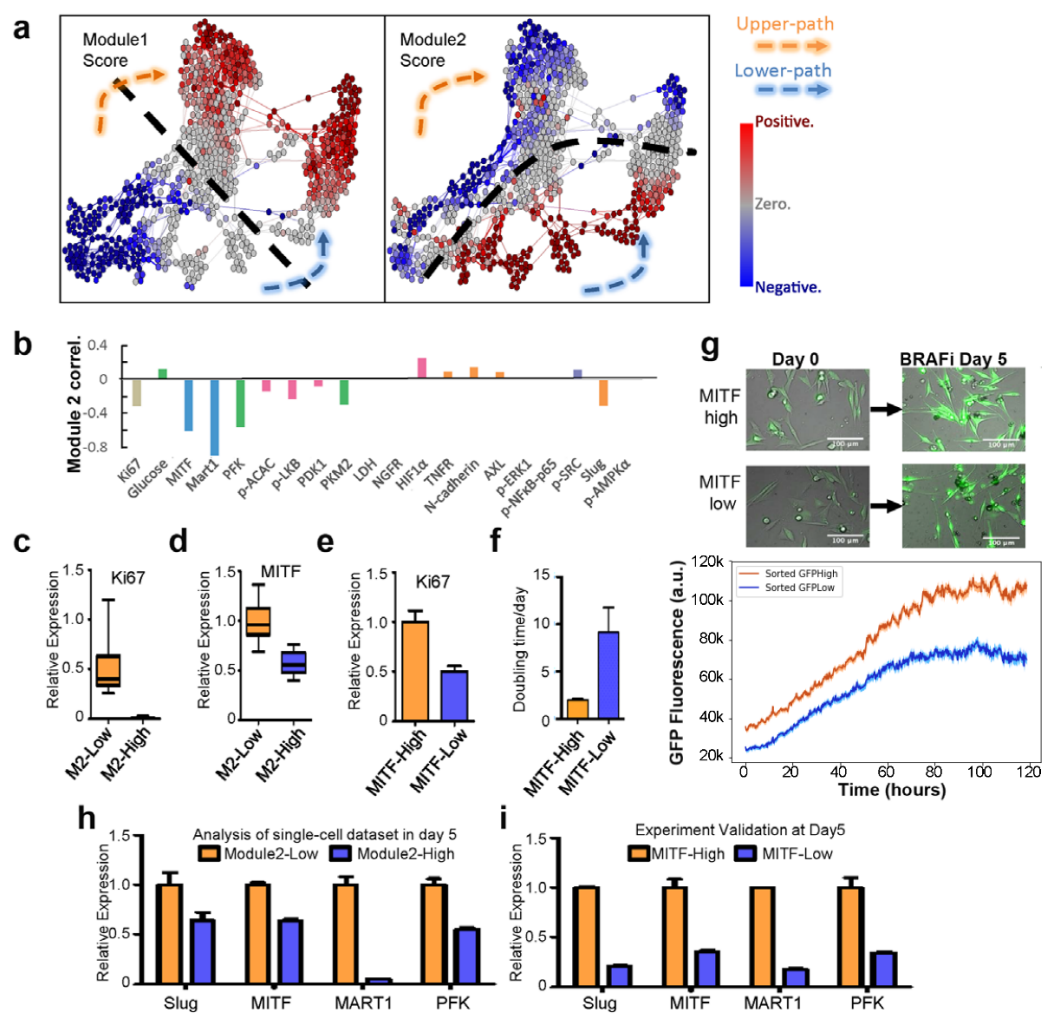


Fig. 3. Surprisal analysis identifies time-dependent and path-specific analyte modules that explain the bifurcated trajectories and identify MITF as a transcription factor regulating the bifurcation. **a.** Visualization of the influence score of the two regulatory modules identified from surprisal analysis. Module 1 is time-dependent, while module 2 exhibits a path-specific pattern. The dashed black lines indicate the region for which the respective module scores of each cell approach zero. **b.** Pearson correlation between individual marker levels and the module 2 score. **c, d.** Ki67 and MITF expression level in module 2 score-high and -low subpopulations at day 0. **e.** Ki67 relative expression, measured by q-PCR in sorted MITF-high and MITF-low cells at day 0. **f.** Doubling time measured in treatment-naïve condition, collected from sorted MITF-high and MITF-low cells at day 0. **g.** Single-cell time-lapsed microscopy analysis of MITF-activity during 5 days of BRAFi. Top panel: Time-lapse images of sorted GFP-High and GFP-low cells before and after 5 days of BRAFi. Bottom panel: Average trace representing MITF activity dynamics across single MITF-Low (blue trace) and MITF-High (orange trace) cells over 5 days of BRAFi. Shading indicates SEM of the mean. **h.** Slug, MITF, MART1, and PFK relative expression levels in

module2 score-high and -low subpopulations, collected from cells at day 5 and analyzed from single-cell dataset. **i.** Slug, MITF, Mart1, and PFK expression, measured by q-PCR in sorted MITF-high and MITF-low day-0 cells that have been treated with BRAFi for 5 days.

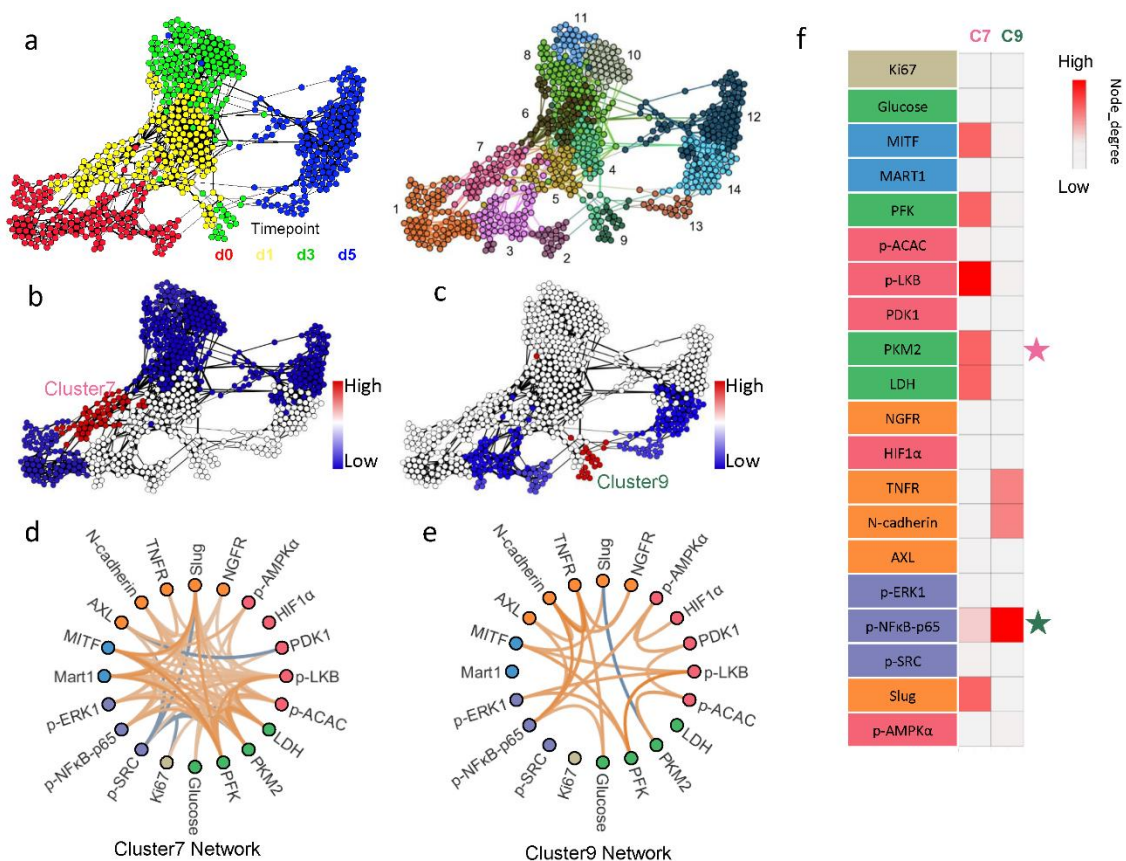


Figure 4. Critical point analysis (SNAI) and network analysis of two trajectories. **a.** Clustering of all cells into 4 time point-defined subpopulations. Left panel is FLOW-MAP with cells color coded by drug exposure time. Right panel is FLOW-MAP with cell color-coded as one of the 14 subpopulations defined from clustering analysis. **b.** Critical point transition analysis for upper path. Critical point index SNAI is calculated within each subpopulation associated with the upper path and color-coded onto the FLOW-MAP. Red indicates higher SNAI value, while blue represents lower SNAI value. Cluster7, shown where labeled, shows the highest SNAI value in the upper path. **c.** Critical point transition analysis for lower path. Critical point index SNAI is calculated within each subpopulation associated with the lower path and color-coded onto the FLOW-MAP. Red indicates higher SNAI value, while blue represents lower SNAI value. Cluster9, shown where labeled, shows the highest SNAI value in the lower path. **d.** Marker-marker correlation networks, extracted from SCBC data within cluster7 cells. The correlation strengths are reflected in the color of each edge (orange indicates positive correlation and blue indicates negative correlation). **e.** Marker-marker correlation networks, extracted from SCBC data within cluster9 cells. The correlation strengths are reflected in the color of each edge (orange indicates positive correlation and blue indicates negative correlation). **f.** Importance score of each node within each network, as defined by node-degree. Colors indicate the node-degree value of each node

within cluster7 or cluster9 networks. Nodes labeled with stars were further-tested with drug perturbation.

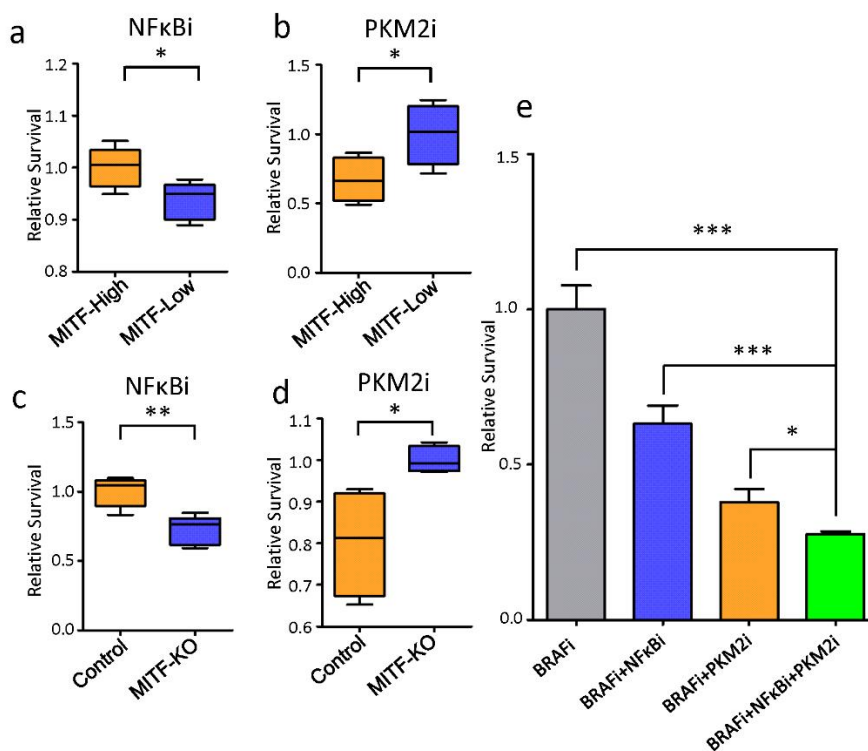
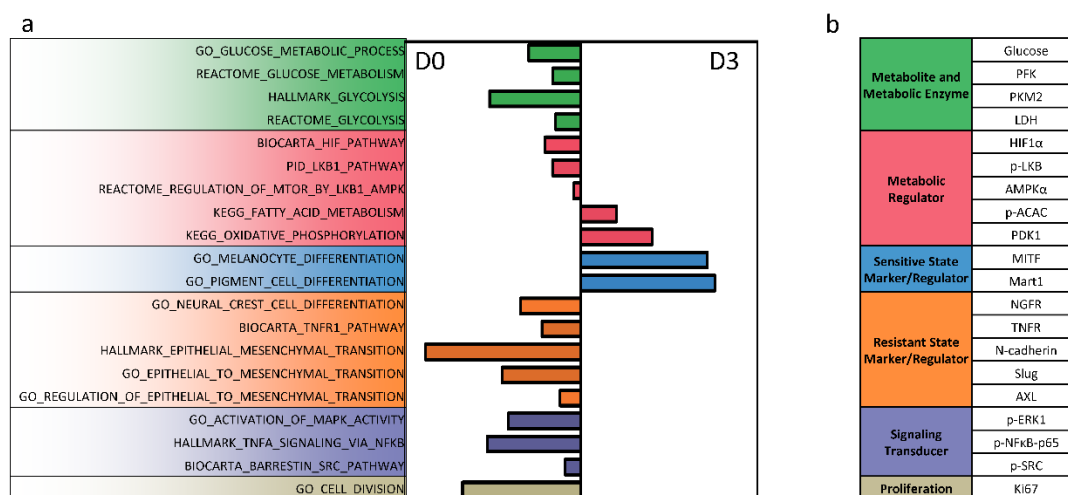


Figure 5. Differential drug sensitivity of cells associated with two trajectories. **a.** MITF-GFP reporter cell line were sorted for MITF-high and MITF-low subpopulation before drugging. The sorted cells were then treated with BRAFi+NFKBi combination for 5days and then harvest for cell number counting. Relative cell survival of sorted MITF-high and MITF-low cells after undergoing BRAFi+NFKBi combination therapy for 5 days were plotted. Survival data were normalized to MITF-high sample. **b.** MITF-GFP reporter cell line were sorted for MITF-high and MITF-low subpopulation before drugging. The sorted cells were then treated with BRAFi+PKM2i combination for 5days and then harvest for cell number counting. Relative cell survival of sorted MITF-high and MITF-low cells after undergoing BRAFi+PKM2i combination therapy for 5 days were plotted. Survival data were normalized to MITF-low sample. **c.** MITF knockdown cells and control cells were treated with BRAFi+NFKBi combination for 5days and then harvest for cell number counting. Relative cell survival of sorted control and MITF-sh cells after undergoing BRAFi+NFKBi combination therapy for 5 days were plotted. Survival data were normalized to control sample. **d.** MITF knockdown cells and control cells were treated with BRAFi+PKM2i combination for 5days and then harvest for cell number counting. Relative cell survival of sorted control and MITF-sh cells after undergoing BRAFi+PKM2i combination therapy for 5 days were plotted. Survival data were normalized to MITF-KO sample. **e.** M397 cell treated

with BRAFi, BRAFi+NFKBi, BRAFi+PKM2i, and BRAFi+NFKBi+PKM2i for 5 days were harvest for cell number counting. Relative cell survival of cells after undergoing BRAFi, BRAFi+NFKBi, BRAFi+PKM2i, or BRAFi+PKM2i+NFKBi therapy for 5 days were plotted. Survival data were normalized to cells undergoing BRAFi monotherapy treatment.

Supplementary Information

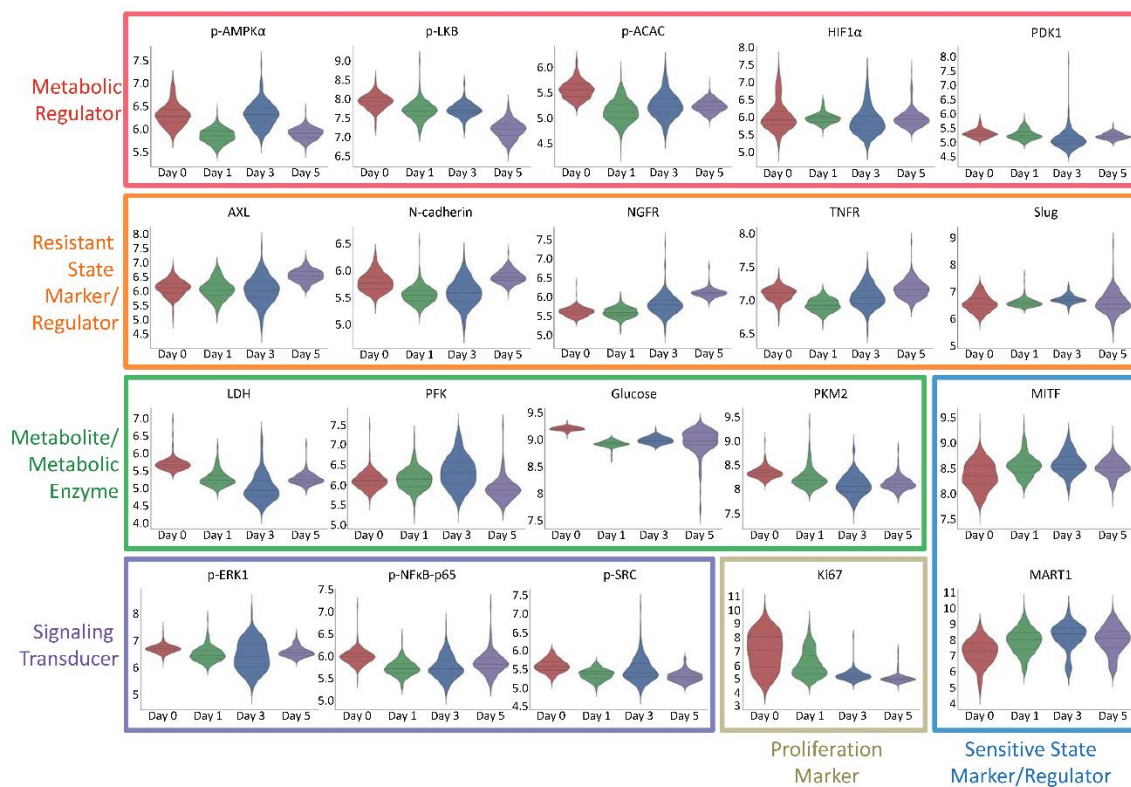
Supplementary Figures



Supplementary Figure 1. Transcriptomic analysis guided panel marker selection

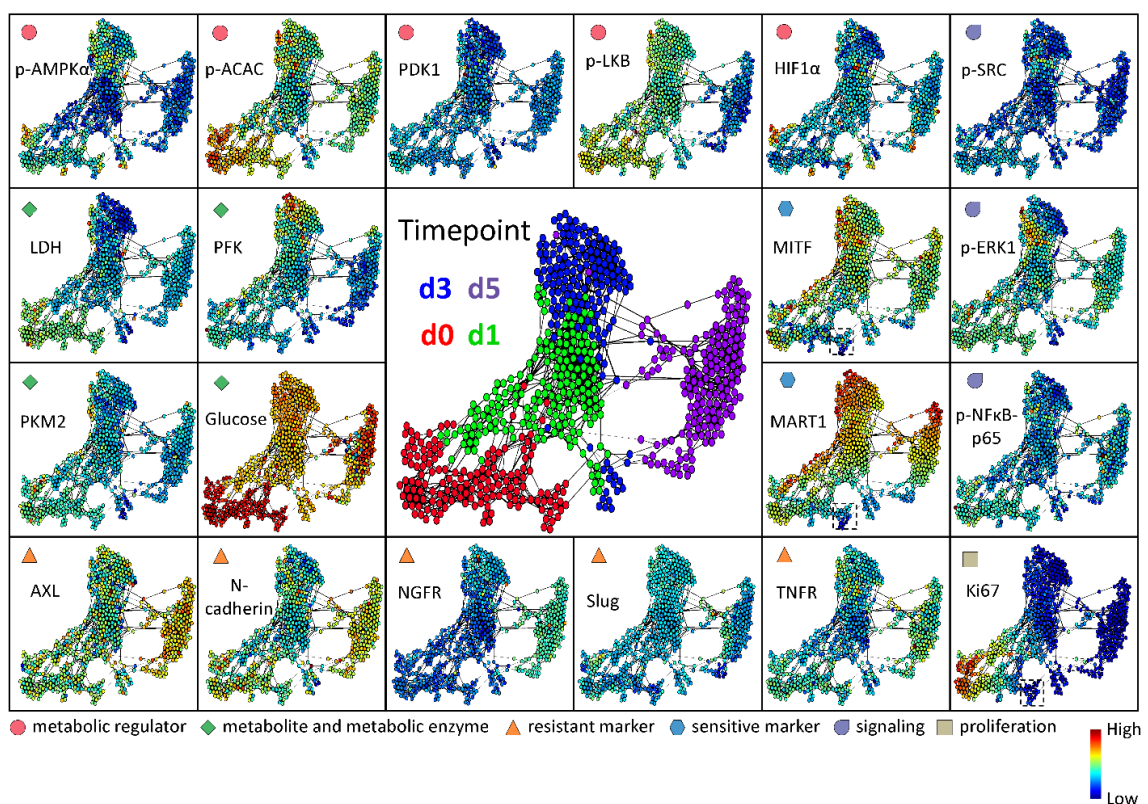
a. Pathways that are differentially altered from day 0 to day 3 after BRAFi treatment. Each row represents a certain signaling pathway and each bar indicates normalized enrichment score (NES) calculated from geneset enrichment analysis (GSEA) of cells harvested at day 3 versus day 0. Each pathway is color-coded by its functional category as described in Fig. S1b.

b. Panel of markers per pathway selected to quantify with single-cell barcode chip (SCBC) analysis. 20 markers were selected for SCBC analysis. Markers with similar biological function are organized together and color-coded by functional category.



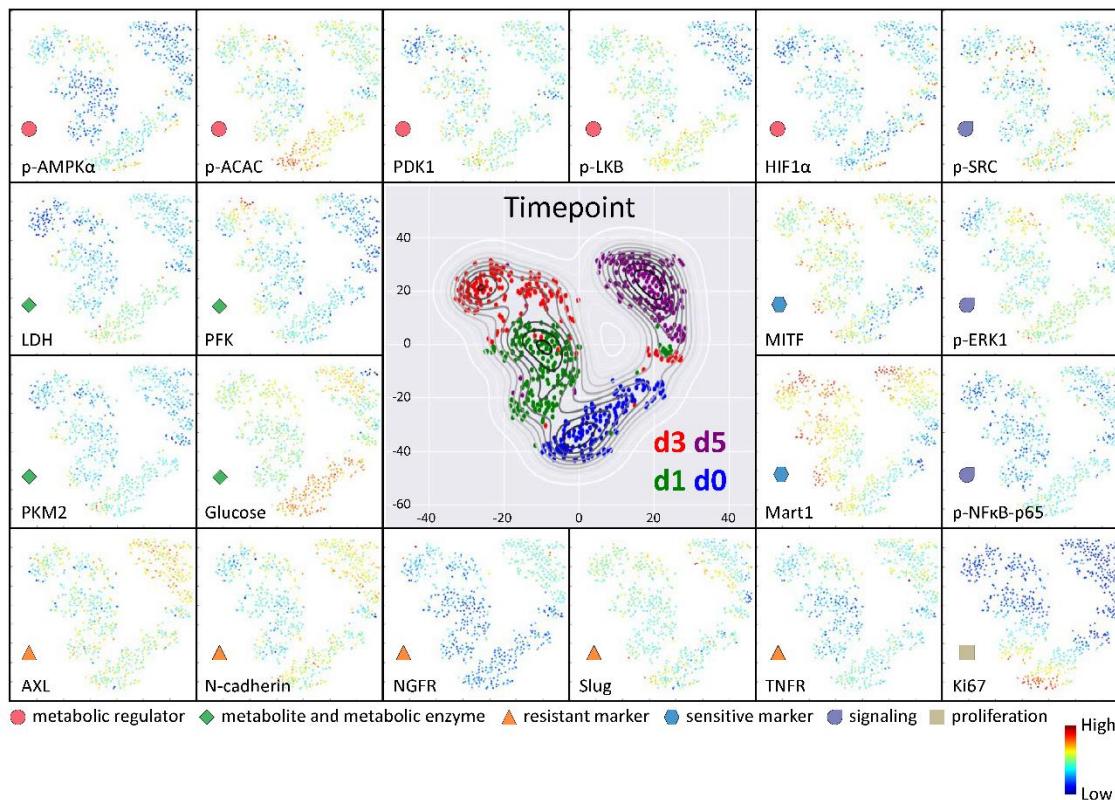
Supplementary Figure 2. Distribution of all 20 markers across 4 time points.

Each of the 20 plots represents the distributions of a certain marker level across 4 time points. Y-axis represents natural log of measured marker level. Markers within the same functional category are boxed together. Border color of each plot corresponds to the functional category of each marker, as described in Fig. 1a.

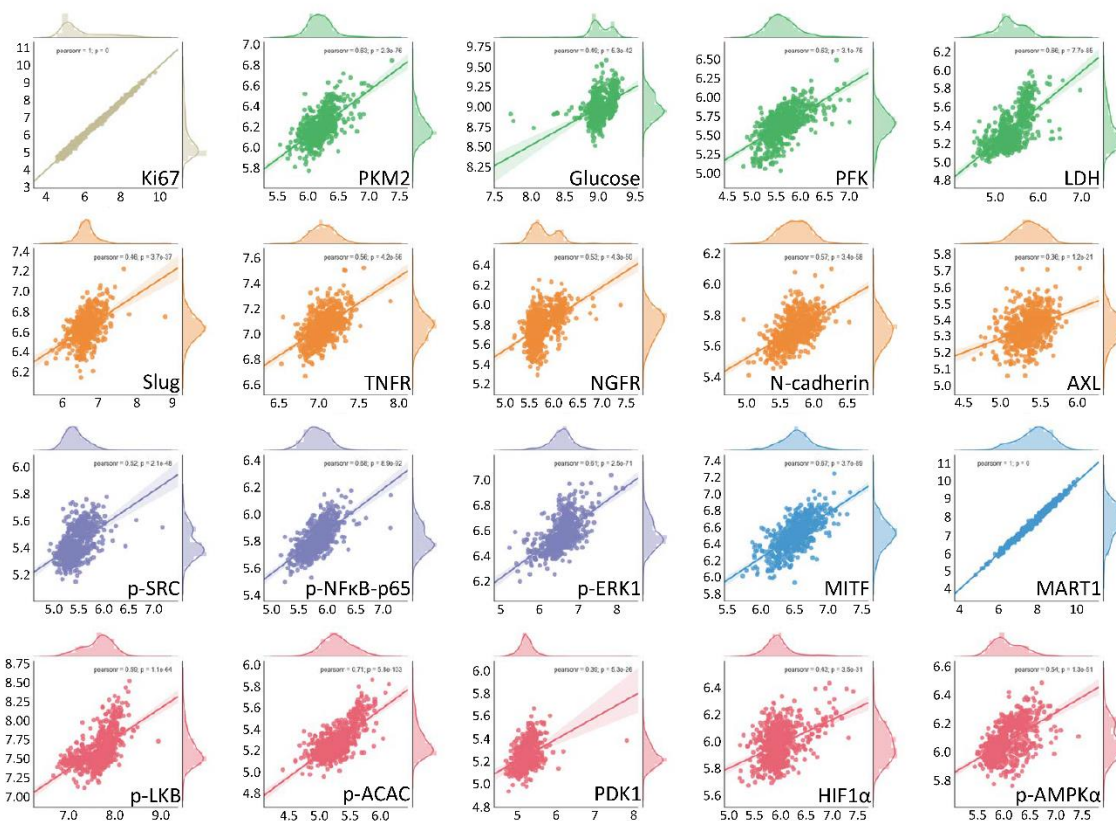


Supplementary Figure 3. Visualization of integrated single-cell proteomic and metabolic analysis data by FLOW-MAP.

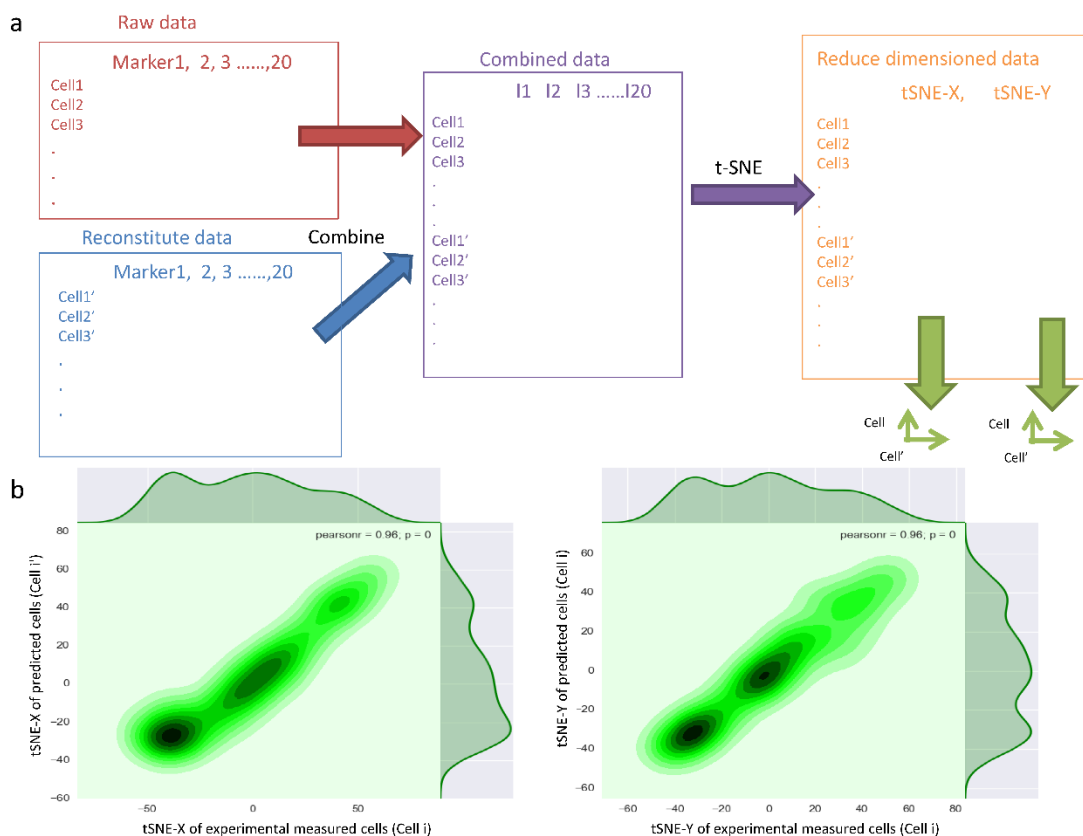
Each dot represents an individual cell. The distance between each pair of cells represents the overall multi-omic dissimilarity between them. Cell pairs that are close enough are linked with an edge in between. The colors of the dots in the central panel represent BRAFi exposure time (0, 1, 3, or 5 days) of the corresponding cells. Dot colors in the other panels represent the abundance of each marker in each cell. Markers belonging to the same functional category, as described in the bottom of the figure, were assigned to a certain shape and color. The dashed-line box in the panels for MIF, MART1, and Ki67 levels shows a small subpopulation of day-0 cells that are slow cycling with less melanocytic phenotype.



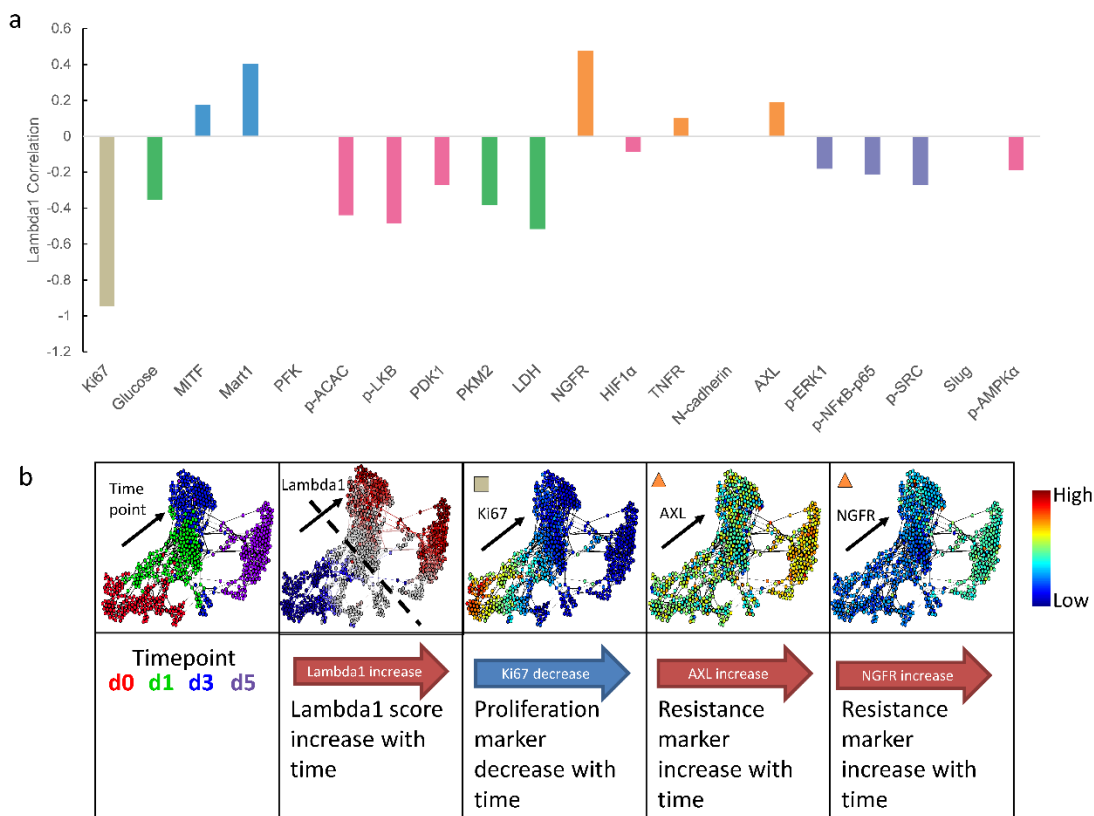
Supplementary Figure 4. Dimension reduction with t-SNE and marker abundance visualization. Each dot per plot represents an individual cell. The distance between each pair of dots represents the overall multi-omic dissimilarity between that pair of cells. The dot colors in the central panel represent the drug exposure time of each cell. Dot colors in the other panels represent the abundance of the specified marker in each cell. Markers that belong to the same functional category were assigned to a certain shape and color, as described in the bottom of the figure. T-SNE visualizations show both the heterogeneity that exists at baseline as well as the progression across time through two separate paths.



Supplementary Figure 5. Two modules from surprisal analysis recapitulated the original experimental measured marker levels. Each plot represents an individual marker. Each dot within a single plot represents a single cell. The x-axis value of each dot represents the experimentally measured marker expression within a cell. The y-axis value of each dot represents the predicted marker level of the same cell as calculated by surprisal analysis of only module1 and module2. The strong positive correlation between the x- and y-axis values indicate that surprisal analysis of the two modules recapitulates experimentally measured marker levels per cell.



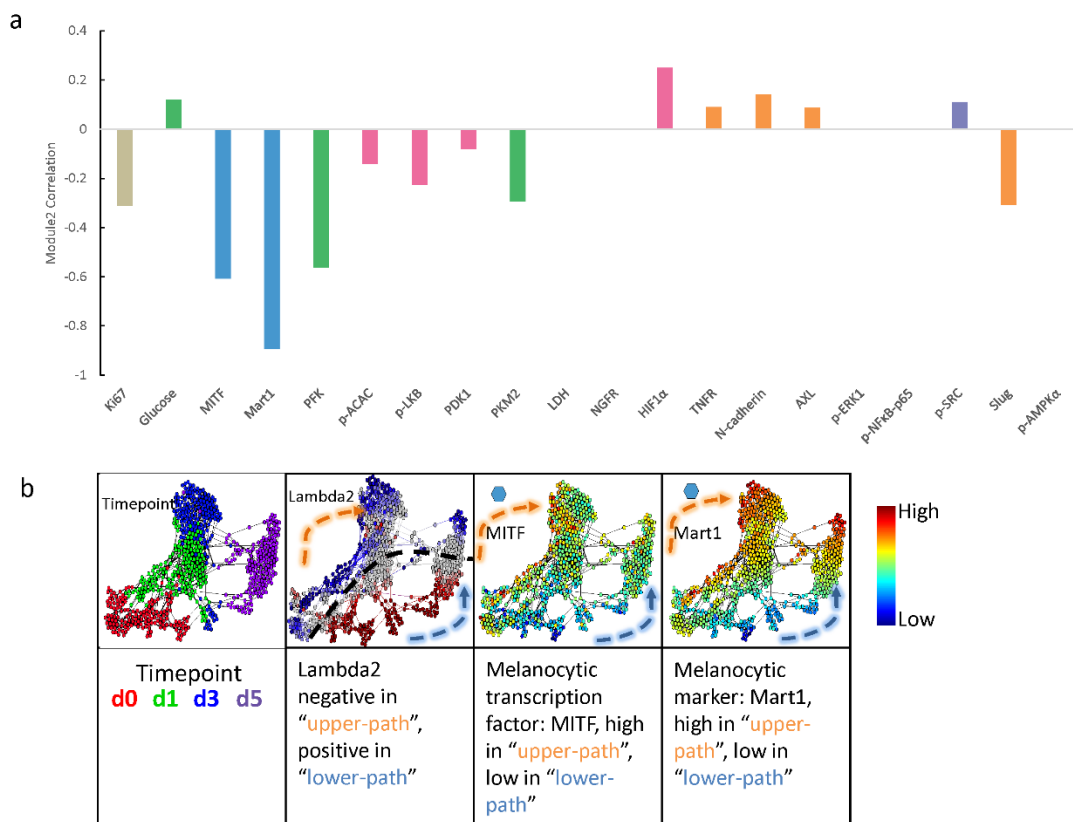
Supplementary Figure 6. Two modules from surprisal analysis recapitulated the overall experimental measured marker levels. **a.** Schematic illustration of workflow to project raw data and surprisal analysis-predicted data onto the same 2-dimensional space. Each cell has measured levels of all 20 markers. Similarly, each cell also has predicted levels of all 20 markers as calculated from surprisal analysis. The raw and surprisal-predicted data matrices were combined to make a bigger matrix with double the original number of rows, each row representing a cell from raw data or predicted data. Each column represents a single marker, with each matrix value representing a single cell's abundance of a marker. The combined, 20-dimensional dataset was projected onto a single t-SNE map where cells with similar levels of all 20 markers will be in nearby coordinates. **b.** Each dot represents an individual cell. In the left panel, the x-axis represents the t-SNE x-value of the cell projected from raw data, while the y-axis represents the t-SNE x-value of the cell projected from surprisal analysis-predicted data. The right panel is similar to left panel, but instead compared t-SNE y-values. The linear, $x = y$ plots indicate that single cells, as projected from raw data and from surprisal analysis-predicted data, are in the same location in a reduced dimension; therefore, the experimentally measured and surprisal analysis-predicted expression profiles of all 20 markers are similar.



Supplementary Figure 7. Lambda1 associated markers displayed time dependent changes.

a. Pearson correlation of marker level vs. module1 score (lambda1) across cells from all timepoints of BRAFi exposure. Correlations that are not statistically significant (i.e. $p > 0.05$) are not shown.

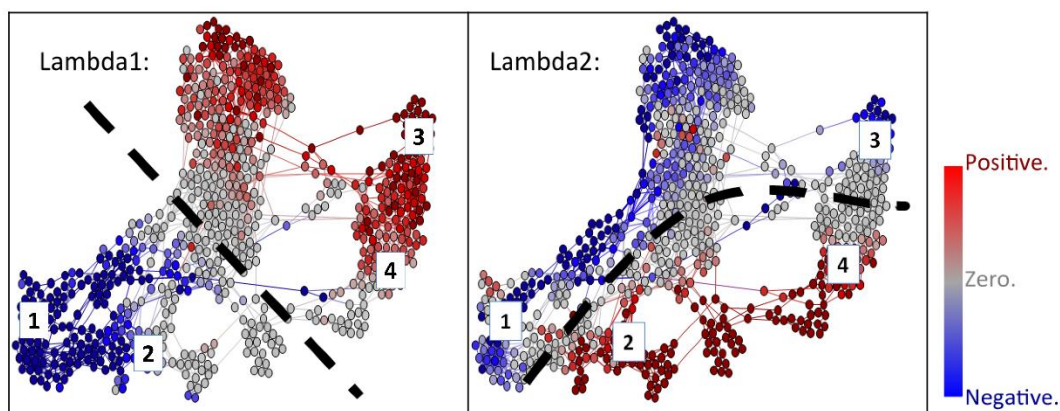
b. Representative markers that showed strongest positive (AXL, NGFR) or negative (Ki67) correlation with module1 score are shown in individual cells on FLOW-MAP.



Supplementary Figure 8. Lambda2 associated markers displayed path-specific expression patterns.

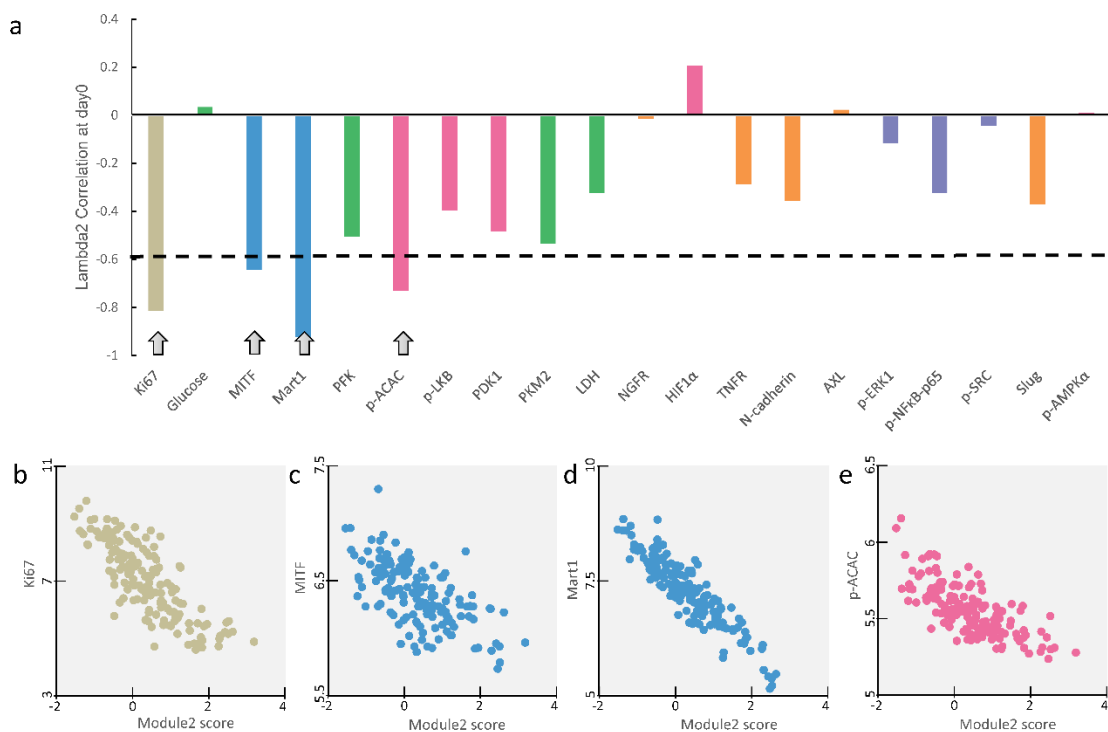
a. Pearson correlation of marker level with module2 score (lambda2) across cells from all time points after BRAFi exposure. Correlations that are not statistically significant (i.e. $p > 0.05$) were not shown.

b. Representative markers that showed strongest negative correlation with module1 score are shown in individual cells on FLOW-MAP.

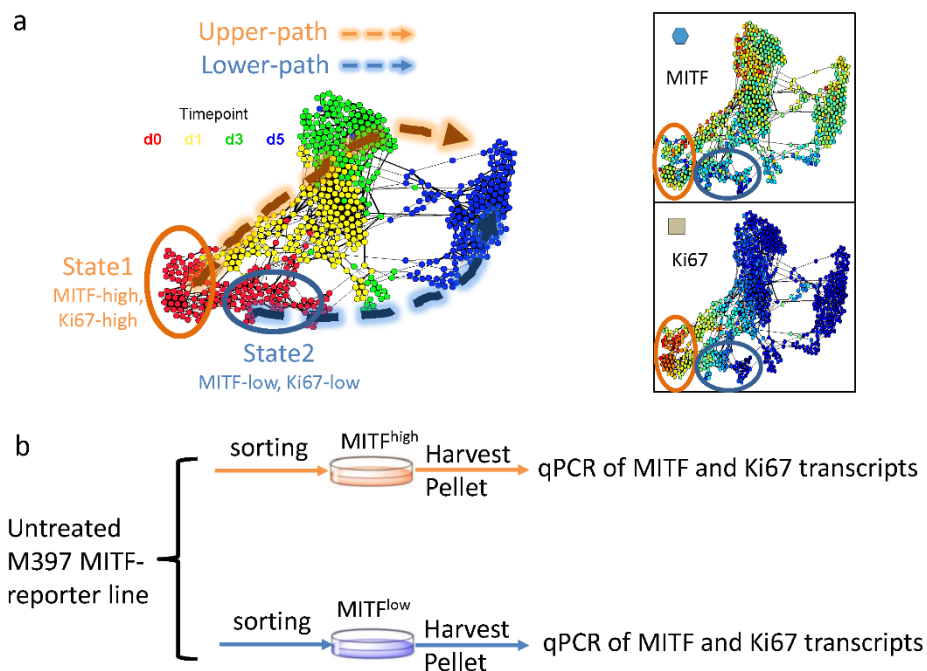


Supplementary Figure 9. Four different cell states inferred from Module1 and Module2 associated biophysical barriers.

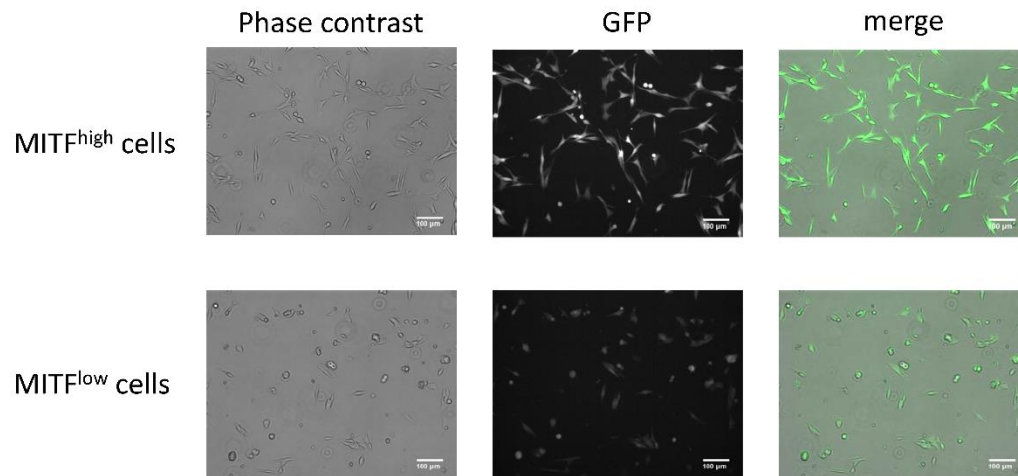
Module1 and module2-associated barriers, as defined by the points at which a module score changes sign, separate the cells into roughly 4 different states, labeled from 1 to 4. States 1 and 2 are separated from states 3 and 4 by the module1-associated barrier. States 1 and 3 are separated from states 2 and 4 by the module2-associated barrier.



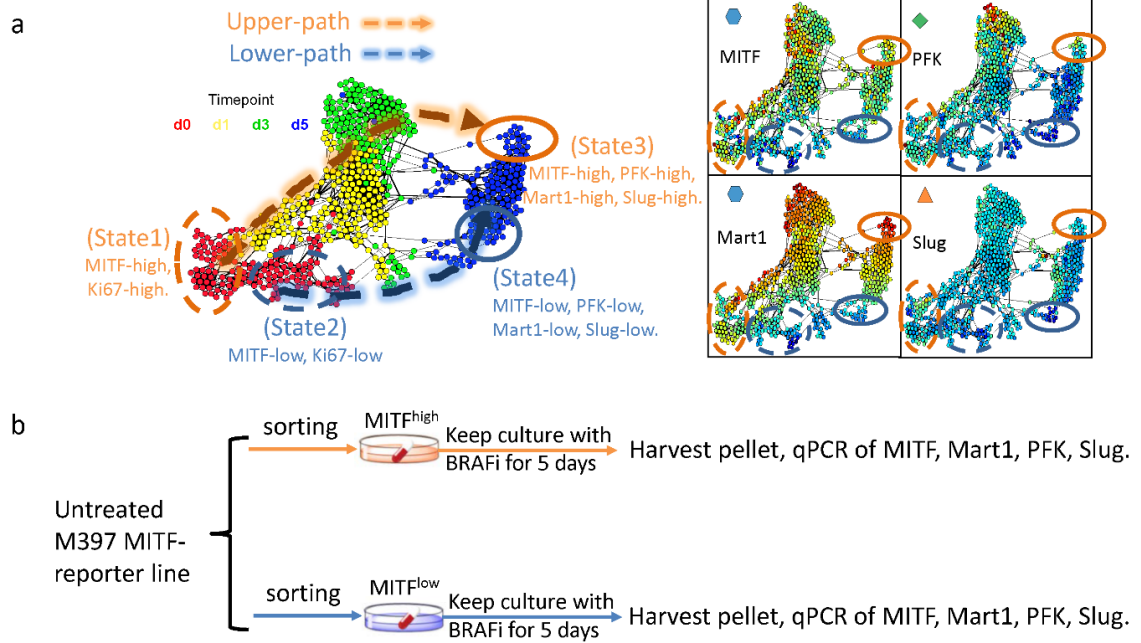
Supplementary Figure 10. Day-0 cell analysis of marker correlation with module2, suggesting MITF as the driver for bifurcation in cell state transition trajectories. a. Pearson correlation of marker level and module2 score in day 0 cells from single-cell dataset. The four most highly-correlated markers are labeled with gray arrows. **b.** Scatter plots showing expression levels of the four most highly-correlated markers versus module2 score in day-0 cells from single-cell dataset.



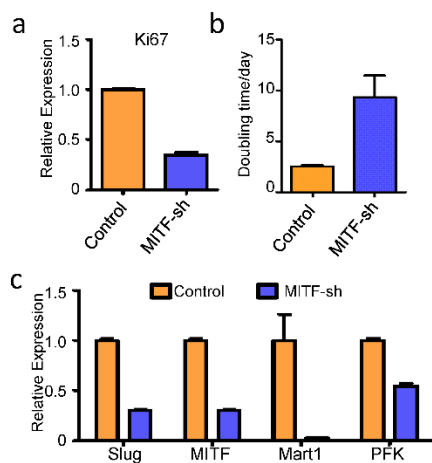
Supplementary Figure 11. Illustration of MITF-reporter line sorting experiment on untreated cells. **a.** Untreated cells in state 1 and state 2 showed significantly different levels of MITF and Ki67. **b.** For MITF-GFP reporter line, cells with higher GFP level and lower GFP level were sorted out using FACS. The sorted cells were then harvested for qPCR quantitation of MITF and Ki67 expression.



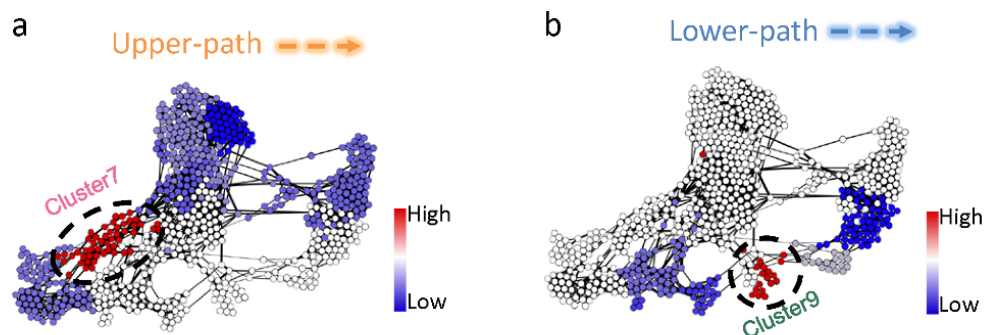
Supplementary Figure 12. Sorted state 1 and state 2 cells shows different MITF-GFP level and morphology.



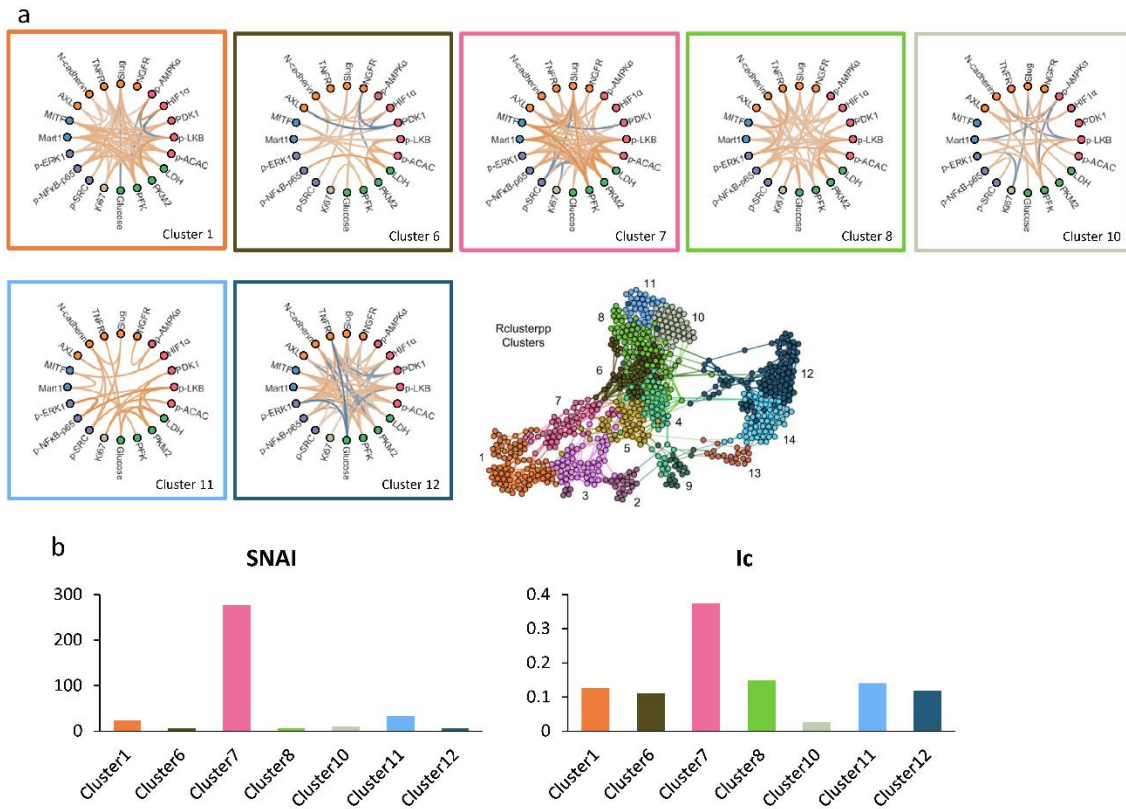
Supplementary Figure 13. Illustration of MITF-reporter line sorting and drug treatment experiments. **a.** Day-5 cells in state 3 and state 4 showed different levels of MITF, MART1, PFK and Slug. **b.** For MITF-GFP reporter line, cells with higher GFP level and lower GFP level were sorted out using FACS. The sorted cells were then treated with BRAFi for another five days, then harvested for qPCR quantitation of MITF, MART1, PFK and Slug expression.



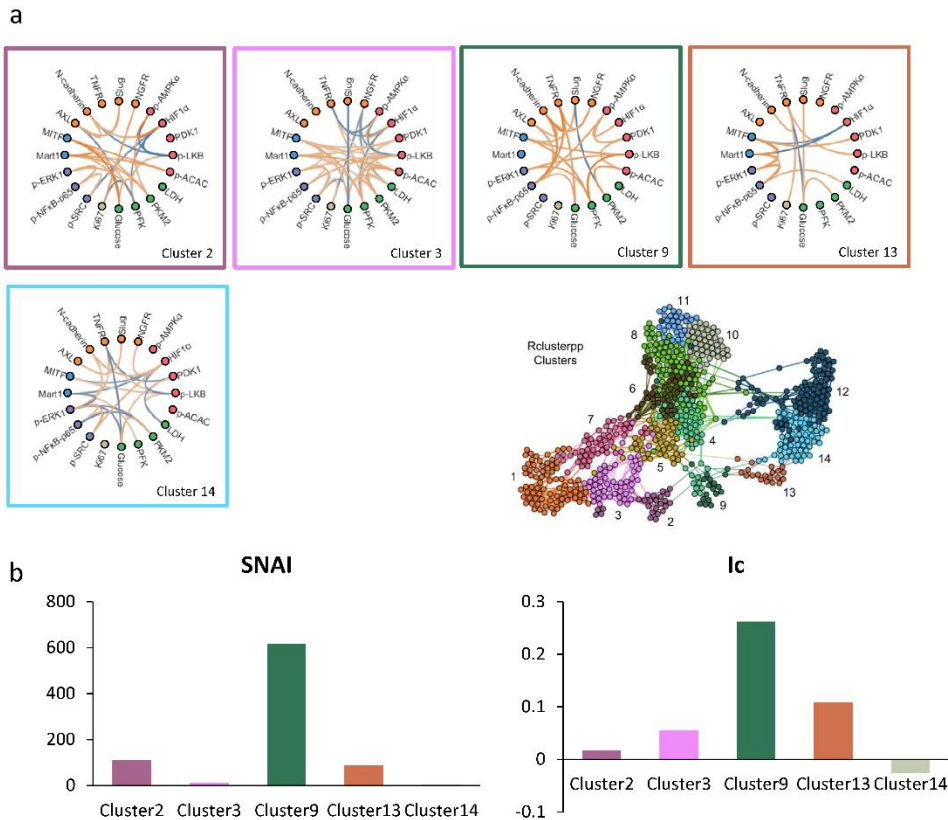
Supplementary Figure 14. MITF knock-down cells showed similar phenotype as sorted state 2 day-0 cells which will follow the bottom trajectory to become state 4-like cells upon 5days of BRAFi. **a.** Expression level of Ki67 from qPCR of MITF knockdown cells versus control cells. **b.** Measured doubling time of MITF-knockdown cells versus control cells. **c.** Expression level of MITF, MART1, PFK, and Slug after 5 days of BRAFi treatment in control cells and MITF-knockdown cells.



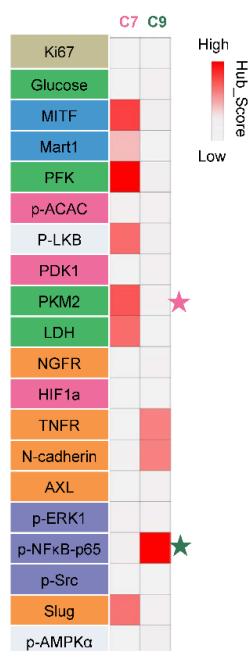
Supplementary Figure 15. Ic value of single cells for critical point transition analysis of each trajectory. **a.** Critical point transition analysis for upper path. Critical point index I_c is calculated within each subpopulation associated with the upper path and color-coded onto the FLOW-MAP. Red indicates higher I_c value. Blue represents lower I_c value. Cluster 7, circled and labeled, shows the highest I_c value in the upper path. **b.** Critical point transition analysis for lower path. Critical point index I_c is calculated within each subpopulation associated with the lower path and color-coded onto the FLOW-MAP. Red indicates higher I_c value. Blue represents lower I_c value. Cluster 9, circled and labeled, shows the highest I_c value in the lower path.



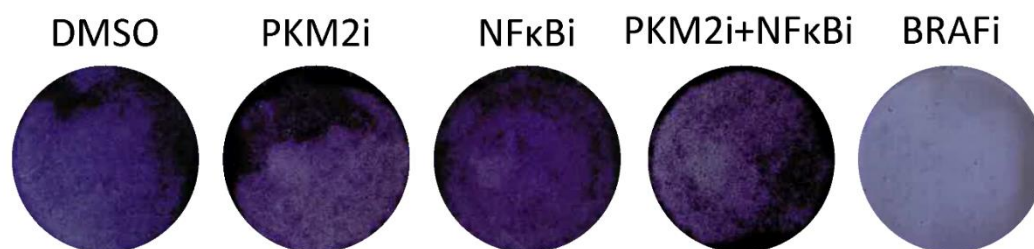
Supplementary Figure 16. Network structure and respective SNAI and Ic values for subpopulations associated with the upper path. **a.** Network of subpopulations associated with the upper path. Each network structure plot is bordered by the color label of the corresponding cluster. **b.** SNAI and Ic values of networks associated with subpopulations in the upper path.



Supplementary Figure 17. Network structure and respective SNAI and Ic values for subpopulations associated with the lower path. **a.** Network of subpopulations associated with the lower path. Each network structure plot is bordered by the color label of the corresponding cluster. **b.** SNAI and Ic values of networks associated with subpopulations in the lower path.



Supplementary Figure 18. Hub-score of each node at networks for cluster7 (C7) and cluster9 (C9). Colors in C7 and C9 columns indicate the hub-score value of each node found within the cluster 7 or cluster 9 networks, respectively. Nodes labeled with stars were further tested using drug perturbation.



Supplementary Figure 19. Short-term clonogenic assay for 397 cells. M397 was treated with either DMSO control or PKM2i or NFκBi or PKM2i+NFκBi or BRAFi. No significant toxicity to the cells was observed for using PKM2i or NFκBi or combination of both.

Reference:

1. Druker BJ, Ohno-Jones S, Talpaz M, Kantarjian H, Resta DJ, Peng B, et al. Efficacy and safety of a specific inhibitor of the BCR-ABL tyrosine kinase in chronic myeloid leukemia. *N Engl J Med.* 2001;344: 1031–1037. doi:10.1056/NEJM200104053441401
2. Chapman PB, Hauschild A, Robert C, Haanen JB, Ascierto P, Larkin J, et al. Improved Survival with Vemurafenib in Melanoma with BRAF V600E Mutation. *N Engl J Med.* 2011;364: 2507–2516. doi:10.1056/nejmoa1103782
3. Flaherty KT, Puzanov I, Kim KB, Ribas A, McArthur GA, Sosman JA, et al. Inhibition of Mutated, Activated BRAF in Metastatic Melanoma. *N Engl J Med.* 2010;363: 809–819. doi:10.1056/nejmoa1002011
4. Mok TS, Wu Y-L, Thongprasert S, Yang C-H, Chu D-T, Saijo N, et al. Gefitinib or Carboplatin–Paclitaxel in Pulmonary Adenocarcinoma. *N Engl J Med.* 2009;361: 947–957. doi:10.1056/nejmoa0810699
5. Ramirez M, Rajaram S, Steininger RJ, Osipchuk D, Roth MA, Morinishi LS, et al. Diverse drug-resistance mechanisms can emerge from drug-tolerant cancer persister cells. *Nat Commun.* 2016;7. doi:10.1038/ncomms10690
6. Pisco AO, Brock A, Zhou J, Moor A, Mojtahedi M, Jackson D, et al. Non-Darwinian dynamics in therapy-induced cancer drug resistance. *Nat Commun.* 2013;4. doi:10.1038/ncomms3467
7. Salgia R, Kulkarni P. The Genetic/Non-genetic Duality of Drug ‘Resistance’ in Cancer. *Trends in Cancer.* 2018. pp. 110–118. doi:10.1016/j.trecan.2018.01.001
8. Wei W, Shin YS, Xue M, Matsutani T, Masui K, Yang H, et al. Single-Cell Phosphoproteomics Resolves Adaptive Signaling Dynamics and Informs Targeted Combination Therapy in Glioblastoma. *Cancer Cell.* 2016;29: 563–573. doi:10.1016/j.ccell.2016.03.012
9. Liao BB, Sievers C, Donohue LK, Gillespie SM, Flavahan WA, Miller TE, et al. Adaptive Chromatin Remodeling Drives Glioblastoma Stem Cell Plasticity and Drug Tolerance. *Cell Stem Cell.* 2017;20: 233–246.e7. doi:10.1016/j.stem.2016.11.003
10. Hugo W, Shi H, Sun L, Piva M, Song C, Kong X, et al. Non-genomic and Immune Evolution of Melanoma Acquiring MAPKi Resistance. *Cell.* 2015;162: 1271–1285. doi:10.1016/j.cell.2015.07.061
11. Waddington CH. The epigenotype. 1942. *Int J Epidemiol.* 2012;41: 10–13. doi:10.1093/ije/dyr184
12. Su Y, Wei W, Robert L, Xue M, Tsoi J, Garcia-Diaz A, et al. Single-cell analysis resolves the cell state transition and signaling dynamics associated with melanoma drug-induced resistance. *Proc Natl Acad Sci U S A.* 2017;114. doi:10.1073/pnas.1712064115
13. Tsoi J, Robert L, Paraiso K, Galvan C, Sheu KM, Lay J, et al. Multi-stage Differentiation Defines Melanoma Subtypes with Differential Vulnerability to Drug-Induced Iron-Dependent Oxidative Stress. *Cancer Cell.* 2018;33: 890–904.e5. doi:10.1016/j.ccell.2018.03.017
14. Ramsdale R, Jorissen RN, Li FZ, Al-Obaidi S, Ward T, Sheppard KE, et al. The

- transcription cofactor c-JUN mediates phenotype switching and BRAF inhibitor resistance in melanoma. *Sci Signal*. 2015;8: ra82. doi:10.1126/scisignal.aab1111
15. Nazarian R, Shi H, Wang Q, Kong X, Koya RC, Lee H, et al. Melanomas acquire resistance to B-RAF(V600E) inhibition by RTK or N-RAS upregulation. *Nature*. 2010;468: 973–977. doi:10.1038/nature09626
 16. Fallahi-Sichani M, Moerke NJ, Niepel M, Zhang T, Gray NS, Sorger PK. Systematic analysis of BRAFV600E melanomas reveals a role for JNK/c-Jun pathway in adaptive resistance to drug-induced apoptosis. *Mol Syst Biol*. 2015;11: 797–797. doi:10.15252/msb.20145877
 17. Walsh AM, Kapoor GS, Buonato JM, Mathew LK, Bi Y, Davuluri R V., et al. Sprouty2 Drives Drug Resistance and Proliferation in Glioblastoma. *Mol Cancer Res*. 2015;13: 1227–1237. doi:10.1158/1541-7786.mcr-14-0183-t
 18. Buonato JM, Lazzara MJ. ERK1/2 blockade prevents epithelial-mesenchymal transition in lung cancer cells and promotes their sensitivity to EGFR inhibition. *Cancer Res*. 2014;74: 309–319. doi:10.1158/0008-5472.CAN-12-4721
 19. Titz B, Lomova A, Le A, Hugo W, Kong X, Ten Hoeve J, et al. JUN dependency in distinct early and late BRAF inhibition adaptation states of melanoma. *Cell Discov*. 2016;2. doi:10.1038/celldisc.2016.28
 20. Wei W, Shin YS, Xue M, Matsutani T, Masui K, Yang H, et al. Single-Cell Phosphoproteomics Resolves Adaptive Signaling Dynamics and Informs Targeted Combination Therapy in Glioblastoma. *Cancer Cell*. 2016;29: 563–573. doi:10.1016/j.ccell.2016.03.012
 21. Meyer AS, Miller MA, Gertler FB, Lauffenburger DA. The receptor AXL diversifies EGFR signaling and limits the response to EGFR-targeted inhibitors in triple-negative breast cancer cells. *Sci Signal*. 2013;6. doi:10.1126/scisignal.2004155
 22. Lazzara MJ, Lane K, Chan R, Jasper PJ, Yaffe MB, Sorger PK, et al. Impaired SHP2-mediated extracellular signal-regulated kinase activation contributes to gefitinib sensitivity of lung cancer cells with epidermal growth factor receptor-activating mutations. *Cancer Res*. 2010;70: 3843–3850. doi:10.1158/0008-5472.CAN-09-3421
 23. Ratnikov BI, Scott DA, Osterman AL, Smith JW, Ronai ZA. Metabolic rewiring in melanoma. *Oncogene*. 2017. pp. 147–157. doi:10.1038/onc.2016.198
 24. Parmenter TJ, Kleinschmidt M, Kinross KM, Bond ST, Li J, Kaadige MR, et al. Response of BRAF-mutant melanoma to BRAF inhibition is mediated by a network of transcriptional regulators of glycolysis. *Cancer Discov*. 2014;4: 423–433. doi:10.1158/2159-8290.CD-13-0440
 25. Luo C, Lim JH, Lee Y, Granter SR, Thomas A, Vazquez F, et al. A PGC1 α -mediated transcriptional axis suppresses melanoma metastasis. *Nature*. 2016;537: 422–426. doi:10.1038/nature19347
 26. Pan M, Reid MA, Lowman XH, Kulkarni RP, Tran TQ, Liu X, et al. Regional glutamine deficiency in tumours promotes dedifferentiation through inhibition of histone demethylation. *Nat Cell Biol*. 2016;18: 1090–1101. doi:10.1038/ncb3410
 27. Macosko EZ, Basu A, Satija R, Nemesh J, Shekhar K, Goldman M, et al. Highly parallel genome-wide expression profiling of individual cells using nanoliter droplets. *Cell*. 2015;161: 1202–1214. doi:10.1016/j.cell.2015.05.002
 28. Bendall SC, Simonds EF, Qiu P, Amir EAD, Krutzik PO, Finck R, et al. Single-cell

- mass cytometry of differential immune and drug responses across a human hematopoietic continuum. *Science* (80-). 2011;332: 687–696. doi:10.1126/science.1198704
29. Ma C, Fan R, Ahmad H, Shi Q, Comin-Anduix B, Chodon T, et al. A clinical microchip for evaluation of single immune cells reveals high functional heterogeneity in phenotypically similar T cells. *Nat Med*. 2011;17: 738–743. doi:10.1038/nm.2375
 30. Heath JR, Ribas A, Mischel PS. Single-cell analysis tools for drug discovery and development. *Nature Reviews Drug Discovery*. 2016. pp. 204–216. doi:10.1038/nrd.2015.16
 31. Shaffer SM, Dunagin MC, Torborg SR, Torre EA, Emert B, Krepler C, et al. Rare cell variability and drug-induced reprogramming as a mode of cancer drug resistance. *Nature*. 2017. doi:10.1038/nature22794
 32. Amir EAD, Davis KL, Tadmor MD, Simonds EF, Levine JH, Bendall SC, et al. ViSNE enables visualization of high dimensional single-cell data and reveals phenotypic heterogeneity of leukemia. *Nat Biotechnol*. 2013;31: 545–552. doi:10.1038/nbt.2594
 33. Levine JH, Simonds EF, Bendall SC, Davis KL, Amir EAD, Tadmor MD, et al. Data-Driven Phenotypic Dissection of AML Reveals Progenitor-like Cells that Correlate with Prognosis. *Cell*. 2015;162: 184–197. doi:10.1016/j.cell.2015.05.047
 34. Azizi E, Carr AJ, Plitas G, Cornish AE, Konopacki C, Prabhakaran S, et al. Single-Cell Map of Diverse Immune Phenotypes in the Breast Tumor Microenvironment. *Cell*. 2018;174: 1293-1308.e36. doi:10.1016/j.cell.2018.05.060
 35. Rambow F, Rogiers A, Marin-Bejar O, Aibar S, Femel J, Dewaele M, et al. Toward Minimal Residual Disease-Directed Therapy in Melanoma. *Cell*. 2018;174: 843-855.e19. doi:10.1016/j.cell.2018.06.025
 36. Bendall SC, Davis KL, Amir EAD, Tadmor MD, Simonds EF, Chen TJ, et al. Single-cell trajectory detection uncovers progression and regulatory coordination in human b cell development. *Cell*. 2014;157: 714–725. doi:10.1016/j.cell.2014.04.005
 37. Setty M, Tadmor MD, Reich-Zeliger S, Angel O, Salame TM, Kathail P, et al. Wishbone identifies bifurcating developmental trajectories from single-cell data. *Nat Biotechnol*. 2016;34: 637–645. doi:10.1038/nbt.3569
 38. Haghverdi L, Büttner M, Wolf FA, Buettner F, Theis FJ. Diffusion pseudotime robustly reconstructs lineage branching. *Nat Methods*. 2016;13: 845–848. doi:10.1038/nmeth.3971
 39. Angerer P, Haghverdi L, Büttner M, Theis FJ, Marr C, Buettner F. Destiny: Diffusion maps for large-scale single-cell data in R. *Bioinformatics*. 2016;32: 1241–1243. doi:10.1093/bioinformatics/btv715
 40. Schiebinger G, Shu J, Tabaka M, Cleary B, Subramanian V, Solomon A, et al. Reconstruction of developmental landscapes by optimal-transport analysis of single-cell gene expression sheds light on cellular reprogramming. *DoiOrg*. 2017; 191056. doi:10.1101/191056
 41. Lin Y, Sohn CH, Dalal CK, Cai L, Elowitz MB. Combinatorial gene regulation by modulation of relative pulse timing. *Nature*. 2015;527: 54–58. doi:10.1038/nature15710
 42. Young JW, Locke JCW, Altinok A, Rosenfeld N, Bacarian T, Swain PS, et al.

- Measuring single-cell gene expression dynamics in bacteria using fluorescence time-lapse microscopy. *Nat Protoc.* 2012;7: 80–88. doi:10.1038/nprot.2011.432
43. Locke JCW, Elowitz MB. Using movies to analyse gene circuit dynamics in single cells. *Nature Reviews Microbiology.* 2009. pp. 383–392. doi:10.1038/nrmicro2056
 44. Shi Q, Qin L, Wei W, Geng F, Fan R, Shik Shin Y, et al. Single-cell proteomic chip for profiling intracellular signaling pathways in single tumor cells. *Proc Natl Acad Sci.* 2012;109: 419–424. doi:10.1073/pnas.1110865109
 45. Wei W, Shi Q, Remacle F, Qin L, Shackelford DB, Shin YS, et al. Hypoxia induces a phase transition within a kinase signaling network in cancer cells. *Proc Natl Acad Sci.* 2013;110: E1352–E1360. doi:10.1073/pnas.1303060110
 46. Xue M, Wei W, Su Y, Kim J, Shin YSYS, Mai WXWX, et al. Chemical methods for the simultaneous quantitation of metabolites and proteins from single cells. *J Am Chem Soc.* 2015;137. doi:10.1021/jacs.5b00944
 47. Xue M, Wei W, Su Y, Johnson D, Heath JR. Supramolecular Probes for Assessing Glutamine Uptake Enable Semi-Quantitative Metabolic Models in Single Cells. *J Am Chem Soc.* 2016;138. doi:10.1021/jacs.5b12187
 48. Bailey RC, Kwong GA, Radu CG, Witte ON, Heath JR. DNA-encoded antibody libraries: A unified platform for multiplexed cell sorting and detection of genes and proteins. *J Am Chem Soc.* 2007;129: 1959–1967. doi:10.1021/ja065930i
 49. Fallahi-Sichani M, Becker V, Izar B, Baker GJ, Lin J, Boswell SA, et al. Adaptive resistance of melanoma cells to RAF inhibition via reversible induction of a slowly dividing de-differentiated state. *Mol Syst Biol.* 2017;13: 905. doi:10.15252/msb.20166796
 50. Abildgaard C, Guldborg P. Molecular drivers of cellular metabolic reprogramming in melanoma. *Trends in Molecular Medicine.* 2015. pp. 164–171. doi:10.1016/j.molmed.2014.12.007
 51. Poovathingal SK, Kravchenko-Balasha N, Shin YS, Levine RD, Heath JR. Critical Points in Tumorigenesis: A Carcinogen-Initiated Phase Transition Analyzed via Single-Cell Proteomics. *Small.* 2016;12: 1425–1431. doi:10.1002/sml.201501178
 52. Larkin J, Fisher. Vemurafenib: a new treatment for BRAF-V600 mutated advanced melanoma. *Cancer Management and Research.* 2012. p. 243. doi:10.2147/cmar.s25284
 53. López B, Aguilar D, Orozco H, Burger M, Espitia C, Ritacco V, et al. A marked difference in pathogenesis and immune response induced by different Mycobacterium tuberculosis genotypes. *Clin Exp Immunol.* 2003;133: 30–37. doi:10.1046/j.1365-2249.2003.02171.x
 54. Zunder ER, Lujan E, Goltsev Y, Wernig M, Nolan GP. A continuous molecular roadmap to iPSC reprogramming through progression analysis of single-cell mass cytometry. *Cell Stem Cell.* 2015;16: 323–337. doi:10.1016/j.stem.2015.01.015
 55. Zadran S, Arumugam R, Herschman H, Phelps ME, Levine RD. Surprisal analysis characterizes the free energy time course of cancer cells undergoing epithelial-to-mesenchymal transition. *Proc Natl Acad Sci U S A.* 2014;111: 13235–40. doi:10.1073/pnas.1414714111
 56. Levine RD. Molecular reaction dynamics. *Molecular Reaction Dynamics.* 2005. doi:10.1017/CBO9780511614125

57. Remacle F, Kravchenko-Balasha N, Levitzki A, Levine RD. Information-theoretic analysis of phenotype changes in early stages of carcinogenesis. *Proc Natl Acad Sci.* 2010;107: 10324–10329. doi:10.1073/pnas.1005283107
58. Kravchenko-Balasha N, Shin YS, Sutherland A, Levine RD, Heath JR. Intercellular signaling through secreted proteins induces free-energy gradient-directed cell movement. *Proc Natl Acad Sci.* 2016;113: 5520–5525. doi:10.1073/pnas.1602171113
59. Kravchenko-Balasha N, Wang J, Remacle F, Levine RD, Heath JR. Glioblastoma cellular architectures are predicted through the characterization of two-cell interactions. *Proc Natl Acad Sci.* 2014;111: 6521–6526. doi:10.1073/pnas.1404462111
60. Alter O, Brown PO, Botstein D. Singular value decomposition for genome-wide expression data processing and modeling. *Proc Natl Acad Sci.* 2000;97: 10101–10106. doi:10.1073/pnas.97.18.10101
61. Hoek KS, Eichhoff OM, Schlegel NC, Döbbeling U, Kobert N, Schaerer L, et al. In vivo switching of human melanoma cells between proliferative and invasive states. *Cancer Res.* 2008;68: 650–656. doi:10.1158/0008-5472.CAN-07-2491
62. Müller J, Krijgsman O, Tsoi J, Robert L, Hugo W, Song C, et al. Low MITF/AXL ratio predicts early resistance to multiple targeted drugs in melanoma. *Nat Commun.* 2014;5. doi:10.1038/ncomms6712
63. Bargaje R, Trachana K, Shelton MN, McGinnis CS, Zhou JX, Chadick C, et al. Cell population structure prior to bifurcation predicts efficiency of directed differentiation in human induced pluripotent cells. *Proc Natl Acad Sci.* 2017;114: 2271–2276. doi:10.1073/pnas.1621412114
64. Mojtahedi M, Skupin A, Zhou J, Castaño IG, Leong-Quong RYY, Chang H, et al. Cell Fate Decision as High-Dimensional Critical State Transition. *PLoS Biol.* 2016;14: 1–13. doi:10.1371/journal.pbio.2000640
65. Su Y, Shi Q, Wei W. Single cell proteomics in biomedicine: High-dimensional data acquisition, visualization, and analysis. *Proteomics.* 2017;17. doi:10.1002/pmic.201600267
66. Richard A, Boullu L, Herbach U, Bonnafoux A, Morin V, Vallin E, et al. Single-Cell-Based Analysis Highlights a Surge in Cell-to-Cell Molecular Variability Preceding Irreversible Commitment in a Differentiation Process. *PLoS Biol.* 2016;14. doi:10.1371/journal.pbio.1002585
67. Lu Y, Xue Q, Eisele MR, Sulistijo ES, Brower K, Han L, et al. Highly multiplexed profiling of single-cell effector functions reveals deep functional heterogeneity in response to pathogenic ligands. *Proc Natl Acad Sci.* 2015;112: E607–E615. doi:10.1073/pnas.1416756112
68. Li Z, Cheng H, Shao S, Lu X, Mo L, Tsang J, et al. Surface Immobilization of Redox-Labile Fluorescent Probes: Enabling Single-Cell Co-Profiling of Aerobic Glycolysis and Oncogenic Protein Signaling Activities. *Angew Chemie - Int Ed.* 2018;57: 11554–11558. doi:10.1002/anie.201803034
69. Xu AM, Liu Q, Takata KL, Jeoung S, Su Y, Antoshechkin I, et al. Integrated measurement of intracellular proteins and transcripts in single cells. *Lab Chip.* 2018;18: 3251–3262. doi:10.1039/c8lc00639c
70. Anchang B, Hart TDP, Bendall SC, Qiu P, Bjornson Z, Linderman M, et al.

- Visualization and cellular hierarchy inference of single-cell data using SPADE. *Nat Protoc.* 2016;11: 1264–1279. doi:10.1038/nprot.2016.066
71. van Dijk D, Sharma R, Nainys J, Yim K, Kathail P, Carr AJ, et al. Recovering Gene Interactions from Single-Cell Data Using Data Diffusion. *Cell.* 2018;174: 716–729.e27. doi:10.1016/j.cell.2018.05.061
 72. Gut G, Tadmor MD, Pe’Er D, Pelkmans L, Liberali P. Trajectories of cell-cycle progression from fixed cell populations. *Nat Methods.* 2015;12: 951–954. doi:10.1038/nmeth.3545
 73. Spitzer MH, Gherardini PF, Fragiadakis GK, Bhattacharya N, Yuan RT, Hotson AN, et al. An interactive reference framework for modeling a dynamic immune system. *Science (80-).* 2015;349. doi:10.1126/science.1259425
 74. O’Connell MP, Marchbank K, Webster MR, Valiga AA, Kaur A, Vultur A, et al. Hypoxia induces phenotypic plasticity and therapy resistance in melanoma via the tyrosine kinase receptors ROR1 and ROR2. *Cancer Discov.* 2013;3: 1378–1393. doi:10.1158/2159-8290.CD-13-0005
 75. Garraway LA, Widlund HR, Rubin MA, Getz G, Berger AJ, Ramaswamy S, et al. Integrative genomic analyses identify MITF as a lineage survival oncogene amplified in malignant melanoma. *Nature.* 2005;436: 117–122. doi:10.1038/nature03664
 76. Konieczkowski DJ, Johannessen CM, Abudayyeh O, Kim JW, Cooper ZA, Piris A, et al. A melanoma cell state distinction influences sensitivity to MAPK pathway inhibitors. *Cancer Discov.* 2014;4: 816–827. doi:10.1158/2159-8290.CD-13-0424
 77. Porporato PE, Dhup S, Dadhich RK, Copetti T, Sonveaux P. Anticancer targets in the glycolytic metabolism of tumors: A comprehensive review. *Front Pharmacol.* 2011;AUG. doi:10.3389/fphar.2011.00049
 78. Gupta SC, Sundaram C, Reuter S, Aggarwal BB. Inhibiting NF- κ B activation by small molecules as a therapeutic strategy. *Biochimica et Biophysica Acta - Gene Regulatory Mechanisms.* 2010. pp. 775–787. doi:10.1016/j.bbagr.2010.05.004
 79. Vogel CJ, Smit MA, Maddalo G, Possik PA, Sparidans RW, van der Burg SH, et al. Cooperative induction of apoptosis in NRAS mutant melanoma by inhibition of MEK and ROCK. *Pigment Cell Melanoma Res.* 2015;28: 307–317. doi:10.1111/pcmr.12364
 80. Atefi M, Avramis E, Lassen A, Wong DJL, Robert L, Foulad D, et al. Effects of MAPK and PI3K pathways on PD-L1 expression in melanoma. *Clin Cancer Res.* 2014;20: 3446–3457. doi:10.1158/1078-0432.CCR-13-2797
 81. Sommer C, Straehle C, Kothe U, Hamprecht FA. Ilastik: Interactive learning and segmentation toolkit. *Proceedings - International Symposium on Biomedical Imaging.* 2011. pp. 230–233. doi:10.1109/ISBI.2011.5872394
 82. Li G, Bethune MT, Wong S, Joglekar A V., Leonard MT, Wang JK, et al. T cell antigen discovery via trogocytosis. *Nat Methods.* 2019;16: 183–190. doi:10.1038/s41592-018-0305-7